Design, Development and Testing of Metal Hydride based Cooling Systems for Stationary and Mobile Applications

A thesis submitted in partial fulfilment of the requirements for the degree of

Doctor of Philosophy

Submitted by

R. Nithin Narmada

(Roll No. 146103007)

Department of Mechanical Engineering

Indian Institute of Technology Guwahati

Guwahati – 781039, Assam, India

April 2021

Department of Mechanical Engineering

Indian Institute of Technology Guwahati

Guwahati-781039, Assam, India

THESIS CERTIFICATE

This is to certify that the work contained in this thesis entitled **Design, Development and Testing of Metal Hydride based Cooling Systems for Stationary and Mobile Applications**, being submitted by Mr. R. Nithin Narmada (Roll. No. 146103007) for the award of the degree of **Doctor of Philosophy**, is a record of bonafide research carried out by him under my guidance and supervision at the Department of Mechanical Engineering, Indian Institute of Technology Guwahati. The work embodied in this thesis has not been submitted to elsewhere for the award of any degree or diploma.

Dr. P. Muthukumar

Professor

Department of Mechanical Engineering

Indian Institute of Technology Guwahati

Guwahati-781039, Assam, India

April 2021

Department of Mechanical Engineering

Indian Institute of Technology Guwahati

Guwahati-781039, Assam, India

STATEMENT

This is to certify that I have carried out the research work in this thesis entitled **Design, Development and Testing of Metal Hydride based Cooling Systems for Stationary and Mobile Applications** under the guidance of **Prof. P. Muthukumar**, at the Department of Mechanical Engineering, Indian Institute of Technology Guwahati. The results documented in this thesis are achieved by me and have not been submitted elsewhere for award of any degree.

In keeping with the general practice of reporting scientific observation, due acknowledgement has been made wherever the work described is based on the findings of other investigations.

R. Nithin Narmada

Roll. No.: 146103007

Centre for Energy

Indian Institute of Technology Guwahati

Guwahati-781039, Assam, India

April 2021

Dedicated to

my family, teachers and friends

for their steadfast trust, guidance and support

ACKNOWLEDGEMENTS

First and foremost, I express my sincerest gratitude to my supervisor Prof. P. Muthukumar, for his invaluable guidance with constant and patient support while supervising my pursuit of research. Through his vast knowledge and rich experience in the field of research, he has inspired me and guided me to find ways of approaching the problems and finding solutions. The continuous care along with variety of opportunities provided by him has helped me grow as a student and as a human. I am highly indebted to him for his untiring commitment and willingness to lead me through various hardships that are directly and indirectly associated with the academic growth. I am forever obligated to him for the trust he placed in me that has resulted in the successful conclusion of this thesis research and the holistic growth of myself.

I am tremendously grateful to my doctoral committee members, Prof. U.K. Saha, Prof. Amaresh Dalal and Dr. R. Anandalakshmi for providing me with their indispensable suggestions and insightful critiques that has helped me shape my path of research undertaking. I am particularly thankful to Dr. C. Somayaji, for his continuous directions that helped me during the earlier days of research. I am grateful to Dr. S. Senthilmurugan for the valuable opportunity presented by him. I convey my heartfelt thanks to Dr. A K. Dass and Dr. S. K. Dwivedy (ex. HOD) and Dr. S. Senthilvelan (HOD) for providing all the facilities and opportunities needed during my research work, and financial support extended by the Department of Mechanical Engineering. I take this opportunity to thank all the faculty members and staff for valuable teachings and discussion that were ingrained as part of my learning curve. I would further thank the Institute and the authorities for supporting me during this strenuous journey.

I convey my earnest thanks to the Department of Science and Technology, Government of India, for their financial support (Project no. DST/IMRCD/BRICS/PilotCall2/RICS-MH/2018(G)). I am thankful to Council of Scientific and Industrial Research, Government of India, for providing me with travel grant under Travel Grant and Symposia Management Scheme (Sanction No. TG/10043/18-HRD) for presenting my research in 10th International Conference on Applied Energy 2018. I am deeply grateful to Dr. A. Mani, Professor, Department of Mechanical Engineering, Indian Institute of Technology Madras, for directing me to undertake the first step towards research. I convey my thanks to Mr. D. Chetri, Mr. Nip Borah and Mr. R. Saikia for their help and suggestions for clearing various bottlenecks encountered in implementation of the research work. I would like to thank Mr. Jogan, Mr. Hemant and Mr. Satyajit in helping me set up my experimental components.

I am specially thankful to Mr. A. Prabhakaran and his firm (M/s Shakunth Aqua Products, Chennai) for fabrication of reactors that are custom made and required special care and attention in terms of workmanship. In particular, I am thankful to Mr. Raja Ganesan, Mr. Prakash, Mr. Dass, Mr. Raju, Mr. Suresh and Mr. Antony for their skilled workmanship that converted my conceptual designs into efficient real world reactors.

I express my sincere thanks to Dr. S. Anbarasu for teaching the basics of reactor design and fabrication insights that helped me develop my designs. I am further thankful to the past and present members of my fellow metal hydride research team comprising of Mr. J. Sunku Prasad, Mr. Alok Kumar, Mr. Sayantan Jana, Mr. P. Vivek Selvam, Mr. Manojkumar S. Patil, Mr. K. Malleswararao and Mr. Abhishek Parida for their constant support as friends and colleagues, facing the same hardships and assisting without hesitation, which has helped to progress my

research. I am further thankful to my seniors and lab mates including Dr. Ch.C.R. Rao, Dr. K. Vigneshwaran, Dr. Lav Kr. Kaushik, Dr. Devakanta Rabha, Dr. H. Niyas, Dr. B. Kiran Naik, Dr. Sangjukta Devi, Dr. Jasinta P Ekka, Dr. DVN Lakshmi, Mr. G. Sureandhar, Mr. Gurpreet Singh Sodhi, Mr. Viswanth, Mr. Mrinal Bhowmik, Ms. Sunita Deb, Mr. Arunkumar, Ms. Pratibha Maurya and Mr. Pratap for their constant support and valuable friendship. I express my thanks to Wg Cdr. Chandru, Dr. Arunkumar C., Dr. D. Thiagarajan, Dr. Johnney M., Dr. Vignesh Babu, Dr. Dhamodharan, Mr. C.K.R. Avinash, Mr. Md. Tariq Hassan, Mr. Nirmal M., Mr. Jyothis A and Mr. Senthil S. for making the time spent in this Institute, a memorable experience.

I express my warm gratitude to Dr. Abdurahiman, Mrs. Usha Krishnan, Ms. Namita and Mr. V. Sriram, whose continuous love and support gave me the motivation to complete the thesis work. I am taking a moment to thank my father, Dr. P. Raju, for helping me reach the state I am today through his consistent life changing thought processes and approach to life in itself, for his constant vigilance and directions that has paved my way. As an epitome of my gratefulness, I am rendered wordless to express my deepest gratitude for my mother, Ms. Vetrichelvi and my sister, Ms. R. Narmada Nithin whose love, care and support has nurtured me, strengthened me and empowered me to be the person I am today. I thank the innumerous elders, pioneers and leaders who in the walks of academic research, social justice and environmental defence have paved the way for countless persons like me to reach this stage of life.

Sincerely,

R. Nithin Narmada

April 2021

ABSTRACT

In the present energy scenario, increase in global warming and energy demand are two major issues growing at an alarming rate, despite various measures being taken to control them. Despite being environmentally harmful, fossil fuels play a major role in meeting today's world energy requirement. With the depletion of fossil fuels and drastic rise in greenhouse gases emissions, there is an urgent need for shifting towards clean and renewable energy based technologies, which generate near zero emission of greenhouse gases. Hydrogen is such a fuel (energy carrier) that contains an enormous amount of energy per unit mass and meets all the above criteria. Storage of hydrogen is the most challenging task in Hydrogen Economy. Solid state hydrogen storage in the form of metal hydrides (MH) offers several benefits over the other modes of storage. In addition, interaction of hydrogen with MH offers multiple thermal management applications for which MH can be tailor made for offering high volumetric energy density. A rigorous research work is being carried out to implement MH in on-board applications, which demands compact and lighter in mass MH reactors. Further, there is a minimal issue of leakage as hydrogen in MH is a solid solution. Because of the promising nature of MH, the research in this field has been paced up in this century. Another major advantage of MH based storage system is the availability of auxiliary cooling effect during discharge of hydrogen. The major bottleneck for the commercialization of MH based systems is its low gravimetric storage capacity. This induces the need for focused research in the field of MH based thermal machines.

The widely preferred cooling mechanism is the one based on vapour compression refrigeration system (VCRS), which utilizes chemicals as working fluid and high grade energy input for its operation. There is a dire need for sorption based mechanism that utilizes low grade energy such as MH based thermal machines. However, they offer low COP and low specific alloy outputs. Compressor driven metal hydride based cooling systems (CDMHCS) are a preferable alternative, and can compete with VCRS as green energy alternative by utilizing input power sourced from renewable energy. Another comparative advantage of CDMHCS is that it employs hydrogen as working fluid, which is ecofriendly in contrast to most of refrigerants. There is a profound lack of practically adaptable strategy when it comes to the design of

compact reactors with enhanced heat transfer characteristics. Some of the devised approaches are too complex and demand higher manufacturing cost. Improvement in heat and mass transfer characteristics of metal hydride bed is highly emphasized. Numerous experimental investigations were conducted to study the effect of various parameters on the performance of the MH based thermal machines. However, experimental investigations conducted on industrial scale MH based hydrogen storage and cooling systems are very limited. Experimental investigations reported on CDMHCS were quite inadequate compared to the demand of these systems. There is a great scope for improvement in terms of its COP and specific cooling output.

The major objectives of the present research has been framed to address this research gap: (i) to select alloys that are suitable for operation in near ambient conditions and are better candidates for metal hydride based storage and cooling systems; (ii) to develop a novel design methodology that balances the enhanced heat transfer characteristics of the hydrogen storage or thermal management systems against the parasitic thermal mass; (iii) to predict and analyze the storage performance and heat transfer characteristics of reactor designed based on developed methodology using valid numerical model; (iv) to develop an experimental set-up and conduct parametric and performance investigations on MH based cooling system considering industrial scale reactor; and (v) to develop an experimental set-up and conduct performance investigation on metal hydride based compressor driven cooling system, employing the designed reactors.

A novel set of arithmetic correlations are developed as a base guiding principle for the design of cylindrical reactors with embedded cooling tubes (ECT). The underlying principle of this design methodology is to evenly distribute the ECT within the MH bed, thereby reducing bed thickness while balancing the design against the resulting parasitic thermal mass of the empty reactor. Performance of these designed reactors are analysed by developing thermal models and solving them numerically. While modelling the MH reactor, gas transport phenomenon within MH bed, combined heat and mass transfer characteristics arising from absorption and desorption reaction, variable wall convective boundary at ECT interface and variation of hydrogen concentration within the bed are taken into consideration. Based on the proposed design methodology, lab scale prototype with 41 ECT reactor is designed and compared with 60 ECT and 55 ECT reactors. The absorption performance of these reactor designs are analysed considering 4 kg of $MmNi_{4.7}Fe_{0.3}$ at supply condition of 50 bar, 25 °C and 24 lpm HTF flow

rate, while the desorption performance is analysed at 25 °C and 15 lpm of HTF flow rate. The influence of reactor design is found to be more prominent towards the temperature distribution within bed than the hydriding rate. The bed temperature variation within bed of 41 ECT reactor is seen to be uniformly distributed as opposed to the cases of 55 ECT and 60 ECT reactors. During desorption, the drop in average bed temperature of 41 ECT reactor is perceived to be sharper which results in HTF outlet temperature of 23 °C. Through the design methodology, industrial scale reactors with 50 kg alloy capacity are developed and their storage performance is analysed numerically. By selecting the best design among them, the effects of varying supply pressure (5 to 35 bar), absorption temperature (20 °C to 35 °C) and HTF flow rate (10 lpm to 35 lpm) on the hydriding performance of $LaNi_{4.7}Al_{0.3}$ (50 kg) are analysed. Among the designs, 6 inch reactor with 99 ECT depicts best hydriding rate and heat transfer characteristics. It achieves total hydrogen storage capacity (HSC) of 1.29 wt% in 2060 s, while 80% of HSC is attained within 430 s. The numerical results are validated against experimental results and good agreement is observed between them.

From the analysed reactor designs, lab scale and industrial scale reactors were fabricated for open cycle MH based hydrogen storage and cooling systems (MHHSCS) and closed cycle CDMHCS. The 55 ECT reactor was fabricated and filled with 4 kg of $MmNi_{4.7}Fe_{0.3}$. Upon activation, the hydriding performance of this lab scale prototype was analysed at different supply pressures (10 bar to 70 bar) and absorption temperatures (5 °C to 25 °C). The dehydriding rate and cooling performance of this lab scale reactor were investigated at different desorption temperatures of 5 °C to 30 °C with HTF flow rate of 15 lpm. At 25 °C and 24 lpm flow rate, supply pressure below 40 bar resulted in poor hydriding rate. The storage capacity was increased by ~3.25 times in 676 s when supply pressure was increased from 40 bar to 70 bar. The amount of cooling was increased by 25.5% when desorption temperature was increased from 5 °C to 25 °C at 15 lpm flow rate, with peak output and SCP of 2.3 kW and 279 W/kg of cooling alloy, respectively. The desorption was found to be so rapid that ice formation on the periphery of reactor surface was observed during reaction. When the study was extended to industrial scale reactor, the performance was comparatively low. The effect of varying supply pressure (40 bar to 70 bar) and the effect of varying desorption temperature (5 °C to 25 °C) on the respective absorption and desorption performances of industrial scale model were also investigated. Hydrogen storage capacity of 0.75 wt% (~300 g) was attained by the industrial scale reactor within 364 s. The desorption performance is comparatively slow in the industrial scale reactor, as the bulk of the alloy causes an inherent limitation leading to slower

desorption kinetics. At 25 °C and 50 lpm flow rate, 4088.6 kJ of cooling was produced in 3360 s, at an average rate of 1.2 kW. By utilizing two identical lab scale ECT reactors, CDMHCS of different alloys were developed and their performance during quasi continuous cold generation was analysed. The experimental setup of CDMHCS was formulated with two identical 60 ECT reactors filled with 2.75 kg of $LmNi_{4.91}Sn_{0.15}$ to analyse the COP and SCP of the system. The operating parameters including cycle time (4 min to 16 min), cold fluid flow rate (4 lpm to 16 lpm), refrigeration temperature (10 °C to 20 °C) and sink temperature (25 °C to 35 °C) were varied. For $LmNi_{4.91}Sn_{0.15}$ based CDMHCS, increase in cycle time from 4 min to 8 min resulted in corresponding reductions of 43% and 46% in COP and SCP. Similar trend was observed with increase in cold fluid flow rate as well. Increase in refrigeration temperature from 10 °C to 20 °C at sink temperature of 25 °C, resulted in maximum increase in COP and SCP by 64.2% and 70.3%, respectively. The operating condition of 20 °C refrigeration temperature and 25 °C sink temperature with cold fluid flow rate of 8 lpm in 8 min cycle resulted in maximum COP and SCP values of 2.2 and 53.5 W/kg of total alloy, respectively. When the investigation was extended to $La_{0.7}Ce_{0.1}Ca_{0.3}Ni_5$ based CDMHCS, it was noted that the cooling output rate was steady due to steady dehydriding rate of the alloy. Due to this steady rate of desorption, the cooling performance was not as robust as that of above system, even though 41 ECT reactor depicted better cooling performance than 60 ECT. Maximum COP of 0.53 and SCP of 66.2 W/kg were achieved at cycle time of 8 min with cold fluid flow rate of 6 lpm, refrigeration temperature of 25 °C and sink temperature of 25 °C.

For $MmNi_{4.7}Fe_{0.3}$ based HSCS, absorption pressure of 50 bar at ambient temperature with HTF flow rate of 25 to 30 lpm resulted in commendable storage performance. Desorption at same temperature and flow rate would led to ample cooling output. This system is suitable for fuel cell based vehicles and stationary fuel stack structures, wherein hydrogen is supplied at pressure above 70 bar. These applications would benefit from the auxiliary cooling produced by the system. By developing CDMHCS with ECT reactors, small scale air conditioners and on-board cooling systems are a definite possibility, which would be competitive with conventional VCRS system. With near ambient sink temperature and lower cold fluid flow rate and shorter cycle time, competitive COP and SCP can be achieved with minimum energy input.

NOMENCLATURE

Alphabets

A	:	Number of metal atoms
b	:	Bed thickness [mm]
c	:	Concentration, [H/M ratio]
C	:	Reaction rate constant [s^{-1}]
c_p	:	Specific heat capacity [J/kg K]
D	:	Diameter [mm]
E	:	Activation energy [J/mol H_2]
Em	:	Energy meter reading [kWh]
h	:	Outer radius of porous filter [mm]
HTF	:	Volumetric heat transfer fluid flow rate [lpm]
K	:	Permeability [m^2]
k	:	Thermal conductivity [W/m K]
L	:	Length [mm]
M	:	Molecular weight [g/mol]
m	:	Mass [kg]
$\dot{m}$	:	Mass flow rate [kg/s]
N	:	Number of tubes
n	:	Number of moles [mol]
P	:	Pressure [bar]
P_s	:	Supply pressure [bar]
p	:	Pitch [mm]

Q	:	Volumetric heat [W/m^3]
$\dot{Q}$	:	Rate of heat transfer [W]
Q_{cold}	:	Cumulative cooling [kJ]
R	:	Radius [mm]
R_u	:	Universal gas constant [J/mol K]
r	:	Radius of tubes [mm]
s	:	Number of stacks
T	:	Temperature [°C]
t	:	At any given time [s]
t_{wall}	:	Thickness of tubes [mm]
U	:	Overall heat transfer coefficient [W/m^2 K]
$\vec{u}$	:	Velocity vector [m/s]
V	:	Volume [m^3]
$\tilde{V}$	:	Volumetric flow rate [m^3/s]
W_c	:	Compressor work [kW]

Greek symbols

ΔH	:	Enthalpy of reaction [J/mol H_2]
ΔS	:	Entropy of reaction [J/mol H_2 K]
ΔT	:	Difference in temperature [°C]
ε	:	Porosity
ζ	:	Rate of mass of hydrogen [kg/m^3 s]
μ	:	Dynamic viscosity [Pa s]
ρ	:	Density [kg/m^3]
ρ_{ss}	:	Effective density of MH at saturation state [kg/m^3]
ρ_0	:	Effective density of MH [kg/m^3]
σ_h	:	Allowable stress [MPa]

φ_s	:	Slope factor
φ_o	:	Slope constant
φ	:	Hysteresis factor

Subscripts

a	:	Absorption, Alloy
ang	:	Angular
avg	:	Average
cold	:	Cooling
CR	:	Critical
cy	:	Cycle
d	:	Desorption
e	:	Effective
end	:	Final
eq	:	Equilibrium
eqi	:	Initial equilibrium
f	:	Heat transfer fluid
g	:	Gas
hcy	:	Half cycle
i	:	Inner
ini	:	Initial
j	:	Positive integer
max	:	Maximum
MH	:	Metal hydride alloy
o	:	Outer
op	:	Outer periphery of porous filter
R	:	Metal reactor
r	:	Radial

re	:	Radial at end
rs	:	Radial near supply
s	:	Solid phase
t	:	At given time
total	:	Total
vavg	:	Volume averaged
grad	:	Gradient
0	:	Ambient, initial

Abbreviations

CDMHCS	:	Compressor Driven Metal Hydride Based Cooling System
CDMHHP	:	Compressor Driven Metal Hydride based Heat Pumps
COP	:	Coefficient of Performance
DOE	:	Department of Energy
ECT	:	Embedded Cooling Tubes
HTF	:	Heat Transfer Fluid
HSC	:	Hydrogen Storage Capacity
MH	:	Metal Hydride
MHCS	:	Metal Hydride based Cooling Systems
MHHP	:	Metal Hydride based Heat Pumps
MHHSCS	:	Metal Hydride based Hydrogen Storage and Cooling Systems
SCP	:	Specific Cooling Power
PCT	:	Pressure-Concentration-Temperature

TABLE OF CONTENTS

LIST OF FIGURES

LIST OF TABLES

CHAPTER 1

INTRODUCTION

1.1 Energy scenario

In the recent times, the rapid advancement in technology is leading to significant increase in global energy demand. The major contribution of energy supply to meet this demand is arising from conventional energy sources. The utilisation of these fossil fuels lead to emissions of greenhouse gases and pollutants that deteriorate the environment and result in global warming. The fossil fuel reserves are limited and depleting faster, which is an additional concern. Hence, the need of the hour is the replacement of fossil fuels by renewable energy based technologies in a global scale. The International Renewable Energy Agency has drafted an indepth global energy modelling framework – REmap 2050, to map out the measures needed to increase the share of renewables in global energy supply while reducing the CO_2 emissions (Gielen et al., 2019). Under current and planned energy policies, the energy related CO_2 emissions would increase to 35 Gt/yr in 2050. The emissions need to be reduced to 9.7 Gt/yr by 2050 to limit

the global warming to well below 2 °C, as agreed upon by 196 countries in the Paris Agreement (UNFCCC, 2016). As represented in Fig.1.1, the renewable energy share must increase in total energy supply to achieve the reduction of 94% in CO_2 emissions. By combining renewable energy and energy efficiency along with end user electrification, the share of renewable energy in total energy supply would be increased from 14% in 2015 to 63% in 2050. A six-fold increase in the current annual growth rate of renewable energy supply is needed to achieve this target.

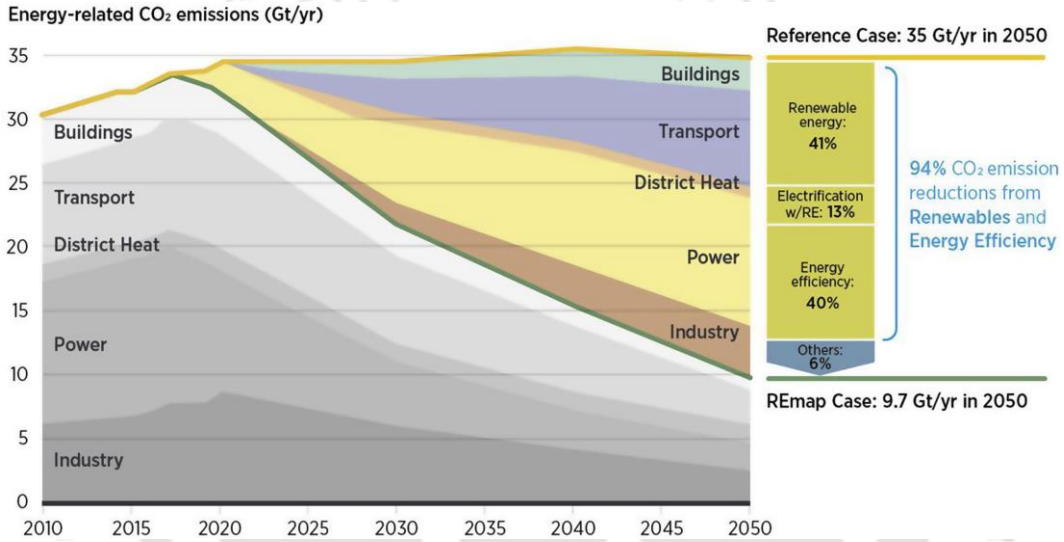

Fig.1.1. The current and projected energy related carbon dioxide emissions

(Gielen et al., 2019)

Towards meeting the nationally determined contributions as part of the Paris Agreement, India had increased its clean energy research, development and deployment spending from 58.59 million USD in 2016 to 110.61 million USD in 2018, through its various governmental agencies (IEA, 2020). As of 2019, the installed power capacity from renewables increased by 200 GW globally, with major contribution from solar photovoltaics. Adaptation of climate emergency by various nations in their policymaking has given the necessary drive towards the improvement in share of renewable energy. The alternatives and cost reduction solutions being developed by the research community are another prominent factor in this improvement. A

total spending of 418 million USD has been reported by private sector industries active in energy technologies, along with 900 million USD investment towards the research on efficient and alternate fuel cell vehicles by automobile sector. This highlights the national and global shift away from the present hydrocarbon economy towards the low carbon economy. The renewable sources and their energy supply are abundant and their utilisation results in near zero emission of greenhouse gases. However, they are highly intermittent in nature, driving researchers to develop utilisation and storage technologies for their efficient implementation.

1.2 Hydrogen economy

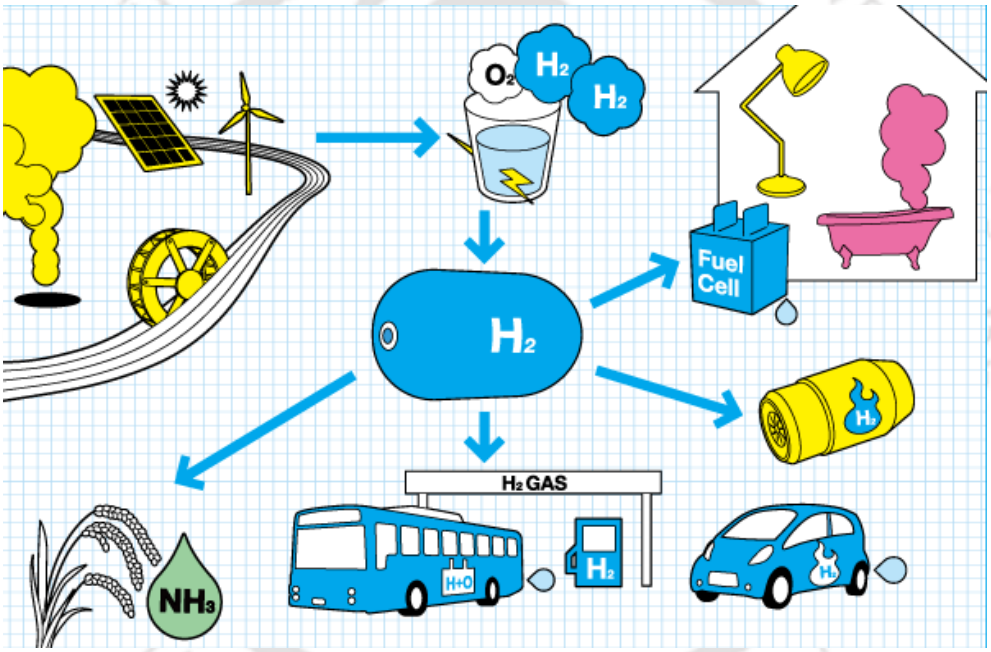

Fig.1.2. Versatility of hydrogen (Ariizumi, 2010)

The shift in the fuel research is focussed towards carbon neutral fuel, thereby eliminating emission of greenhouse gases. Wood, which is the primitive fuel, has higher ratio of carbon to hydrogen atoms (10 atoms of C to 1 atom of H) than coal (2 atoms of C to 1 atom of H). Subsequent evolution of fuels to petroleum and natural gas have further reduced carbon to hydrogen atom ratio (Balachandar et al., 2013). With decrease in carbon to hydrogen atom ratio in each fuel, its energy efficiency increased as well as the carbon dioxide emissions decreased

prominently. Following this trend, hydrogen with zero carbon atoms emerges as the ultimate fuel. The Lower Heating Value of hydrogen is 119.9 MJ/kg, which is 2.7 times that of gasoline (Häussinger et al., 2000). Considering this aspect, researches have been directed towards the development of hydrogen internal combustion engines. Understanding the engine efficiency and emissions, and hardware development for commercialisation are the primary focus of these researches (Yip et al., 2019). Parallelly, hybridisation of existing compressed natural gas fuel engines with hydrogen mixtures is being taken up by few automobile industries. This hybridisation has resulted in reduced emissions and energy consumption (Gupta et al., 2020; U.S. Department of Energy, 2009).

Apart from fuel applications, hydrogen is an excellent energy carrier as well. Energy can be converted into hydrogen and then can be stored, transported, utilised and reconverted back at the user end, similar to electricity. The additional advantage of hydrogen as an energy carrier is its high energy content per unit mass. At present, majority of hydrogen production is from fossil fuels through thermal and thermochemical conversion processes. Additionally, hydrogen production through biochemical and photochemical processes are gaining traction due to the associated environmental advantages. Though hydrogen production through water electrolysis is energy intensive in nature, off-peak generation of power from renewable energy sources such as solar energy, wind energy, geothermal energy, tidal energy, etc. would lead to cleaner production process (Aydin et al., 2021; Yukesh Kannah et al., 2021). Similarly, supply of hydrogen to fuel cells at the user end results in power generation with clean water as the only by-product. This completes the clean energy cycle of hydrogen economy.

1.3 Hydrogen storage technologies

The storage of hydrogen is the major bottleneck when it comes to implementation of hydrogen economy. It is the lightest gas in the atmosphere, with a density of 0.0838 kg/m^3 at Normal Temperature and Pressure (U.S. Department of Energy, 2015a). This results in a very low

volumetric energy density and poses a major challenge when the question of storage and transportation of hydrogen is encountered. There is a need for a compact, lightweight, safe and economical storage solution, which would help in realising the stationary and mobile applications of hydrogen. Following are the broad areas of ongoing research that is focused upon overcoming this bottleneck (Moradi and Groth, 2019):

- Compressed hydrogen gas
- Liquified hydrogen
- Cryo-compressed hydrogen
- Material based hydrogen storage

Though the approaches are different, their solution methodology is focussed towards a common goal. United States Department of Energy (DOE) has set targets for automotive, material handling and portable power applications (U.S. Department of Energy, 2015b). For instance, the DOE had fixed a system gravimetric capacity of 5.5 wt% and volumetric capacity of 40 g/L as the on-board hydrogen storage target, to be achieved by 2020. The DOE has further fixed an ultimate target so as to achieve a refuelling distance of at least 500 km for light motor vehicles (Zacharia and Rather, 2015).

Compressed hydrogen storage is a commercially viable physical storage method wherein hydrogen gas is compressed to 350 to 700 bar pressure and stored in tanks termed as Type IV tanks. These are carbon fiber composite tanks with high density polymer linings which can withstand this enormous pressure. Base case gravimetric capacities of 5.5 wt% and 5.2 wt% have been achieved in 350 bar and 700 bar tanks, respectively, to store 5.6 kg of usable hydrogen (Hua et al., 2011). Most of the commercial vehicles with on-board compressed hydrogen storage are implemented with Type IV 700 bar tanks (Nonobe, 2017; Sinigaglia et al., 2017). The system volumetric capacities of 17.6 g/L and 26.3 g/L have been attained in 350 bar and 700 bar tank designs, which are well below 2020 DOE target. The second major

challenge being addressed in this technology is the high compression energy. Considering real-time systems, the estimated work of compression was 15.5% of Lower Heating Value (Jensen et al., 2007). Apart from these two concerns, the thermal management of the storage tank during fast filling has to be addressed as well, wherein three main thermodynamic phenomena causes a rise in gas temperature (Liu et al., 2010).

Comparatively, liquefying and storing hydrogen leads to higher volumetric capacity, as high as 70 g/L (Ren et al., 2017), which is on par with the ultimate DOE target. However, the liquid hydrogen has to be maintained at -252 °C at ambient pressure, due to the very low critical temperature of hydrogen, which is -240.15 °C (U.S. Department of Energy, 2015c). This has been achieved by utilising double walled metallic vessels with evacuated space in between, and insulating the inner vessel, which lead to vacuum superinsulation. The primary disadvantage of this technology is the energy consumption of the liquefaction process in itself. Practically, the energy consumption in the liquefaction process ranges between 37% and 45% of Lower Heating Value (Jensen et al., 2007). Even with precooling and utilisation of mixed refrigerant, the specific energy consumption is still about 21% of Lower Heating Value. The secondary concern is the boil-off losses, wherein the surrounding heat is utilised by the liquid hydrogen to evaporate (Züttel, 2003). The loss is the function of the size, shape and insulation of the storage vessel, and for smaller tanks that are used for on-board applications, the boil-off losses could be 2 – 3% per day, making the technology very energy-intensive.

By combining the positive features of both the above technologies, cryo-compressed storage is being developed. Cooling the compressed hydrogen gas, causes it to become denser and ultimately reduces the pressure inside the vessel. For instance, 750 bar is required at room temperature to store 4.1 kg of hydrogen gas in 100 L. On the other hand, compressed cryogenic storage requires 150 bar to store the same volume at -196 °C (Zhou et al., 2004). However, this technology requires further investigation for it to be commercially viable. Alternatively, when

liquid hydrogen is stored in cryogenic pressure vessels, it exists with higher density due to increased compressibility. The fill density increases to 87 g/L at 240 bar from 70 g/L at 1 bar, at a cryogenic temperature of -253 °C. Further research in optimizing the operating range with more practical day-to-day performance analysis would help this technology become commercial and ecological success.

The above-discussed storage technologies store hydrogen effectively by altering its physical characteristics such as pressure, temperature and phase. When the molecular forces of attraction (Van der Waals), in case of physisorption, and the chemical bonds, in case of chemisorption, are instrumental in storing the hydrogen, then they are termed as material based storage methods. Porous materials with high surface area and an affinity towards hydrogen have been investigated as potential adsorption storage materials. The promising adsorbent materials include metal organic frameworks, carbon-based materials, zeolites and microspheres. As it is a surface phenomenon, the hydrogen binding energy is comparatively low, which facilitates faster reaction kinetics and does not require complex auxiliary thermal management systems (Zhang et al., 2016). However, the low binding energy also results in low temperature requirement for storage. This, combined with comparatively low gravimetric and volumetric capacity, necessitates further research among these materials. When compared with the predominantly available adsorption based storage technologies, carbon nanotube composites exhibit better storage capacity and are of more promising venture. Armchair carbon nanotubes depicted better performance with total hydrogen uptake of 5.5 wt% at ambient conditions (Assfour et al., 2011). The method of synthesizing these composites greatly influences the hydrogen uptake and stability, thereby prompting future research towards stability and operability at ambient conditions for practical utilisation (Rather, 2020).

Compared to these physisorption based storage materials, chemisorption based storage materials are more stable prompting detailed research on their synthesis and utilisation.

Complex hydrides are ionic compounds derived from hydrogen containing anions such as alanates, nitrides, borohydrides and beryllium hydrides, wherein hydrogen is covalently bonded to the central atom in the complex. The complex hydrides are formed between these anions and metal cations, such as Li^+, Na^+, K^+, Mg^{2+} and Ca^{2+} (Cheng et al., 2017; Sakintuna et al., 2007). Though complex hydrides are characterized by high theoretical gravimetric capacity, their reversibility is a big hurdle, especially in the operable range. Hydrogen can also be stored in a liquid organic hydrogen carrier. The organic carrier 1-methylindole depicted gravimetric capacity of 5.76 wt% when investigated and the volumetric capacity was 59 g/L (Yang et al., 2018). Hydrogenation occurred at 60 bar and 130 °C with 5 wt% Ru/Al_2O_3 catalyst, while dehydrogenation occurred at 160 °C to 190 °C with 5 wt% Pd/Al_2O_3 catalyst. Despite their commendable storage capacity, their operating range and reaction kinetics have to be improved in a cost effective manner for them to be viable storage technology.

In comparison, intermetallic hydrides are chemical compounds formed by hydrogen with metals or metal alloys and are interestingly reversible in nature (Sastri et al., 1998). The advantage of metal hydride (MH) alloys is that their composition can be tailor made to possess operating conditions favourable to specific applications. One of the most widely investigated MH alloy has been $LaNi_5$, which forms hydride $LaNi_5H_6$. At 3.7 bar and 40 °C, it resulted in a volumetric capacity of 115 g/L and gravimetric capacity was 1.6 wt% (Nazir et al., 2020). Comparatively, alkaline earth metal based alloys such as Mg_2Ni and Mg exhibited respective gravimetric capacity of 3.8 wt% and 7.6 wt%, which are highest reported value amongst MH (Bououdina et al., 2006). Compared to other storage methods, the ease of operation evident in MH based systems are well appreciated. In contrast, the heavier mass of the system is the primary hurdle in its practical applicability. The research of the present study provides a stepping-stone towards overcoming this hurdle.

1.4 Thermodynamics of metal hydrides

Metal hydrides formed by alkaline earth, transition and rare earth metals are of primary interest for their versatility in composition and resultant operating conditions for solid-state storage of hydrogen. The absorption reaction leads to formation of MH and is exothermic in nature, while the desorption of hydrogen from MH is an endothermic reaction, which can be represented as,

$$Metal + H_2 \underset{desorption}{\overset{absorption}{\rightleftharpoons}} MH + Heat \qquad \text{(Eqn.1.1)}$$

This reversible interaction of hydrogen with MH and the associated energy interactions project this technology for versatile hydrogen storage and thermal management systems. The absorption of hydrogen by MH alloy occurs in following two processes:

$$M + \frac{A}{2} H_2 \Leftrightarrow MH_A\,(\alpha - phase) \qquad \text{(Eqn.1.2)}$$

$$MH_A + \frac{B-A}{2} H_2 \Leftrightarrow MH_B\,(\beta - phase) \qquad \text{(Eqn.1.3)}$$

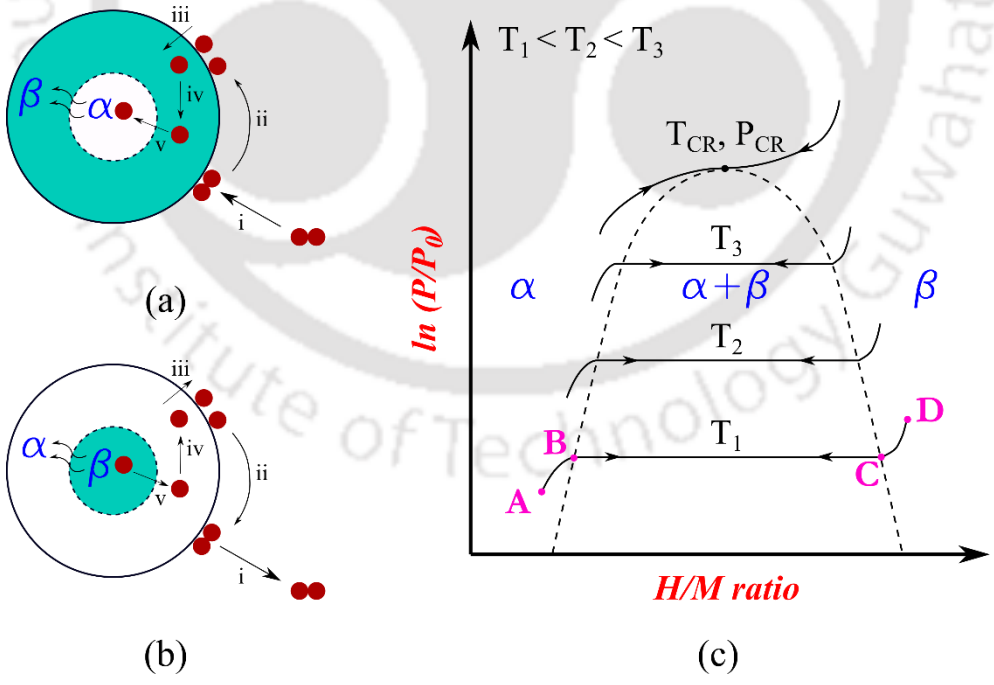

Fig.1.3. Reaction partial steps during (a) absorption and (b) desorption processes considering spherical particle, and (c) representation of an ideal Pressure-Concentration-Temperature diagram

Assuming metal particle to be spherical in structure with constant diameter, the hydride formation is considered to initiate at the outer surface (metal/gas interface) and the concentration gradient grows inward towards the center of the particle (Martin et al., 1996). At microscopic level, the absorption of hydrogen by metal particle occurs in five distinct stages, as depicted in Fig.1.3 (a):

i. physisorption of hydrogen molecules;
ii. dissociation of hydrogen molecules into individual atoms (chemisorption);
iii. diffusion of hydrogen atoms into the bulk through surface penetration;
iv. diffusion of hydrogen atoms through the hydride layer;
v. hydride formation at the interface of metal and hydride.

During α-phase, the hydrogen atoms occupy the interstitial sites of the metal lattice in a random fashion to form solid solution. Upon saturation, the hydrogen atoms form bond with metal atoms leading to lattice expansion and stable formation of hydride (β-phase). Concentration of hydrogen in MH is defined as ratio of hydrogen atoms to that of metal atoms per mole of alloy (H/M ratio). With increase in concentration, the thickness of β-phase grows inward transforming the α-phase. When the pressure, concentration and temperature are measured during an ideal absorption/desorption reaction, the resultant curves would be as represented in the ideal pressure-concentration-temperature (PCT) diagram in Fig.1.3 (c). The PCT curves have three distinct parts, viz. α-phase, (α+β) phase and β-phase. In region AB, two components (metal and hydrogen) and two phases (solid and gas) exists concurrently. Based on Gibbs' phase rule (Eqn.1.4), the degree of freedom is two (pressure and temperature).

$$f = C - p + 2 \qquad \text{(Eqn.1.4)}$$

Considering an isothermal experiment at constant temperature T_1, the amount of absorbed hydrogen is related only to the pressure and this relation obeys Sieverts' Law (Richmond et al., 2010).

This is represented as,

$$c_{H_2} \propto \sqrt{P_{H_2}} \qquad \text{(Eqn.1.5)}$$

Hence in α-phase, increase in pressure leads to a marginal increase in concentration. This corresponds to the initial steep slope (AB) in the ideal PCT diagram. At point B, saturation of hydrogen atoms at interstitial sites is initiated causing hydride formation. Transition region BC is termed as (α+β) phase, wherein two solid phases (metal and metal hydride) and one gas phase (hydrogen) exists concurrently. Hence, degree of freedom is one, which leads to a constant pressure condition. In essence, absorption reaction occurs at constant equilibrium bed pressure and this region is called plateau region. The width of this plateau determines the amount of hydrogen that is reversibly stored at constant pressure. As the temperature increases ($T_1 < T_2 < T_3$), the plateau pressure increases and the width of the plateau decreases, until the critical temperature (T_{CR}). At point C, α-phase has completely transformed into β-phase, signifying complete saturation state of hydride formation. Further addition of hydrogen in CD region results in sharp increase in pressure as per Sieverts' Law.

At critical temperature (T_{CR}), α-phase continuously converts to β-phase, without the benefit of the transition plateau region. Therefore, desirable MH should possess stable and wider plateau region at requisite operating pressure and temperature while its critical temperature must be very high. As depicted in Fig.1.3 (b), the desorption of hydrogen from MH occurs in reverse (steps v to i), transforming from β-phase to α-phase following the same principle. The PCT curves depicted in Fig.1.3 (c) are of ideal reactions, which are seldom realized in actual MH systems. PCT diagram of actual absorption/desorption reaction is represented in Fig.1.4 (a). There are two distinct deviations observed in actual reaction, namely sloping and hysteresis. Due to inherent impurities, stresses and surface inhomogeneities in the metal, different parts of it absorb hydrogen at different pressures, thereby depicting sloping instead of flat horizontal plateaus. The second effect is the hysteresis gap between absorption and desorption curves,

resulting in lower desorption pressure for same temperature. The most probable reason for this effect is the irreversible plastic deformation occurring in metal matrix due to lattice expansion during hydriding (Sastri et al., 1998). The relation between equilibrium bed pressure (P_{eq}) and temperature (T) is governed by van't Hoff equation. When relative pressure is plotted against inverse of absolute temperature for given MH, actual van't Hoff plot would be obtained, as depicted in Fig.1.4 (b).

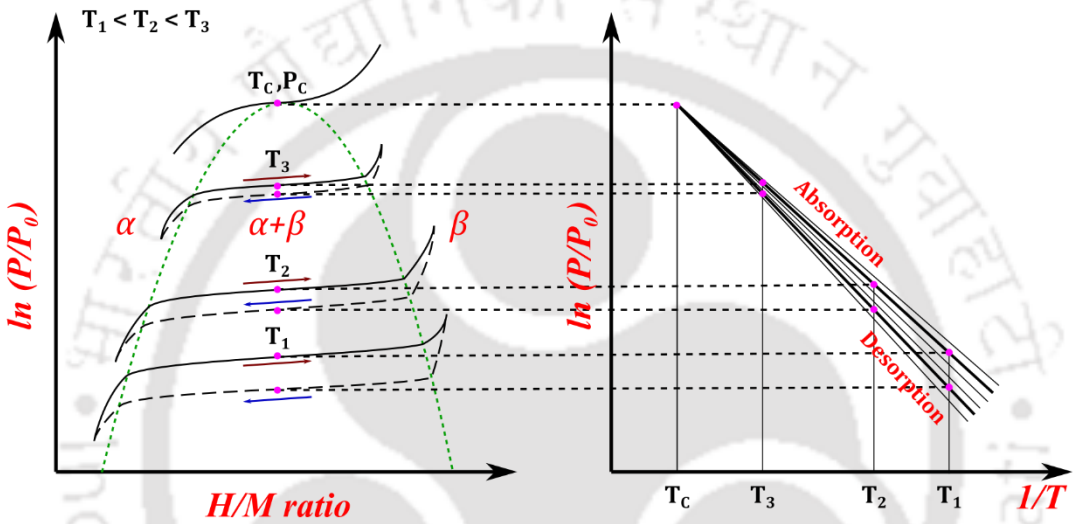

Fig.1.4. Representation of (a) actual Pressure-Concentration-Temperature diagram and (b) actual van't Hoff plot

As it can be observed, slight deviations in plot occur due to sloping and hysteresis. The negative slope of the plot represents the enthalpy of reaction (ΔH), while the intercept denotes entropy of the reaction (ΔS). Taking the effects of hysteresis and sloping into consideration, modified van't Hoff equation (Nishizaki et al., 1983) is considered in the present study to represent the thermodynamics of the reaction:

$$\ln\left(\frac{P_{eq}}{P_0}\right)=\left[\frac{\Delta S}{R_u}-\frac{\Delta H}{R_u T}+(\varphi_s \pm \varphi_0)\times\tan\left(\pi\left(\frac{c_t}{c_{end}}-\frac{1}{2}\right)\right)\pm\frac{\varphi}{2}\right] \quad \text{(Eqn.1.6)}$$

In this equation, P_0 denotes ambient pressure while c and c_{end} respectively represents concentration at any given time 't' and final concentration. The constants φ_s and φ_0 denote sloping factor and sloping constant while φ denotes hysteresis factor. The arithmetic sign '+' is considered during absorption reaction while the arithmetic sign '–' is considered during desorption.

1.5 Applications of metal hydrides

Depending upon the metal alloy composition, MH alloys can be predominantly categorized into AB, A_2B, AB_2, AB_3 and AB_5 types wherein the metal A facilitates the hydrogen storage capacity while the metal B influences the operating conditions and kinetics of the reaction (Sandrock, 1997). The metal A is generally from the group of lanthanide and rare earth metals (e.g. La, Ce, Pr, Nd) or alkaline earth metals (e.g. Mg, Ca), while metal B is generally from transition metals (e.g. Ti, V, Cr, Zr, Co). As MH are non-stoichiometric compounds, substitution of principle alloy metals (A or B) with other metals such as Al, Fe, Ni, Mn, etc. assists in reducing the effects of hysteresis or sloping and modifies plateau pressures favourably (Libowitz, 1962). Considering this versatility in alloy compositions resulting in tailor-made PCT characteristics, MH is proposed for various applications of thermal management along with hydrogen storage and utilisation.

As discussed in Section 1.3, MH are versatile solid state hydrogen storage solution with high volumetric energy density. Low temperature MH such as La, Ti and Zr based hydrides are preferred for their ease of operation in near ambient conditions. However, their gravimetric storage capacities are below 2 wt%. In contrast, Mg and Mg based MH possess storage capacities in the range of 5 – 7 wt%. However, their operating temperature is above 300 °C. The primary avenue for hydrogen storage application is in fuel cells for both stationary and mobile applications. Depending upon the type of fuel cell mechanism, the operating conditions vary widely, which in turn are met by suitable MH alloy (Lototskyy et al., 2017). Along with

these fuel cell applications, hydrogen compression is required at the filling stations. Thermally operated multistage hydrogen compressors can be constructed by careful selection of MH alloys for each stage based on their PCT characteristics (Muthukumar et al., 2012a). The hydrogen is pressurized by absorbing it at low pressure and low temperature, and desorbing it at higher pressure. With absence of moving parts and utilisation of low grade heat input, they are advantageous over their mechanical counterparts that require continuous maintenance. Another advantage of using MH based hydrogen compressor is that the purity of hydrogen improves. This has led to another niche application of hydrogen purification, which is required in various industrial applications. As the hydrogen is produced primarily from fossil fuels, there are lot of impure gases such as CO and CO_2. MH based purification is possible due to the fact that during absorption, only hydrogen is absorbed thereby separating it from the impurities (Grashoff et al., 1983). After flushing out the impure gases, pure hydrogen can be obtained upon desorption. Any negative effects on MH by the impurities can be counteracted by regeneration of the alloy.

Along with resourcefulness in hydrogen related applications, MH can be utilised for various thermal management applications by utilising the associated energy interactions during absorption and desorption. MH can store heat energy thermo-chemically in the form of enthalpy of formation (Lototskyy et al., 2015). It constitutes a coupled system with low temperature and high temperature MH alloys operating in conjunction. By utilising the available heat input from solar or waste heat, hydrogen is desorbed by high temperature MH, which is then absorbed by low temperature MH by rejecting the ambient heat. Upon requirement, the low temperature MH consumes atmospheric heat and desorbs the hydrogen to high temperature MH, thereby producing the requisite thermal output. Similarly, heat transformers, heating pumps and refrigeration systems are developed using MH based energy interactions (Muthukumar and Groll, 2010).

By the selection of suitable alloy pairs and heat transfer fluid, heat upgradation, heating and/or cooling systems can be devised. MH alloys for these applications should possess following properties (Muthukumar et al., 2003):

- high enthalpy of formation and high storage capacity
- pressure variation should be less with increase in temperature
- moderate operating pressure

By employing the combination of these alloys, available heat input can be upgraded to higher output while rejecting sink heat to ambient through transfer of hydrogen from one alloy to another. Similarly, the available heat input can be downgraded to provide favourable heating output or by utilising available heat input to produce requisite cooling effect by taking advantage of the heat interactions associated with absorption and desorption reactions. This is the underlying principle behind thermally driven MH based heating and cooling system. Two reactors containing different MH alloy are coupled such that hydrogen can flow freely by utilising the pressure gradient between the beds. This pressure gradient is attained by heat transfer at different temperatures suitable to PCT characteristics of individual alloy. Depending upon the application and alloy chosen, requisite heating and/or cooling effect can be obtained at these temperatures. The current study delves deep into the MH based cooling systems, which would be further discussed in detail.

1.6 Motivation of the thesis

As discussed in Section 1.2, hydrogen based economy is instrumental in shifting towards cleaner energy consumption and utilisation. Hydrogen, being a versatile energy carrier and fuel, is indispensable towards realizing this economy. With utilisation of hydrogen, comes the storage and transportation limitations that can be positively addressed by MH based solid state storage solutions. Considering this storage solution and the associated energy interactions, clean energy conversion and utilisation systems can be developed, prompting the need for

enhanced research in this field. Towards this focus, design standards of MH alloy reactors (containers) with enhanced heat transfer characteristics are required, especially for industrial scale applications. Concurrently, the heat and mass transfer phenomena need to be understood in detail to attain this design standard. Based on this understanding, practical applications with clear knowledge of operating conditions need to be established. In particular, MH based cooling systems are to be studied in detail as they can have widespread utilisation when implemented in conjunction with hydrogen storage solutions for stationary and mobile applications. This is the motivational drive of the present thesis.

1.7 Thesis structure

As discussed in this chapter, the practical implementation of MH based cooling systems depend on the alloy selection based on their characteristics, understanding of heat and hydrogen transfers associated with the alloys, design of efficient MH reactors and performance investigation of operating parameters. To study them in detail, this thesis is organized in six chapters. Description of each chapter is briefed below:

Chapter 1 starts with a brief introduction about the current energy scenario and associated hydrogen economy with focus on hydrogen storage technologies. As a prominent hydrogen storage solution, thermodynamics and applicability of MH based systems are discussed in detail. The versatility of MH and the need for focused research has been presented as the motivation of this thesis work.

Chapter 2 details the state-of-art on the various aspects associated with metal hydride. The underlying principle of alloy selection, the simultaneous heat and mass transfer phenomenon that forms the basis of the hydrogen sorption, and various factors that influences the performance of MH based systems are reviewed. Both numerical and experimental investigations into the conceptualization and performance prediction are discussed through

reported literature. On the basis of the reviewed literature, objectives of the present thesis have been framed.

In Chapter 3, a novel methodology for design of reactors with embedded cooling tube (ECT) configuration is developed. To understand the influence of the improved reactor design on hydrogen absorption and study its performance, three dimensional thermal model of lab scale and industrial scale reactor are developed. Comparative performance investigation of these reactors are discussed along with studying the storage performance of industrial scale $LaNi_{4.7}Al_{0.3}$ based hydrogen storage system under various operating conditions.

Chapter 4 presents the design and fabrication of lab scale and industrial scale reactors based on the developed design methodology. To analyse and understand the industrial scale MH based hydrogen storage and cooling systems (MHHSCS), an open cycle experimental set-up is formulated with reactors containing $MmNi_{4.7}Fe_{0.3}$. Compressor Driven MH based Cooling System (CDMHCS) is proposed as an alternative to conventional cooling systems. To understand and analyze the performance of CDMHCS, closed cycle experimental set-up has been formulated. Reactors with $LmNi_{4.91}Sn_{0.15}$ and $La_{0.7}Ce_{0.1}Ca_{0.3}Ni_5$ are investigated as part of CDMHCS.

Chapter 5 discusses the results of the numerical simulation and experimental investigation in detail. By comparing the absorption and desorption performance of lab scale ECT reactors, the reactors suitable for experimental investigation have been identified. Absorption characteristics of $LaNi_{4.7}Al_{0.3}$ contained in industrial scale reactor is studied and the enhanced heat transfer characteristics of the reactor design have been verified. Performance of open cycle MH based hydrogen storage and cooling system (MHHSCS) has been investigated with both lab scale and industrial scale reactors filled with $MmNi_{4.7}Fe_{0.3}$. Further, the performance of closed cycle CDMHCS providing appreciable quasi-continuous cooling output is investigated with $LmNi_{4.91}Sn_{0.15}$ and $La_{0.7}Ce_{0.1}Ca_{0.3}Ni_5$, filled in designed reactors.

Chapter 6 outlines the key conclusions drawn from the various studies into the operation and performance of industrial scale MH based hydrogen storage and cooling systems and compressor driven MH based cooling systems reported in this work. The scope for the future research work in the development of MH based cooling systems for on-board applications is presented as well.

CHAPTER 2

STATE OF THE ART

2.1 Preface

Considering the emergent requirement of hydrogen based economy, the research has been extensively focused towards understanding, design, development and analysis of metal hydride (MH) based hydrogen storage and thermal management systems. Several experimental and numerical investigations have been carried out on MH based systems focusing on the improvement in heat and mass transfer characteristics of MH bed during the absorption and desorption reactions. The systematic approach considered towards reviewing this literature has been depcted in Fig.2.1. As simultaneous heat and mass transfer occurs in conjunction with chemical reactions during the absorption and desorption processes, the in-depth understanding of MH alloy behaviour and reaction kinetics is of paramount importance. Both numerical and experimental investigations of heat and mass transfer characteristics of MH bed along with performance investigation of the developed systems have been reviewed in detail. As the

reactions are heat driven mass transfer phenomena, additional focus have been imparted in reviewing the heat transfer augmentation techniques that have been theoretically proposed and practically implemented. Considering stationary and on-board cooling applications, thermally driven and compressor driven MH based heat pumps (MHHP) and cooling systems (MHCS) have been extensively reviewed from reported literature both in computational aspect and experimental investigations.

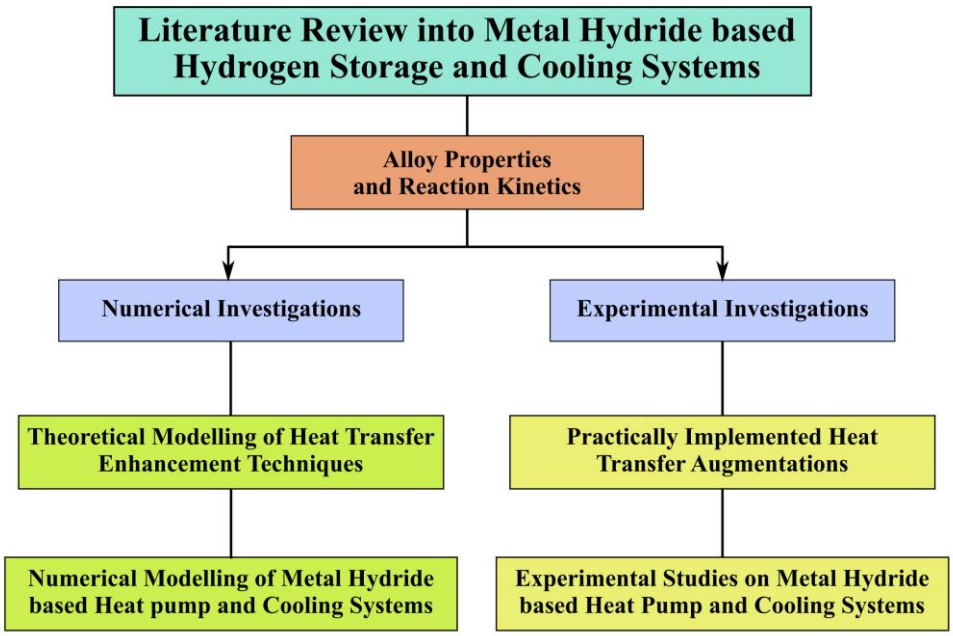

Fig.2.1. Flowchart depicting the approach towards the literature review of metal hydride based hydrogen storage and cooling systems

2.2 Studies on alloy properties and reaction kinetics

As the variation of metal hydride alloy compositions affect their practical applicability, the influence of the elemental substitutions on the alloy properties have been investigated extensively. Along with these studies, the reaction kinetics during absorption and desorption reaction have been widely modelled with focus on improving the pace of reaction. Muthukumar et al. (2003) have extensively discussed the selection of metal hydrides for different applications such as heat pump/heat transformer, hydrogen compressor, energy storage and

hydrogen storage, considering the enthalpy and entropy of formation and slope factors. A screening procedure with two step strategy for selection of alloy pairs for operation in MHHP has been proposed by Yang et al. (2008). In the first step, the plateau slope and the pressure difference have been taken into account while considering hysteresis, and the alloy pairs have been chosen that can fit the requisite operating condition. In the second step, the performances of the feasible alloy pairs have been evaluated to select the better alloys. Due to high advancements in the field of material science today, a wide range of metal alloys/materials are found to be applicable in MH systems.

Diaz et al. (1979) have investigated Al substitution on $LaNi_5$ as this alloy is stable for reversible absorption of hydrogen. The lattice parameters and cell volume of the resultant $LaNi_{5-y}Al_y$ compounds have been determined by X-ray diffraction method. From the reaction isotherms, it was observed that the plateau pressures decreased with increase in aluminium content. The similar trend was observed in hydrogen capacity as well, though $LaNi_4Al$ was found to be more stable and higher enthalpy than $LaNi_5$. An isobaric experimental apparatus with mass flow meter was developed by Miyamoto et al. (1983) to study the reaction kinetics of $LaNi_5$. It was observed that ln (P/P_0) can be used to best describe the effect of hydrogen pressure on reaction rate. The equilibrium pressure of $LaNi_{4.9}Al_{0.1}$ was determined using the same apparatus and was found to be lower than that of $LaNi_5$, thereby corroborating the reported literature. A practical study of $LaNi_5$ desorption kinetics was carried out under isothermal conditions, wherein the effect of heat transfer was concluded to be the rate controlling step (Goudy et al., 1983).

Oliver et al. (1985) studied the effect of hydriding on lattice structure of alloy $LaNi_{4.7}Sn_{0.3}$ using X-ray diffraction measurements. An increase of 17% in lattice cell volume was observed upon hydriding. The capacity loss of Misch-metal based alloys due to thermal cycling ($MmNi_{4.5}Al_{0.5}$ and $MmNi_{4.15}Fe_{0.85}$) were investigated by Kim and Lee (1987). Even after 3000

cycles, the hydrogen capacity decreased only by 7.6% and 6% for $MmNi_{4.5}Al_{0.5}$ and $MmNi_{4.15}Fe_{0.85}$, respectively in the range of 30 °C to 150 °C and 25 °C to 60 °C. Recovery treatment of $MmNi_{4.5}Al_{0.5}$ after 3000 cycles had resulted in 40% improvement while subsequent treatment after further 2000 cycles had resulted only in 17% improvement in reversible storage capacity. Han and Lee (1989) determined the rate-controlling step by investigating the hydriding kinetics of $LaNi_5$ and $LaNi_{4.7}Al_{0.3}$. At low supply pressure, the chemisorption on the surface of alloy particles was determined to be the rate-controlling step. When the driving force is larger due to higher supply pressure, the nucleation and growth of the hydride phase was observed to be controlling the reaction. However, the diffusion of hydrogen through the hydride layer was identified as the rate-controlling factor at later stage of hydriding reaction.

Singh et al. (2004) identified that Fe substitution in $MmNi_5$ resulted in improvement of hydrogen storage capacity, due to the higher electron attractive power of Fe. $MmNi_{4.9}Fe_{0.1}$ depicted a storage capacity of 1.66 wt%, which reduced to 1.57 wt% and 1.46 wt%, respectively in $MmNi_{4.7}Fe_{0.3}$ and $MmNi_{4.5}Fe_{0.5}$. Additionally, with increase in Fe, decrease in sloping and equilibrium pressure have been observed. With single (Al) and multiple (Al, Co, Mn, Fe) alloy substitutions for Ni in $MmNi_5$ alloy have been studied by Kumar et al. (2009). They observed that the substitution resulted in higher stability, increased enthalpy of formation, reduction in plateau pressure and decrease in hysteresis as the unit cell volume increased. The reaction PC isotherms and kinetics of $LaNi_{3.8}Al_{1.0}M_{0.2}$ (M=Ni, Cu, Fe, Al, Cr, Mn) were measured in the temperature range of 140 to 220 °C, by volumetric method (Li et al., 2009). Substitution of Cr in place of partial Ni had resulted in comparatively easier activation. The reaction plateau pressure found to increase in the following order of substitution of M: Mn < Cr < Al < Fe < Cu < Ni, as the unit cell was found to increase in an opposite trend. The time taken by the alloys

decreased in the order of Mn > Cr > Al > Fe > Cu > Ni to desorb 90% of the maximum hydrogen capacity.

Muthukumar et al. (2009a) measured the PCT characteristics of 4 different alloys under near isothermal absorption and desorption reaction to understand the effect of hydrogen concentration on their reaction enthalpies. With experimental curve fitting, reaction enthalpies of $LaNi_5$, $LaNi_{4.7}Al_{0.3}$, $LmNi_{4.91}Sn_{0.15}$, $Ti_{0.99}Zr_{0.01}V_{0.43}Fe_{0.09}Cr_{0.05}Mn_{1.5}$ and $MmCo_{0.72}Al_{0.87}Fe_{0.04}Ni_{3.91}$ were expressed as a fourth order polynomial function of hydrogen concentration. It was further observed that the reaction enthalpies of these MH decreased gradually between 2% and 15% with increase in concentration. The hydriding kinetics of $LmNi_{4.91}Sn_{0.15}$, $LaNi_{4.7}Al_{0.3}$ and $LaNi_5$ have been analysed using Johnson–Mehl–Avrami (JMA) model and Jander diffusion model (JDM) by Muthukumar et al. (2009b) under near isothermal conditions. The Jander diffusion model was observed to closely match the experimental data, which resulted in hydrogen diffusion into hydride layer in the plateau region being identified as the rate controlling mechanism for these alloys. The activation energies were obtained as 28.0, 29.1 and 27.7 kJ/mol H_2, respectively for $LmNi_{4.91}Sn_{0.15}$, $LaNi_{4.7}Al_{0.3}$ and $LaNi_5$ alloys. Li et al. (2010) studied the influence of Mn substitution on the hydrogen storage properties of $LaNi_{3.8}Al_{1.2-x}Mn_x$, where x was varied as 0.2, 0.4 and 0.6. With increase in Mn content, both plateau pressure and hydrogen storage capacity were observed to increase, while absorption kinetics was noted to be marginally slower. The thermochemical properties of eight La, five Mm and three Ti based alloys were estimated by Selvam et al. (2013) at various operating conditions. Through a third order polynomial function, reaction enthalpies have been expressed in terms of hydrogen storage capacity. The desorption enthalpies were found to be 3% to 18% higher than their respective absorption enthalpies for La and Ti based alloys. With increase in hydrogen concentration, the reaction enthalpies were found to decrease by 2.1 – 8.5%, 3 – 7.5% and 7 – 9%, respectively for La, Mm and Ti based alloys.

Wei et al. (2017) have reviewed six major techniques to investigate the hydrogenation properties of MH alloys. For porous materials, the gravimetric method is found to be reliable and less sensitive to uncertainties in temperature and pressure measurement, with consideration of sample protection and buoyancy correction. Though thermal desorption spectra was observed to be complex for interpretation, it has been perceived to be most suitable for studying desorption properties. Sieverts apparatus was noted to be robust, simple and cost effective, but not suitable for low density MH alloys. For in-situ experimental investigations, neutron scattering techniques has been identified for extracting plethora of data. However, the method is expensive due to the beam source employed. The prominent contributions reported in literature regarding the alloy properties and reaction kinetics have been summarized in Table 2.1.

2.3 Studies on heat and mass transfer characteristics

Several mathematical models along with experimental validation have been reported in literature to study the couple heat and mass transfer characteristics of MH alloy during absorption and desorption reactions. It is of paramount importance to understand the heat and mass transfer characteristics of the MH alloys along with the influence of operating parameters on their performance to evaluate their suitability for practical applications. Groll et al. (1987) emphasized the need for in-depth understanding of the PCT characteristics of the alloy for their implementation in thermal machines. They reported that the enhanced heat and mass transfer inside the hydride bed, high external heat transfer coefficient and good thermal contact between hydrides to the reactor wall increased the reaction rate. They observed absorption and desorption times of 3-4 min and 4-5 min, respectively for 90% hydrogen transfer in reaction beds of 20 mm outer diameter. The reaction beds also contained Al foam and two small hydrogen flow channel for better heat and mass transfer.

Sun and Deng (1989) developed a mathematical model that factored the effective thermal

conductivity as well as the physical properties of MH for predicting the heat and mass transfer characteristics. They determined the temperature and concentration profiles of $TiMn_{1.5}$ based reaction beds at 30 °C, 40 °C and 50 °C. The model was evident of the need for optimum design of metal hydride reactors leading to enhanced metal hydride heat transfer and rapid reaction rates. Gopal and Murthy (1992) predicted the heat and mass transfer characteristics of $LaNi_{4.7}Al_{0.3}$ in annular cylindrical reaction beds using a one-dimensional mathematical model. They developed non-dimensional correlations based on their analysis and concluded that the effective thermal conductivity of the bed should be as large as possible while the bed thickness should be small to achieve better heat and mass transfer in reaction bed. They further developed model based on nonlinear, unsteady partial differential equations to predict heat and mass transfer characteristics of the same alloy. However, they had considered coupled reaction beds of rectangular configuration in this analysis. They reported that the metal hydrides with smaller activation energies and higher reaction rate constants have offered shorter cycle time.

A two-dimensional mathematical model to predict the heat and mass transfer characteristics of MH bed during absorption has been developed by Jemni and Nasrallah (1995) and solved numerically by method of finite domains. Based on the time-space evolution PCT characteristics, they concluded that the selection of reactor geometry, inlet pressure and inlet temperature have prominent influence on the system. They had employed $LaNi_5$ for their investigations and further modeled the desorption reaction of the same alloy (Jemni and Nasrallah, 1995b). They accounted the effect of difference between the solid and gas temperature, as well as that of the variation of gas pressure in the numerical model. They observed an increase in the effective thermal conductivity of the MH resulted in significant improvement of performance for the bed.

Guo and Sung (1998) developed $LaNi_{4.7}Al_{0.3}$ based unsteady two dimensional model to determine the conjugate heat and mass transfer characteristics of MH with Al sheet insertions.

They found that the heat transfer and reaction rate were significantly improved with insertion of Al sheets and the improvement was better with reduction of gap between Al sheets and bed. They concluded that for given thickness of bed, there exists an optimal distance between bed and Al sheet insertions. Metal hydride formation in La rich Misch-metal alloy ($LmNi_5$) has been modelled considering complex heat and mass transfer characteristics along with chemical reactions in hydride bed (Mat and Kaplan, 2001). The results were presented with temperature and concentration histories along with isotherms and isoconcentration contours at chosen locations. Hydride formation was observed to be faster at locations with lower equilibrium pressure. Increase in temperature due to exothermic reaction slowed down the rate of hydride formation, thereby emphasizing the need for efficient heat removal. The hydride formation was found to proceed from hydrogen inlet and cooled walls.

Aldas et al. (2002) developed three-dimensional model to predict heat and mass transfer, fluid flow and chemical reactions in MH bed using a general purpose PHOENICS code. Though initial hydride formation was observed to be uniform, increase in bed temperature resulted in reduction in rate of formation. As the effect of fluid flow influenced the temperature profile of the bed, the rate of reaction was observed to be faster near the cooling interfaces. However, it did not significantly affect the overall amount of hydrogen absorbed. Askri et al. (2003) predicted the hydriding characteristics of La and Mg based alloys using two-dimensional model with additional focus on the effect of radiation in the MH bed. The $LaNi_5$ model was considered to operate between 20 °C and 77 °C while the Mg-H_2 was considered to absorb at 362 °C and desorb at 397 °C. The results depicted that the radiative effects are negligible in case of low temperature MH alloy such as $LaNi_5$, while the effects cannot be ignored for high temperature MH such as Mg based alloys and are particularly sensitive to absorption coefficient of the media. Bilgili and Ataer (2005) analyzed the hydrogen absorption of porous metal bed using two dimensional heat and mass transfer model in cylindrical coordinates. They considered an

annular cylindrical bed of $LaNi_5$ with cooling at both internal and external surfaces. Upon plotting the concentration across various radial and axial locations, it was observed that the MH bed near cooling boundaries attained the highest value. It was concluded that the porous metal bed with high thermal conductivity and specific heat with improved geometry that facilitates high cooling rate would result with high hydrogen absorption rate.

Muthukumar et al. (2007) conducted a two-dimensional numerical investigation into the coupled heat and mass transfer characteristics during absorption of $MmNi_{4.6}Al_{0.4}$ in an annular cylindrical reactor. The storage performance of the MH based reactor has been predicted for different supply pressures and absorption temperatures using Fluent 6.1.22, while the effects of bed parameters such as overall heat transfer coefficient and bed thickness have been analyzed as well. At supply pressure of 30 bar and absorption temperature of 25 °C, the bed absorbed maximum of 13.1 g per kg of alloy. It was further observed that for given configuration, bed thickness of 5 mm resulted in rapid rate of reaction. Using Fluent 6.2, transient two dimensional heat and mass transfer in cylindrical MH bed have been analyzed by Phate et al. (2007), while the influence of length to diameter (L/D) ratio of MH bed on hydrogen transfer has been emphasized as well. The radial variation in temperature and concentration has been observed to be more significant than that of axial direction, reiterating the importance of bed thickness on hydrogen absorption.

A lumped numerical model was proposed by Gambini et al. (2008) to predict the dynamic performance of $MmNi_{4.6}Fe_{0.4}$ based real life system at different operating conditions. Validity of the model was demonstrated with reported experimental results in literature. The model was able to predict the storage system performance when connected with fuel cell based application where desorption at constant flow rate has to be maintained. To evaluate the coupled heat and mass transfer characteristics during desorption of $MmNi_{4.6}Al_{0.4}$ and $MmNi_{4.6}Fe_{0.4}$, Muthukumar et al. (2009c) have developed a two-dimensional model using Fluent 6.1.22. Temperature and

concentration profiles at various radial locations and amount of hydrogen desorbed were predicted by varying desorption temperature in the range of 30 °C to 50 °C and bed thickness in between 5 mm and 15 mm. At desorption temperature of 50 °C, $MmNi_{4.6}Al_{0.4}$ and $MmNi_{4.6}Fe_{0.4}$ respectively depicted a desorption of 1.28 wt% and 1.11 wt%. It was further reiterated that with lower bed thickness, faster desorption reaction is possible.

Chung and Ho (2009) incorporated the expansion volume evident in practical MH storage reactors while developing a two dimensional numerical model. A cylindrical bed of 25 mm radius and 80 mm in height with an expansion volume height of 20 mm has been considered. Pure hydrogen flow was considered in the expansion volume domain while porous media flow in the MH bed. Heat convection due to thermal buoyancy had developed a retardation effect to heat transfer at cooling interfaces. Muthukumar and Ramana (2009, 2010) developed two-dimensional coupled heat and mass transfer models to study the absorption and desorption characteristics of cylindrical MH reactor containing $MmNi_{6.4}Al_{0.4}$, with additional focus on the effect of variable wall convective boundary condition. The effect of this boundary condition was found to be significant for bed thickness above 7.5 mm. While modelling the absorption at supply pressure of 20 bar for bed thickness of 17.5 mm, difference in absorption time of 300 s was observed due to this boundary condition. Similarly, for desorption at 30 °C, difference in desorption time was 375 s. Melnichuk and Silin (2012) have proposed general design guidelines for efficient MH reactor design using non-dimensional parameters. Thermal management of MH reactor has been the most relevant aspect of the study as it is the major limiting factor for hydriding and dehydriding characteristics of the system. Three MH alloys namely, $LaNi_5$, $Ti_{1.1}CrMn$ and Mg have been studied, and a single non-dimensional parameter called non-dimensional conductance has been identified as the most important parameter, which is a measure of the fraction of heat generation rate due to hydriding that can be removed by the heat exchanger. Higher value of this parameter amounts to higher heat transfer rates. They

further introduced another parameter called non-dimensional fill time, which was observed to be inversely proportional to non-dimensional conductance for heat transfer dominated reactor design. Patil and Gopal (2013a, 2013b) have presented two-dimensional models of an annular cylindrical reactor filled with $MmNi_{4.6}Al_{0.4}$. It was observed that entropy generation in system was primarily due to heat transfer effects. By varying hydrogen supply pressure and external fluid temperature, entropy generation could be reduced on the cost of increase in cycle time. They postulated that by balancing entropy generation against cycle time, optimum operating conditions could be obtained.

Mohammadshahi et al. (2016) have presented a comprehensive review on mathematical modelling of MH based systems for hydrogen storage applications. Most of the models presented in the review have dedicated their primary focus on effective thermal management improvements for optimum hydrogen storage performance. The review also has discussed the validity of various assumptions during modelling. The assumptions of local thermal equilibrium, treatment of hydrogen as an ideal gas and neglecting heat transfer by mass convection have been validated under normal operating conditions. Significant conclusions reported in the literature about the heat and mass transfer characteristics of MH have been summarized in Table 2.2.

2.3.1 Numerical studies on heat transfer enhancement techniques

Various techniques of heat transfer enhancement have been proposed and numerically simulated in literature, to highlight the improvement in reaction rate due to the proposed design. Mohan et al. (2007) proposed $LaNi_5$ based reactor with embedded filters and cooling tubes. Effects of operating and geometric parameters on the hydriding characteristics have been studied. Ratio of container radius to pitch was varied from 3 to 7 resulting in variation of number of tubes from 31 to 163. The bed thickness was varied between 10 mm and 27.5 mm, while the diameter of cooling tube was varied between 5 mm and 20 mm. Reduction in bed

thickness to 10 mm and increase in cooling tube diameter to 20 mm, individually resulted in better absorption performance. Among the configurations, 85 number of tubes was found to be optimum.

Askri et al. (2009a) developed a three-dimensional computational model to predict the heat and mass transfer characteristics of $MmNi_{4.6}Al_{0.4}$ based reactor designed with fins. They based this on experimental finned reactor reported in literature (Muthukumar et al., 2005) and found good agreement between the predicted and reported results. The effect of bed parameters such as length, thickness and thermal conductivity of the fins along with overall heat transfer coefficient on hydrogen storage performance have been predicted. Consideration of fins had enhanced the heat transfer and resulted in 40% improvement of absorption rate to attain 90% of storage capacity. They further evaluated the impact of tank wall thermal mass on hydriding process (Askri et al., 2009b). They observed that the tank wall thermal mass could be neglected by replacing it with thermal conductance during heat transfer analysis. Four different storage reactor designs have been considered, among which reactor with concentric heat exchanger finned tube that facilitates HTF flow had resulted in 80% improvement in storage performance.

Mellouli et al. (2009) have analysed the impact of metal foam heat exchanger in $LaNi_5$ based reactor through a two-dimensional heat and mass transfer model. The effects of metal foam properties such as base material, pore size and foam density on hydrogen storage performance have been studied. At supply condition of 10 bar and 20 °C, the time required to absorb 90% of hydrogen was reduced by 60% due to inclusion of metal foam. Among the considered foam properties, Al foam with pore size of 0.125 mm and foam density of 12% resulted in maximum absorption performance.

Mellouli et al. (2010) proposed two-dimensional mathematical model to optimize the heat and mass transfer characteristics of $LaNi_5$ based reactor with finned spiral heat exchangers for fuel cell application. The effects of pitch, length, thickness and arrangement of fins on the

absorption performance of MH reactor have been studied. Use of circular fins resulted in 66% improvement in absorption rate for storing 90% of hydrogen when compared to without fins case. A two-dimensional thermal model was developed by Muthukumar et al. (2012b) employing $MmNi_{4.6}Al_{0.4}$ based reactor with different configuration of ECT to evaluate the hydriding characteristics at various operating conditions. For cylindrical reactor of 50 mm in diameter, configuration with 20 ECT and an outer cooling jacket depicted best absorption performance at supply pressure of 30 bar, absorption temperature of 20 °C and overall heat transfer coefficient of 1250 W/m^2K. The same configuration was extended for industrial scale reactor of 300 mm in diameter, resulting in 48 ECT configuration capable of storing 150 kg of MH alloy. The industrial scale reactor required absorption time of 2120 s for reaching 96% of storage capacity.

Bao et al. (2013a) developed a three-dimensional multiphysics model to predict the heat and mass transfer characteristics of a cylindrical reactor model containing five heat transfer tubes and four hydrogen transfer tubes. This model depicted better absorption performance when compared with traditional annular cylindrical model. A dimensionless parameter has been defined to estimate the error due to assumption that neglects the variation in HTF temperature in MH reactor. Further sensitivity analysis carried out on the effect of various parameters on the absorption time resulted with following sequence of priority: the effective thermal conductivity of the metal hydride > the flow rate of the heat transfer fluid > contact resistance > the heat exchanger tube material. This research group further developed an optimization procedure based on computational fluid dynamics-Taguchi combined method for the design of MH reactor with internal heat exchanger tubes (Bao et al., 2013b). Considering a cylindrical MH bed of 50 mm in diameter and 100 mm in length, the optimum number of internal heat exchanger tubes were determined to be 10, each having a diameter of 8 mm and distributed at a pitch of 18 mm. Ma et al. (2014) proposed a finned multi tubular MH reactor and analysed

the absorption performance through three-dimensional mathematical model. They varied the fin configurations such as radius, thickness and number of fins to observe the resultant effect of absorption performance of reactor filled with $LaNi_5$. Maximizing fin radius, thickness and fin number resulted in better performance, as expected.

The geometrical variation of ECT in a cylindrical reactor was studied in detail by Anbarasu et al. (2014a) through two-dimensional mathematical model using COMSOL Multiphysics 4.3. They predicted the minimum reaction time while varying the ECT configuration within cylindrical shell by varying the internal angles between tubes at each stack, resulting models with 24 to 70 ECT. Among the configurations, 60 ECT model was observed to depict best performance which was further employed in three-dimensional mathematical model to predict the hydriding/dehydriding performance at various operating conditions by considering 2.75 kg of $LmNi_{4.91}Sn_{0.15}$. Their numerically predicted results were in good agreement with experimentally observed data. Ferekh et al. (2015) compared the effect of internal fins and metal foams as measure of heat transfer augmentation through three dimensional transient hydrogen absorption model of ZrCo based hydrogen storage bed. Though both features resulted in commendable storage performance, inclusion of internal metal foams in MH bed was adjudged to be a better technique considering it resulted in increase of effective thermal conductivity while maintaining overall thermal mass.

A three-dimensional numerical heat and mass transfer model was used by Sekhar et al. (2015) to compare hydrogen absorption of $MmNi_{4.6}Al_{0.4}$ based storage reactor with four different heat transfer configurations: internal cooling with (i) straight, or (ii) helically coiled tubing, or external cooling, (iii) without and (iv) with transversal fins. Among these configurations, internal cooling with helical tubing and external cooling with transversal fins depicted best performance, followed by external cooling without fins and least performance by internal straight tubes. For the studied geometry, increasing the overall heat transfer coefficient beyond

800 W/m^2K did not result in discernible improvement. Singh et al. (2015) proposed a cylindrical reactor design containing an annular heat exchanger tube embedded with radial copper fins for storing 1 kg of $LaNi_5$ alloy. Through three-dimensional mathematical model, absorption characteristics of the reactor were predicted under various operating conditions. At supply pressure of 15 bar, with HTF at 25 °C and flowing at 1 m/s, the complete absorption up to 1.34 wt% required 1080 s. Increase in number and thickness of fins had resulted in improvement in absorption performance of selected reactor design.

A detailed review on various heat transfer techniques employed in MH based hydrogen storage systems has been presented by Afzal et al. (2017). Among the techniques, they had considered enhancement in thermal conductivity through metal foams and MH compacts, reduction in bed thickness through tubular reactor models, increase in heat transfer area through consideration of embedded HTF tubes, cooling jacket, fins as well as selection of favourable operating parameters. It has been observed that improvement in both thermal conductivities of the bed and heat transfer coefficient of the system has to be considered concurrently for achieving an effective system design. This consideration addresses both heat transfer within bed and heat removal from the bed. However, for bed thickness of 10 mm and lower, internal heat transfer enhancement ceases to be a necessity. Recently, Bouzgarrou et al. (2019) have proposed control volume Lattice Boltzmann method based on unstructured grids for solving the heat and mass transfer in MH reactor containing 4.2 kg of $LaNi_5$ alloy. Their approach predicted the absorption phenomena correctly and was 8 times faster in computing when compared with control volume finite element method. In their analysis, they had considered six different reactor configurations, some of which were included with internal heat exchangers. Among these configurations, the sixth one with internal heat exchanger and empty zones reduced absorption time 87% when compared with their basic configuration. Various theoretical reactor

designs and heat transfer enhancement techniques proposed have been summarized in Table 2.3. Additionally, few reactor designs have been represented in Fig.2.2.

2.3.2 Numerical investigations on MH based heat pump and cooling systems

Both thermally driven and compressor driven MH based heat pump and cooling systems have been numerically conceptualised and investigated to understand their dynamic behaviour and effect of operating conditions on them.

A chemical heat pump with two different MH filled in two reactors each was modelled by Nishizaki et al. (1983). $LaNi_{4.7}Al_{0.3}$ was employed as regeneration alloy while $LaNi_5$ was employed as refrigeration alloy. The four reactor system facilitated achieving COP of 0.8 through sensible heat exchange between reactors of same alloy. Using slurry heat exchanger, Kim et al. (1997b), proposed a finite thermodynamics model to study compressor driven MH based air conditioner considering important parameters including pressure ratio of compressor, compressor efficiency and total heat conductance between heat exchangers and reservoirs. For their thermodynamic model, they observed that increase in total heat conductance until 2×10^6 W/K resulted in improvement of COP and cooling power, beyond which it had no effect. Increase in compressor efficiency improved cooling performance, however increase in pressure ratio from 3 to 13 resulted in decrease of COP to 2.3. Gopal and Murthy (1995a) predicted the performance of MH refrigerator working with ZrMnFe and $MmNi_{4.5}Al_{0.5}$ alloy pair by solving coupled heat and mass transfer equations of the two reactor system. The heat source and refrigeration temperatures were respectively varied between 140-155 °C and 0-10 °C while sink temperature was fixed at 35 °C which resulted in COP as high as 0.7. MH bed thickness of 3 mm resulted in an effective thermal conductivity of 4 W/mK.

A detailed mathematical taking into consideration the transient characteristics of CDMHCS with $Zr_{0.9}Ti_{0.1}Cr_{0.55}Fe_{1.45}$ as the working alloy was developed by Mazumdar et al. (2005a). Two finned reactors were considered, each of cylindrical configuration of 20 mm in diameter, with

a reciprocating compressor in between. The aluminium radial fins of 0.15 mm thickness and fin spacing of 316 fins/m have been considered. Maximum COP of 2.2 and SCP of 0.16 kW/kg of total alloy have been achieved through this mathematical model. It has been observed that the selection of suitable alloy and reactor design that facilitate fast reaction kinetics is of paramount consideration. The same research team have developed a novel thermodynamic model to evaluate CDMHCS considering the effects of external heat transfer characteristics (Mazumdar et al., 2005b). They have evaluated the model by considering four alloys, viz. $MmNi_{4.5}Al_{0.5}$, $LaNi_5$, $TiFe_{0.85}Mn_{0.15}$ and $Zr_{0.9}Ti_{0.1}Cr_{0.55}Fe_{1.45}$. Of these alloys, CDMHCS employing compressor of 100 cm^3 swept volume and $MmNi_{4.5}Al_{0.5}$ was observed to yield best performance with COP and SCP of 2.55 and 0.15 kW/kg of total alloy, respectively. Additionally, it was observed that COP decreased while SCP increased with increase in swept volume of compressor until a threshold value, beyond which the variation in swept volume did not influence the cooling performance. From reactor design point of view, it was deduced that the parasitic thermal mass is a limiting factor in the cooling output that can be achieved, as the flow rate of HTF does not influence the performance of CDMHCS beyond a certain value.

Bedbak and Gopal (2005) considered $MmNi_{4.5}Al_{0.5}$, $Fe_{0.85}Mn_{0.15}Ti$ and an assumed hydride of high storage capacity to conduct a comparative performance investigation of CDMHCS employing these hydrides. They observed that if the temperature drop is high, then the alloy chosen is not prominent deciding factor. Hence, reactor design with a focus on attaining commendable temperature drop is of primary requirement. The evaluated COP value might exceed commercial vapour compression systems, if the parasitic losses during thermal cycling are minimized by some form of heat recovery during cycling. However, the technical and economical feasibilities of such measures are to be evaluated. Satheesh et al. (2009) developed unsteady, two-dimensional mathematical model in annular cylindrical configuration to study the MH based cooling system working with $MmNi_{4.6}Al_{0.4}$ and $MmNi_{4.6}Fe_{0.4}$ alloy pair, solved

numerically using finite volume method. At given heat source, heat sink and refrigeration temperatures of 90 °C, 25 °C and 5 °C, respectively, the cycle time was estimated to be 1470 s for constant wall boundary condition, and 1765.5 s for variable wall boundary condition.

Considering five different alloy pairs, Satheesh and Muthukumar (2010a) conducted performance investigation of single stage MHHP by solving unsteady, two-dimensional coupled heat and mass transfer processes in MH bed of cylindrical configuration using a fully implicit finite volume method. The influence of operating temperatures on COP and SCP of the system has been analysed. For given operating temperatures $LmNi_{4.91}Sn_{0.15}$/$Ti_{0.99}Zr_{0.01}V_{0.43}Fe_{0.09}Cr_{0.05}Mn_{1.5}$ alloy pair produced highest SCP of 53.25 W/kg of total mass of system while the maximum COP of 0.66 was predicted for $Zr_{0.9}Ti_{0.1}Cr_{0.9}Fe_{1.1}$/$Zr_{0.9}Ti_{0.1}Cr_{0.6}Fe_{1.4}$ alloy pair. This research team further extended their investigation on double stage double effect MHHP working with $LaNi_{4.1}Al_{0.52}Mn_{0.38}$, $LmNi_{4.91}Sn_{0.15}$ and $Ti_{0.99}Zr_{0.01}V_{0.43}Fe_{0.09}Cr_{0.05}Mn_{1.5}$ alloy system (Satheesh and Muthukumar, 2010b). For heat source, heat rejection, heat sink and refrigeration temperature of 305 °C, 100 °C, 25 °C and 10 °C, respectively, the SCP of system was 48.1 W/kg of total alloy mass and average COP was 0.81.

Muthukumar and Satheesh (2013) proposed a single stage MHHP operating on the crossed van't Hoff principle by employing two regeneration/refrigeration alloy pairs namely, $V_{0.846}Ti_{0.104}Fe_{0.05}$/$Fe_{0.9}Mn_{0.1}Ti$ and $V_{0.855}Ti_{0.095}Fe_{0.05}$/$MmNi_{4.7}Al_{0.3}$. The optimum heat source, heat sink and refrigeration temperatures for $V_{0.846}Ti_{0.104}Fe_{0.05}$/$Fe_{0.9}Mn_{0.1}Ti$ pair were found as 100 °C, 30 °C and 18 °C, respectively, resulting in COP and SCP of 0.89 and 30.8 W/kg of total alloy mass, respectively. Similarly, the COP and SCP were estimated to be 0.86 and 30.3 W/kg of total alloy mass, respectively for $V_{0.855}Ti_{0.095}Fe_{0.05}$/$MmNi_{4.7}Al_{0.3}$ when operated corresponding heat source, heat sink and refrigeration temperature of 127 °C, 30 °C and 10 °C.

Sharma et al. (2015) investigated the influence of dynamic operation conditions on the

performance of MH based cooling system by using $La_{0.9}Ce_{0.1}Ni_5$ and $LaNi_{4.7}Al_{0.3}$ pair. The alloy pair was characterised by both static and dynamic PCT data, and it was observed that the resultant enthalpy and entropy values were significantly different in both modes. For HTF flow rate of 0.08 lpm, reduction in COP by 31.9% and cooling capacity by 57.8% was observed when the dynamic PCT based analysis was compared with the static PCT based analysis. This was because driving potential and transferrable amount of hydrogen significantly reduced for dynamic system, thereby emphasizing the importance of dynamic PCT data.

Sharma and Kumar (2017) have proposed a multi stage multi effect MH based thermodynamic system that employed four different alloys working in conjunction. Four different combinations each containing of four different alloys based on La and Mm have been considered due to their operating feasibility. The thermodynamic cycle facilitated simultaneous effect of heat pump, heat transformer and cooling system. Alloy combination of $La_{0.9}Ce_{0.1}Ni_5$ – $MmNi_{4.4}Al_{0.6}$ – $LaNi_{4.7}Al_{0.3}$ – $MmNi_{3.7}Co_{0.7}Mn_{0.3}Al_{0.3}$, was found best suited for the proposed system resulting 3337 kJ of cooling, 3243 kJ of high grade heat output and 5726 kJ of low grade heat output with overall theoretical COP of 2.22 for cycle time of 3840 s. The commendable theoretical investigations on metal hydride based heat pumps and cooling systems along with their prominent results reported in literature have been summarized in Table 2.4.

2.4 Experimental investigations

Various experimental investigations have been carried out to study the alloys and reactor designs chosen for efficient hydrogen storage performance with emphasis on heat transfer augmentation techniques and effect of operating conditions on hydriding and dehydriding characteristics. Gopal and Murthy (1995b) have experimentally investigated the performance of $MmNi_{4.5}Al_{0.5}$ based hydrogen storage reactor at different HTF temperatures. The need for enhancing the thermal conductivity was perceived from the poor performance of the hydride bed. The performance of $MmNi_{4.6}Al_{0.4}$ and $MmNi_{4.6}Al_{0.4}$ have been experimentally

investigated by Muthukumar et al. (2005) at different supply pressure, absorption temperature and overall heat transfer coefficient. It was noted that for given absorption temperature, the absorption rate and storage capacity were increased with increase in supply pressure. At supply condition of 35 bar and 15 °C, $MmNi_{4.6}Fe_{0.4}$ stored about 1.6 wt%, while $MmNi_{4.6}Al_{0.4}$ attained nearly 1.3 wt% of hydrogen storage capacity. During desorption, higher hot fluid temperature had resulted in faster desorption rate. The reported desorption time for $MmNi_{4.6}Al_{0.4}$ was 250 s while for $MmNi_{4.6}Fe_{0.4}$, it was just 75 s at 50 °C.

Kaplan (2009) experimentally investigated three different cylindrical reactor designs for studying the effect of heat transfer augmentation on charging process of $LaNi_5$ based reactor. The reactor design with water spirally cooling the bed was found to have heat transfer coefficient of 113 W/m^2K and depicted best absorption performance for supply pressure variation from 1 to 10 bar. The hydrogen storage performance of $MmNi_{4.7}Al_{0.3}$ based reactor was investigated both numerically and experimentally by Melnichuk et al. (2010) at various operating conditions. Cylindrical reactor of 50 mm internal diameter was filled with 500 g of alloy. Good agreement was achieved between the numerically simulated data and experimentally observed data.

Sekhar et al., (2016) developed a laboratory scale Totalized Hydrogen Energy Utilization System incorporating MH based hydrogen storage tank and Unitized Reversible Fuel Cell which consists of both fuel cell and water electrolysis in same unit. The storage tank was of stainless steel with an outer diameter of 165.2 mm and length of 1000 mm, provided with internal double coil type heat exchanger made of copper for enhanced heat transfer. The storage tank was filled with 50 kg of $MmNi_5$, resulting in total tank weight of 85 kg. The concentration (H/M ratio) was varied between 0.18 and 0.8 during desorption and absorption reaction, thereby comfortable operating between 1.36 bar and 10.2 bar as demanded by the system.

2.4.1 Practical implementation of heat transfer augmentations

As discussed in Section 2.3.1, various heat transfer augmentation techniques have been proposed through mathematical modelling. However, their realization for practical applications is important for the real world implementation of efficient MH based hydrogen storage and cooling systems. With capillary tube bundle heat exchanger, Linder et al. (2010) developed capillary tube bundle MH reactors to experimentally analyse MH based cooling system employing $LmNi_{4.9}1Sn_{0.15}$ as high temperature alloy and $Ti_{0.99}Zr_{0.01}V_{0.43}Fe_{0.09}Cr_{0.05}Mn_{1.5}$ as low temperature alloy. Due to capillary tube bundle reactor design, half cycle time of 100 s and specific cooling power of 780 W per kg of desorbing alloy were achieved. Souahlia et al. (2011) have developed two reactor geometries to study the effect of reactor design on hydrogen storage performance. The first design contained a cylindrical body with an outer cooling jacket while the second design considered a cylindrical body with internal finned tube heat exchanger through which HTF was supplied. Among these designs, the reactor with internal finned tube heat exchanger depicted better performance, wherein 4 g of hydrogen was absorbed in 32% of the time taken by the other design. Along similar focus, reactor design with internal finned spiral heat exchanger was compared with the above proposed second design (Souahlia et al., 2011b). It was observed that the new design resulted in 20% improvement in performance, though the design was comparatively more complex.

Visaria and Mudawar (2012) developed a complex coiled tube heat exchanger assembly for MH based storage system utilizing 4 kg of high pressure MH ($Ti_{1.1}CrMn$) for fuel cell integration. By occupying only 7% of the internal volume, the coiled tube heat exchanger had resulted in 75% improvement in hydrogen absorption rate. However, in absence of low temperature HTF flow, this system had required 4 times longer to attain the same performance as with HTF flow condition. The concept of MH sheets, which is made up of MH powder, carbon powder and aramid pulp, has been utilized by Yasuda et al. (2013) in developing MHHP

with $TiFe_{0.9}Ni_{0.1}/La_{0.6}Y_{0.4}Ni_{4.9}Al_{0.1}$ as working alloy pair. Usage of MH sheets had resulted in 20% improvement of SCP. It was also postulated that the heat transfer enhancement on cooling output reactor was more important than that of heat source reactor.

Based on the developed design, Anbarasu et al. (2014b; 2014c) had fabricated reactors of 36 ECT and 60 ECT configuration and filled each with 2.75 kg of $LmNi_{4.91}Sn_{0.15}$ to study the effect of operating parameters on both hydriding and dehydriding characteristics. The amount of hydrogen absorbed and the time taken were recorded for varying supply pressure (10 bar to 35 bar), absorption temperature (20 °C to 30 °C) and cooling fluid flow rate (2.2 lpm to 30 lpm). The bed attained maximum storage capacity of 1.8 wt% in 480 s and 600 s, respectively for 60 ECT and 36 ECT reactor configurations at supply condition of 35 bar, 30 °C and 3.2 lpm. The absorption time reduced by 62.5% when the HTF flow rate was increased to 30 lpm and supply pressure was at 25 bar for 60 ECT reactor. Similarly, the dehydriding performance was evaluated by varying the desorption temperature (30 °C to 60 °C) with same variation in HTF flow rate (2.2 lpm to 30 lpm). At 50 °C and 30 lpm flowrate, 60 ECT reactor desorbed its entire hydrogen content in 480 s. Throughout this investigation, the improvement in rapidity of rate of heat transfer and amount of hydrogen transferred due to the ECT reactor configuration was prominently observed. Weckerle et al. (2017) have developed a novel soldered plate reactor design for MH based cooling system. Short half cycle time of less than 1 min was achieved when it was utilized to cool fuel cell to a temperature of about 10 °C. The reactor contained 20 stacked plate with a gap of 1.5 mm and filled with 0.353 kg of Hydralloy C5. Single reactor experiments had resulted in a high specific cooling power of 1.31 kW/kg of alloy. In a coupled reactor system, even while considering the thermal losses, specific cooling power of 0.69 kW/kg of alloy has been achieved. From the literature, noteworthy reactor designs and heat transfer augmentations that have been experimentally devised are summarized in Table 2.5. Some of these designs have been represented in Fig.2.2, as well.

2.4.2 Experimental investigations on MH based heat pump and refrigeration systems

Based on the theoretical analysis and reactor design with heat transfer augmentation techniques, many researchers have reported practical implementation of thermally driven and compressor driven MH based heat pump and cooling systems. Utilizing waste heat exhaust of a bus as high temperature heat source, Ron (1984) proposed a MH based heat pump as an air conditioning system for the bus. They selected $LaNi_{4.7}Al_{0.3}$ as high temperature MH and $MmNi_{4.15}Fe_{0.85}$ as low temperature MH alloys. The high temperature MH alloy was filled in stainless steel tube reactors of 17.5 mm outer diameter with external perpendicular stainless steel fins, while the low temperature MH was made into porous MH compacts with 18 wt% Al matrix and filled stainless steel tube reactors of 14 mm outer diameter with external perpendicular aluminium fins. They obtained SCP of 0.25 kW/kg of desorbing MH while COP was calculated to be in the range of 0.22 to 0.35.

Suda et al. (1991) developed a double-stage thermally driven MH based heat pump working with $LaNi_{4.28}Al_{0.23}$, $MmNi_{4.57}Al_{0.46}Fe_{0.05}$ and $MmNi_{3.98}Fe_{1.04}$. The operating performance of double stage MHHP with two different capacities of 7.72 kW and 77 kW have been experimentally investigated. Quality steam generation in the temperature range of 120-150 °C was achieved. It was observed that increase in reaction time resulted in increase in hydrogen transferred, but the overall thermal output did not increase. It was postulated that for such systems, there exists an optimum cycle time to obtain maximum output. An ideal and actual COP of 0.36 and 0.21 were reported with overall alloy thermal output of 33 W/kg of alloy.

Kim et al. (1997a) developed fast reactors containing copper-coated $LaNi_5$ hydride compacts which produced a specific cooling power of 1.5 kW/kg of alloy for desorption time of 130 s. When copper coated compacts of $Ca_{0.4}Mm_{0.6}Ni_5$ was considered, the specific cooling power improved to 2.2 kW/kg of alloy was obtained (Kim et al., 1998). The measurements were carried out on with single reaction beds, wherein the alloy was filled in copper tube reactor

with external fins for enhancing the outside heat transfer. It was observed that the cooling output of $LaNi_5$ compacts reduced by 55% after 3000 cycles. A two reactor CDMHHP with finned reactors of these MH compacts has been proposed for air-to-air cooling system. Utilizing oil-less compressor, CDMHHP with two fin-tube type reactors each containing 4.2 kg of $Zr_{0.9}Ti_{0.1}Cr_{0.55}Fe_{1.45}$ with gasket type heat conducting matrices for better heat transfer have been developed by Park et al. (2001). At optimum cycle time of 156 s, the air at 24 °C and flowing at 11 m^3/min was cooled with maximum cooling output estimated to be 251 kcal/kg alloy h. However, COP was not measured due to the oil-less type of compressor which made the system uneconomical. Comparatively, Park et al. (2002) demonstrated CDMHHP using oil type compressor and reactor was filled with 3.5 kg of $Zr_{0.9}Ti_{0.1}Cr_{0.55}Fe_{1.45}$. CDMHHP operating between 0.8 and 20 atm achieving COP of 1.8 with half cycle time of 180 s. At airflow rate of 7 Nm^3/min, minimum cooling temperature of 6 °C has been achieved.

Magnetto et al. (2006) developed a prototype of CDMHCS for automotive applications using air compressor. They employed heat exchangers with ring manifold reaction tubes for rapid hydrogen absorption and desorption. In these ring manifolds, specially designed finned tubes of 3.175 mm have been integrated in the form of circular disc with diameter of 203 mm. Then, these ring manifold reaction tubes have been loaded into individual heat exchanger such that each heat exchanger have 3.5 kg of Mm based alloy. For a maximum airflow rate of 7.4 m^3/min, COP of 2.76 to 2.57 with average cooling capacity of 1.5 kW to 2.1 kW was obtained when the ambient temperature was varied from 21 °C to 35 °C. Linder and Kulenovic (2011) proposed a novel operation principle of MH based air conditioner in onboard automobile applications. Ideally selected low temperature MH alloy undergoes regeneration phase where it absorbs the hydrogen at higher pressure while rejecting heat to ambient and produces cooling effect while desorbing hydrogen at lower pressure. By utlising hydrogen storage tank as higher pressure level and fuel cell as lower pressure level, the principle employed two alternating

capillary tube bundle MH reactors in between these levels, each filled with 0.8 kg of $Ti_{0.99}Zr_{0.01}V_{0.43}Fe_{0.09}Cr_{0.05}Mn_{1.5}$. By alternating between the cooling phase of each reactor, quasi-continuous total cooling power of 900 W was achieved. A feasible CDMHHP based on single reactor prototype filled with 3.5 kg of $LmNi_5$ has been proposed by Patel et al. (2013). The COP of the system was experimentally predicted to be 1.1 at HTF temperature of 15 °C. They observed that quasi-continuous cold generation is conceivable by developing CDMHHP employing two identical reactors in the setup. Summary of these investigations into MH based heat pumps and cooling systems along with their performance have been briefed in Table 2.6.

Table 2.1. Summary of reported literature on alloy properties and reaction kinetics

Author(s) and Year	Alloy	Prominent Contributions
Diaz et al. (1979)	$LaNi_5$	➢ Plateau pressures found to decrease with increase in Al substitution.
Miyamoto et al. (1983)	$LaNi_5$	➢ Observed that ln (P/P_0) can be used to best describe the effect of hydrogen pressure on reaction rate.
Goudy et al. (1983)	$LaNi_5$	➢ Effect of heat transfer was found to be the rate-controlling step.
Oliver et al. (1985)	$LaNi_{4.7}Sn_{0.3}$	➢ Observed an increase of 17% in lattice cell volume upon hydriding.
Kim and Lee (1987)	$MmNi_{4.5}Al_{0.5}$, $MmNi_{4.15}Fe_{0.85}$	➢ In the range of 30 °C to 150 °C and 25 °C to 60 °C, corresponding decrease in capacity was only by 7.6% and 6% for $MmNi_{4.5}Al_{0.5}$ and $MmNi_{4.15}Fe_{0.85}$, respectively, after 3000 thermal cycles.
Han and Lee (1989)	$LaNi_5$, $LaNi_{4.7}Al_{0.3}$	➢ At low supply pressure, the chemisorption on the surface of alloy particles was determined to be the rate-controlling step. At higher supply pressure, the nucleation and growth of the hydride phase was found to be the rate-controlling step. ➢ At later stage of hydriding reaction, diffusion of hydrogen through the hydride layer was identified as the rate-controlling step.
Muthukumar et al. (2003)	Multiple alloys	➢ Extensively discussed the selection of metal hydrides for different applications considering the enthalpy and entropy of formation, and slope factor of the alloy.
Singh et al. (2004)	$MmNi_5$	➢ Fe substitution in $MmNi_5$ resulted in improvement of hydrogen storage capacity. ➢ $MmNi_{4.9}Fe_{0.1}$ depicted a storage capacity of 1.66 wt%.

Yang et al. (2008)	Multiple alloys	➢ Proposed two step strategic procedure regarding selection of alloy pairs for operation in MHHP.
Li et al. (2009)	$LaNi_{3.8}Al_{1.0}M_{0.2}$ (M=Ni, Cu, Fe, Al, Cr, Mn)	➢ The reaction plateau pressure found to increase in the following substitution order of M: Mn < Cr < Al < Fe < Cu < Ni. ➢ The time taken to desorb 90% of the maximum HSC decreased in the following substitution order of M: Mn > Cr > Al > Fe > Cu > Ni.
Muthukumar et al. (2009a)	Multiple alloys	➢ With experimental curve fitting, reaction enthalpies were expressed as a fourth order polynomial function of hydrogen concentration.
Muthukumar et al. (2009b)	$LmNi_{4.91}Sn_{0.15}$, $LaNi_{4.7}Al_{0.3}$, $LaNi_5$	➢ Johnson–Mehl–Avrami (JMA) model and Jander diffusion model (JDM) analysed under near isothermal conditions. JDM was observed to closely match the experimental data. ➢ Hydrogen diffusion into hydride layer in the plateau region found to be the rate controlling step.
Li et al. (2010)	$LaNi_{3.8}Al_{1.2-x}Mn_x$	➢ Plateau pressure and hydrogen storage capacity were observed to increase with increase in Mn content.
Selvam et al. (2013)	La, Mm and Ti based alloys	➢ Reaction enthalpies expressed as third order polynomial function in terms of hydrogen storage capacity. ➢ The desorption enthalpies were found to be 3% to 18% higher than their respective absorption enthalpies for La and Ti based alloys.
Wei et al. (2017)	Multiple alloys	➢ Reviewed six major techniques to investigate the hydrogenation properties of MH alloys.

Table 2.2. Summary of reported literature about studies on heat and mass transfer characteristics

Author(s) and Year	Prominent Contributions
Groll et al. (1987)	➢ Emphasized the need for in-depth understanding of the PCT characteristics of the alloy
Sun and Deng (1989)	➢ Developed mathematical model that factored the effective thermal conductivity as well as the physical properties of $TiMn_{1.5}$. ➢ The model was evident of the need for optimum design of metal hydride reactors.
Gopal and Murthy (1992)	➢ One-dimensional mathematical model of $LaNi_{4.7}Al_{0.3}$ in annular cylindrical reaction beds. ➢ Observed that the effective thermal conductivity of the bed should be high while the bed thickness should be small for better heat and mass transfer.
Jemni and Nasrallah (1995a, 1995b)	➢ Two-dimensional mathematical model $LaNi_5$ bed solved numerically by method of finite domains. ➢ Concluded that selection of reactor geometry, inlet pressure and inlet temperature have prominent influence on the system.
Guo and Sung (1998)	➢ Unsteady two-dimensional model. ➢ Heat transfer and reaction rate significantly improved with insertion of Al sheets. ➢ Concluded that for given thickness of bed, there exists an optimal distance between bed and Al sheet insertions.
Mat and Kaplan (2001)	➢ Emphasized the need for efficient heat removal within the bed.
Aldas et al. (2002)	➢ Developed three-dimensional model using a PHOENICS code. ➢ Increase in bed temperature resulted in reduction in rate of hydriding.

Askri et al. (2003)	➢ Two-dimensional model with additional focus on the effect of radiation in the MH bed. ➢ Results depicted that the radiative effects are negligible in case of low temperature MH alloys, while the effects cannot be ignored for high temperature MH alloys.
Bilgili and Ataer (2005)	➢ Two-dimensional model of annular cylindrical bed of $LaNi_5$. ➢ Observed that the MH bed near cooling boundaries attained the highest value of concentration.
Muthukumar et al. (2007)	➢ Two-dimensional model of $MmNi_{4.6}Al_{0.4}$ in an annular cylindrical reactor, solved using Fluent 6.1.22. ➢ Observed that for given configuration, bed thickness of 5 mm resulted in rapid rate of reaction.
Phate et al. (2007)	➢ Transient two-dimensional model of cylindrical MH bed, solved using Fluent 6.2. ➢ Observed that the radial variation in temperature and concentration was more significant than that of axial variation.
Muthukumar and Ramana (2009, 2010)	➢ Developed two-dimensional model of cylindrical MH reactor containing $MmNi_{6.4}Al_{0.4}$, with additional focus on the effect of variable wall convective boundary condition. ➢ Effect of this boundary condition was significant for bed thickness above 7.5 mm.
Patil and Gopal (2013a, 2013b)	➢ Two-dimensional model of annular cylindrical reactor filled with $MmNi_{4.6}Al_{0.4}$. ➢ Postulated that by balancing entropy generation against cycle time, optimum operating conditions could be obtained.
Mohammadshahi et al. (2016)	➢ Comprehensive review on mathematical modelling of MH based systems for hydrogen storage applications. ➢ Major assumptions such as local thermal equilibrium, treatment of hydrogen as an ideal gas and neglecting heat transfer by mass convection have been validated under normal operating conditions.

Table 2.3. Summary of reported literature about numerical studies focusing on heat transfer enhancement techniques

Author(s) and Year	Prominent Contributions
Mohan et al. (2007)	➢ Proposed $LaNi_5$ based reactor with embedded filters and cooling tubes. ➢ Reduction in bed thickness to 10 mm and increase in cooling tube diameter to 20 mm, individually resulted in better absorption performance.
Askri et al. (2009a)	➢ Developed a three-dimensional model of $MmNi_{4.6}Al_{0.4}$ based reactor designed with fins. ➢ Consideration of fins had enhanced the heat transfer and resulted in 40% improvement of absorption rate to attain 90% of storage capacity.
Mellouli et al. (2009)	➢ Impact of metal foam heat exchanger in $LaNi_5$ based reactor through two-dimensional model. ➢ At supply condition of 10 bar and 20 °C, the time to absorb 90% of hydrogen reduced by 60% due to metal foam inclusion.
Muthukumar et al. (2012b)	➢ Developed a two-dimensional thermal model of $MmNi_{4.6}Al_{0.4}$ based reactor with different configuration of ECT. ➢ Formulated industrial scale reactor with 48 ECT configuration, capable of storing 150 kg of MH alloy. The required absorption time of 2120 s for reaching 96% of storage capacity.
Bao et al. (2013a, 2013b)	➢ Developed a three-dimensional model of cylindrical reactor. ➢ Effect of various parameters on the absorption time: the effective thermal conductivity of MH > HTF flow rate > contact resistance > the heat exchanger material. ➢ Developed an optimization procedure based on computational fluid dynamics-Taguchi combined method for reactor design.

Anbarasu et al. (2014a)	➢ Developed two-dimensional mathematical model of cylindrical reactors with ECT and solved using COMSOL Multiphysics 4.3. Three-dimensional mathematical model to predict the hydriding/dehydriding performance at various operating conditions. ➢ Among the configurations, 60 ECT model was observed to depict best performance. Numerically predicted results were in good agreement with experimentally observed data.
Ferekh et al. (2015)	➢ Compared the effect of internal fins and metal foams as heat transfer augmentation through three-dimensional transient model of ZrCo bed. ➢ Inclusion of internal metal foams in MH bed was adjudged to be a better technique.
Singh et al. (2015)	➢ Proposed a three-dimensional model of cylindrical reactor with annular heat exchanger tube embedded with radial copper fins for storing 1 kg of $LaNi_5$. ➢ At supply pressure of 15 bar, with HTF at 25 °C and flowing at 1 m/s, the complete absorption up to 1.34 wt% was predicted in half cycle time of 1080 s.
Afzal et al. (2017)	➢ Detailed review on various heat transfer techniques employed in MH based hydrogen storage systems. ➢ Improvement in both thermal conductivities of the bed and heat transfer coefficient of the system has to be considered concurrently.
Bouzgarrou et al. (2019)	➢ Considered six different reactor configurations, some of which were included with internal heat exchangers. ➢ Configuration with internal heat exchanger and empty zones reduced absorption time by 87% when compared with the basic configuration.

Table 2.4. Summary of reported literature about numerical studies on metal hydride based heat pumps and cooling systems

Author(s) and Year	Prominent Contributions
Nishizaki et al. (1983)	➢ Modelled a chemical heat pump with four reactor system. ➢ Two reactors of $LaNi_{4.7}Al_{0.3}$ as regeneration alloy and two reactors of $LaNi_5$ as refrigeration alloy. ➢ Predicted COP: 0.8.
Kim et al. (1997b)	➢ Proposed a finite thermodynamics model to study compressor driven MH based air conditioner. ➢ Lower pressure ratio of compressor, higher compressor efficiency and higher total heat conductance between heat exchangers and reservoirs resulted in higher COP. ➢ Predicted COP: 1.5 to 4.
Gopal and Murthy (1995a)	➢ MH refrigerator working with ZrMnFe and $MmNi_{4.5}Al_{0.5}$ alloy pair. ➢ Operating temperature range: heat source/sink/refrigeration temperature (T_h / T_m / T_c): 140-155 °C / 35 °C / 0-10 °C. ➢ Predicted COP: 0.7.
Mazumdar et al. (2005a)	➢ CDMHCS with $Zr_{0.9}Ti_{0.1}Cr_{0.55}Fe_{1.45}$ as the working alloy. ➢ Two finned reactors of cylindrical configuration with diameter of 20 mm, with a reciprocating compressor in between. ➢ Predicted COP of 2.2 and SCP of 0.16 kW/kg of total alloy. ➢ Selection of suitable alloy and reactor design that facilitate fast reaction kinetics is of important.
Mazumdar et al. (2005b)	➢ CDMHCS employing four different alloys. ➢ $MmNi_{4.5}Al_{0.5}$ yielded best performance with COP and SCP of 2.55 and 0.15 kW/kg of total alloy, respectively. ➢ Considering reactor design, parasitic thermal mass of reactor is a limiting factor in achieving the cooling output.
Satheesh et al. (2009)	➢ Unsteady, two-dimensional mathematical model of annular cylindrical configuration, solved numerically using finite volume method. ➢ Studied the MHCS working with $MmNi_{4.6}Al_{0.4}$ and $MmNi_{4.6}Fe_{0.4}$ alloy pair.

	➢ At given temperature T_h / T_m / T_c of 90 °C, 25 °C and 5 °C, the cycle time was estimated to be 20.1% more for variable wall boundary condition.
Satheesh and Muthukumar (2010a)	➢ Unsteady, two-dimensional model of single stage MHHP, solved using a fully implicit finite volume method. ➢ MH beds of cylindrical configuration, containing $LmNi_{4.91}Sn_{0.15}$/$Ti_{0.99}Zr_{0.01}V_{0.43}Fe_{0.09}Cr_{0.05}Mn_{1.5}$ alloy pair. ➢ Predicted COP of 0.66 and SCP of 53.25 W/kg of total system mass.
Satheesh and Muthukumar (2010b)	➢ Double stage double effect MHHP working with $LaNi_{4.1}Al_{0.52}Mn_{0.38}$, $LmNi_{4.91}Sn_{0.15}$ and $Ti_{0.99}Zr_{0.01}V_{0.43}Fe_{0.09}Cr_{0.05}Mn_{1.5}$ alloy system. ➢ Heat source, heat rejection, heat sink and refrigeration temperature of 305 °C, 100 °C, 25 °C and 10 °C. ➢ Predicted average COP was 0.81 and SCP of system was 48.1 W/kg of total alloy mass.
Muthukumar and Satheesh (2013)	➢ Single stage MHHP operating on the crossed van't Hoff principle, employing two regeneration/refrigeration alloy pairs namely, $V_{0.846}Ti_{0.104}Fe_{0.05}$/$Fe_{0.9}Mn_{0.1}Ti$ and $V_{0.855}Ti_{0.095}Fe_{0.05}$/$MmNi_{4.7}Al_{0.3}$. ➢ The optimum T_h / T_m / T_c for $V_{0.846}Ti_{0.104}Fe_{0.05}$/$Fe_{0.9}Mn_{0.1}Ti$ pair were found to be 100 °C, 30 °C and 18 °C. ➢ Predicted COP and SCP of 0.89 and 30.8 W/kg of total alloy mass, respectively.
Sharma et al. (2015)	➢ Investigated the influence of dynamic operation conditions on the performance of MHCS. ➢ Considering $La_{0.9}Ce_{0.1}Ni_5$ and $LaNi_{4.7}Al_{0.3}$ pair, reduction in COP by 31.9% and cooling capacity by 57.8% was observed when the dynamic PCT based analysis was compared with the static PCT based analysis.
Sharma and Kumar (2017)	➢ Proposed Multi stage multi effect MH based system that employed four different alloys working in conjunction. ➢ Predicted 3337 kJ of cooling, 3243 kJ of high grade heat output and 5726 kJ of low grade heat output with overall theoretical COP of 2.22 for cycle time of 3840 s.

Table 2.5. Summary of reported literature about experimental investigations on heat transfer augmentations

Author(s) and Year	Prominent Contributions
Linder et al. (2010)	➢ Developed capillary tube bundle MH reactors for MHCS with $LmNi_{4.91}Sn_{0.15}$/$Ti_{0.99}Zr_{0.01}V_{0.43}Fe_{0.09}Cr_{0.05}Mn_{1.5}$ alloy pair. ➢ Achieved half cycle time of 100 s and SCP of 780 W/kg of desorbing alloy.
Souahlia et al. (2011a, 2011b)	➢ Developed different geometries to study the effect of reactor design on hydrogen storage performance. ➢ Complex reactor design with internal finned spiral heat exchanger, resulted in 20% improvement in performance.
Visaria and Mudawar (2012)	➢ Developed a complex coiled tube heat exchanger of $Ti_{1.1}CrMn$ (4 kg) based storage for fuel cell integration. ➢ Occupying 7% of the internal volume, the heat exchanger resulted in 75% improvement in hydrogen absorption rate.
Yasuda et al. (2013)	➢ Utilized MH sheets made of MH powder, carbon powder and aramid pulp in developing MHHP. ➢ $TiFe_{0.9}Ni_{0.1}$/$La_{0.6}Y_{0.4}Ni_{4.9}Al_{0.1}$ as working alloy pair. ➢ Usage of MH sheets resulted in 20% improvement of SCP. ➢ Postulated that heat transfer enhancement on cooling output reactor was more important than heat source reactor.
Anbarasu et al. (2014b, 2014c)	➢ Fabricated reactors of 36 ECT and 60 ECT configuration, filled each with 2.75 kg of $LmNi_{4.91}Sn_{0.15}$. ➢ Bed attained maximum storage capacity of 1.8 wt% in 480 s and 600 s, respectively for 60 ECT and 36 ECT reactors at supply condition of 35 bar, 30 °C and 3.2 lpm. ➢ At 50 °C and 30 lpm flow rate, 60 ECT reactor completely desorbed in 480 s. ➢ Prominently observed rapidity in rate of heat transfer and amount of hydrogen transferred due to the ECT configuration.
Weckerle et al. (2017)	➢ Developed a novel soldered plate reactor design and filled with 0.353 kg of Hydralloy C5 for MHCS. ➢ Single reactor system resulted in SCP of 1.31 kW/kg of alloy. Coupled reactor system resulted in SCP of 0.69 kW/kg of alloy.

Table 2.6. Summary of reported literature about experimental investigations on metal hydride based heat pump and cooling systems

Author(s) and Year	Prominent Contributions
Ron (1984)	➢ Proposed a MHHP as an air conditioner for bus utilizing waste heat exhaust as heat source. ➢ $LaNi_{4.7}Al_{0.3}$ as high temperature and $MmNi_{4.15}Fe_{0.85}$ as low temperature alloys. ➢ Obtained SCP of 0.25 kW/kg of desorbing MH and COP was 0.22 to 0.35.
Suda et al. (1991)	➢ Developed double-stage thermally driven MHHP working with $LaNi_{4.28}Al_{0.23}$, $MmNi_{4.57}Al_{0.46}Fe_{0.05}$ and $MmNi_{3.98}Fe_{1.04}$. ➢ An ideal and actual COP of 0.36 and 0.21, while overall alloy thermal output was 33 W/kg of alloy.
Kim et al. (1998, 1997a)	➢ Developed reactors containing copper-coated $LaNi_5$ producing SCP of 1.5 kW/kg of alloy for desorption time of 130 s. ➢ Achieved 2.2 kW/kg of alloy for copper coated compacts of $Ca_{0.4}Mm_{0.6}Ni_5$. ➢ Cooling output of $LaNi_5$ compacts reduced by 55% after 3000 cycles.
Park et al. (2002, 2001)	➢ CDMHHP with two finned reactors containing 4.2 kg of $Zr_{0.9}Ti_{0.1}Cr_{0.55}Fe_{1.45}$ compacts. ➢ Utilizing oil-less compressor, maximum cooling output was estimated to be 251 kcal/kg alloy h. ➢ CDMHHP using oil type compressor and reactor filled with 3.5 kg of $Zr_{0.9}Ti_{0.1}Cr_{0.55}Fe_{1.45}$. ➢ Achieved COP of 1.8 with half cycle time of 180 s, and minimum cooling temperature of 6 °C.
Magnetto et al. (2006)	➢ CDMHCS for employed heat exchangers with ring manifold reaction tubes. ➢ Obtained COP of 2.76 to 2.57 with average cooling capacity of 1.5 kW to 2.1 kW.
Patel et al. (2013)	➢ Proposed CDMHHP with two reactors, each with 3.5 kg of $LmNi_5$. ➢ Achieved COP of 1.1 at HTF temperature of 15 °C.

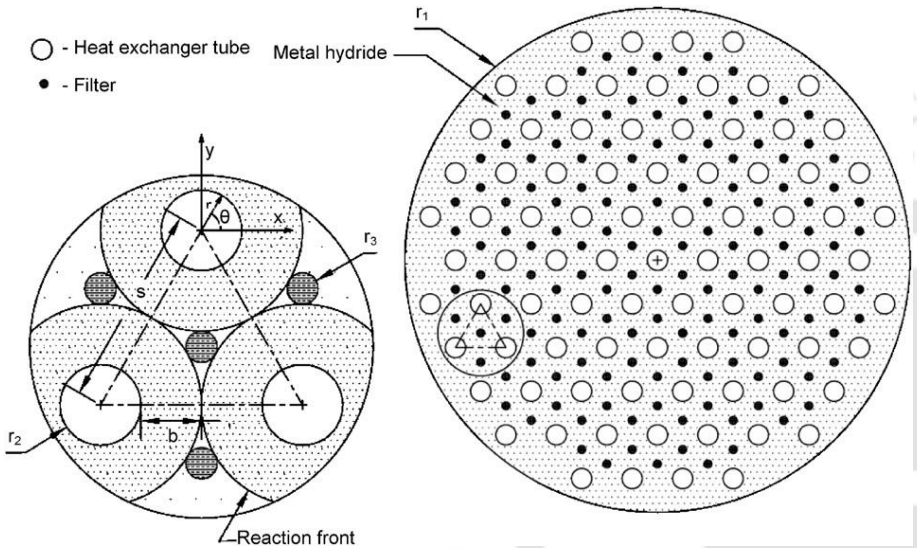

(A) Reactor modelled with embedded filters and cooling tubes (Mohan et al., 2007)

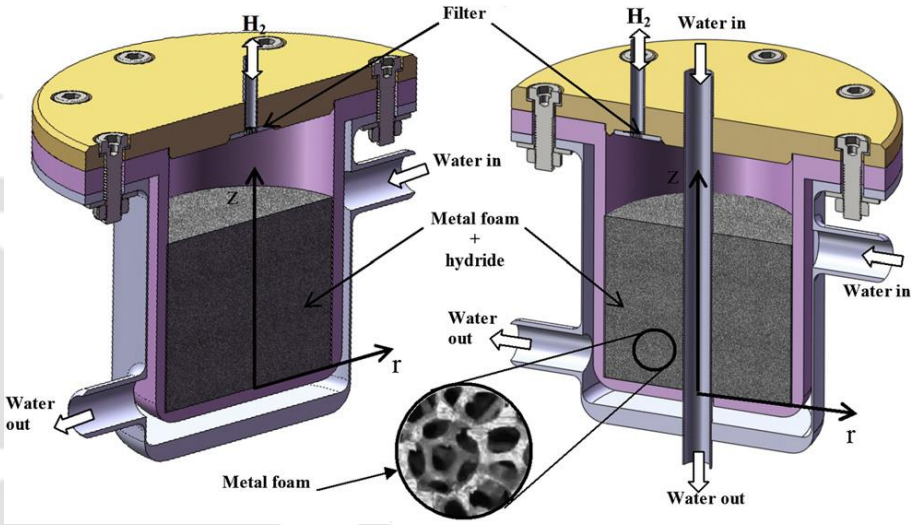

(B) Heat exchanger modelled with metal foam (Mellouli et al., 2009)

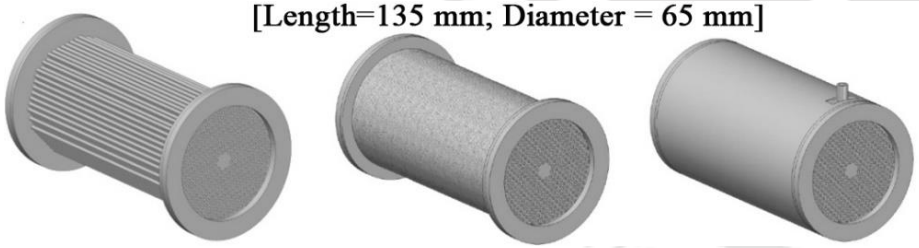

(C) Designed capillary tube bundle MH reactor (Linder et al., 2010)

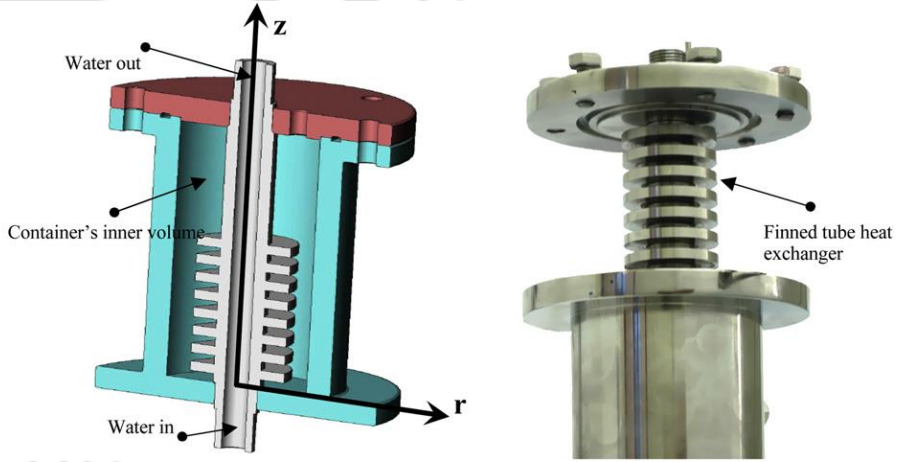

(D) 3D model and pictorial view of finned tube heat exchanger (Souahlia et al., 2011b)

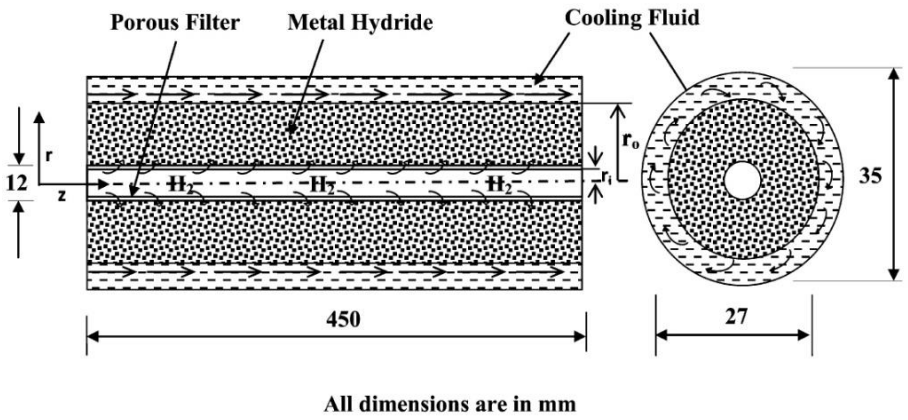

(E) Schematic of modelled co-axial cylindrical reactor (Muthukumar et al., 2012a)

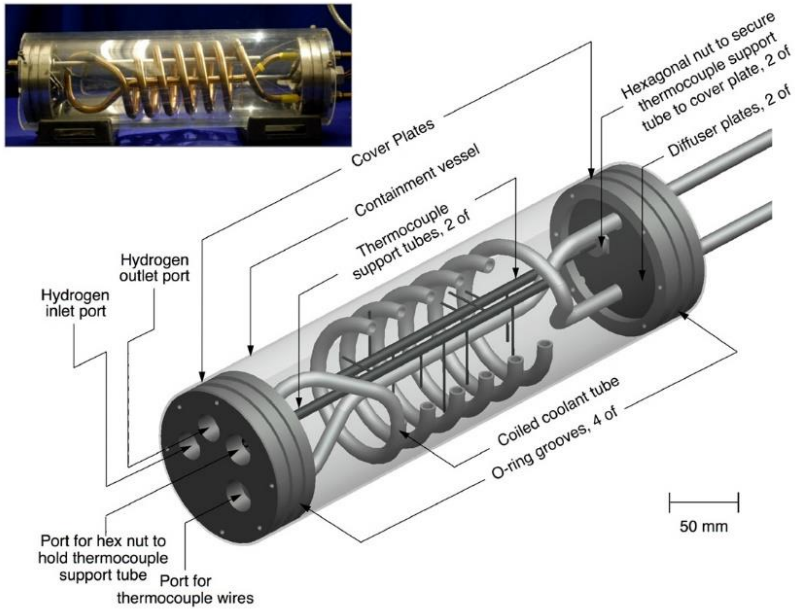

(F) Detailed 3D rendering and pictorial view of coiled-tube heat exchanger (Visaria and Mudawar, 2012)

(G) Pictorial view of 36 and 60 ECT reactor models (Anbarasu et al., 2014b)

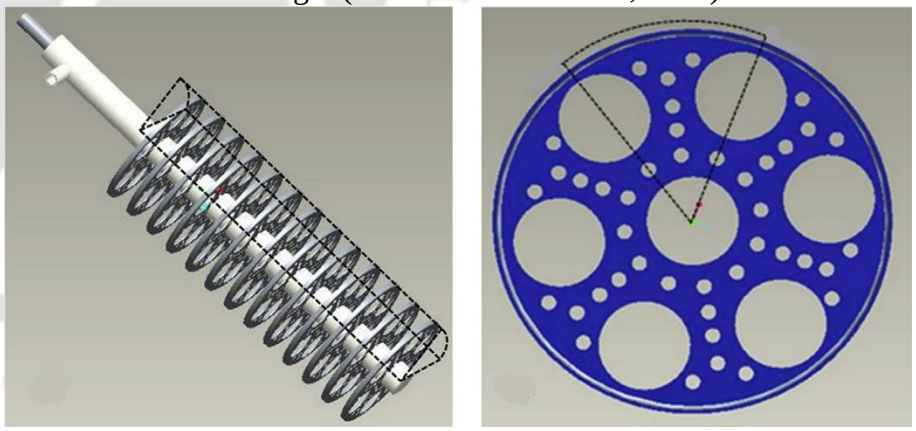

(H) Modelled view of heat exchanger fin assembly and copper fin (Singh et al., 2015)

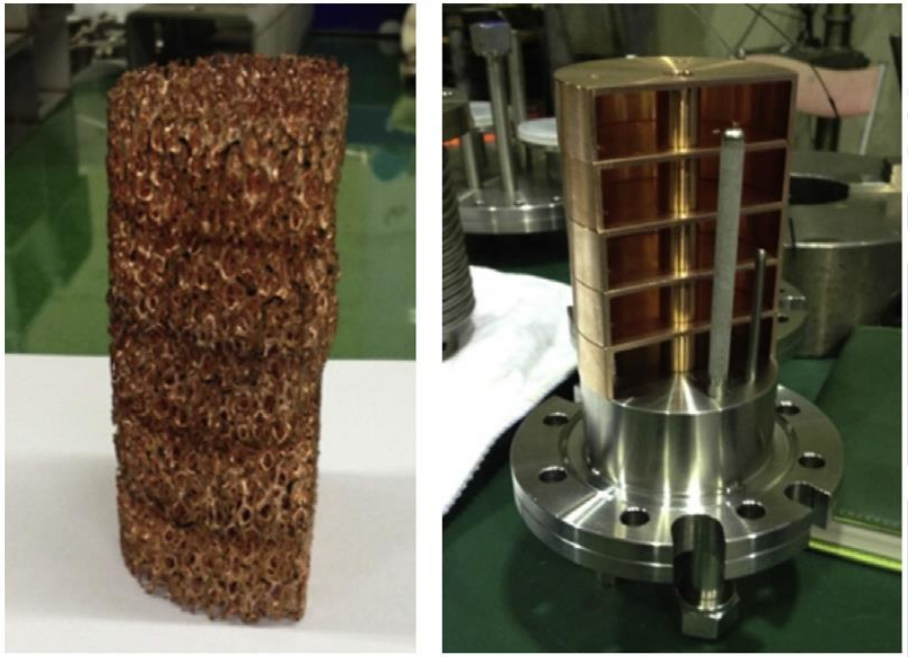

(I) Pictorial view of copper metal foam and copper fin inclusions (Ferekh et al., 2015)

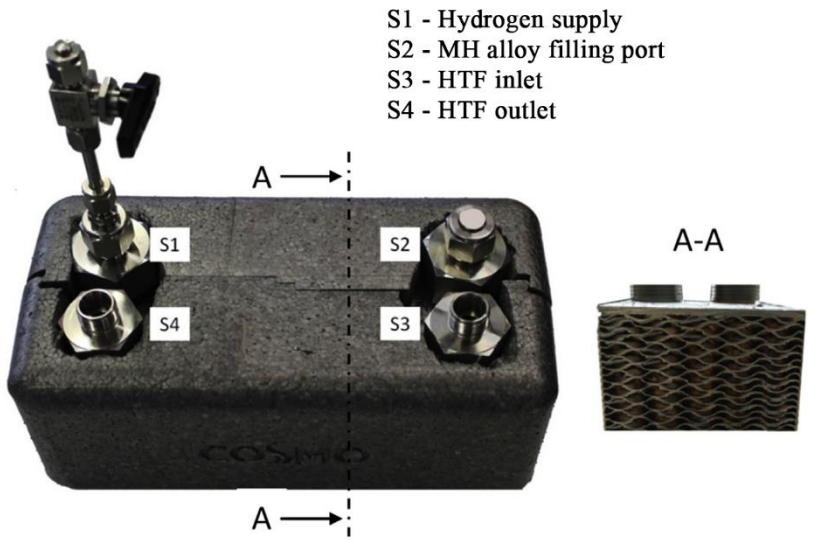

(J) Assembled and cross sectional views of soldered plate reactor (Weckerle et al., 2017)

Fig.2.2. The schematics and details of different metal hydride reactors that have been theoretically modelled and experimentally investigated in the reported literature

2.5 Literature closure

From the extensive literature review, following conclusions have been obtained:

- Various mathematical models have been proposed to analyse the reaction kinetics models and reaction rate equations. Concurrently, multiple studies on MH alloy screening and selection along with their property measurement and characterization have been sufficiently established.
- Heat and mass transfer characteristics of MH based systems have been extensively analysed through development of one-dimensional, two-dimensional and three-dimensional modelling while considering the effects of alloy properties, PCT characteristics, reactor design features and operating conditions.
- Numerical investigations on absorption/desorption of MH based hydrogen storage system have been primarily focused on analysing the effects of operating conditions such as supply pressure, absorption/desorption temperatures, flow rate of heat transfer fluid and overall heat transfer coefficient on the absorption/desorption performance parameter such as rate of reaction and amount of hydrogen transferred. Validity of significant assumptions that are instrumental in modelling have been well established.
- The primary finding of all numerical investigations have been the importance of efficient heat transfer to and from the bed during desorption and absorption reactions. Towards this aspect, various heat transfer enhancement methods have been proposed and their impact have been simulated using developed mathematical models. The enhancement techniques are focussed on improving the effective thermal conductivity and designing MH reactors with high overall heat transfer coefficient.
- Towards the design of reactors with heat transfer enhancement techniques, various features like internal cooling tube, external cooling jacket, internal and external fins,

internal and external coiled tube heat exchangers, embedded filters and cooling tubes as well as capillary tube bundle models have been conceptualised.

- Single stage, double stage double effect and multi stage multi effect MHHP along with CDMHHP and CDMHCS have been modelled based on the alloy PCT characteristics, heat and mass transfer investigations. Even in theoretical consideration, thermally driven system are able to achieve COP of about 0.8 only while CDMHHP and CDMHCS have depicted COP of more than 2.
- Among the reported experimental investigations on MH based hydrogen storage systems, the primary focus is on the improvement of the dynamic heat and mass transfer characteristics of bed to achieve higher capacity in shorter cycle time with improved reaction kinetics. Most of the reported studies have been limited to lab scale prototype reactors and the experimental investigations have studied the effect of operating parameters on absorption and desorption output.
- Though various reactor designs with complex heat transfer augmentations have been modelled, very few designs have been deemed economical and feasible for large scale production, focused towards practical applications. Complex designs further result in more parasitic thermal mass. Moreover, there is a significant deficiency of design methodologies and guiding principles that can facilitate the reactor design with enhanced heat transfer characteristics and nominal thermal mass.
- From the literature review, it is noted that there is limited experimental investigation of MH based heat pump and cooling systems, though various system have been modelled and proposed mathematically. Few CDMHCS and CDMHHP that were experimentally investigated have corroborated the high COP obtained through numerical investigations. Development of these systems would pose significant competition to conventional refrigeration systems.

- Additionally, it has been observed that industrial scale MH based system design and conceptualization have been quite limited with very few reported study on practically implemented systems. Considering the requirement for stationary and mobile applications, design and development of industrial scale MH based hydrogen storage and cooling systems that can be operated in near ambient conditions are of principal importance.

2.6 Thesis objectives

In view of the above conclusions drawn from literature review, the following core objectives are framed for this thesis work:

- To select alloys that are suitable for operation in near ambient conditions and are better candidates for metal hydride based storage and cooling systems.
- To develop a novel design methodology that balances the enhanced heat transfer characteristics of the hydrogen storage or thermal management systems against the parasitic thermal mass.
- To predict and analyze the storage performance and heat transfer characteristics of reactor designed based on developed methodology using valid numerical model.
- To develop an experimental set-up and conduct parametric and performance investigations on MH based cooling system considering industrial scale reactor.
- To develop an experimental set-up and conduct performance investigation on metal hydride based compressor driven cooling system, employing the designed reactors.

2.7 Summary

In this chapter, detailed state-of-art review on the alloy selection, properties and characterization, heat and mass transfer characteristics of MH bed during absorption and desorption reactions, and numerical modelling and experimental performance investigation of

MH based hydrogen storage and cooling systems have been reviewed extensively. Additional focus has been directed towards the heat transfer enhancement techniques conceptualized and implemented practically. Based on the reviewed literature, well established systems and theories have been identified. Furthermore, the research gap has been identified and objectives of the present thesis work have been framed to meet this demand.

CHAPTER 3

DESIGN METHODOLOGY AND THERMAL MODELLING

3.1 Preface

To address the need for guiding principle towards the design of metal hydride (MH) reactors, a novel set of comprehensive arithmetic correlations has been proposed to design cylindrical reactor with embedded cooling tubes (ECT). Using this design methodology, reactors of lab scale and industrial scale can be developed for MH based hydrogen storage and thermal management applications. Based on Standards, different nominal pipe sizes have been considered. The methodology is framed for selection of suitable reactor shell from the available nominal pipe sizes while considering the operational constraint of end user applications. Though various designs have been proposed in the literature, they are observed to be too complex and demand higher manufacturing cost. These designs further result in high parasitic

thermal mass, which is another disadvantage. This methodology provides an adaptable strategy that result in simpler reactor design with ease of fabrication. The mathematical approach considered towards the development of design methodology and performance prediction of MH based hydrogen storage and cooling systems is represented in Fig.3.1.

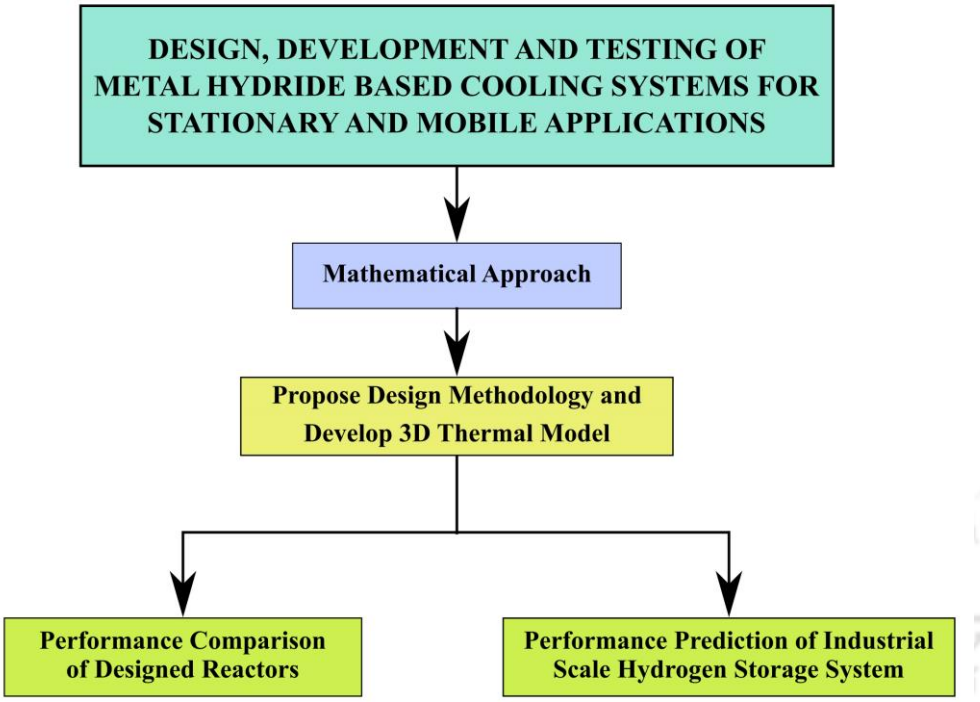

Fig.3.1. Flowchart depicting the mathematical approach to the investigation into metal hydride based hydride hydrogen storage and cooling system

3.2 Design methodology

The underlying principle of this methodology is to select the reactor shell size for required alloy capacity and design them with ECT distribution such that bed thickness at each cooling surface is uniform. This is done while balancing the design against resulting parasitic thermal mass of empty reactor. Utilizing this strategy, reactor design of different scale and multiple avenues of applications can be addressed. Considering hydrogen permeability in metals and prerequisite strength for high pressure applications, stainless steel SS316 is chosen as reactor material. Typical design of ECT reactor based in this methodology has been depicted in Fig.3.2.

A porous filter made of sintered SS316 material with a pore size of 2 μm having an outer diameter of 14 mm and thickness of 2 mm is centrally placed. Hydrogen gas is supplied through the porous filter which facilitates uniform distribution of gas throughout the length of reactor during absorption and also filters MH particles from being carried away by the H_2 gas during desorption.

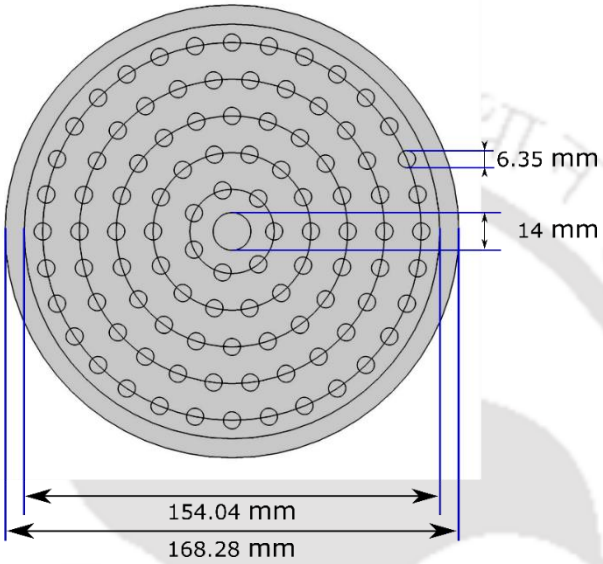

Fig.3.2. Cross sectional schematic view of reactor with embedded cooling tubes using 6 inch nominal diameter cylindrical shell

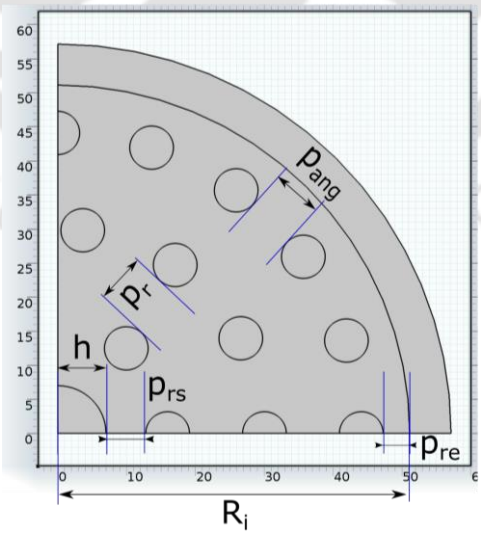

Fig.3.3. Sectional view of typical reactor with embedded cooling tubes representing components of design correlation

ECT are made of SS316 with an outer diameter of 6.35 mm and thickness of 0.89 mm. As represented in Fig.3.2, they are distributed within the reactor shell in a layered formation named as stacks. The radial locations and number of tubes in each stack are deduced based on the developed correlations. The selection of suitable pipe for cylindrical reactor shell from nominal pipe sizes stated in Standards has been briefed in APPENDIX A. Bed thickness (b) is considered as the minimum distance between two cooling interfaces. Various components of design correlations are represented in Fig.3.3, which includes outer radius of porous filter (h), inner radius of cylindrical shell (R_i), radial pitch (p_r) and angular pitch (p_{ang}) between ECT. Further, 'p_{rs}' represents radial pitch between supply porous filter and ECT of first stack while 'p_{re}' represents radial pitch between ECT of last stack and inner periphery of reactor shell. As the bed thickness should be uniform between ECT both in angular and radial direction,

$$p_r = p_{ang} = b \qquad \text{(Eqn.3.1)}$$

Since, the periphery of reactor shell and supply filter are considered to be adiabatic, only the ECT interfaces provide heat transfer. Hence, 'p_{re}' is estimated as half of bed thickness,

$$p_{re} = 0.5 * b \qquad \text{(Eqn.3.2)}$$

Placement of first stack around supply porous filter is difficult as it involves welding of ECT and supply porous filter onto end flange plates. Based on prior design and fabrication experience, a factor of 1.5 is considered for estimation of 'p_{rs}' as,

$$p_{rs} = 1.5 * p_{re} \qquad \text{(Eqn.3.3)}$$

Based on these considerations, a relation between bed thickness (b) and number of stacks (s) is devised using 'R_i' from Fig.3.2 as,

$$R_i = h + s*(2r_o) + (s-1)p_r + p_{re} + p_{rs} \qquad \text{(Eqn.3.4)}$$

where 'r_o' denotes outer radius of ECT. Using above correlations, R_i is rewritten as,

$$R_i = h + s*(2r_o) + (s-1)b + 0.5*b + 0.75*b$$

which essentially provides the relation between '*s*' and '*b*' as,

$$b = \frac{R_i - h - s*(2r_o)}{(s + 0.25)} \qquad \text{(Eqn.3.5)}$$

Value of bed thickness (*b*) is estimated for fixed 'R_i', '*h*' and 'r_o' values while varying the number of stacks (*s*). From reported literatures, it is observed that higher bed thickness leads to poor conductive heat transfer within MH bed. However, decreasing it to a very low value leads to a case of over-optimization wherein the parasitic thermal mass of resulting design will be too high. Taking input from the reported effect of bed thickness on reaction kinetics of MH (Chibani et al., 2018; Muthukumar et al., 2007), value of '*b*' has been ensured between 5 to 10 mm while varying '*s*' among positive integers. To better explain this strategy, the bed thickness and ratio of empty reactor mass to 50 kg alloy mass are estimated for different '*s*' values considering 6 inch and 4 inch nominal size shells, as represented in Fig.3.4.

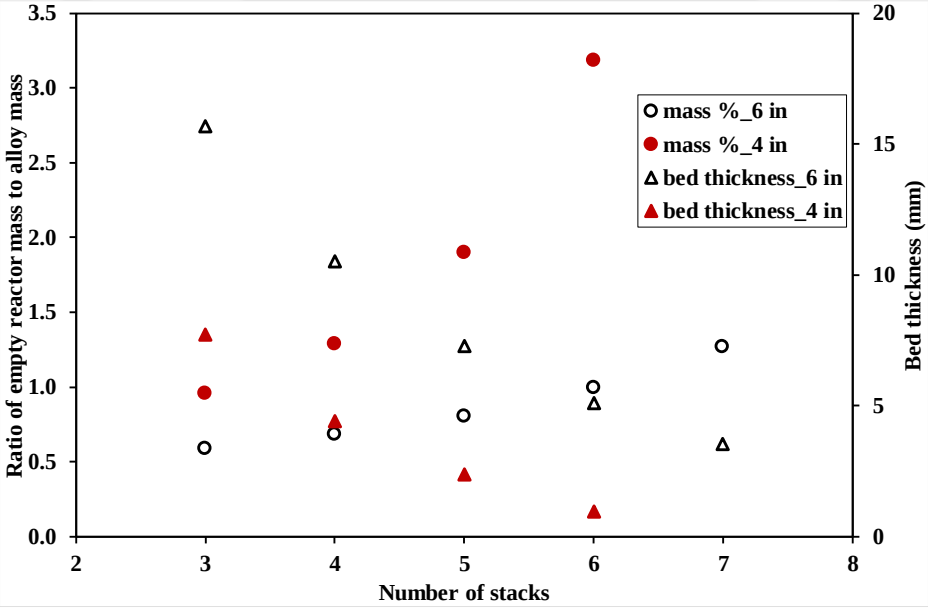

Fig.3.4. Influence of number of stacks on bed thickness and ratio of empty reactor mass to alloy mass

It is observed from Fig.3.4, that in case of 6 inch nominal size reactor, 3 and 4 stack structures resulted in respective bed thickness of 15.68 mm and 10.5 mm which are quite adverse for heat transfer. Though the corresponding bed thickness are 5.11 mm and 3.53 mm for 6 and 7 stack

structure, the resultant reactor mass are respectively 1 and 1.26 times than that of alloy mass, which would result in more parasitic thermal mass. Hence, 5 stack structure having 7.29 mm bed thickness with mass ratio of 0.803 is chosen. From Fig.3.4, it is also inferred that the 4 inch model having 3 stack structure with bed thickness of 7.72 mm is ideal. Analysis of 5 inch and 8 inch reactor shells resulted in 4 and 6 stack structures, respectively. Considering the pitch and radius of ECT, radial location of first stack (R_1) and j^{th} stack (R_j) are deduced from 'b' and 's' values as,

$$R_1 = h + p_{rs} + r_o \quad \text{(Eqn.3.6)}$$

$$R_j = R_{j-1} + p_r + 2*r_o \quad \text{(Eqn.3.7)}$$

where, 'j' is varied here from 2 to 's'. From location of j^{th} stack, number of ECT in j^{th} stack (N_j) is estimated as,

$$N_j = \frac{2\pi * R_j}{2*r_o + p_r} \quad \text{(Eqn.3.8)}$$

where, 'j' is varied here from 1 to 's'. The resulting 'N_j' is rounded off to next positive integer as it represents number of ECT. Summation of ECT in each stack lead to total number of ECT (N_{total}) as,

$$N_{total} = \sum_{j=1}^{s} N_j \quad \text{(Eqn.3.9)}$$

Considering 50 kg of alloy mass (m_{MH}) and effective density of MH alloy at saturated state (ρ_{ss}), required volume for MH alloy storage is estimated as,

$$V_{MH} = 1.2 * \frac{m_{MH}}{\rho_{ss}} \quad \text{(Eqn.3.10)}$$

wherein a safety factor of 1.2 is considered to account for volumetric expansion during absorption of MH. Considering the alloys suitable for proposed systems, ρ_{ss} has been considered as 4000 kg/m^3. Required length of reactor (L) is estimated by considering the required volume and available cross sectional area for MH storage.

It is given by,

$$L = \frac{V_{MH}}{\pi(R_i^2 - N_{total} * r_o^2 - h^2)} \quad \text{(Eqn.3.11)}$$

Hence, mass of empty reactor (m_R) is estimated as,

$$m_R = \rho_R \pi L[(R_o^2 - R_i^2) + N_{total} * (r_o^2 - r_i^2)] \quad \text{(Eqn.3.12)}$$

where 'ρ_R' denotes density of SS316, 'R_o' and 'r_i' respectively denote outer radius of reactor shell and inner radius of ECT. Determining the ratio of empty reactor metal mass to alloy mass of 50 kg (m_R/m_{MH}) is a crucial factor for reactor design. Based on these correlations, reactors of 4 inch, 5 inch, 6 inch and 8 inch nominal pipe sizes are designed as detailed in Table 3.1.

Table 3.1. Evaluated design parameters based on developed correlations for shells of different nominal pipe size

Nominal pipe size (inch)	Outer diameter (mm)	Thickness (mm)	Radial location of each stack	No. of tubes at each stack	Total no. of tubes	Reactor length	Mass ratio (m_R/m_{MH})
4	114.30	6.02	15.96	07	40	2262.69	0.955
			30.03	13			
			44.10	20			
5	141.30	6.55	15.77	07	67	1445.47	0.868
			29.58	14			
			43.39	20			
			57.20	26			
6	168.28	7.12	15.64	07	99	1001.27	0.803
			28.28	14			
			42.92	20			
			56.56	26			
			70.20	32			
8	219.08	8.18	16.93	07	136	552.53	0.653
			32.28	13			
			47.63	20			
			62.98	26			
			78.33	32			
			93.68	38			

It is interesting to note that the bed thickness of all these designs ranged between 7.29 mm and 9 mm only. The designed assembly of cylindrical shell with supply porous filter and ECT arrangement is collectively termed as principal reactor chamber. In the physical model, end flange plates having thickness 1.5 times that of reactor shell thickness are welded onto both ends of principal chamber. Supply tube is welded onto porous filter while auxiliary fluid flow chambers are welded onto the end flange plates. They act as HTF collection chambers at inlet and outlet of the ECT. Based on the nominal pipe sizes and total number of ECT, the reactors are respectively labelled as RI_4in_41ECT, RII_5in_67ECT, RIII_6in_99ECT and RIV_8in_136ECT. Only the principal chamber of the reactor designs are considered for the numerical modelling.

3.3 Thermal modelling

While modelling the MH reactor, gas transport phenomenon within MH bed, combined heat and mass transfer characteristics arising from absorption and desorption reaction, variable wall convective boundary at ECT interface and variation of hydrogen concentration within bed have been considered.

3.3.1 Assumptions

To simplify the model, following valid assumptions reported in literature have been considered (Askri et al., 2003; Jemni and Nasrallah, 1995b, 1995a; Mellouli et al., 2010; Muthukumar and Ramana, 2009, 2010):

- Ideal gas consideration for hydrogen gas.
- Local thermal equilibrium between the gas and metal hydride bed is valid.
- For low temperature hydrides, the effect of radiative heat transfer is neglected.
- The solid phase is isotropic and has uniform porosity.

- The centrally placed porous filter is adiabatic and allows only hydrogen to pass through.
- Hydrogen gas is supplied to the reactor at a known constant pressure.
- Thermal conductivity and specific heat capacity of chosen alloy are independent of pressure, temperature and concentration of hydrogen.
- The reactor shell is assumed to be well insulated so that there is no heat transfer with surroundings.

3.3.2 Governing equations

Following governing equations are utilized to model and simulate the system.

Reaction rate:

The rate of mass of hydrogen absorbed (ζ_a) or desorbed (ζ_d) per unit volume per unit time by the MH is given as

$$\zeta_a = C_a \exp\left(-\frac{E_a}{R_u T}\right) \ln\left(\frac{P_s}{P_{eq}}\right)\left(\rho_{ss} - \rho_t\right) \quad \text{(Eqn.3.13)}$$

$$\zeta_d = C_d \exp\left(-\frac{E_d}{R_u T}\right)\left(\frac{P_{eq} - P_d}{P_{eq}}\right)\left(\rho_t - \rho_0\right) \quad \text{(Eqn.3.14)}$$

where 'C_a' and 'C_d' respectively denote reaction rate constant during absorption and desorption, 'R_u' is universal gas constant, 'P_s' and 'P_{eq}' respectively denote supply pressure and equilibrium pressure of MH alloy while 'P_d' denotes desorption pressure and 'T' is the temperature within MH bed. Similarly, 'E_a' and 'E_d' respectively denote activation energy during absorption and desorption reaction while 'ρ_t' denotes the density of MH alloy at any given time 't' and 'ρ_{ss}' represents density of MH at saturation state.

Mass balance:

During absorption, the bed acts as a sink for the hydrogen. Considering the sink term as rate of mass of hydrogen absorbed, the hydrogen mass balance equation is formulated, while the absorbed mass is source term for the solid phase (Muthukumar et al., 2012b; Muthukumar and Ramana, 2009),

$$\varepsilon \frac{\partial \rho_g}{\partial t} + \nabla.(\rho_g \vec{u}) = -\zeta_a \quad \text{(Eqn.3.15)}$$

$$(1-\varepsilon) \frac{\partial \rho_t}{\partial t} = \zeta_a \quad \text{(Eqn.3.16)}$$

where 'ρ_g' denotes the density of hydrogen gas within the bed, '$\vec{u}$' is the velocity vector and 'ε' represents porosity. During desorption, the bed acts as a source for the hydrogen. Hence, the hydrogen and hydride mass balance equations can be formulated as,

$$\varepsilon \frac{\partial \rho_g}{\partial t} + \nabla.(\rho_g \vec{u}) = \zeta_d \quad \text{(Eqn.3.17)}$$

$$(1-\varepsilon) \frac{\partial \rho_t}{\partial t} = -\zeta_d \quad \text{(Eqn.3.18)}$$

Density of hydrogen gas (ρ_g) can be evaluated from ideal gas equation,

$$\rho_g = \frac{P_g M_g}{R_u T} \quad \text{(Eqn.3.19)}$$

where 'P_g' is the gas pressure and while 'M_g' is the molecular weight of gaseous hydrogen.

Mass balance equation for heat transfer fluid (HTF) is given by,

$$\nabla.\vec{u}_f = 0 \quad \text{(Eqn.3.20)}$$

where '$\vec{u}_f$' is the velocity vector of HTF.

Momentum balance:

Velocity of hydrogen flow inside MH bed ($\vec{u}$) is modelled considering pressure gradient using Darcy's Law as given by,

$$\vec{u} = -\left(\frac{K}{\mu_g}\right)\nabla P \quad \text{(Eqn.3.21)}$$

where 'K' is the permeability of the MH bed and 'μ_g' is the dynamic viscosity of hydrogen gas.

The momentum of HTF is governed by,

$$\rho_f\left(\frac{\partial \vec{u}_f}{\partial t} + u_f.\nabla \vec{u}_f\right) = -\nabla P_f + \mu_f \nabla^2 \vec{u}_f \quad \text{(Eqn.3.22)}$$

where 'ρ_f' and 'μ_f' respectively denote the density and dynamic viscosity of HTF.

Energy balance:

Considering local thermal equilibrium between the MH bed and hydrogen gas, a combined energy equation is written as (Muthukumar et al., 2012b),

$$(\rho c_p)_e \frac{\partial T}{\partial t} + (\rho c_p)_g (\vec{u}.\nabla T) = k_e \nabla^2 T \pm Q \quad \text{(Eqn.3.23)}$$

where 'Q' is the heat source/sink term during absorption/desorption reaction.

The heat source (Q_a) and heat sink term (Q_d) are respectively considered as,

$$Q_a = \zeta_a\left(\frac{\Delta H_a}{M_g}\right) \quad \text{(Eqn.3.24)}$$

$$Q_d = \zeta_d\left(\frac{\Delta H_d}{M_g}\right) \quad \text{(Eqn.3.25)}$$

where 'ΔH_a' is the absorption enthalpy and 'ΔH_d' is the desorption enthalpy.

In the energy balance equation, effective heat capacity ($(\rho c_p)_e$) is given by,

$$(\rho c_p)_e = (1-\varepsilon)(\rho c_p)_s + \varepsilon(\rho c_p)_g \quad \text{(Eqn.3.26)}$$

where '$(\rho c_p)_g$' denotes heat capacity of gas phase, while '$(\rho c_p)_s$' represents heat capacity of solid phase. Similarly, the effective thermal conductivity is obtained as,

$$k_e = (1-\varepsilon)k_s + \varepsilon k_g \quad \text{(Eqn.3.27)}$$

In case of HTF, energy equation is formulated as,

$$(\rho c_p)_f \frac{\partial T_f}{\partial t} + (\rho c_p)_f (\vec{u}_f . \nabla T_f) = k_f \nabla^2 T_f \quad \text{(Eqn.3.28)}$$

where $(\rho c_p)_f$ is the heat capacity, 'k_f' is the thermal conductivity and 'T_f' is the temperature of HTF.

van't Hoff equation:

To evaluate the equilibrium bed pressure during absorption and desorption process, modified van't Hoff equation (Nishizaki et al., 1983) is considered,

$$\frac{P_{eq}}{P_0} = \exp\left[\frac{\Delta S}{R_u} - \frac{\Delta H}{R_u T} + (\varphi_s \pm \varphi_o) \times \tan\left(\pi\left(\frac{c_t}{c_{end}} - \frac{1}{2}\right)\right) \pm \frac{\varphi}{2}\right] \quad \text{(Eqn.3.29)}$$

where 'P_0' denotes atmospheric pressure, 'ΔS' is the entropy of reaction, while 'φ_s', 'φ_o' and 'φ' respectively denote slope factor, slope constant and hysteresis factor. Concentration is the ratio of number of hydrogen atoms absorbed over the total number of metal atoms present per mole of alloy (H/M ratio). Concentration at any given time 't' is given by 'c_t' while final concentration is represented as 'c_{end}'. The arithmetic sign '+' is considered for absorption reaction, while '–' is considered for desorption reaction, due to the effects of sloping and hysteresis.

Hydrogen storage capacity:

Considering mass (m_{MH}) and molecular weight (M_{MH}) of MH alloy, number of moles of hydrogen absorbed/desorbed (n_g) is estimated.

Number of moles of hydrogen absorbed/desorbed (n_g) is given by,

$$n_g = \frac{m_{MH} A_{MH} (c_t - c_{ini})}{2M_{MH}} \quad \text{(Eqn.3.30)}$$

where 'c_{ini}' represents initial concentration while 'A_{MH}' denotes number of metal atoms per mole of alloy. Resultant mass of hydrogen absorbed/desorbed is evaluated as,

$$m_g = n_g M_g \quad \text{(Eqn.3.31)}$$

The hydrogen storage capacity (HSC) is the mass of hydrogen absorbed/desorbed (m_g) with respect to mass of MH alloy (m_{MH}) at any given time 't', often expressed in terms of weight percentage (wt%). This is obtained using above equations as,

$$HSC\,(wt\%) = \frac{m_g}{m_{MH}} \times 100\% = \frac{A_{MH} M_g (c_t - c_{ini})}{2M_{MH}} \times 100\% \quad \text{(Eqn.3.32)}$$

Maximum or total HSC is given by,

$$Maximum\,HSC\,(wt\%) = \frac{A_{MH} M_g (c_{end} - c_{ini})}{2M_{MH}} \times 100\% \quad \text{(Eqn.3.33)}$$

3.3.3 Initial and boundary conditions

Initial conditions:

Initially at time 't' = 0, temperature of bed and HTF are considered to be uniform throughout model at the ambient temperature (T_0):

$$T_{s(r,\theta,z)} = T_{g(r,\theta,z)} = T_{(r,\theta,z)} = T_{f(z)} = T_0 \quad \text{(Eqn.3.34)}$$

Pressure and MH density are supposed to be uniform throughout the model at ambient pressure (P_0) and the effective density of MH at initial state (ρ_0), respectively:

$$\rho_{t(r,\theta,z)} = \rho_0 \quad \text{(Eqn.3.35)}$$

$$P_{g(r,\theta,z)} = P_0 \quad \text{(Eqn.3.36)}$$

Boundary conditions:

The outer boundary of the metal hydride reactor is assumed to be adiabatic throughout the process (t > 0),

$$\left.\frac{\partial T}{\partial r}\right|_{r=R_i} = 0 \qquad \text{(Eqn.3.37)}$$

where R_i is the periphery of the reactor model. The porous filter is assumed to be adiabatic:

$$\left.\frac{\partial T}{\partial r}\right|_{r=r_{op}} = 0 \qquad \text{(Eqn.3.38)}$$

where r_{op} is the outer radius of the porous filter. The pressure along the porous filter is uniform throughout the process (t > 0). During absorption reaction, along the wall of porous tube,

$$P_g\big|_{r=r_{op}} = P_s \qquad \text{(Eqn.3.39)}$$

Similarly, during desorption reaction,

$$P_g\big|_{r=r_{op}} = P_d \qquad \text{(Eqn.3.40)}$$

In the case of HTF, normal inflow velocity at inlet of the ECT is calculated from area-averaged velocity of HTF during the process as,

$$u_f\big|_{z=L} = \frac{\tilde{V}}{\pi r_o^{\,2}} \qquad \text{(Eqn.3.41)}$$

where $\tilde{V}$ is the volume flow rate of HTF (m^3/s) and r_o is the outer radius of the ECT.

Temperature at inlet of the ECT is specified to be at the absorption/desorption temperature during the process (T_a/T_d):

$$T_f\big|_{z=L} = T_a \qquad \text{(Eqn.3.42)}$$

$$T_f\big|_{z=L} = T_d \qquad \text{(Eqn.3.43)}$$

The HTF flows through the ECT inside the bed.

The convective boundary condition at each cooling tube interface is given by,

$$k_e \frac{\partial T}{\partial r}(r_o) = k_f \frac{\partial T_f}{\partial r}(r_o) \quad \text{(Eqn.3.44)}$$

3.4 Solution methodology

The solution procedure and the assumptions to simplify the governing equations are similar to the one presented in Muthukumar et al. (2012b). To solve the developed numerical model, commercial software COMSOL Multiphysics 5.3 has been utilized with the mesh of computational domain being free tetrahedral mesh. Utilizing this computational medium, energy equation of bed and HTF (convection and conduction mode heat transfer), hydrogen mass (diffusion) and momentum (Darcy's law) transport equations, and mass and momentum transport of HTF (Laminar flow) are concurrently solved. Specific parameters such as rate of hydrogen absorption, rate of hydrogen desorption, variation of concentration and equilibrium pressure have been evaluated by incorporating user-defined functions. The developed thermal model has been simulated considering the ECT geometry obtained from the design methodology. As a representation, implementation of RIII_6in_99ECT reactor design in the numerical simulation is represented in Fig.3.5, wherein Fig.3.5 (a) represents the front view of reactor, detailing the ECT distribution within and Fig.3.5 (b) represents the cross sectional side view of the reactor, which has been axially sectioned along axis Z-Z'. From these representations, the geometry of RIII_6in_99ECT reactor design is realized which is further implemented in numerical simulation, as represented in Fig.3.5 (c). The flow of hydrogen and HTF within bed is also depicted.

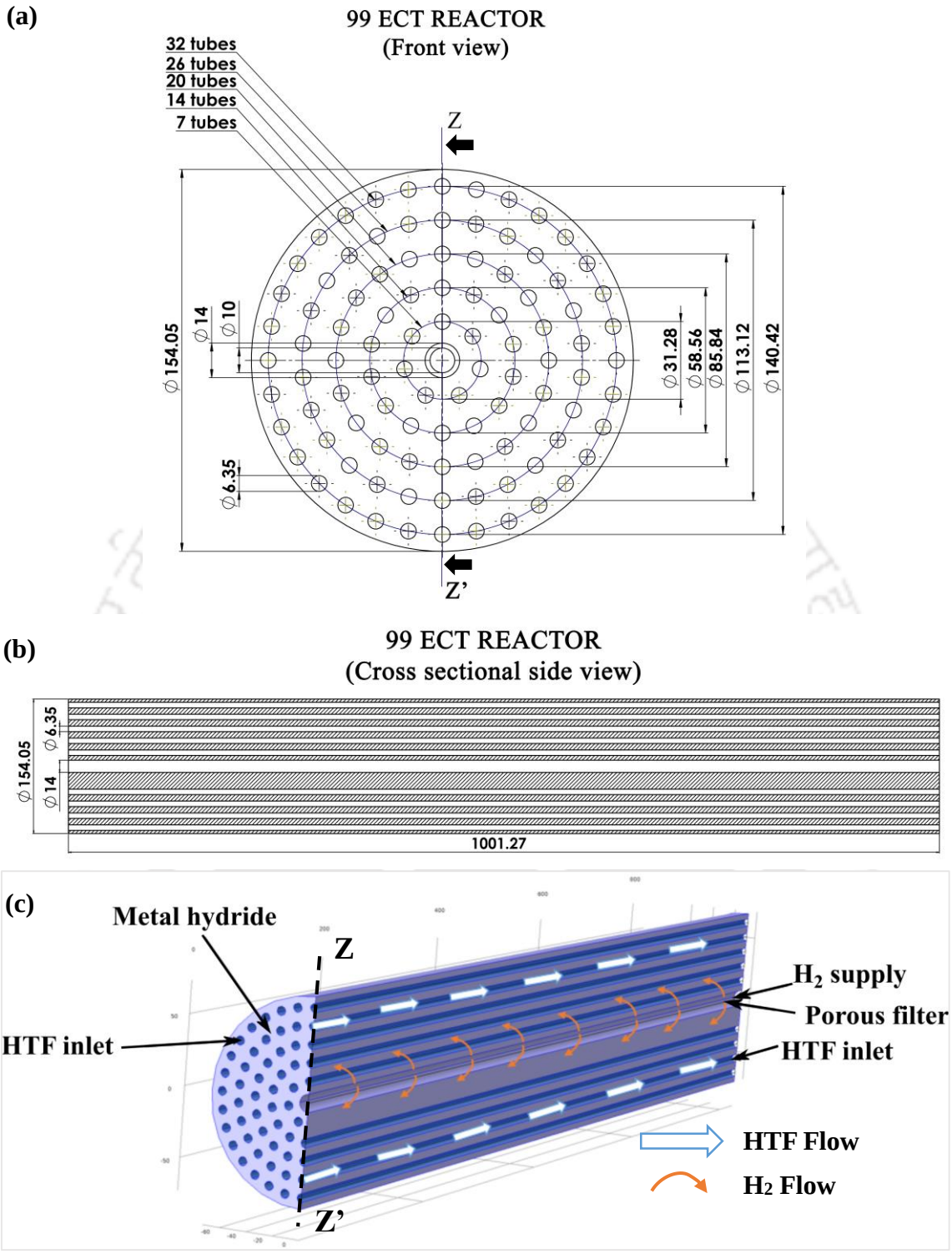

Fig.3.5. (a) Schematic view of 99 embedded cooling tubes arrangement, (b) Cross sectional side view of designed reactor with 6 inch nominal shell, and (c) Schematic view of 3D half sectional (along Z-Z') embedded cooling tubes reactor model implemented in thermal modelling (all dimensions are in mm)

Mesh generation and numerical treatment:

For meshing the domains and boundaries, free tetrahedral and free triangular meshes are chosen, respectively, as best suited to mesh curved geometry with little distortion of mesh. Additional care is taken to ensure that the smaller sections such as ECT are discretized with sufficient number of elements. Meshing features offered by the software that includes boundary layers and corner refinement have been utilized as well near the critical zones of the model such as ECT and porous filter interface.

Grid independence tests are conducted on the developed thermal models of lab scale and industrial scale prototypes, as discussed in Section 5.2.1 and Section 5.3.1, respectively. As the models address solving transient phenomena, time dependent solver is used to solve the set of equations. Time stepping was done based on backward differentiation formula, which comprises of an initial minimum time step and a maximum time step. The time stepping is dynamic and adaptive in nature, wherein it varies on the basis of error value from the previous iteration. In the current modelling approach, the initial minimum time step is set to 0.01 s, while maximum time step is not set. This allows the time step to be maximized automatically and solve the problem with least computational expense. As the developed geometry of the reactors are symmetrical about axis Z-Z', half-sectional models of actual reactors along this axis, as represented in in Fig.3.5 (c) are considered in the computational domain.

3.4.1 Performance comparison of proposed reactor designs

The proposed methodology is for ECT based reactor design suitable for any scale of operation. To understand the enhanced absorption and desorption of reactors from proposed design, lab scale prototype of 60 ECT reported in experimental investigation has been considered for comparative performance analysis Anbarasu et al. (2014b, 2014c). Following the design principle of Anbarasu et al. (2014a), another lab scale prototype with 55 ECT is being proposed as well, as described in Section 4.2.4. To weigh against these prototypes, 41 ECT reactor is

designed through the novel methodology to fill 4 kg of $MmNi_{4.7}Fe_{0.3}$. Length of all prototypes are fixed at 160 mm for comparative analysis.

Table 3.2. Thermo-physical properties of $MmNi_{4.7}Fe_{0.3}$ and hydrogen along with constants used in this analysis

Parameters	Values
Properties of $MmNi_{4.7}Fe_{0.3}$	
Density of metal	8500 kg/m^3
Specific heat of metal	419 J/kg K
Effective thermal conductivity of metal	0.5 W/m K
Porosity	0.5
Effective density at saturation	4300 kg/m^3
Effective density of solid	4250 kg/m^3
Activation energy	23000 J/mol-H_2
Entropy of reaction	87.4 J/mol-H_2 K
Enthalpy of reaction	25000 J/mol-H_2
Properties of hydrogen	
Thermal conductivity of hydrogen	0.127 W/m K
Specific heat of hydrogen	14283 J/kg K
Density of hydrogen	0.0838 kg/m^3
Constants used	
Universal gas constant	8.314 J/mol K
Reaction constant	300 s^{-1}
Slope factor	0.35
Constant	0.15
Hysteresis	0.2

The alloy $MmNi_{4.7}Fe_{0.3}$ has been selected for this comparative analysis, as it has been extensively researched and suitable for MH based cooling systems (Lototskyy et al., 2014; Singh et al., 2004). The thermo-physical properties of $MmNi_{4.7}Fe_{0.3}$ and hydrogen along with constants used in this comparative analysis are listed in Table 3.2. Upon validating the model with experimental results, the absorption performance of the ECT reactors are predicted and compared at supply pressure of 50 bar, absorption temperature of 25 °C and HTF flow rate of 24 lpm. Similarly, their desorption performance is predicted at desorption temperature of 25

°C and HTF flow rate of 15 lpm. Based on the analysis, favourable ECT reactors have been selected for further experimental investigations.

3.4.2 Performance prediction of industrial scale hydrogen storage system

Based on the proposed methodology, industrial scale reactor designs RI_4in_41ECT, RII_5in_67ECT, RIII_6in_99ECT and RIV_8in_136ECT have the ability to contain 50 kg of MH alloy, and their dimensions are listed in Table 3.1. In this analysis, the proposed designs are compared with each other based on their absorption performance of 50 kg of $LaNi_{4.7}Al_{0.3}$ at supply pressure of 30 bar and absorption temperature of 25 °C with HTF flow rate of 60 lpm.

Table 3.3. Thermo-physical properties of $LaNi_{4.7}Al_{0.3}$ and hydrogen along with constants used in this analysis (Choi and Mills, 1990; Hahne and Kallweit, 1998)

Parameters	Values
Properties of $LaNi_{4.7}Al_{0.3}$	
Density of metal	7440 kg/m^3
Specific heat of metal	420 J/kg K
Effective thermal conductivity of metal	0.65 W/m K
Porosity	0.5
Effective density at saturation	3770 kg/m^3
Effective density of solid	3720 kg/m^3
Activation energy	33900 J/mol-H_2
Entropy of reaction	107.4 J/mol-H_2 K
Enthalpy of reaction	33820 J/mol-H_2
Properties of hydrogen	
Thermal conductivity of hydrogen	0.127 W/m K
Specific heat of hydrogen	14283 J/kg K
Density of hydrogen	0.0838 kg/m^3
Constants used	
Universal gas constant	8.314 J/mol K
Reaction constant	250 s^{-1}
Slope factor	0.3
Constant	0.005
Hysteresis	0.098

Table 3.4. Range of operating parameters considered in this performance analysis

Operating parameters	**Values**
Supply pressure (P_s)	5, 10, 15, 20, 25, 30, 35 bar
Absorption temperature (T_a)	20, 25, 30, 35 °C
HTF flow rate (HTF_a)	10, 15, 20, 25, 30, 35 lpm

Based on this comparative analysis, the most suitable design is chosen for analyzing the of operating parameters on the absorption performance. The thermo physical properties of $LaNi_{4.7}Al_{0.3}$ and hydrogen along with constants used in this comparative analysis are listed in Table 3.3. The range of operating conditions chosen for hydrogen supply pressure, absorption temperature and HTF flow rate have been listed in

Table 3.4.

3.5 Summary

In this chapter, a novel methodology has been formulated for design of reactors with ECT configuration. Using this methodology, reactor designs of both lab scale and industrial scale can be developed based on the chosen alloy. In order to compare the advantage of this methodology, lab scale prototype 41 ECT reactor design has been developed and compared with other ECT reactor designs. The absorption and desorption performance of 4 kg of $MmNi_{4.7}Fe_{0.3}$ filled in this lab scale models have been compared. To understand the influence of the improved reactor design on hydrogen absorption performance, three-dimensional numerical model of industrial scale reactor designed using the methodology and containing 50 kg of $LaNi_{4.7}Al_{0.3}$ has been developed. The effects of various operating parameters on this absorption performance have been studied.

CHAPTER 4

EXPERIMENTAL METHODOLOGY

4.1 Preface

Having established a design methodology that is instrumental in designing both lab scale and industrial scale reactors for hydrogen storage and thermal management applications, it is incumbent to test the enhanced heat transfer and associated improvement in performance of these reactors. Based on methodology, reactors were fabricated for both lab scale and industrial scale for testing the performances of open and closed cycle metal hydride (MH) based cooling systems. The open cycle MH based hydrogen storage and cooling system has been experimentally investigated by implementing lab scale prototype and industrial scale reactors. Meanwhile, closed cycle compressor driven MH based cooling system has been investigated using an established alloy and newly synthesized alloy, wherein their cooling performances have been compared. As part of these experimental investigations, suitable experimental setups and investigative procedures have been formulated, alloys were selected, reactors were

fabricated and their performance have been investigated under various operating conditions. A flowchart of the experimental approach into different modes of MH based cooling system has been represented in Fig.4.1.

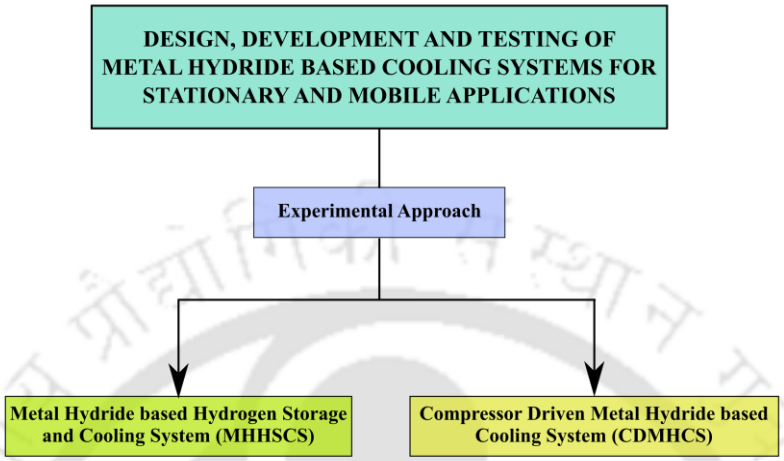

Fig.4.1. Flowchart depicting the different modes of metal hydride based cooling system being investigated

4.2 MHHSCS: MH based hydrogen storage and cooling system (Open cycle)

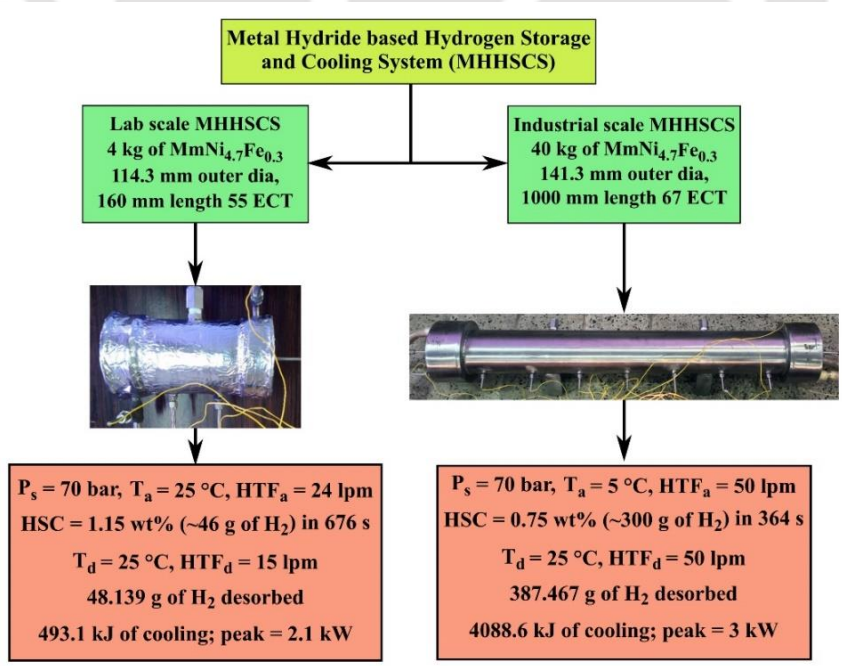

Fig.4.2. Flowchart of metal hydride based hydrogen storage and cooling systems (open cycle) being investigated

Fuel cells are being used extensively in stationary and mobile applications. Specifically, fuel cell based vehicles require onboard hydrogen storage system. Motive of MH based hydrogen storage and cooling system (MHHSCS) is to address this requirement. Therefore, the experimental methodology has been framed to investigate the operation and the performance variation of MHHSCS at various operating conditions. The MHHSCS being investigated have been briefed as a flowchart, represented in Fig.4.2.

4.2.1 Experimental setup of MHHSCS

The experimental setup of MHHSCS primarily consists of MH reactor connected with a hydrogen supply cylinder with attached gas regulator, Coriolis mass flow meter, data acquisition system connected with computer, constant temperature baths, centrifugal pump, high pressure bellow valves and fittings of Swagelok make for hydrogen transfer to/from MH reactor during absorption/desorption processes.

Pressure transmitter (accuracy: ± 0.5 bar) connected to a constant DC power source was attached in the supply line to monitor the supply pressure. The schematic of the experimental setup during absorption half cycle is represented in Fig.4.3, while Fig.4.4 depicts the schematic view of setup during desorption half cycle. Auxiliary components such as turbine type water flow meter (WFM), flow control valves and braided hoses have been utilized for heat transfer fluid (HTF) transport through the MH reactor from recirculating constant temperature baths during the experiment. The amount of hydrogen transferred to/from the reactor was monitored using Coriolis mass flow meter (sensitivity: 0.001 g; accuracy: ± 0.35%).

Metal-sheathed K-type thermocouples (accuracy: ± 0.5 °C) were used to sense the temperature of MH bed and HTF, while the temperature data was recorded through data acquisition system with a transient response of 1 s. Suitable hydrogen flow circuit was fabricated, using the stated valves and fittings of 1/4 inch line size. Hydrogen supply line of MH reactor along with the inlet and outline line for Coriolis mass flow meter are common for both absorption and

desorption processes. As seen in Fig.4.3 and Fig.4.4, hydrogen flows through specific path during absorption and desorption half cycle. The cyclic operating procedure of experimental setup has been detailed in subsequent Section 4.2.2. Hydrogen supply pressure (P_s) was fixed using SS316 gas regulator while monitoring through pressure transmitter.

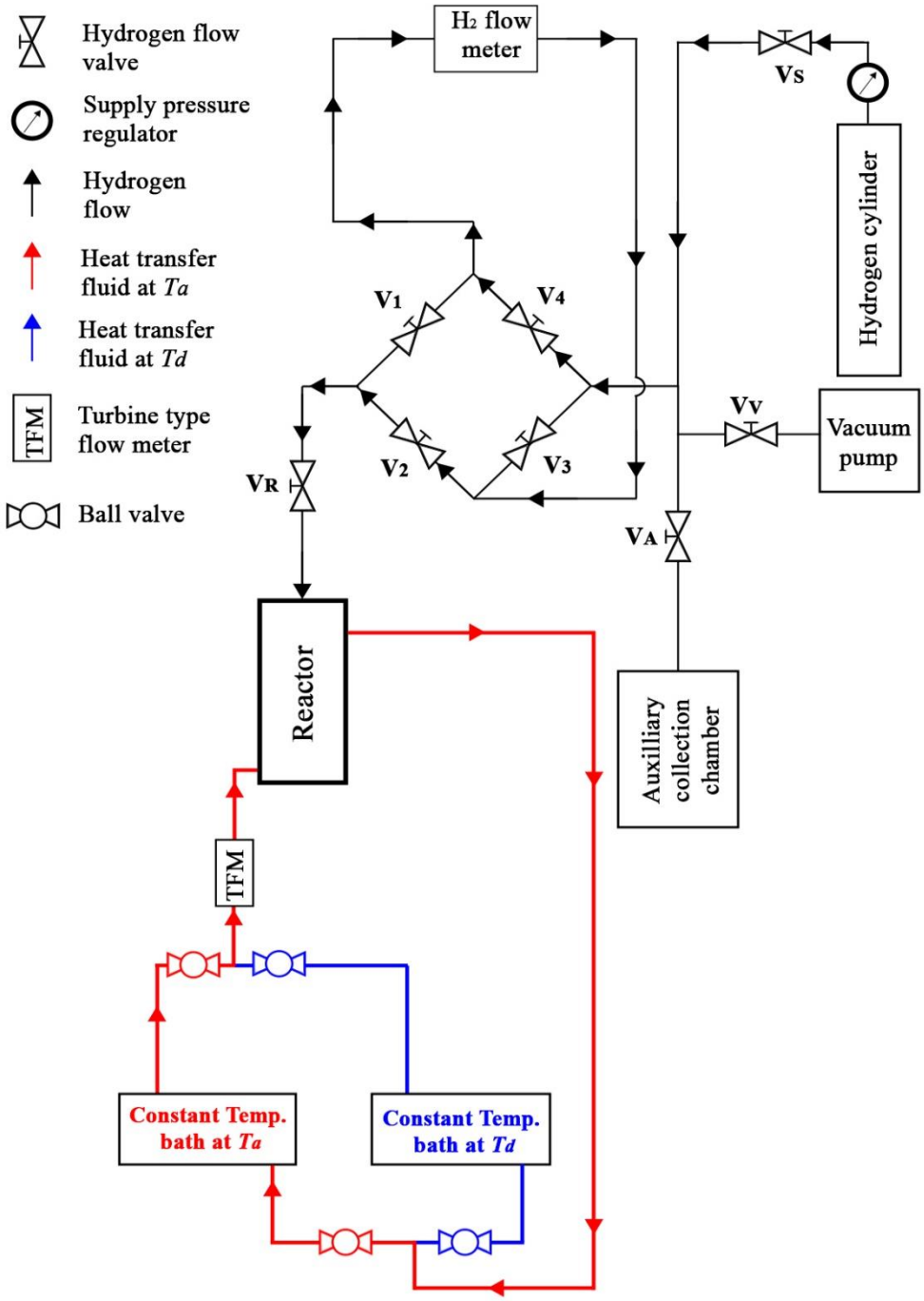

Fig.4.3. Schematic view of experimental test setup for metal hydride based hydrogen storage and cooling system during absorption half cycle

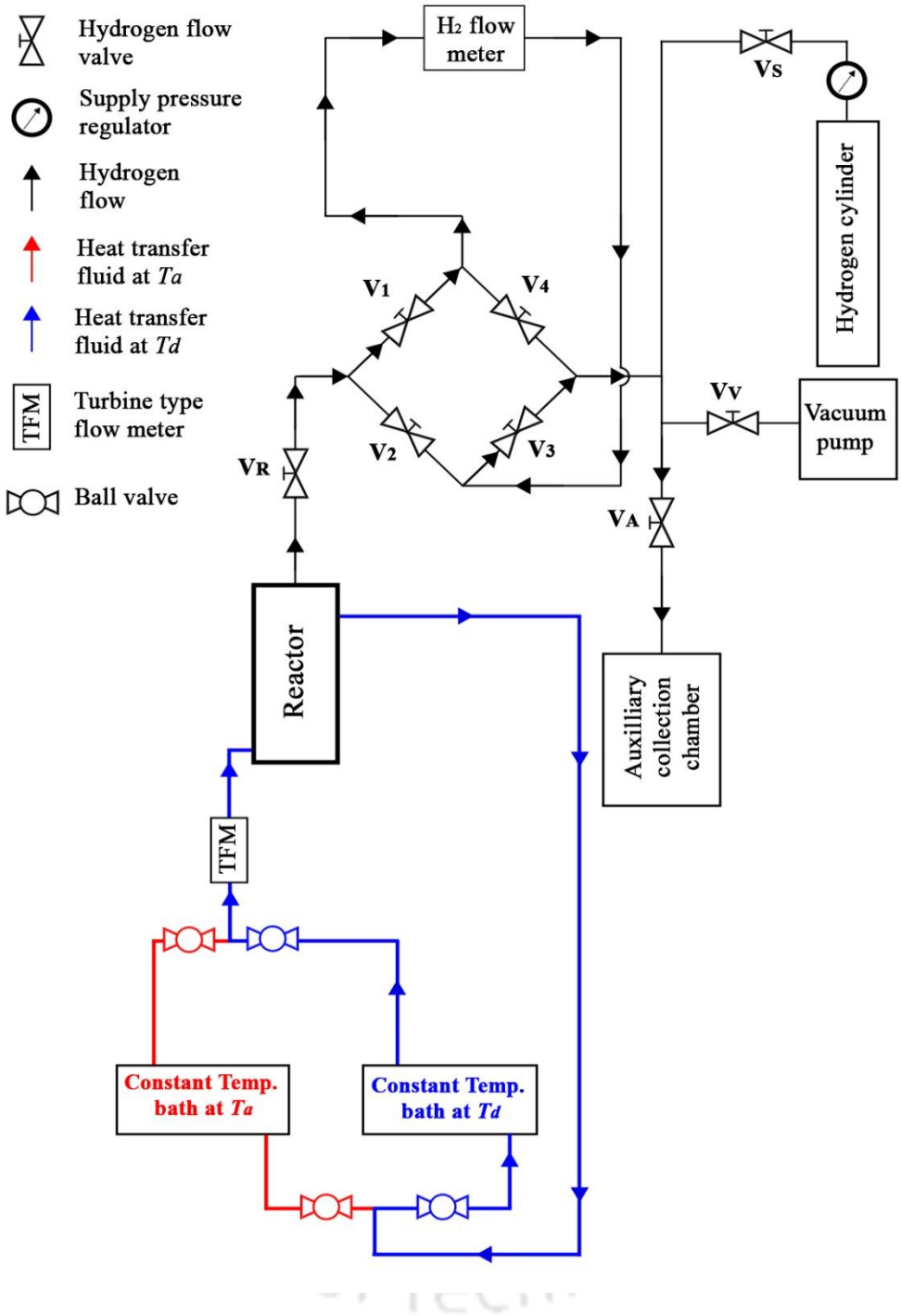

Fig.4.4. Schematic view of experimental test setup for metal hydride based hydrogen storage and cooling system during desorption half cycle

Between cycles, the MH reactor and the hydrogen flow circuit may need to be evacuated down to 10^{-3} mbar such that no other gases are present. Considering this aspect, 2.5 hp rotary vacuum pump has been connected to gas flow circuit through valve V_V. The vacuum pump has inbuilt

digital Pirani and Penning gauges to monitor the vacuum pressure. Argon gas has been used as test gas to check for leakage in the circuit and MH reactor before activation. Both hydrogen and argon gas used in this experimental investigation were of high purity (99.999%). Throughout this investigation, water was used as HTF.

4.2.2 Experimental procedure and performance parameters of MHHSCS

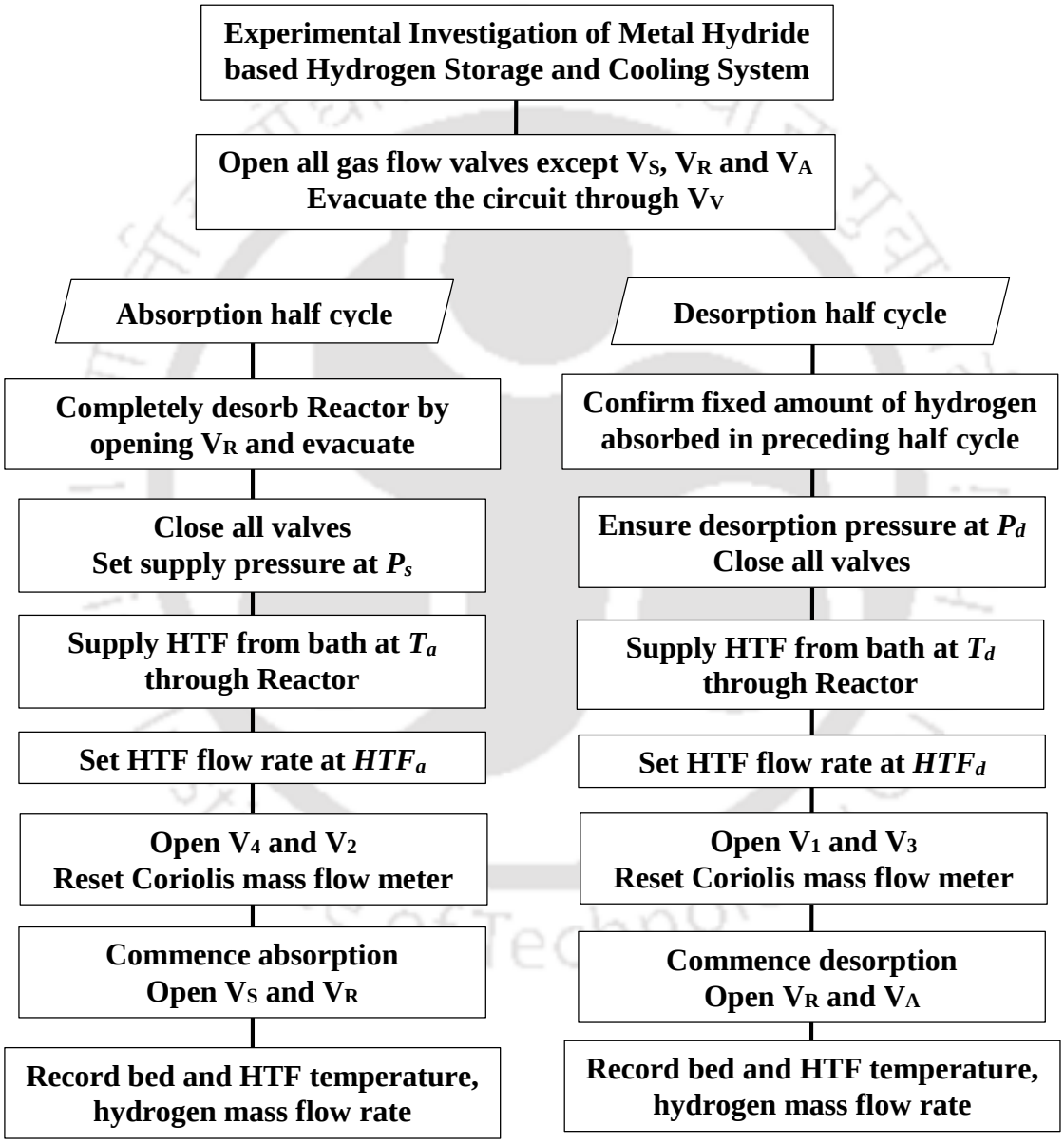

Fig.4.5. Flowchart depicting experimental procedure of metal hydride based cooling system during cyclic investigation

The experimental cycle of MHHSCS is an open cycle with two halves, namely absorption half cycle and desorption half cycle, as described in Fig.4.5. Prior to each half cycle, all hydrogen flow control valves except V_S, V_R and V_A are opened and entire circuit is evacuated through vacuum pump. During absorption half cycle, the reactor is also evacuated and then closed. Supply pressure is set at P_s and hydrogen flows from supply cylinder to MH reactor through valves V_S, V_4, V_2 and V_R. Due to absorption reaction, there is an evolution of heat within the MH bed. HTF flowing at HTF_a from constant temperature bath maintained at absorption temperature (T_a) removes the evolved heat, thereby improving the hydriding rate of the reaction. The half cycle is continued until the MH bed attains its maximum storage capacity or desired capacity under the given operating conditions. The flow rate of HTF was set at fixed value of HTF_a and HTF_d during absorption and desorption process, respectively, using a flow control valve while monitoring the flow rate through turbine type water flow meter (WFM).

During desorption half cycle, HTF maintained at desorption temperature (T_d) from constant temperature bath flows at HTF_d through the MH reactor. Utilizing the available heat input, the MH bed desorbs the hydrogen, which is then released to auxiliary collection chamber maintained at P_d through valves V_R, V_3, V_1 and V_A. This concludes one complete cycle of MHHSCS. In-between each half cycle, temperature of MH bed is brought to set temperature of T_a/T_d before absorption/desorption half cycle through HTF. Similarly, through operation of valves, the hydrogen flow circuit is brought to set pressure of P_s/P_d before absorption/desorption half cycle. From the Coriolis mass flow meter, the instantaneous amount of hydrogen transferred was monitored, based on which hydriding/dehydriding rate and hydrogen absorption and desorption capacity were estimated. By measuring the HTF temperature at inlet and outlet of MH reactor, the temperature drop in HTF across the bed was obtained.

For a given half cycle, instantaneous rate of heat transfer (kW) at time '*t*' during absorption/desorption process is $\dot{Q}_t$, which is estimated by,

$$\dot{Q}_t = \dot{m}_{HTF} * c_{p_{HTF}} * \Delta T_{HTF_t} \quad \text{(Eqn.4.1)}$$

where, 'ΔT_{HTFt}' is the difference in temperature (°C) between the HTF outlet and inlet at that specific time '*t*' and 'c_{pHTF}' represents specific heat capacity of HTF, taken as 4.187 kJ/kg °C. The mass flow rate (kg/s) of HTF ($\dot{m}_{HTF}$) was obtained from flow rate of HTF (HTF_a/HTF_d) and the water density, which has been considered as 1000 kg/m^3. Based on the rate of heat transfer during desorption and the half cycle time, cumulative cooling (Q_{cold}) for each desorption half cycle has been estimated as well.

Based on the obtained amount of cumulative cooling produced, average specific cooling power of the alloy (W/kg of desorbing alloy) can be estimated as,

$$SCP = \frac{Q_{cold}}{t_{hcy} * m_{MH}} \quad \text{(Eqn.4.2)}$$

where, 't_{hcy}' denotes total desorption half cycle time (s) and 'm_{MH}' denotes mass of desorbing alloy (kg). The effects of different operating parameters on these performance parameters are investigated during the experiments. The uncertainties in the experimental measurements were estimated using the method adopted by Kline and McClintock (1953). The uncertainty in measuring HTF flow rate and hydrogen supply pressure was ± 1.01% and ± 5.0%, respectively while, the uncertainty in assessment of hydrogen storage capacity (HSC) was estimated as ± 0.17%. Tests were performed over 100 cycles and no significant change in the capacities were observed. In each stage of parametric investigation, the experiments have been conducted twice, and the average performance values have been reported.

4.2.3 Alloy selection for MHHSCS

Apart from the general alloy characteristics required for MH based heat pump and cooling systems, the selected alloy for operation of MHHSCS must fulfil the following pressure-concentration-temperature (PCT) characteristic requirements as well:

- The alloy should possess absorption equilibrium pressure below 30 bar at ambient temperature.
- Similarly, the desorption equilibrium pressure of alloy should be comparatively higher than ambient pressure at low temperature.

This criterion has been arrived at considering the potential operation of MHHSCS with fuel cell while producing useful cooling output. Based on these criteria, $MmNi_{4.7}Fe_{0.3}$ (Singh et al., 2004) has been chosen as suitable alloy for MHHSCS (procured from M/s Whole Win (Beijing) Materials Sci. & Tech. Co. Ltd., China).

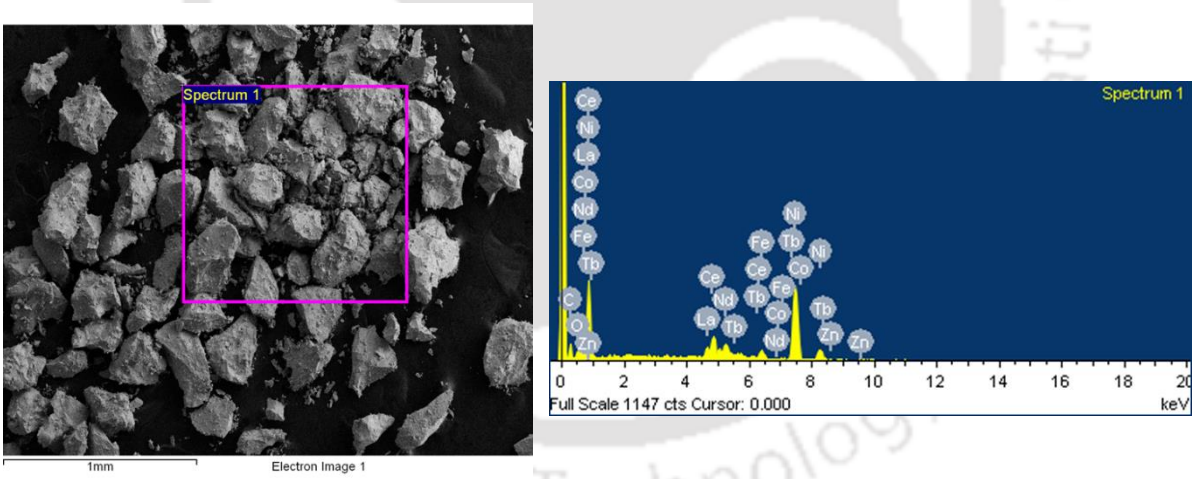

(a) (b)

Fig.4.6. (a) Secondary electron map and (b) corresponding spectrum obtained from energy dispersive X-ray analysis of $MmNi_{4.7}Fe_{0.3}$ sample

From energy dispersive X-ray analysis of alloy sample, the particle size and chemical composition were confirmed by developing secondary electron map and corresponding spectrum, as represented in Fig.4.6 (a) and (b), respectively. From the spectrum, the chemical

composition of alloy was confirmed to be $MmNi_{4.7}Fe_{0.3}$, matching the composition stated by the supplier, while from the secondary electron map, particle sizes were observed to vary in the range of 100 to 200 μm.

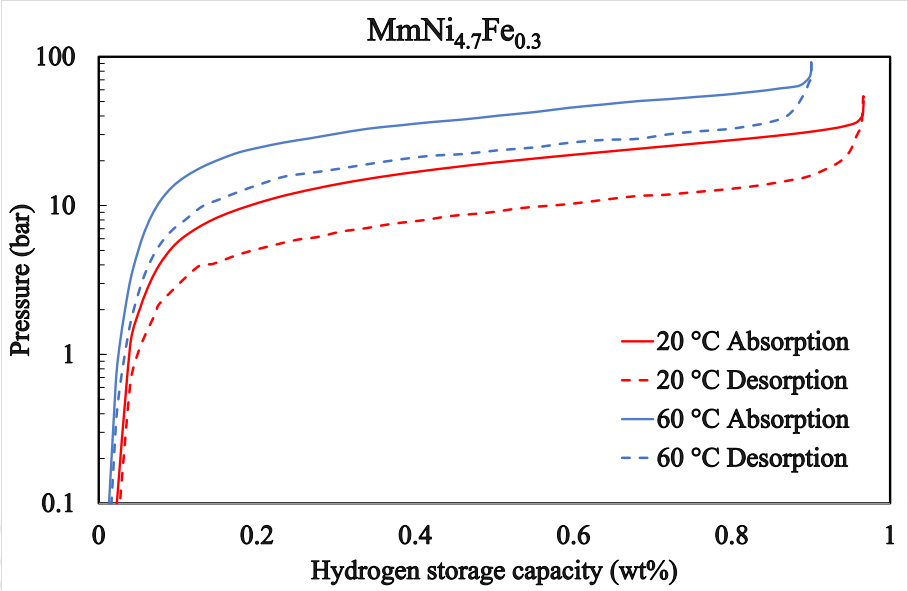

Fig.4.7. Pressure-Concentration-Temperature characteristics of $MmNi_{4.7}Fe_{0.3}$ at 20 °C and 60 °C

The absorption and desorption PCT characteristics of $MmNi_{4.7}Fe_{0.3}$ at 20 °C and 60 °C has been depicted in Fig.4.7. It is perceived that the chosen alloy meets the selection criteria of open cycle MHHSCS.

4.2.4 Lab scale prototype model

For the lab scale prototype model, reactor was designed by modifying the design principle stated by Anbarasu et al. (2014a). Upon fabrication, this lab scale prototype was filled with 4 kg of $MmNi_{4.7}Fe_{0.3}$ by following standard safety protocols. The reactor has 55 ECT arranged uniformly in three stacks to provide enhanced heat transfer during the absorption/desorption process. The shell and tube type MH reactor has a length of 160 mm and was fabricated using SS316. The reactor shell is of 114.3 mm in outer diameter with a thickness of 6.02 mm. The dimensional specification of the reactor and the arrangement of ECT in each stack are presented

in Fig.4.8 (a). The shell side was filled with the MH alloy while the HTF streamed through the tube side. The hydrogen transfer to/from the MH bed takes place through the cylindrical SS316 sintered porous tube of 2 µm porosity placed at the center of the reactor as shown. The porous filter has an outer diameter of 12.7 mm and thickness of 1.27 mm. One end of the filter is closed while the other end is open to the hydrogen supply tube. Each ECT has a length of 160 mm with an outer diameter of 6.35 mm and a thickness of 0.89 mm. At stack radii of 16 mm, 29 mm and 42 mm, correspondingly 9, 18 and 28 ECT have been placed in three stack structure. The intermediate distance between the outer surfaces of ECT was found to vary between 3 mm and 4.8 mm in angular direction, while in radial direction, it varied between 5.9 mm and 6.6 mm.

The designed assembly of reactor shell, porous filter and ECT is collectively termed as principle reactor chamber. As depicted in Fig.4.8 (b), end flange plates were welded onto both ends of principle chamber using TIG welding. The thickness of the flange plates is 1.5 times that of reactor shell. Supply tube was welded onto porous filter while auxiliary fluid flow chambers were welded onto the end flange plates. They act as HTF collection chambers at inlet and outlet of the ECT. These chambers facilitate uniform flow of HTF through the ECT. The inlet and outlet of HTF were selected such that the flow of HTF was in the opposite direction to that of hydrogen supply. As depicted in Fig.4.8 (b), MH alloy was filled through the alloy filling port (A) and the hydrogen was transferred to/from the reactor through the hydrogen supply tube (B). A secondary SS316 inline filter of 2 µm had been attached with before control valve at supply end as an added deterrent to prevent the MH alloy powder from leaving the reactor. Metal-sheathed K-type thermocouples were attached to the reactor through weld fittings (C), and similar metal-sheathed K-type thermocouples were attached using fittings (D) to sense HTF inlet and outlet temperature.

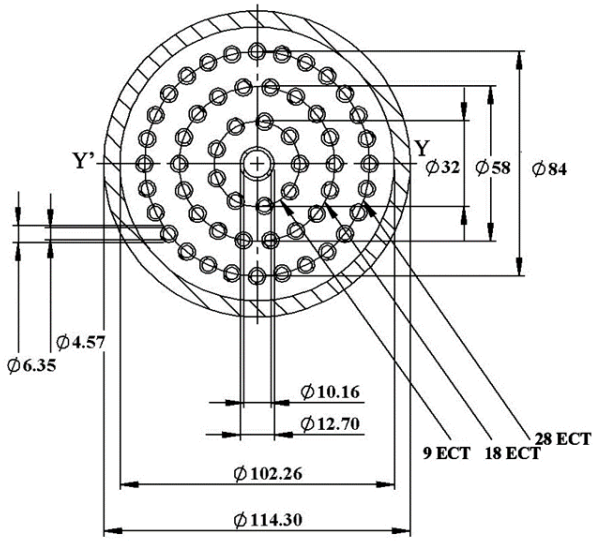

(a)

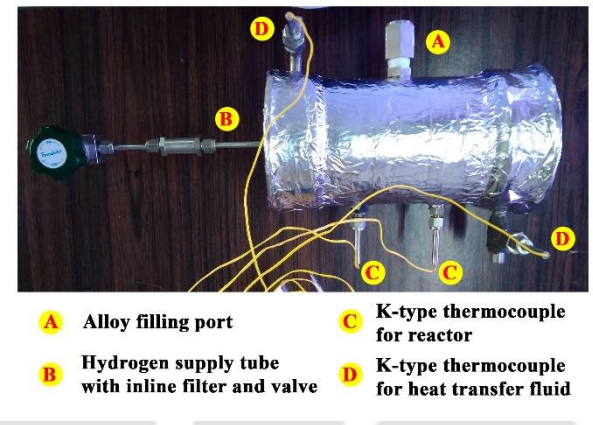

(b)

Fig.4.8. Reactor configuration - (a) schematic view of 55 embedded cooling tubes arrangement (all dimensions are in mm), (b) pictorial view of the insulated reactor with labels

The metal-sheathed K-type thermocouples for reactor (C) were placed at 50 mm distance from the front and back flanges such that their sensing ends were at a depth of 30 mm from the outer periphery. Care was taken while placing these thermocouples such that the sensing ends were in shell space and not touching the tube surface within the reactor. While reporting the bed temperature, average of the values sensed by these two thermocouples have been considered. Before the parametric investigation, the reactors were well insulated using polyurethane foam of thickness 12 mm and plastered with self-adhesive aluminium foil tape, as depicted in Fig.4.8 (b).

Activation of lab scale model:

The 55 ECT reactor filled with 4 kg of $MmNi_{4.7}Fe_{0.3}$ has to be activated by considering the alloy PCT characteristics. While preparing the system for activation, the reactor and the gas flow circuit have been made leak proof through systematic leakage testing by using argon at 100 bar supply pressure. The system was in this pressurised condition for nearly 48 h, to ensure leak-proof system. Then the system was evacuated down to 10^{-3} mbar vacuum pressure. The evacuated system was then flushed with hydrogen gas at 5 bar which ensured the absence of any other gases in the bed. The bed was then evacuated while being maintained at 60 °C. Further, hydrogen was supplied at 50 bar while the bed was maintained at 30 °C and HTF was flowing at flow rate of 24 lpm.

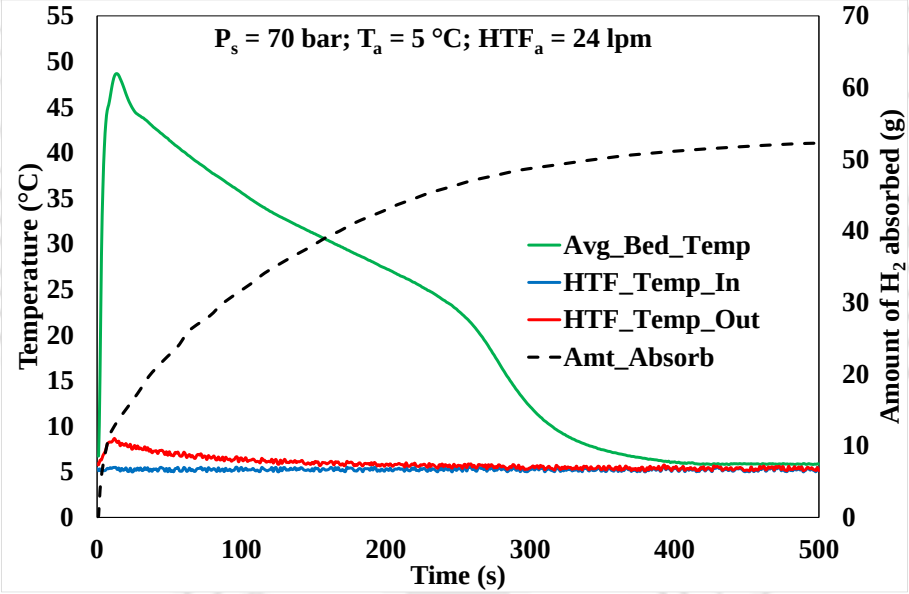

Fig.4.9. Variation of temperature and amount of hydrogen absorbed during 31st absorption cycle

. In the first activation absorption cycle, 1.321 g of hydrogen was absorbed. The bed was evacuated to 10^{-3} mbar at 90 °C and the absorption process was reiterated in a cycle. Even after 12 activation cycles, the bed absorbed just 10.818 g of hydrogen. Hence, further activation was attempted at 5 °C while hydrogen being supplied at 70 bar. Significant improvement in the

absorption was observed and in 31st absorption cycle the alloy reached a peak HSC of 1.36 wt%. The temperature distribution in the MH bed and HTF temperature (inlet and outlet) during this 31st activation cycle, and the quantity of hydrogen absorbed are presented in Fig.4.9. The MH bed reached peak temperature of 48.6 °C within 20 s of the absorption cycle, and in the initial 250 s, it had absorbed about 48 g of hydrogen (~1.2 wt%), which further reached to 54.413 g in 503 s.

Performance investigation of lab scale MHHSCS:

In order to identify the suitable absorption/desorption operating conditions for the lab scale MHHSCS, a systematic parametric study has been carried out. During absorption half cycle, hydrogen supply pressure and absorption temperature were individually varied among a range of values, as summarized in Table 4.1. Similarly, desorption temperature was varied during desorption, as stated.

Table 4.1. Range of operating parameters considered in this parametric investigation

Half cycle	Investigation	Parameters	Values
Absorption	Effect of varying supply pressure	Supply pressure (P_s)	10, 20, 30, 40, 50, 60 and 70 bar
		Temperature (T_a)	25 °C
		HTF flow rate (HTF_a)	24 lpm
	Effect of varying absorption temperature	Supply pressure (P_s)	40 bar
		Temperature (T_a)	5, 10, 15, 20 and 25 °C
		HTF flow rate (HTF_a)	15 lpm
Desorption	Effect of varying desorption temperature	Desorption pressure (P_d)	1 bar
		Temperature (T_d)	5, 10, 15, 20, 25 and 30 °C
		HTF flow rate (HTF_d)	15 lpm

These parameters have been considered based on the operational feasibility and the potential application of lab scale MHHSCS. The effect of these parametric variation on the average bed temperature along with stated performance parameters of storage capacity and heat transfer

were analysed. To effectively compare the effects of the operating parameters on the desorption performance of the system, it was always ensured that the reactor was filled with fixed amount of hydrogen (1.25 wt%) before each desorption cycle of this investigation.

4.2.5 Industrial scale model

For the industrial scale model, configuration of RII_5in_67ECT based on the developed design methodology has been considered. This industrial scale model has been filled with 40 kg of $MmNi_{4.7}Fe_{0.3}$. This reactor configuration has 67 ECT arranged uniformly in four stack structure, as depicted in Fig.4.10 (a), and was fabricated with SS316. The principle chamber is of 1000 mm in length with outer diameter of 141.3 mm and thickness of 6.55 mm. The structure of the industrial scale model is similar to that of the lab scale prototype model. However, the porous filter in this model has an outer diameter of 14 mm and thickness of 2 mm. ECT of same dimension have been distributed following the configuration of RII_5in_67ECT. The intermediate distance between the outer surfaces of ECT was 7.46 mm uniformly in both angular and radial direction.

As depicted in Fig.4.10 (b), end flange plates were welded onto both ends of principle chamber using TIG welding. The HTF collection chambers in this model were provided with more volume considering the scale of the model. Similar to lab scale prototype, the inlet and outlet of HTF were selected such that the flow of HTF was in the opposite direction to that of hydrogen supply. As depicted in Fig.4.10 (b), two alloy filling ports were welded onto the reactor shell (A). A hydrogen supply tube has been directly welded onto the front flange plate, through which hydrogen is transferred to/from the reactor (B). Considering the size of model, seven numbers of metal-sheathed K-type thermocouples for reactor (C) were placed at interval of 143 mm in between each other. Their sensing ends were placed at a depth of 45 mm from the outer periphery. While representing the bed temperature variation, average of the values

sensed by all seven thermocouples have been considered. Additionally, metal-sheathed K-type thermocouples have been affixed at the HTF inlet and outlet.

(a)

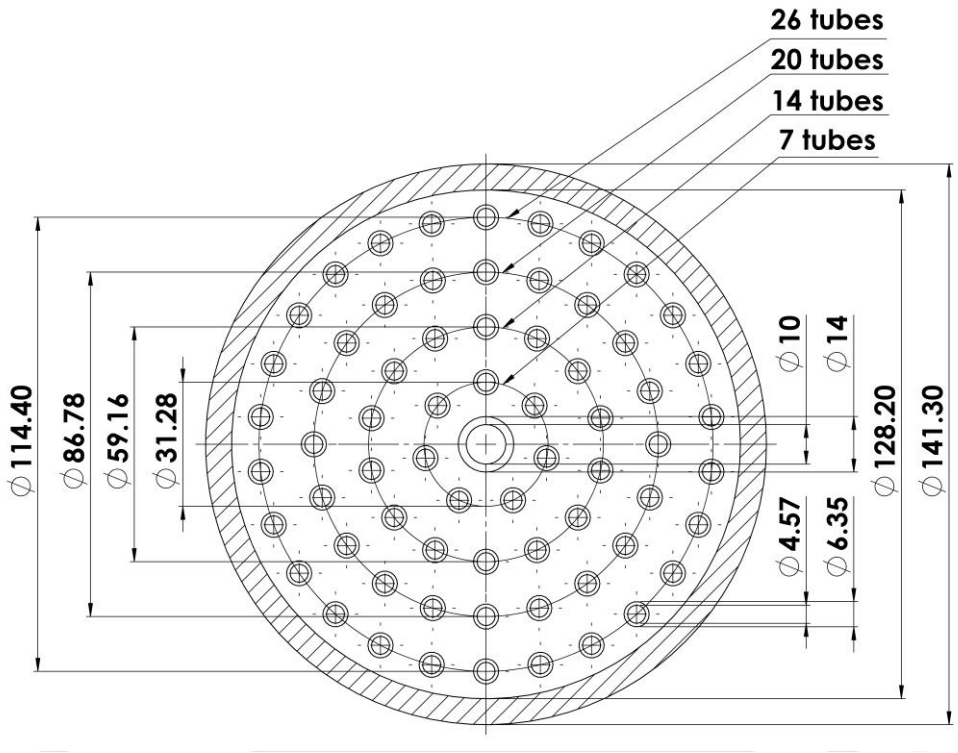

(b)

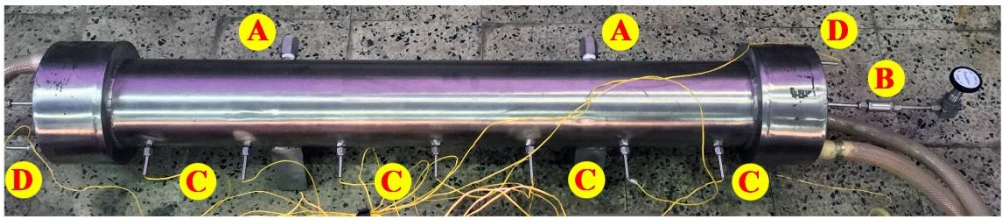

A Alloy filling port

B Hydrogen supply tube with inline filter and valve

C K-type thermocouple for reactor

D K-type thermocouple for heat transfer fluid

Fig.4.10. RII_5in_67ECT Reactor configuration - (a) schematic view of embedded cooling tubes arrangement (all dimensions are in mm) and (b) pictorial view of the industrial scale reactor

Activation of industrial scale model:

For activation of 67 ECT reactor, same procedure as lab scale prototype was followed. After leak testing and complete evacuation down to 10^{-3} mbar vacuum pressure, the reactor was flushed with hydrogen at 20 bar. Then the bed was evacuated while being maintained at 80 °C.

Based on the activation performance of lab scale and the PCT characteristics of the alloy, the temperature and pressure limits were fixed. Hydrogen was supplied at 60 bar while the bed was maintained at 5 °C with HTF flow rate of 25 lpm. An initial amount of 93.302 g was absorbed in the first cycle, after which the bed was evacuated at 90 °C and the cycle was repeated. To improve the performance, the activation temperature was reduced to 5 °C. In the 10th cycle, the bed attained its maximum HSC of 1.4 wt% with absorption of 557.612 g of hydrogen in 5915 s, as represented in Fig.4.11. There was a break in the cycle, as first supply cylinder was emptied at 2380 s due to absorption. Though smooth transition was attempted in changing supply line to standby cylinder, there was a break nonetheless, marked as distinct regime in Fig.4.11. The average temperature variation within the MH bed and the inlet and outlet temperature of HTF during the final activation cycle have been represented along with the amount of hydrogen absorbed.

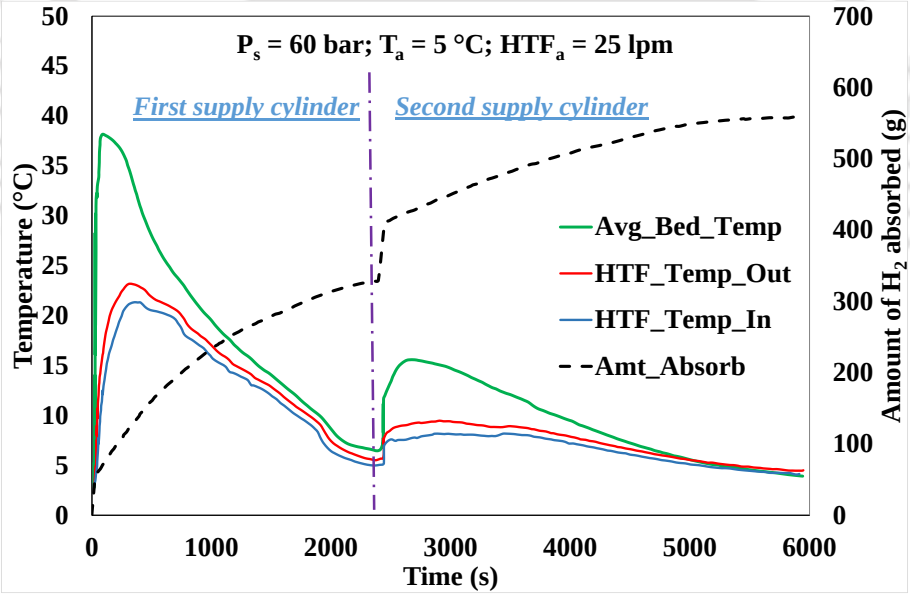

Fig.4.11. Amount of hydrogen absorbed and variation of temperature during final absorption cycle

The bed attained peak temperature of 38 °C in 117 s, while the HTF temperature also increased by about 20 °C due to the sudden evolution of heat and the lower HTF flow rate. The bed had

attained HSC of 0.83 wt% in 2380 s. The absorption performance was comparatively slower due to the scale of the model.

Performance investigation of industrial scale MHHSCS:

Considering the inputs obtained from the performance investigation of 55 ECT reactor filled with 4 kg of $MmNi_{4.7}Fe_{0.3}$, the parameters to investigate the industrial scale reactor with 40 kg of of $MmNi_{4.7}Fe_{0.3}$ were selected. As the effect of supply pressure was predominant during absorption and the desorption temperature during desorption half cycle of this MH, these parameters were varied during the investigation. The range of values considered for each parameter has been tabulated in Table 4.2. Before the desorption investigative half cycles, 400g of absorbed amount of hydrogen (1 wt%) was ensured for effective comparison. The effect of these parameters on the absorption and desorption performance were analysed.

Table 4.2. Range of operating parameters considered in this parametric investigation

Half cycle	Investigation	Parameters	Values
Absorption	Effect of varying supply pressure	Supply pressure (P_s)	40, 50, 60 and 70 bar
		Temperature (T_a)	5 °C
		HTF flow rate (HTF_a)	50 lpm
Desorption	Effect of varying desorption temperature	Desorption pressure (P_d)	1 bar
		Temperature (T_d)	5, 15 and 25 °C
		HTF flow rate (HTF_d)	50 lpm

4.3 CDMHCS: Compressor Driven MH based cooling system (Closed cycle)

In onboard automobile applications and small-scale air conditioning applications, compressor driven MH based cooling systems (CDMHCS) are observed to be a promising alternative to conventional systems. As the alloy can be tailor-made for specific operating condition and the system is ecofriendly with hydrogen as working fluid, the understanding of its operating principle and investigation of its real time performance is framed by this methodology. As part of the investigation, newly configured alloy has been procured and implemented in the

CDMHCS. Additionally, another CDMHCS has been formulated with an established alloy to compare the performances. The CDMHCS being investigated have been briefed as a flowchart, represented in Fig.4.12.

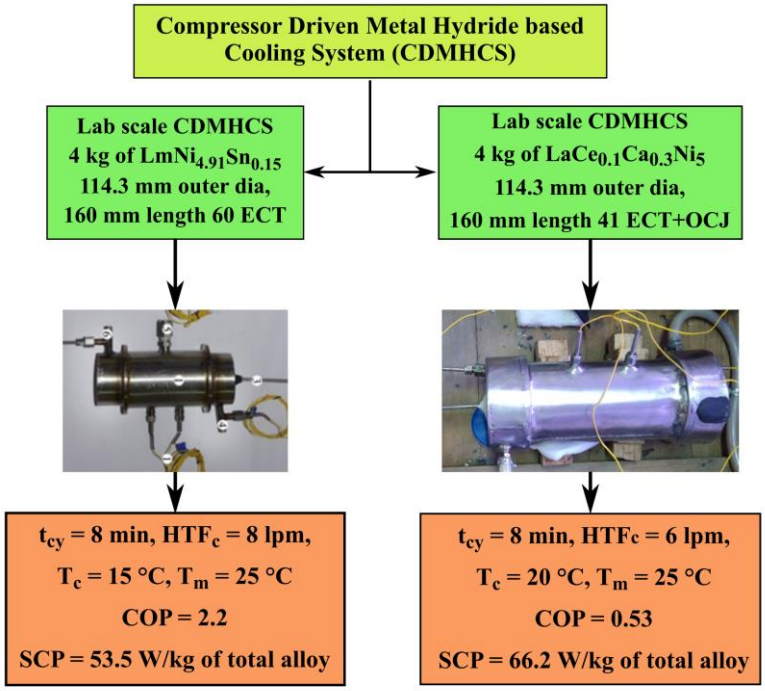

Fig.4.12. Flowchart depicting the compressor driven metal hydride based cooling systems (closed cycle) being investigated

4.3.1 Operating principle of CDMHCS

The operation layout of CDMHCS is similar to that of a conventional vapour compression refrigeration system, as represented in Fig.4.13 (a). In a typical cycle, the refrigerant is expanded through the expansion valve which enables it to produce desirable cooling effect (Q_{in}) at the evaporator. After removing the heat and compressed, the refrigerant rejects the heat Q_{out} at ambient temperature. The primary difference between conventional system and CDMHCS is that the evaporator and condenser of the conventional system are replaced by two identical metal hydride reactors in CDMHCS. In the CDMHCS, during first half cycle, one

reactor absorbs hydrogen (say reactor B) by rejecting heat ($Q_{B,out}$) at near ambient temperature, T_m, while the other reactor (reactor A) desorbs hydrogen by absorbing heat ($Q_{A,in}$) at low temperature, T_c, producing the useful cooling effect. As represented in Fig.4.13 (b), the roles of the reactors are reversed in second half cycle.

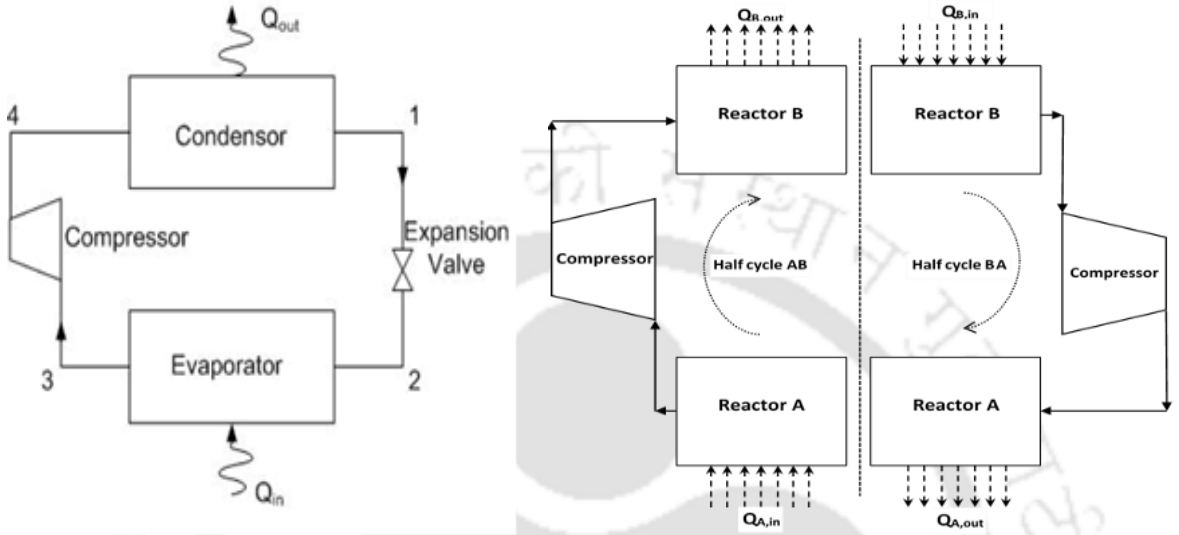

(a) (b)

Fig.4.13. Operating principles of (a) vapour compression refrigeration system and (b) compressor driven metal hydride based cooling system

During the second half cycle, reactor B desorbs the hydrogen while producing useful cooling effect ($Q_{B,in}$) at refrigeration temperature (T_c), while reactor A absorbs this hydrogen while rejecting the heat of absorption ($Q_{A,out}$) at the sink temperature (T_m). A mechanical compressor is employed to provide the necessary driving force for the circulation of hydrogen from one reactor to another reactor during every half cycle. This results in quasi-continuous cold generation cyclically. The stepwise detailed investigative procedure of CDMHCS has been discussed in the Fig.4.17.

4.3.2 Experimental setup and procedure of CDMHCS

The experimental setup consists of two identical ECT reactors, each filled with same amount of MH alloy. As the CDMHCS operates in two half cycles, the schematic of the experimental

setup during first half cycle has been illustrated in Fig.4.14, while the schematic of the experimental setup during the second half cycle has been represented in Fig.4.15.

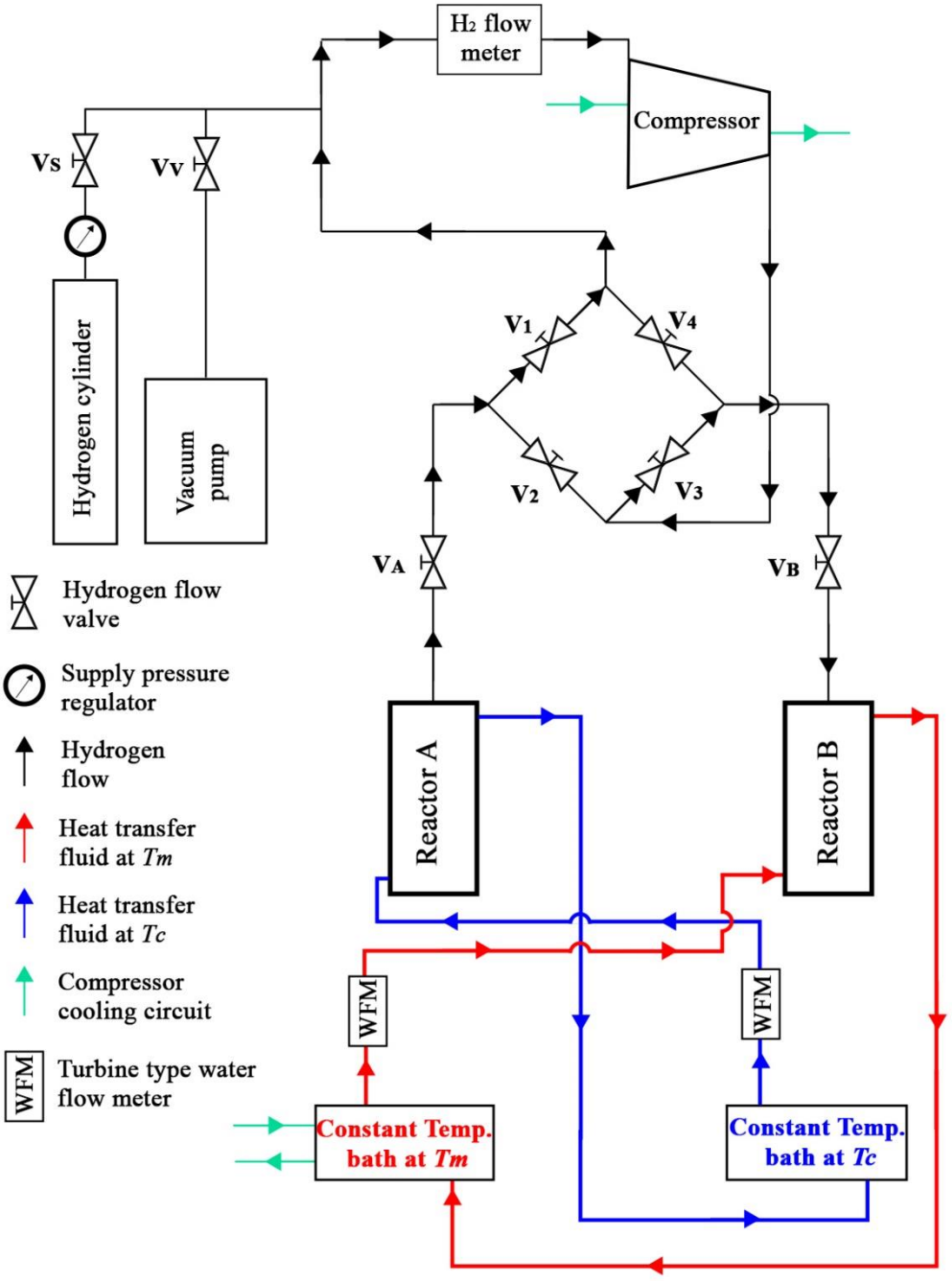

Fig.4.14. Schematic view of compressor driven metal hydride based cooling system experimental setup during first half cycle

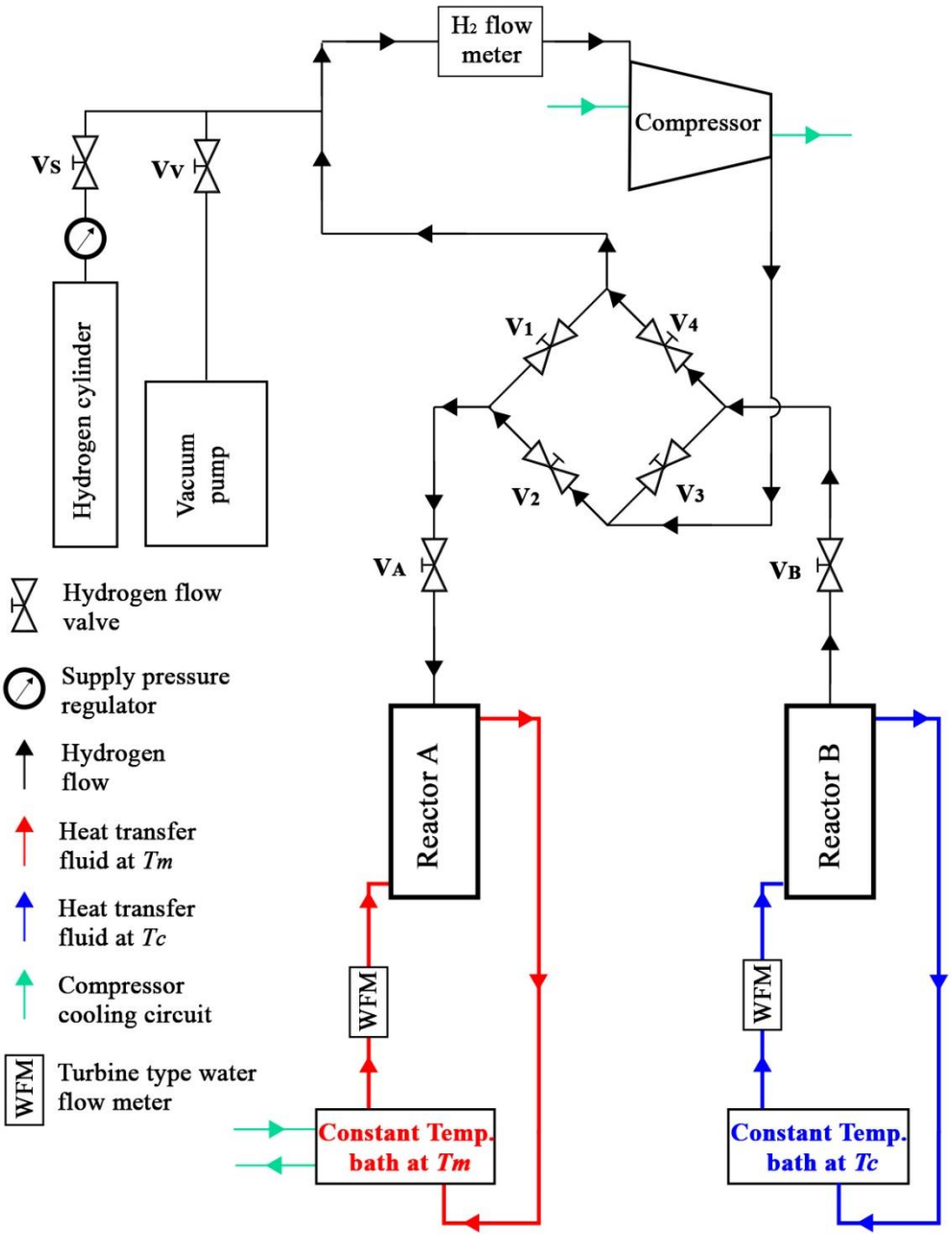

Fig.4.15. Schematic view of compressor driven metal hydride based cooling system experimental setup during second half cycle

The hydrogen flowed from Reactor A to Reactor B during the first half cycle, while the hydrogen flowed in reverse during the second half cycle. The flow of HTF were directed accordingly to facilitate the processes as absorption and desorption are heat driven mass

transfer phenomenon. The reactors were coupled with the help of a customized hydrogen compressor, Coriolis mass flow meter, flow control valves and heat transfer fluid (HTF) circuits.

As the compressor and Coriolis mass flow meter are unidirectional in their flow, while the absorbing and desorbing reactors interchange for each half cycle, the hydrogen flow control valves are arranged in full wave bridge rectifier configuration. This configuration ensures that the desorbing reactor is always connected to the suction line of the compressor and the absorbing reactor is connected to the delivery line of the compressor. The hydrogen specific compressors available in market are of very high capacity and energy intensive in nature. Hence, hermetically sealed reciprocating compressor suitable for conventional systems have been procured and customized. Specifically, in this experimental setup, hermetically sealed reciprocating compressor for R-134a refrigeration system with power rating of 1.5 kW has been customized. The compressor was cut open and the electrical circuits were reinforced with high temperature sheaths with no possibility of internal sparks. Then it was welded shut using TIG welding. Using silver brazing, copper cooling pipes of ¼ inch nominal size were brazed on to the surface of the compressor at an intermediate distance of 30 mm from top to bottom. This arrangement facilitates in circulation of cooling water uniformly around the compressor during hydrogen specific operation. Synthetic polyolester oil was used for lubrication and Danfoss oil separator was attached at the compressor discharge line to filter the oil from discharged hydrogen.

It was found to operate comfortably in the pressure range of 1 to 15 bar and the electrical energy consumption of the compressor was obtained using an energy meter (accuracy: ± 2%). Amount of hydrogen transferred during each half cycle between the coupled reactors was measured using Coriolis mass flow meter (sensitivity: 0.001 g; accuracy: ± 0.35%). Swagelok valves and fittings of 1/4 inch line size were utilized to frame the hydrogen flow circuit. Two recirculating

constant temperature baths, maintained at refrigeration and sink temperature, respectively were utilized during the experimental investigation. For flow of HTF, ball valves and braided hoses were used to frame the HTF flow circuit. Turbine type water flow meters (WFM) were connected after centrifugal pumps of the constant temperature baths, to observe the HTF flow rate. The HTF flow circuit has been framed such that the HTF at refrigeration temperature (T_c) can flow through desorbing reactor while HTF at sink temperature (T_m) flows through the absorbing reactor simultaneously.

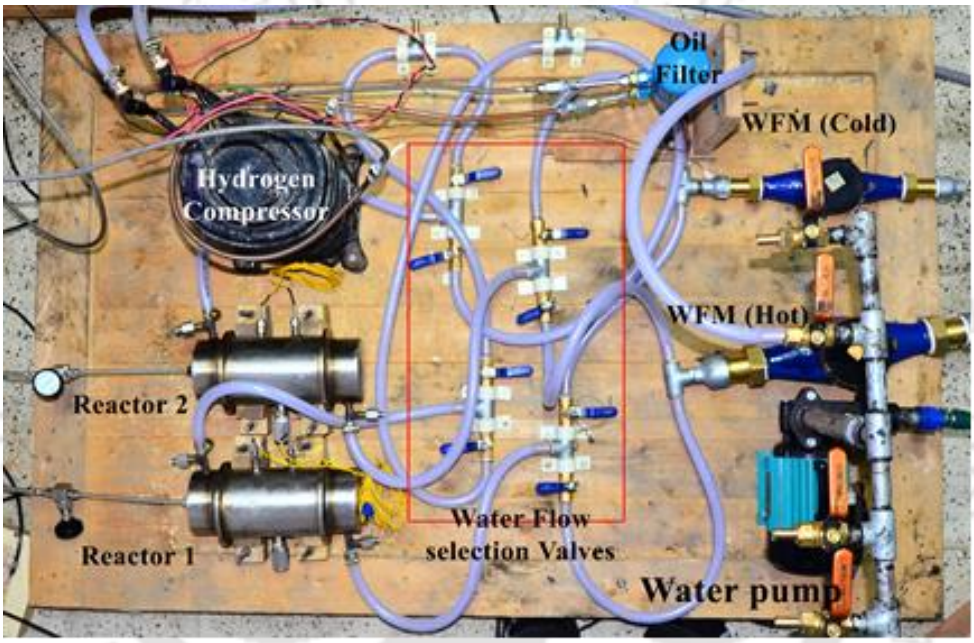

Fig.4.16. Pictorial view of the experimental setup with heat transfer fluid flow circuit

The pictorial representation of the compressor, identical reactors and the HTF flow circuit have been portrayed in Fig.4.16. Water has been used as HTF in this experimental investigation. The reactors have been fitted with metal-sheathed K-type thermocouples (accuracy: ± 0.5 °C) to sense the bed temperature, and HTF temperature at the inlet and outlet of the reactors. The sensed data was recorded through data acquisition system, with a transient response of 1 s. Hydrogen supply cylinder and vacuum pump have been connected to the hydrogen flow circuit through valves V_S and V_V, respectively so that the circuit can be charged with hydrogen or completely evacuated as and when necessary.

The stepwise operating procedure of experimental investigation into CDMHCS is represented in Fig.4.17. Prior to commencing the cyclic operation, Reactor A was absorbed completely and Reactor B was completely evacuated following the procedure detailed for open cycle system. Then the reactors were connected in CDMHCS mode, as illustrated in Fig.4.14 and Fig.4.15. Then the entire hydrogen flow circuit was evacuated and all valves were closed.

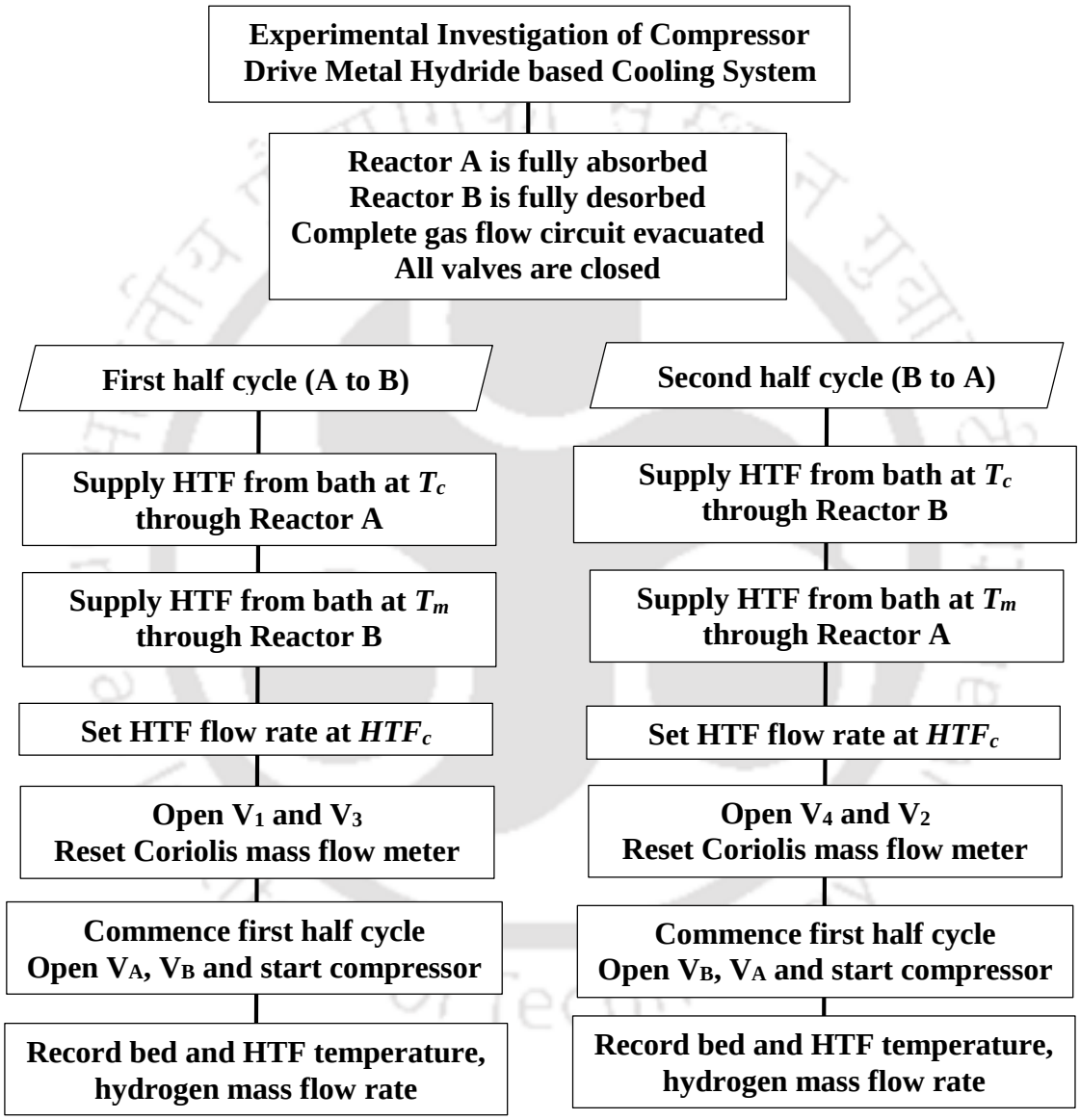

Fig.4.17. Flowchart depicting experimental procedure of compressor driven metal hydride based cooling system during cyclic investigation

The circuit was framed such that the saturated reactor was connected to suction line while the evacuated reactor to the discharge line. With this configuration, first half cycle was initiated by

allowing HTF from constant temperature bath at T_c to flow through Reactor A while HTF at T_m flowed through Reactor B at fixed flow rate of HTF_c, while valves V_1 and V_3 were opened. To commence, first half cycle, valves V_A and V_B were simultaneously opened while switching on the compressor. The half cycle was continued till there was no transfer of hydrogen detected. Then, the process was repeated in next half cycle in reverse direction, following steps listed in Fig.4.17. This cyclic procedure was continued till same amount of hydrogen was transferred in each half cycle, which ensured that both reactors had attained same level of reversible storage capacity at given operating conditions.

4.3.3 Performance parameters of CDMHCS

Based on the selected operating conditions, the performance of CDMHCS has been investigated on the basis of following parameters. From the Coriolis mass flow meter, the instantaneous amount of hydrogen transferred is monitored and by measuring the HTF temperature at inlet and outlet of MH reactors, the temperature variation in HTF across the bed was obtained. During each half cycle, the instantaneous rate of cooling output (kW) produced by desorbing reactor ($\dot{Q}_t$) at time '*t*', is estimated by,

$$\dot{Q}_t = \dot{m}_{HTF} * c_{p_{HTF}} * \Delta T_{HTF_t} \qquad \text{(Eqn.4.3)}$$

where, ΔT_{HTFt} is the difference in temperature (°C) between the HTF inlet and outlet of the desorbing reactor at that specific time '*t*'. As discussed, c_{pHTF} represents specific heat capacity of HTF, while $\dot{m}_{HTF}$ represents the mass flow rate of HTF (kg/s) obtained from HTF flow rate and the fluid density. Based on the rate of cooling output during each half cycle, cumulative cooling (Q_{cold}) for entire cycle was estimated. From this the average specific cooling power for the closed cycle (W/kg of total alloy) can be estimated as,

$$SCP = \frac{Q_{cold}}{t_{cy} * m_{MH\_total}} \qquad \text{(Eqn.4.4)}$$

In the above equation, 't_{cy}' denotes cycle time (s) and 'm_{MH_total}' denotes total mass of MH alloy (kg) in the CDMHCS.

Coefficient of Performance (COP) of the system has been estimated from the average cooling effect and compressor work as,

$$COP = \frac{\dot{Q}_{avg}}{W_c} \quad \text{(Eqn.4.5)}$$

where $\dot{Q}_{avg}$ denotes the average cooling effect (kW) obtained by,

$$\dot{Q}_{avg} = \frac{Q_{cold}}{t_{cy}} \quad \text{(Eqn.4.6)}$$

The compressor work (W_c) is the power input to the compressor for the given full cycle, estimated by,

$$W_c = \frac{3600*(Em_{end} - Em_{ini})}{t_{cy}} \quad \text{(Eqn.4.7)}$$

where, 'Em_{end}' and 'Em_{ini}' are the final and initial reading of energy meter (kWh), respectively.

Ideally, the amount of heat lost by HTF must be equal to the amount of heat required for desorbing the hydrogen from MH bed, which establishes that the bed takes necessary heat completely from the HTF. However, the MH consumes available heat energy from HTF, reactor wall and its own bed to desorb the hydrogen. Hence, estimation of COP solely based on the cooling output from HTF does not reflect the total cooling ability of the reactor. To quantify this ability of the reactor, the reactor effectiveness is being defined as the ratio of actual heat lost by HTF to the amount of heat required for desorption.

The reactor effectiveness is estimated by,

$$\text{Reactor}_{eff} = \frac{Q_{cold}}{n_g * \Delta H_d} \quad \text{(Eqn.4.8)}$$

where 'n_g' is the number of moles of hydrogen transferred and 'ΔH_d' is the molar enthalpy of formation during desorption process. The effect of different operating parameters such as

refrigeration temperature, sink temperature, cycle time and HTF flow rate on these performance parameters has been the evaluating factor for this experimental investigation. The reactors have been well insulated with polyurethane foam of 13 mm thickness before the actual performance investigation. The maximum uncertainties in the estimation of COP and SCP were about ± 3.65% and ± 3.05%, respectively. As the two reactors were identical with similar performance characteristics, the results of one reactor has been primarily discussed during investigation. However, in each cycle of parametric investigation, the average performance values of the cycle considering both reactors have been reported.

4.3.4 CDMHCS I: Investigation with an established alloy

Considering the compressor driven operation of the system, the selected alloy should meet following PCT requirements apart from the general requirements for MH based heat pump and cooling systems:

- The alloy should possess absorption equilibrium pressure below discharge pressure of the compressor (12 - 15 bar) at ambient temperature.
- The desorption equilibrium pressure of alloy should be much higher than the suction pressure of the compressor (0.2 - 1 bar) at refrigeration temperature.

These conditions are chosen such that same alloy can be absorbed and desorbed by the driving force of compressor. From reported literature, $LmNi_{4.91}Sn_{0.15}$ has been chosen as the established alloy for comparative system investigation. As represented in Fig.4.19, the PCT characteristics of the alloy are favourable with desorption equilibrium pressure of 2 bar at 20 °C. Even absorption equilibrium pressure is well below 10 bar even at 60 °C. Anbarasu et al. (2014b, 2014c) have studied the favourable absorption and desorption performance of this alloy filled in 60 ECT reactor. They had reported commendable absorption and desorption performance from storage system point of view. As these reactors impart both ECT reactor design and favourable alloy, two 60 ECT reactors developed under their investigation has been

implemented in the formulated CDMHCS. Each reactor has been filled with 2.75 kg of alloy and has been fitted with K-type metal-sheathed thermocouples to monitor bed and HTF temperature variation.

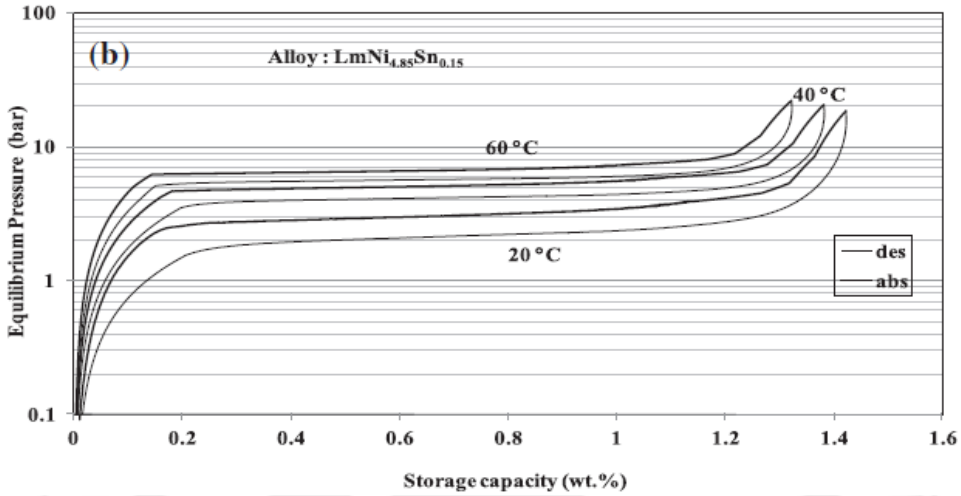

Fig.4.18. Pressure-Concentration-Temperature characteristics of $LmNi_{4.91}Sn_{0.15}$ (Selvam et al., 2013)

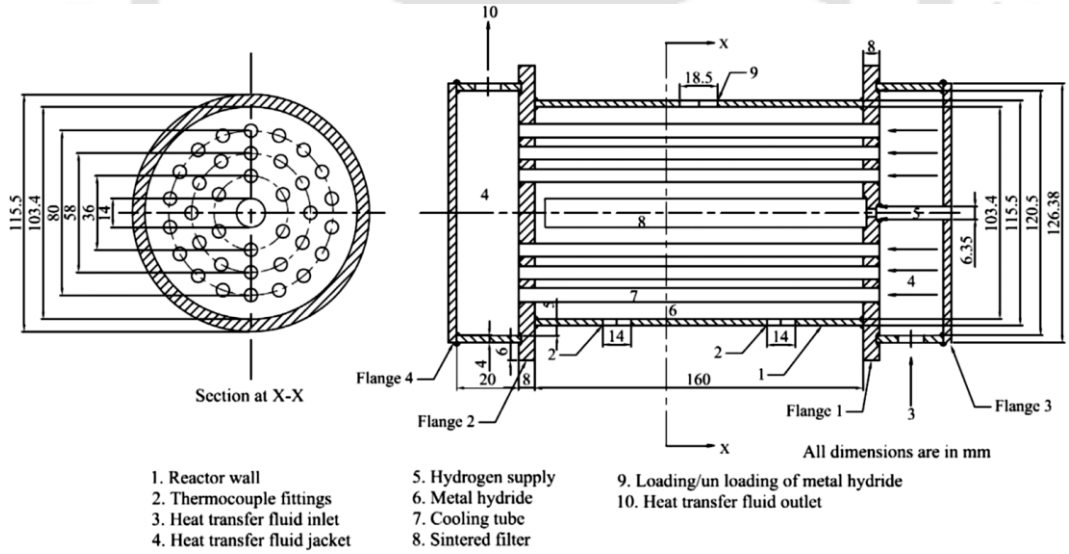

Fig.4.19. The schematic view 60 embedded cooling tubes reactor developed by Anbarasu et al. (2014b)

Similar to ECT reactors discussed in this study, this 60 ECT reactor has been fabricated with SS 316 material with ECT of 6.35 mm outer diameter. As represented in Fig.4.19, the reactor has

an outer diameter of 115.5 mm with a thickness of 6.05 mm. To store 2.75 kg, the reactor length has been fixed at 160 mm considering ample volume for expansion. The 60 ECT have been distributed considering angular pitch and the design have been detailed in the literature (Anbarasu et al., 2014a). The activation details of the alloy has been reported as well.

Performance investigation of $LmNi_{4.91}Sn_{0.15}$ based CDMHCS:

The performance investigation was conducted by varying the refrigeration (T_c) and sink temperature (T_m) along with variation of cold fluid flow rate (HTF_c) and cycle time (t_{cy}). The effect of each parameter was investigated by varying it among the set of values as summarized in Table 4.3, while fixing the other parameters at a reference value, as denoted.

Table 4.3. Range of operating parameters considered in performance investigation of $LmNi_{4.91}Sn_{0.15}$ based compressor driven metal hydride based cooling system

Investigation	Parameters	Values
Effect of varying cycle time	Refrigeration Temperature (T_c)	15 °C
	Sink Temperature (T_m)	25 °C
	Cycle time (t_{cy})	4, 8, 12 and 16 min
	Cold fluid flow rate (HTF_c)	8 lpm
Effect of varying cold fluid flow rate	Refrigeration Temperature (T_c)	15 °C
	Sink Temperature (T_m)	25 °C
	Cycle time (t_{cy})	8 min
	Cold fluid flow rate (HTF_c)	4, 8, 12 and 16 lpm
Effect of varying refrigeration temperature	Refrigeration Temperature (T_c)	10, 15 and 20 °C
	Sink Temperature (T_m)	25 °C
	Cycle time (t_{cy})	8 min
	Cold fluid flow rate (HTF_c)	8 lpm
Effect of varying sink temperature	Refrigeration Temperature (T_c)	15 °C
	Sink Temperature (T_m)	25, 30 and 35 °C
	Cycle time (t_{cy})	8 min
	Cold fluid flow rate (HTF_c)	8 lpm

These parameters have been considered based on the real time applicability of the system and the operational range of the chosen alloy. The effect of these parametric variation on the performance of the CDMHCS has been discussed in detail.

4.3.5 CDMHCS II: Investigation with a new alloy

Taking into account the growing necessity of CDMHCS, new alloys are being synthesized and evaluated for their suitability in application. For investigation, new alloy with composition of $La_{0.7}Ce_{0.1}Ca_{0.3}Ni_5$ has been selected (commercially procured as LCC1 alloy from M/s Whole Win (Beijing) Materials Sci. & Tech. Co. Ltd., China) based on PCT characteristics of the alloy, as represented in Fig.4.20. The desorption equilibrium pressure of 1 bar and absorption equilibrium pressure of 2 bar at 25 °C, with commendable peak HSC of 1.6 wt%. The particle size and chemical composition were confirmed from energy dispersive X-ray analysis of alloy sample by developing secondary electron map and corresponding spectrum, as represented in Fig.4.21 (a) and (b), respectively. The particle sizes were found to vary in the range of 10 to 100 μm while the chemical composition was confirmed to be $La_{0.7}Ce_{0.1}Ca_{0.3}Ni_5$ from the spectrum.

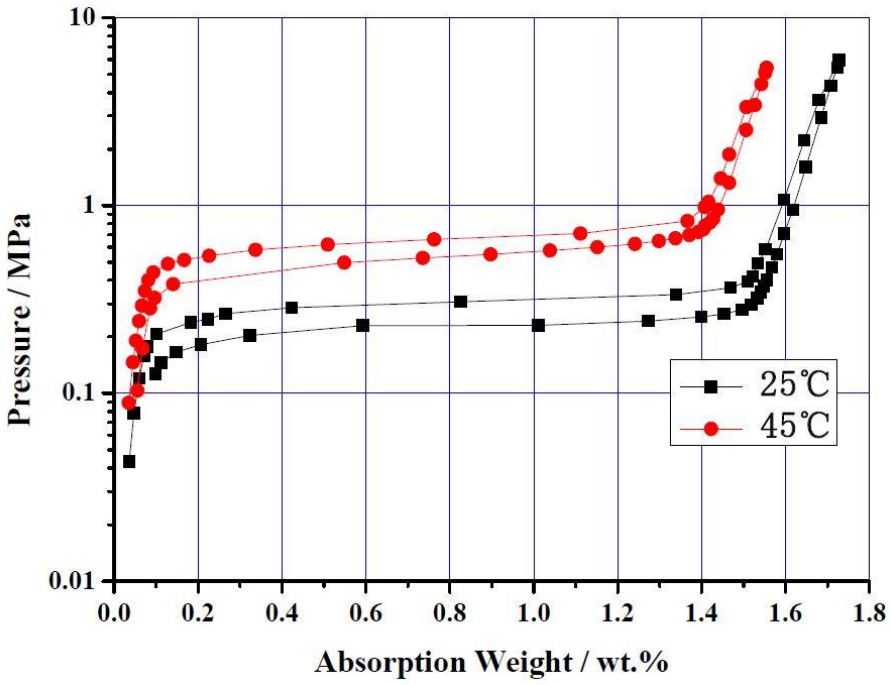

Fig.4.20. Pressure-Concentration-Temperature characteristics of $La_{0.7}Ce_{0.1}Ca_{0.3}Ni_5$

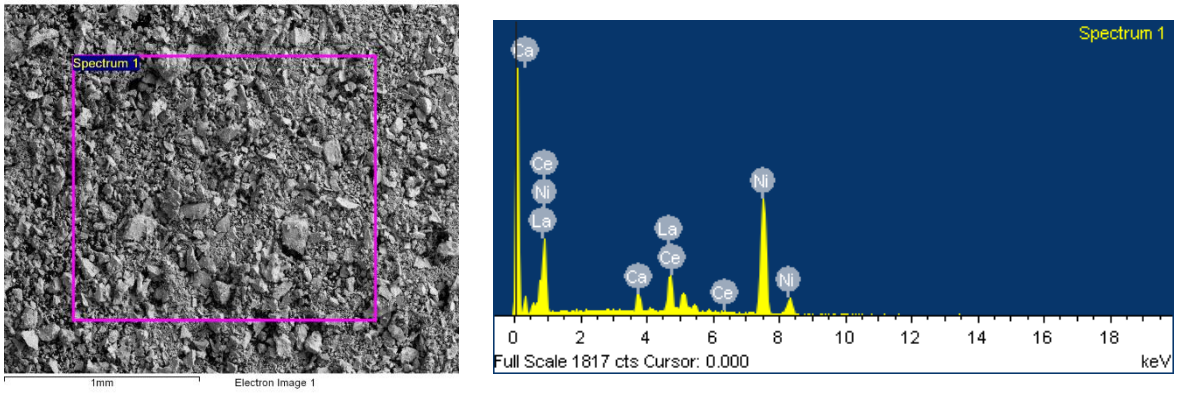

(a) (b)

Fig.4.21. (a) Secondary electron map and (b) corresponding spectrum obtained from energy dispersive X-ray analysis of $La_{0.7}Ce_{0.1}Ca_{0.3}Ni_5$ sample

Based on developed design methodology and comparative analyses, two identical units of 41 ECT reactor following RI_4in_41ECT configuration have been developed, each with length of 160 mm to accommodate 3.75 kg of $La_{0.7}Ce_{0.1}Ca_{0.3}Ni_5$ alloy. The 41 ECT are distributed uniformly in three stacks structure to provide enhanced heat transfer during operation. Similar to 55 ECT reactor, this model has a shell of 114.3 mm in outer diameter with a thickness of 6.02 mm, fabricated using SS316.

The dimensional specification of the reactor and the arrangement of ECT in each stack are presented in Fig.4.22 (a). The shell side of each reactor has been filled with 3.75 kg of $La_{0.7}Ce_{0.1}Ca_{0.3}Ni_5$ and the hydrogen transfer to/from the bed takes place through the centrally placed cylindrical SS316 sintered porous tube of 2 µm porosity. Based on the methodology, at stack radii of 16 mm, 30 mm and 44 mm, correspondingly 7, 14 and 20 ECT have been placed in three stack structure. The intermediate distance between the outer surfaces of ECT was 7.72 mm uniformly in both angular and radial direction. As an additional advantage, these 41 ECT reactors have been fitted with outer cooling jacket (OCJ), around the reactor outer shell to form a channel width of 10 mm around the periphery of the reactor. This was done so by wrapping a SS316 sheet of 1.5 mm thickness around the shell while providing enough provision for welding the alloy filling port and thermocouple weld fittings.

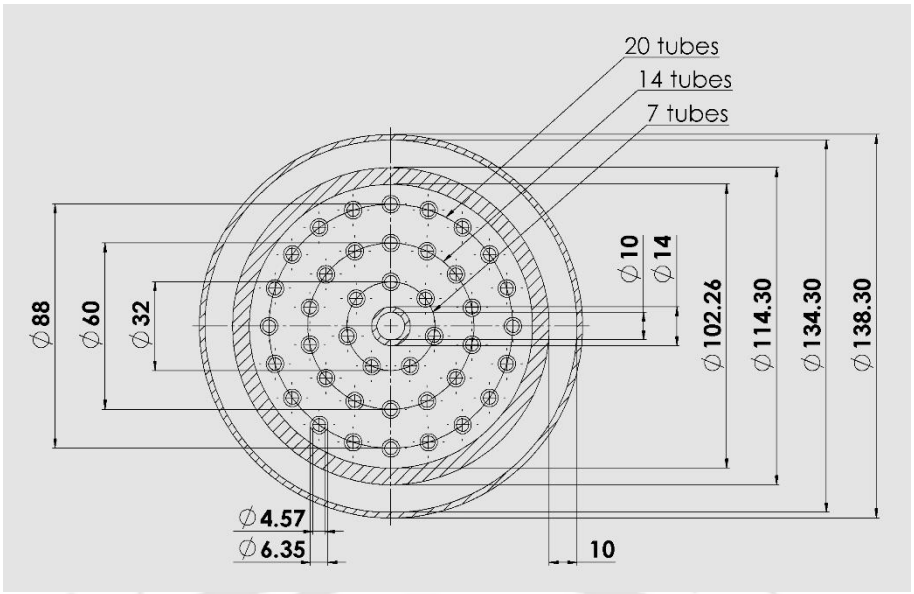

(a)

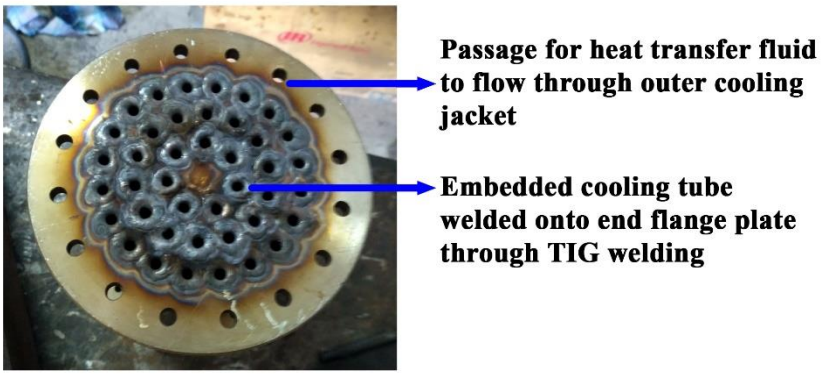

(b)

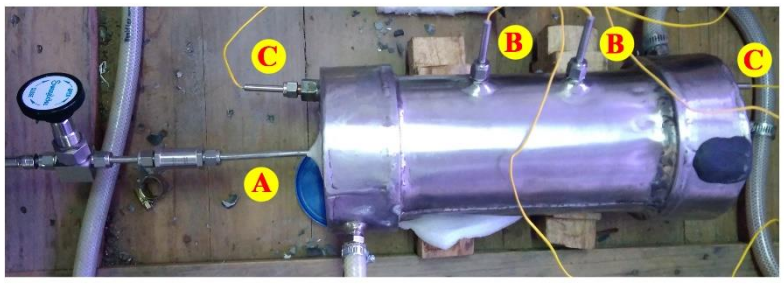

(c)

Fig.4.22. (a) Schematic view of reactor with 41 embedded cooling tubes along with outer cooling jacket (all dimensions are in mm), (b) back view of the reactor during welding and (c) pictorial view of the fabricated reactor (before insulation)

Through TIG welding, the shell and ECT were welded onto the flange plates carefully, as depicted in Fig.4.22 (b). The pictorial view of the 41 ECT reactor placed in the experimental setup (before insulation) has been represented in Fig.4.22 (c), from which it can be observed that the flange plates and auxiliary fluid flow chambers have been welded onto the both ends of principle chamber. As discussed before, supply tube (A) was welded onto porous filter while auxiliary fluid flow chambers were welded onto the end flange plates, acting as HTF reservoirs at inlet and outlet. The inlet and outlet of HTF were selected such that the flow of HTF was in the opposite direction to that of hydrogen supply. The alloy was filled through the alloy filling port, while K-type thermocouples have been fitted to the reactor through weld fittings. The metal-sheathed K-type thermocouples for reactor (B) were placed at 50 mm distance from the front and back flanges such that their sensing ends were at a depth of 30 mm from the outer periphery. The thermocouples were attached without grazing any of the ECT, and the reported bed temperature corresponds to average of the values sensed by these two thermocouples. Metal-sheathed K-type thermocouples have been attached directly onto inlet and outlet fluid chambers through fittings (C) to sense the HTF temperature. A secondary inline filter has been fitted in the supply line before the control valve as an additional filter. Before the performance investigation, the 41 ECT reactors each with an OCJ, have been well insulated using polyurethane foam and plastered with self-adhesive aluminium foil tape.

Activation of $La_{0.7}Ce_{0.1}Ca_{0.3}Ni_5$ in 41 ECT reactors:

The activation procedure as prescribed for low temperature alloys have been followed. However, considering the smaller particle size of the alloy and the PCT characteristics of the alloy, it has been strictly advised that the alloy should not be subjected to higher pressure or temperature, as it may lead to pulverization of the alloy, rendering it unusable. During activation, each reactor was individually activated following the same procedure. The circuit was checked for any leakage at about 100 bar using argon gas for 48 h. The same method was

followed to check the empty reactors as well. However, after filling the alloy, the reactor systems were not subjected to pressure higher than 50 bar. After evacuating the entire system to 10^{-3} mbar vacuum pressure, it was flushed with hydrogen gas at 5 bar and further evacuated while being maintained at 40 °C. This ensured that there were no other gases or moisture present in the bed. Evacuation at higher temperature additionally assists in expanding the lattice structure to receive the hydrogen atoms.

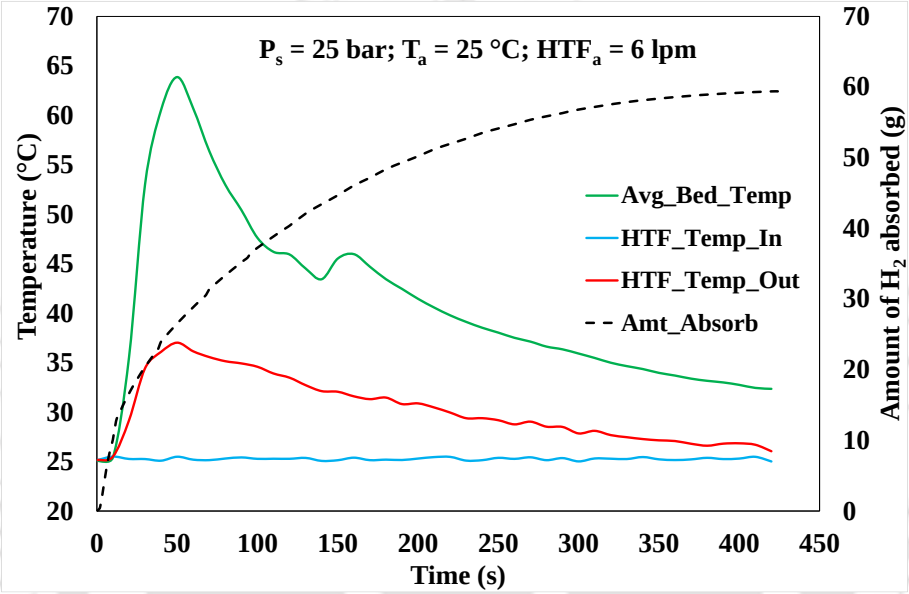

Fig.4.23. Variation of temperature and amount of hydrogen absorbed by $La_{0.7}Ce_{0.1}Ca_{0.3}Ni_5$ during 3rd activation cycle

In the first cycle, hydrogen was supplied at 40 bar while the bed was maintained at 25 °C. Throughout the performance investigation of new alloy, HTF flow rate was maintained at 6 lpm. In the first activation absorption cycle itself, HSC of 1.05 wt% was attained with 41.825 g of hydrogen being absorbed in 960 s by one of the reactors. The bed was evacuated to 10^{-3} mbar at 40 °C and the process was repeated. In second cycle, the supply pressure was reduced to 25 bar and the absorption capacity improved to 1.35 wt% in 705 s. By the third cycle complete activation with peak HSC of 1.58 wt% was attained within just 420 s. The robustness in terms of absorption depicted by this alloy has been keenly observed. The complete activation cycle of the reactor has been represented in Fig.4.23. The bed attained average temperature of

64 °C within 50 s, which dropped down to 32 °C by end of the cycle. The efficient heat transfer characteristics of the bed can be observed from the temperature gain of the HTF. At 50 s, the HTF outlet was at 37 °C which was a temperature gain of 12 °C.

Performance investigation of $La_{0.7}Ce_{0.1}Ca_{0.3}Ni_5$ based CDMHCS:

As this is a new alloy with comparatively narrower range of operating conditions, the investigative parameters have been framed by taking the performance investigation of $LmNi_{4.91}Sn_{0.15}$ based CDMHCS into consideration. The primary investigative focus has been directed towards the effect of variation of refrigeration temperature and cycle time, as they have been perceived to direct stronger impact on the overall performance of the system. The range of values varied for each parameter has been tabulated in Table 4.4. The cycle time was varied during the investigation of effect of refrigeration and sink temperature on the overall cooling performance of the system.

Table 4.4. Range of operating parameters considered in performance investigation of $La_{0.7}Ce_{0.1}Ca_{0.3}Ni_5$ based compressor driven metal hydride based cooling system

Investigation	Parameters	Values
Effect of varying refrigeration temperature	Refrigeration Temperature (T_c)	10, 15, 20 and 25 °C
	Sink Temperature (T_m)	25 °C
	Cycle time (t_{cy})	4, 8, 12, 16, 20, 24 and 28 min
	Cold fluid flow rate (HTF_c)	6 lpm
Effect of varying sink temperature	Refrigeration Temperature (T_c)	20 °C
	Sink Temperature (T_m)	25 and 35 °C
	Cycle time (t_{cy})	4, 8, 12, 16, 20, 24 and 28 min
	Cold fluid flow rate (HTF_c)	6 lpm

4.4 Summary

In this chapter, the experimental open and closed cycle MH based cooling systems are presented. As part of this investigation, the operating principles of open cycle MH based hydrogen storage and cooling system, and closed cycle compressor driven MH based cooling systems have been established. Based on the reported PCT characteristics, alloys suitable for

these systems have been identified. Using developed design methodology and reported literature, ECT reactors of both lab scale and industrial scale were fabricated and tested with selected alloys. The activation of these alloys filled in designed reactors have been studied in detail. Ultimately, the effects of operating parameters on the performances of these developed systems have been investigated extensively.

CHAPTER 5

RESULTS AND DISCUSSION

5.1 Preface

Based on the developed numerical model and proposed design methodology, embedded cooling tube (ECT) lab scale reactors have been designed and their comparative performance has been studied. Concurrently, the performance of an industrial scale hydrogen storage system has been analysed under various operating conditions using the same tools. Based on these analyses, reactors have been fabricated and implemented in the experimental investigations of open and closed MH based cooling systems, where their operational feasibility and the parametric influence on their performance have been discussed in detail. From the observed results and laid out discussions, the focus is to obtain a holistic understanding of these cooling systems.

5.2 Performance comparison of lab scale ECT reactor designs through thermal modelling

Among the various ECT reactor designs for lab scale reactors, three different configurations viz. 60 ECT, 55 ECT and 41 ECT have been chosen for this comparative analysis. Before comparing their performances, the validity of the developed thermal model to predict the performance of these lab scale ECT reactor designs have to be established.

5.2.1 Grid independent test

To understand the effect of the selected grid size on the accuracy of the performance prediction, grid independent was conducted on volume average bed temperature (T_{Vavg}) variation of 55 ECT reactor lab scale reactor filled with $MmNi_{4.7}Fe_{0.3}$ during absorption reaction. The dimensions of the lab scale prototype is that of the fabricated model discussed in Section 4.2.4. The analysis was conducted at supply pressure (P_s) of 40 bar, absorption temperature (T_a) of 5 °C with HTF flow rate (HTF_a) of 15 lpm for four different grids, as represented in Fig.5.1. Number of elements of grid 1, grid 2, grid 3 and grid 4 have been summarized in Table 5.1, along with variation in T_{Vavg} at absorption time, t = 30 s and t = 600 s.

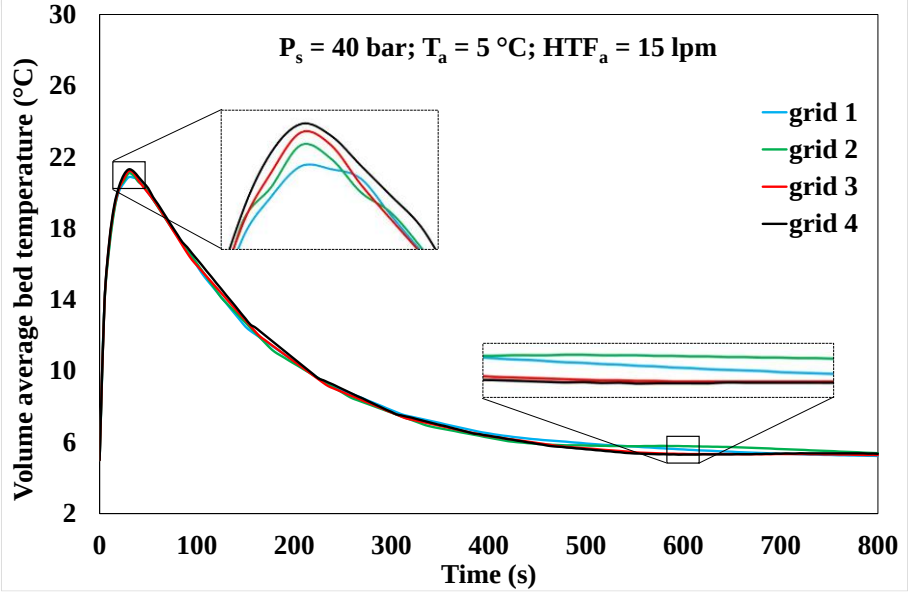

Fig.5.1. Volume average bed temperature variation of 55 embedded cooling tubes reactor for different grid sizes

Table 5.1. Grid elements and performance variation during absorption process

Name	Number of elements	T_{Vavg} @ t = 30 s	T_{Vavg} @ t = 600 s
grid 1	8,18,287	20.9 °C	5.6 °C
grid 2	10,95,933	21.1 °C	5.8 °C
grid 3	12,93,902	21.2 °C	5.4 °C
grid 4	14,56,328	21.3 °C	5.3 °C

The variation in peak temperature at t = 30 s is very minuscule. Comparatively, variation of T_{Vavg} at t = 600 is significant enough for comparison. With 34% increase in number of elements from grid 1 to grid 2, the peak T_{Vavg} increases to 21.1 °C with 3.6% refinement in result at t = 600 s. A refinement of 6.9% in T_{Vavg} at t = 600 s can be observed by implementing grid 3 with 18% increase in grid size. Considering grid 4 with 12.6% increase in number of grid elements, the refinement in results is only 1.9%. Hence, grid 3 with 12,93,902 elements is implemented for this numerical investigation, considering computational expense.

5.2.2 Model validation

To validate the numerical results, the experimental investigation of $MmNi_{4.7}Fe_{0.3}$ filled in 55 ECT reactor has been selected, as described in Section 5.4. At T_a of 25 °C and HTF_a of 24 lpm, the hydriding characteristics of the 55 ECT reactor is predicted at P_s of 40 bar and 60 bar, as depicted in Fig.5.2 (a) and (b). The numerically predicted results are able to portray the trend observed during the absorption of hydrogen stored as well as the heat gain in the HTF. However, the initial surge witnessed for about 30 s in both phenomena is not captured. This might be due to the uncertainties encountered in the estimated values of thermo-physical properties of this alloy, which has been primarily obtained through reported literature. The maximum deviation in the trend is estimated to be 4.7% and 5.4% in hydrogen storage capacity (HSC) estimation at P_s of 40 and 60 bar, respectively. Similarly, in the case of HTF outlet temperature prediction, the corresponding deviations is within ± 1%. While validating the desorption reaction at HTF flow rate (HTF_d) of 15 lpm and varying desorption temperature

(T_d), it has been observed that the numerical prediction is in good agreement with the experimentally recorded results.

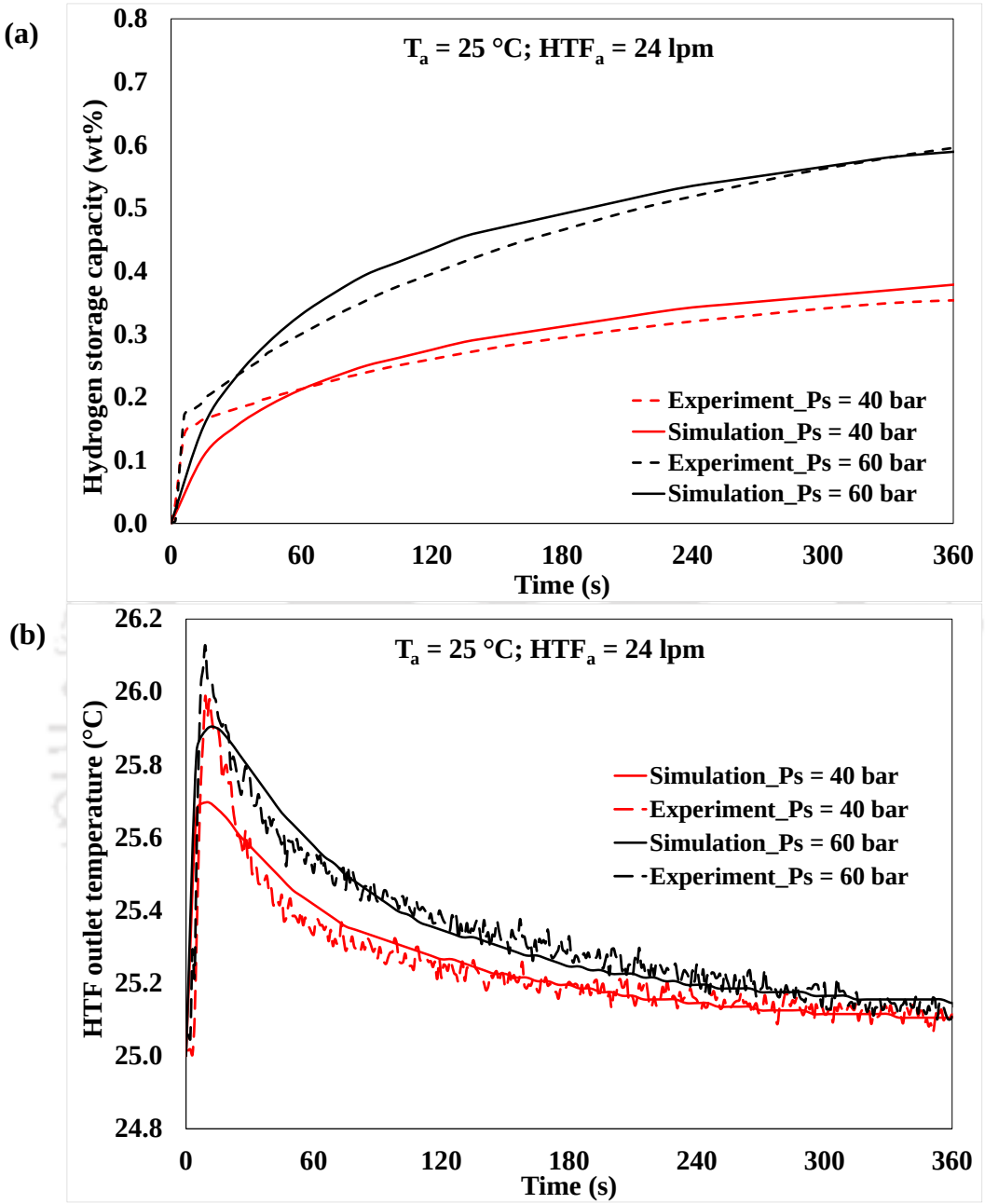

Fig.5.2. Validation of numerically simulated (a) hydrogen storage capacity and (b) heat transfer fluid outlet temperature of 55 embedded cooling tubes reactor during absorption

The validation of the amount of hydrogen desorbed during T_d of 25 °C and 5 °C have been portrayed in Fig.5.3 (a), while Fig.5.3 (b) represents the validation of HTF outlet temperature variation at T_d of 25 °C. Due to the rapid desorption characteristic of the alloy, the rate of hydrogen desorption predicted is slightly faster than the actual dehydriding rate. The maximum

deviations encountered in estimation hydrogen desorption capacity are 9.2% at 25 °C and 9.7% at 5 °C, while in the case of HTF outlet temperature prediction at 25 °C, it is 1.3%.

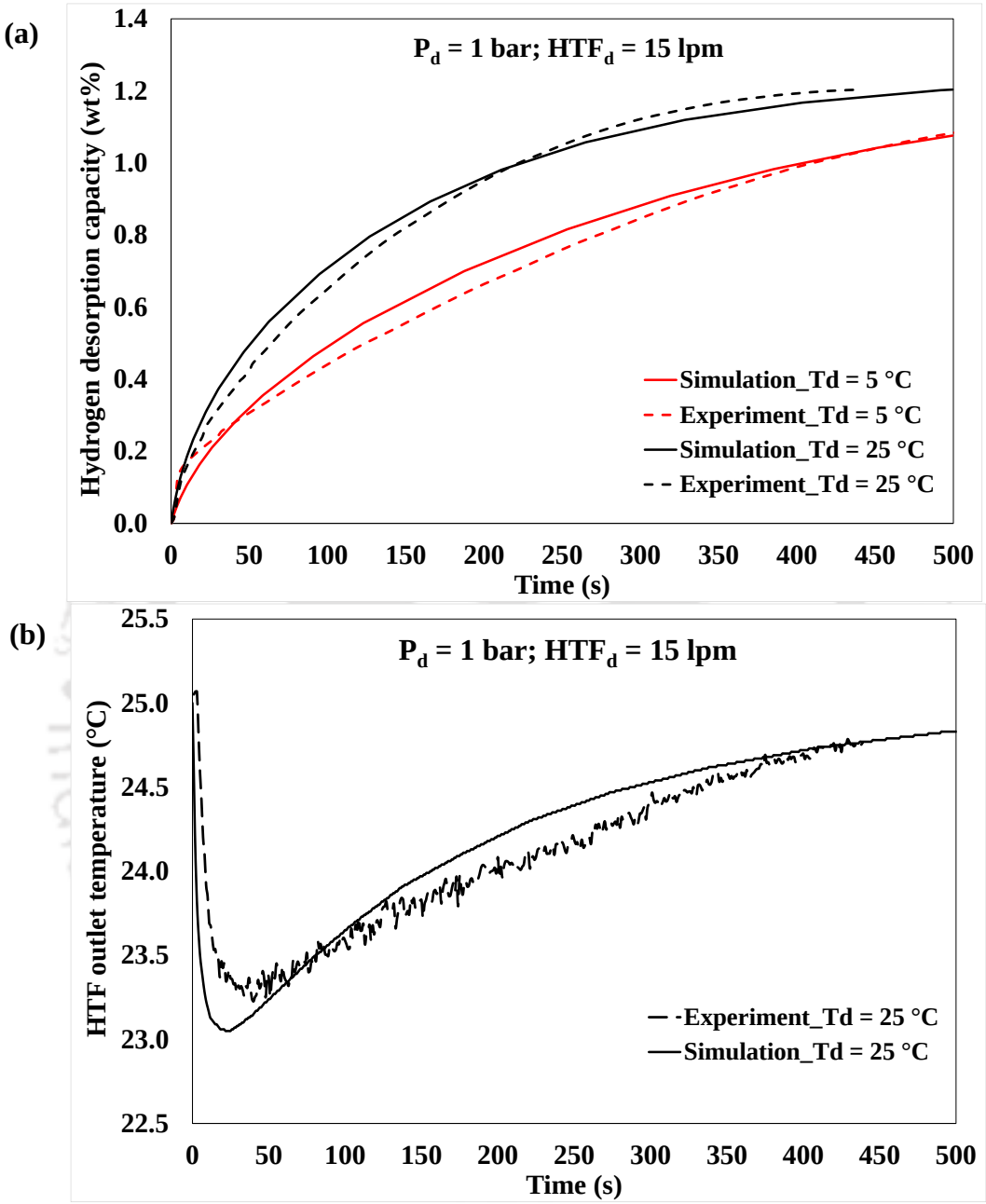

Fig.5.3. Validation of numerically simulated (a) hydrogen desorption capacity and (b) heat transfer fluid outlet temperature of 55 embedded cooling tubes reactor during absorption

The observed deviations are primarily due to the uncertainty in the values of constants used in the desorption model. However, the simulated result reflects the behaviour of experimental data closely and the deviations are within acceptable limits. Hence, validity of the developed models is found to be acceptable, especially in predicting the interaction with HTF which is the primary focus for MH based cooling systems.

5.2.3 Comparison of absorption characteristics

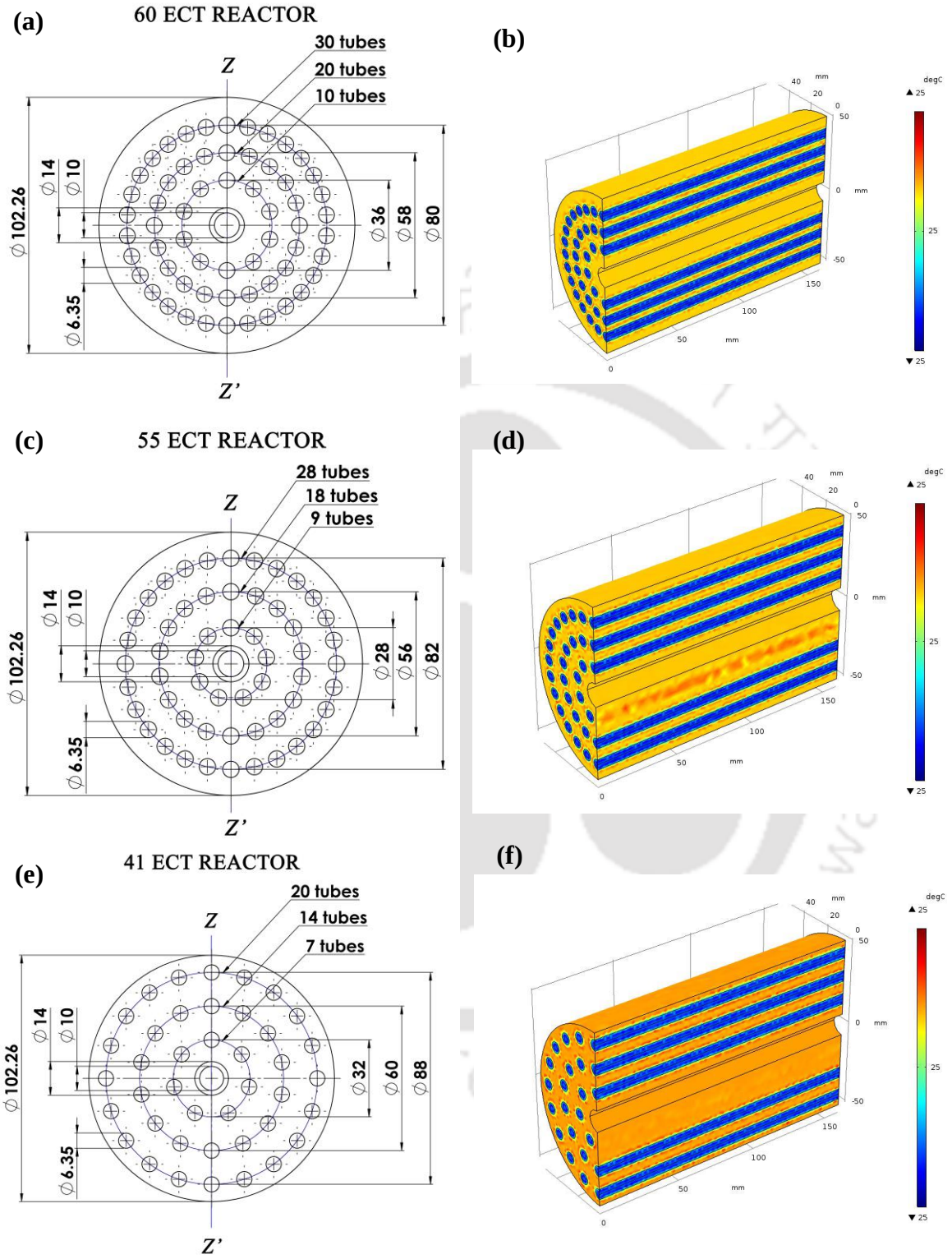

Fig.5.4. Schematics including embedded cooling tube arrangement of reactors with (a) 60 ECT, (c) 55 ECT and (e) 41 ECT, and temperature distribution of numerically simulated half sectional models of (b) 60 ECT, (d) 55 ECT and (f) 41 ECT at 25 °C and t = 0 s

Using the valid thermal models, the performance of the lab scale reactor designs are compared. At absorption condition of 50 bar pressure and 25 °C temperature with HTF_a of 24 lpm, the hydrogen storage capacities of 41 ECT, 55 ECT and 60 ECT reactor are studied. For the purpose of comparative analysis, all reactors are considered to be of 160 mm in length, containing same alloy, $MmNi_{4.7}Fe_{0.3}$. The schematics of the reactors detailing the ECT arrangement within the bed for all three designs are depicted in Fig.5.4 (a)-(f), along with the temperature distribution half sectional models of all three designs (half sectional model) at 25 °C and t = 0 s. As observed from Fig.5.5 (a), there is minuscule difference in the hydriding rate achieved through these reactors. Both 55 ECT and 60 ECT reactors attain HSC of 0.64 wt% in 450 s, while for 41 ECT reactor, it is slightly more by 2.4%. Maximum difference is observed at 150 s, when 60 ECT reactor has HSC of 0.39 wt%, which is 2.4% and 4.9% lesser than that of 55 ECT and 41 ECT reactors. Fig.5.5 (b) represents the variation in HTF outlet temperature, which delineates the absorption of these models significantly. All the models portray rapid increase in HTF temperature during initial duration and drop towards inlet temperature, as is the characteristic of ECT reactors. However, the peak value symbolizes the absorption ability while the rate of temperature decrease reflects the heat transfer characteristics of the reactor. In this consideration, both 41 and 55 ECT reactors are better as they achieve respective peak HTF outlet temperature of 25.9 °C and 25.8 °C as opposed to 25.5 °C of 60 ECT. Even between these two designs, 41 ECT reactor is better with achieving 25 °C in 300 s.

This difference in their absorption performance is clearly understood by observing the variation in the bed temperature of all three reactors at absorption time of t = 25 s and t = 150 s through pictorial sliced views portrayed in Fig.5.6 (a)-(f). At t = 25 s, average bed temperature of both 60 ECT and 55 ECT reactors has reached 44.9 °C. The uneven distribution in bed temperature can be noted clearly with angular distribution being more favoured than the radial distribution.

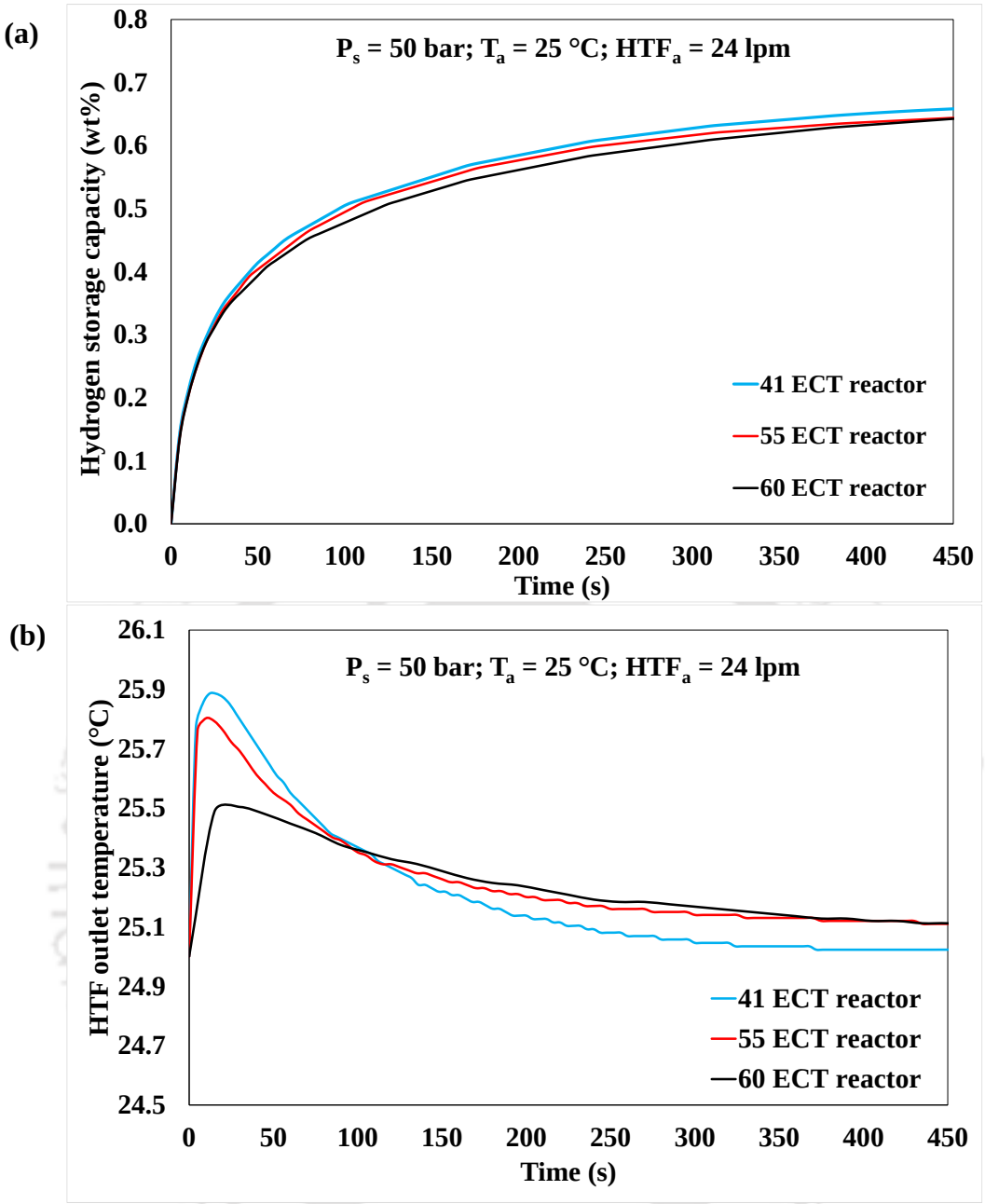

Fig.5.5. Performance comparison of (a) hydrogen storage capacity and (b) heat transfer fluid outlet temperature for different reactor designs during absorption

At t = 150 s, the better performance of 55 ECT reactor is seen in comparison to 60 ECT reactor, where the bed temperature is comparatively higher near the outer periphery and inner porous filter for the 60 ECT reactor, and this difference is less pronounced in 55 ECT reactor. Compared to these designs, the 41 ECT reactor has distinctly uniform temperature distribution in all direction at t = 25 s, with average bed temperature of 49.3 °C. The same uniformity is reflected at t = 150 s as well, where the average bed temperature is 32.3 °C. Even in the case

of 41 ECT, the temperature near porous filter is slightly higher as the design incorporates more radial pitch in first stack due to welding of ECT around porous filter.

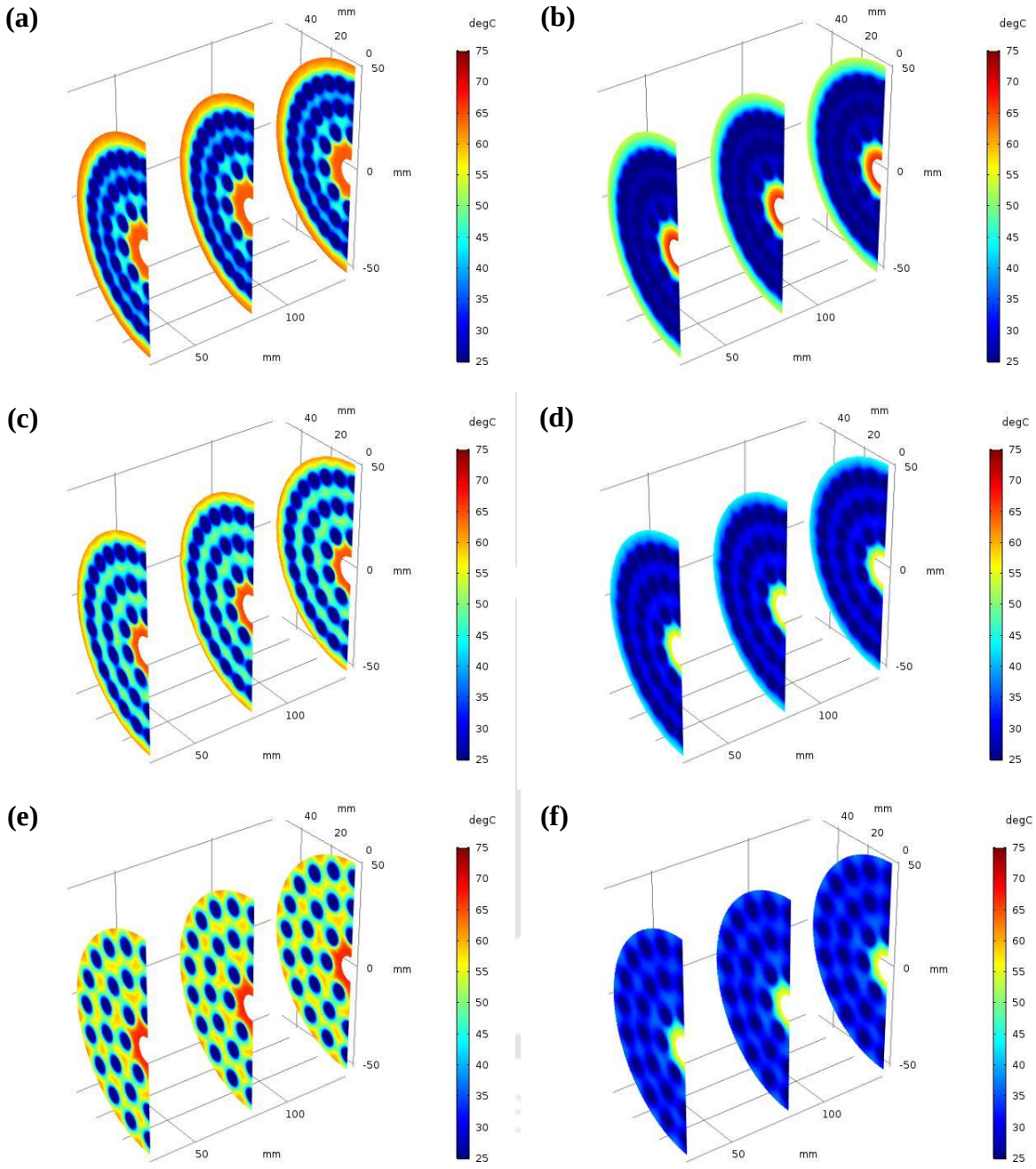

Fig.5.6. Pictorial sliced views of hydride bed temperature during absorption at time, t = 25 s for (a) 60 ECT, (c) 55 ECT and (e) 41 ECT, and at time, t = 150 s for (b) 60 ECT, (d) 55 ECT and (f) 41 ECT (ECT: Embedded Cooling Tubes)

5.2.4 Comparison of desorption characteristics

The difference in desorption performance of all these designs, at T_d of 25 °C with HTF_d of 15 lpm, is more noticeable than the difference in absorption performance. The variation in hydrogen desorption capacity is represented in Fig.5.7 (a), where 1 wt% is desorbed within 150 s by 60 ECT reactor. However, for same duration, the amount of hydrogen desorbed is 5.2% and 8.6% more in case 55 ECT and 41 ECT reactor, respectively.

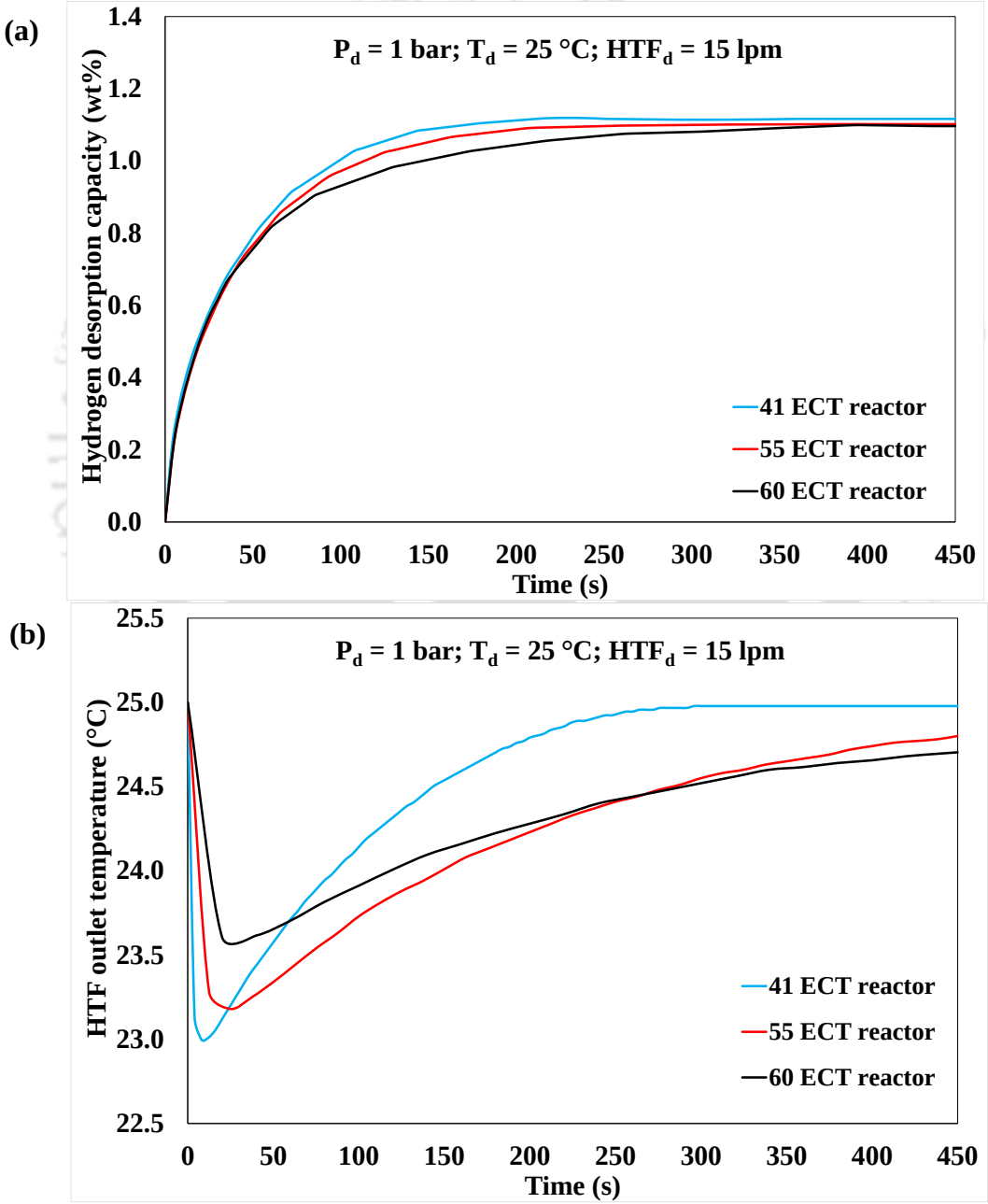

Fig.5.7. Performance comparison of (a) hydrogen desorption capacity and (b) heat transfer fluid outlet temperature for different reactor designs during desorption

The HTF outlet temperature variation for these models are remarkably distinct, as observed from Fig.5.7 (b). The drop in HTF outlet temperature to 23 °C, 23.2 °C and 23.6 °C in 8 s, 25 s and 40 s, respectively is observed for 41 ECT, 55 ECT and 60 ECT reactors.

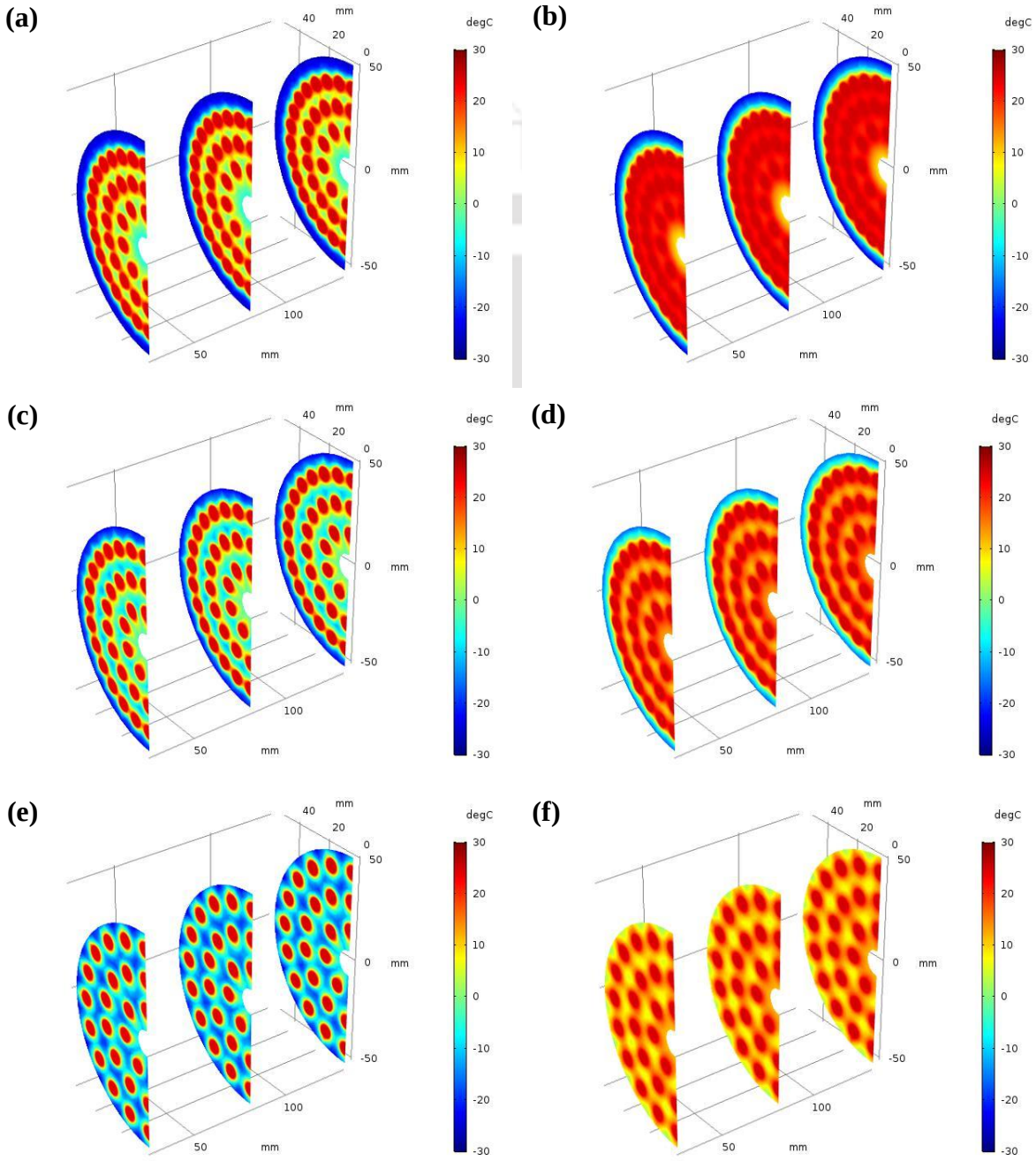

Fig.5.8. Pictorial sliced views of hydride bed temperature during desorption at time, t = 40 s for (a) 60 ECT, (c) 55 ECT and (e) 41 ECT, and at time, t = 150 s for (b) 60 ECT, (d) 55 ECT and (f) 41 ECT (ECT: Embedded Cooling Tubes)

In case of desorption, the rapid drop in bed temperature signifies faster dehydriding kinetics, while rate of increase in temperature towards inlet reveals the heat transfer characteristics. Considering this aspect, 41 ECT reactor facilitates better desorption and thereby the cooling performance. The desorption characteristics portrayed by 55 ECT reactor is commendable as well, which can be observed from the variation in bed temperature represented in Fig.5.8 (a)-(f). At time t = 40 s during desorption, 60 ECT reactor portrays three distinct temperature region with very low temperature near outer periphery, HTF temperature among the bed near ECT and average of these temperature near the porous filter. Comparatively, the distribution is uniform in the case of 55 ECT with slightly varied distribution in the vicinities of outer periphery and porous filter. At t = 150 s, the similar difference is seen with distinctly different temperature zones in 60 ECT reactor, which is less prominent in 55 ECT reactor. Both at t = 40 s and 150 s, the bed temperature variation is uniform for 41 ECT reactor with the bed depicting low temperature at t = 40 s and near HTF temperature within t = 150 s, reflecting the enhanced heat transfer ability of this design. Considering the absorption and desorption characteristics facilitated by these reactor designs, 41 ECT and 55 ECT reactors are considered in the development and experimental investigation of various MH based cooling systems in this study. To further understand and observe the enhanced heat transfer characteristics of ECT reactors developed using the proposed design methodology, the storage performance of an industrial scale reactor is predicted through thermal modelling.

5.3 Performance prediction of industrial scale hydrogen storage system through thermal modelling

The absorption performance of industrial scale reactor filled with 50 kg of $LaNi_{4.7}Al_{0.3}$ alloy is being investigated through numerical modelling. Initially the validity of the model has been established. The best reactor design among different configurations is selected based on its hydriding performance for further parametric analysis.

5.3.1 Grid independent test

To analyse the effect of grid size variation on the accuracy of numerical prediction, a grid independent test is conducted on T_{Vavg} variation during the absorption reaction of RIII_6in_99ECT reactor model containing 50 kg of $LaNi_{4.7}Al_{0.3}$ alloy. For this analysis, models of different grid sizes are generated and their details along with the duration of computation are presented in Table 5.2. The observed result of grid independent analysis is portrayed in Fig.5.9. It can be observed that at a given absorption condition of 30 bar, 25 °C with HTF flow rate of 45 lpm, there is a significant change in the bed temperature variation and in computation time when the number of elements is increased from 6,89,929 (grid 1) to 8,52,989 (grid 2). For 14.9% increase in computation duration, nearly 5% reduction is witnessed in absorption time.

Table 5.2. Grid elements and time taken for absorption process

Name	Number of elements	Computation duration	Absorption time
grid 1	6,89,929	27966 s	2640 s
grid 2	8,52,989	32137 s	2510 s
grid 3	10,53,580	38229 s	2470 s
grid 4	11,77,945	42639 s	2460 s

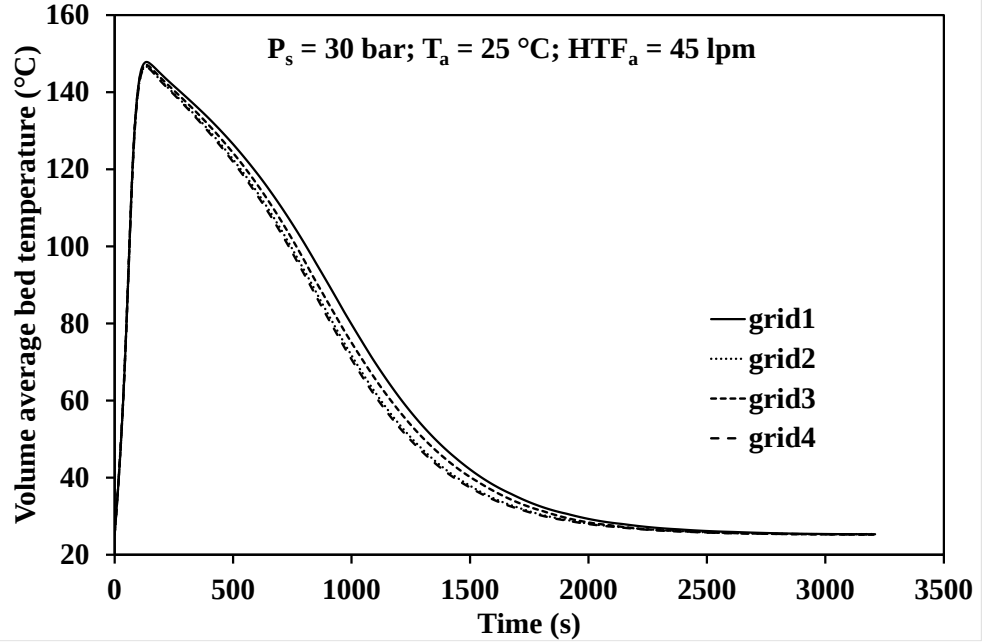

Fig.5.9. Volume average bed temperature variation of RIII_6in_99ECT for different grid sizes

When grid size was increased further to 10,53,580 (grid 3), 19% increase in computation duration results in 2% refinement in results. Further refinement is not perceived when number of elements is increased beyond grid 3 to grid 4 with 11,77,945 elements. Hence, further mesh improvement beyond grid 4 is not performed and mesh properties of grid 3 is selected for this computational study.

5.3.2 Validation of the model

To validate the numerical results, fabricated model of RIII_6in_99ECT which was filled with 40 kg of $LaNi_{4.7}Al_{0.3}$ alloy has been considered. The length of the model is shortened to 700 mm, as the filled alloy mass was 40 kg. The physical model of reactor is represented in Fig.5.10, wherein the principle chamber is of RIII_6in_99ECT configuration based on the design methodology. As per the design, the SS 316 cylindrical shell is of 168.28 mm in outer diameter and 7.12 mm in thickness. A sintered SS316 tube having an outer diameter of 14 mm and thickness of 2 mm has been centrally placed in the principle chamber. In a five stack structure around the sintered tube, 99 ECT has been distributed as per configuration. The tubes are of SS 316 having an outer diameter of 6.35 mm and thickness of 0.89 mm.

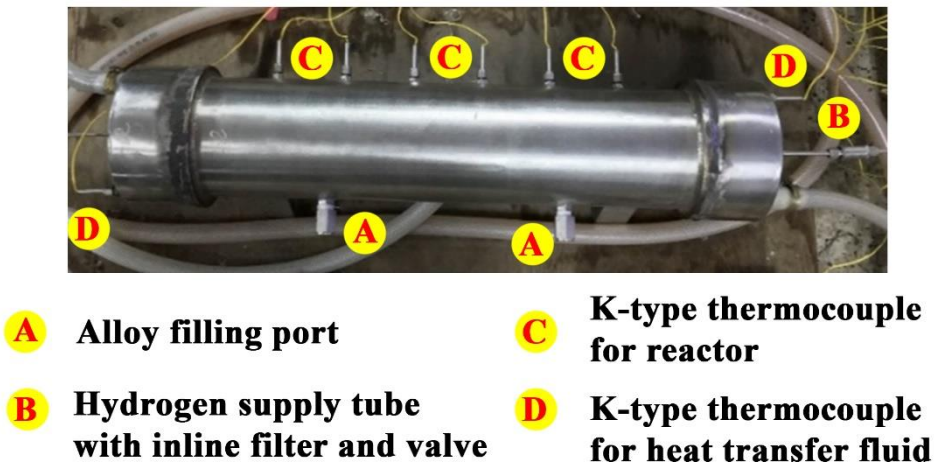

Fig.5.10. Physical model of RIII_6in_99ECT reactor

In the physical model, this principle chamber was welded on both ends to 10 mm thick circular plates, which have been termed as end flange plates. On both outside ends, auxiliary fluid flow chambers were welded onto the end flange plates as shown in Fig.5.10. The alloy was filled through two weld ports on periphery of the reactor (A). Hydrogen supply tube (B) was welded onto end flange plates such that the supplied hydrogen flows directly through the porous tube inside reactor. The temperature at various locations of the hydride bed was sensed using metal sheathed K-type thermocouples (C). The thermocouples were axially located with an interval of 100 mm between them while their sensing ends were at a depth of 45 mm from outer periphery. The first thermocouple was axially located at a distance of 100 mm from the inlet end flange plate.

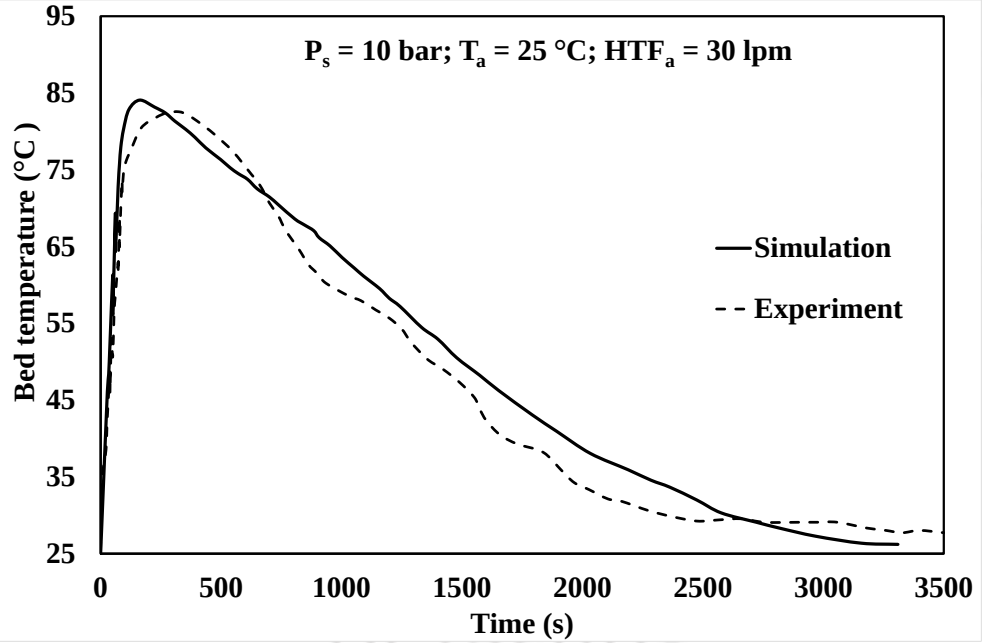

Fig.5.11. Validation of bed temperature

The experiment was conducted at supply pressure of 10 bar and absorption temperature of 25 °C with 30 lpm water flow rate. The numerical model of RIII_6in_99ECT reactor with 40 kg MH alloy is simulated at the same absorption condition. The hydride bed temperature of the numerical model is evaluated at same locations corresponding to the thermocouple sensing ends in the physical model. The arithmetic average bed temperature is evaluated from both

experimental investigation and numerical simulation as compared in Fig.5.11, and a good agreement is observed between them. The average bed temperature is predicted to be maximum at 86 °C in numerical simulation, while it was at 82.7 °C in experimental analysis. There was a slight delay in experimental average bed temperature attaining its peak value compared to the numerical prediction. This deviation was observed during the initial stage of absorption reaction and can be attributed to non-uniform porosity of actual MH bed. However, deviation is well within ± 4% when the predicted average bed temperature is compared with corresponding experimental data.

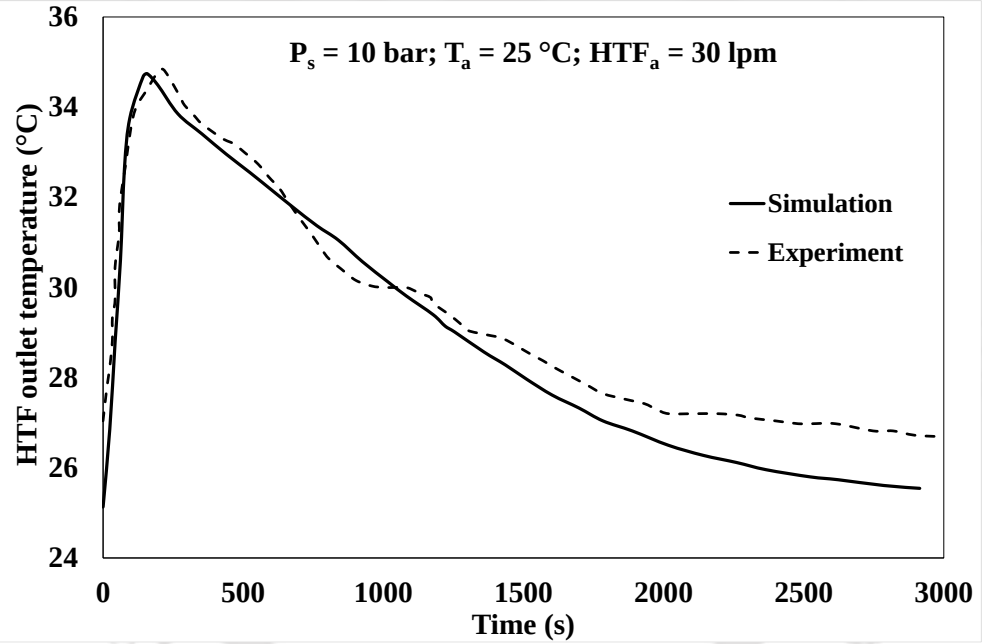

Fig.5.12. Validation of heat transfer fluid outlet temperature

The predicted HTF outlet temperature is compared and validated with outlet HTF temperature of experimental analysis as shown in Fig.5.12. The maximum temperature of HTF is predicted to be 34.7 °C whereas in experiment, it was 34.8 °C after a delay of about 60 s. HTF outlet temperature of experiment attained 27 °C as opposed to 25 °C in case of predicted value, due to slight increment in HTF inlet temperature during experiment.

5.3.3 Effect of reactor configuration

Having established the validity of the overall model through above analysis, numerical models of the different reactor configurations namely RI_4in_40ECT, RII_5in_67ECT, RIII_6in_99ECT and RIV_8in_136ECT are developed for 50 kg of $LaNi_{4.7}Al_{0.3}$ alloy and simulated at an absorption condition of 30 bar and 25 °C with water flow rate of 60 lpm. The observed variation of T_{Vavg}, HSC and HTF outlet temperature are discussed in detail.

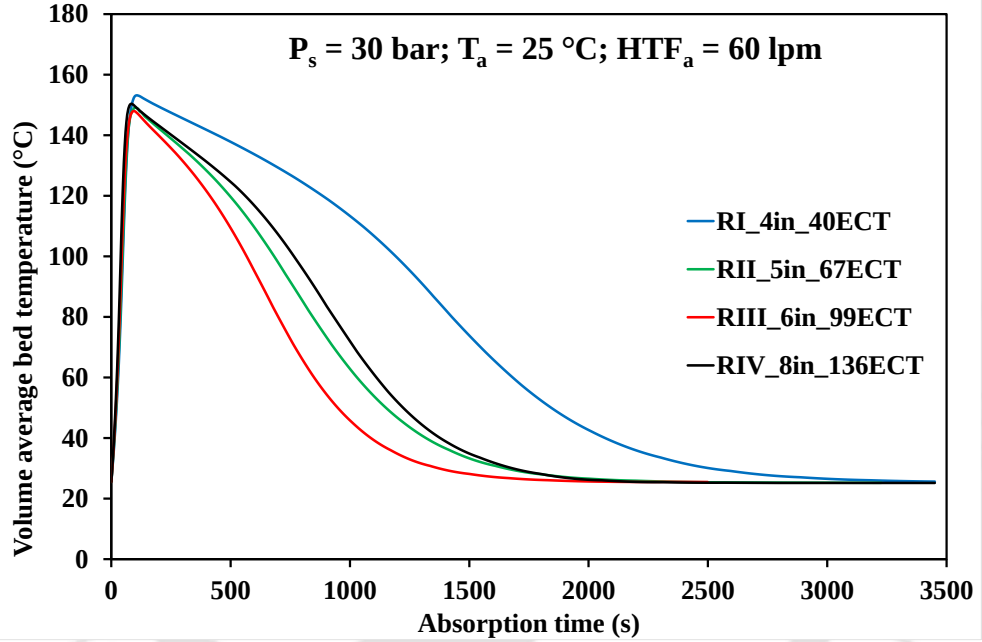

Fig.5.13. Effect of reactor geometry on volume average bed temperature variation

Variation of volume average bed temperature:

The effect of reactor configuration on the variation of the volume average bed temperature (T_{Vavg}) during absorption is represented in Fig.5.13. As the mass of alloy is same in all models, the dimensions and ECT arrangement of each reactor configuration plays a crucial role on hydriding rate. Initially, the absorption is rapid due to substantial pressure gradient between equilibrium bed pressure and supply pressure. This leads to rapid evolution of exothermic heat that causes sudden increase in bed temperature. This mechanism of interaction is same for all configurations which was reflected by their peak value of T_{Vavg}. The evolving heat of absorption

is removed by HTF wherein the arrangement of ECT influences the interaction. Among the reactor configurations, RIII_6in_99ECT exhibits rapid absorption kinetics, while hydriding of RI_4in_40ECT is comparatively slow due to its length of 2262.7 mm. In RI_4in_40ECT, temperature of HTF flowing throughout reactor length increases to such an extent that the temperature gradient between bed and HTF reduces which affects the heat removal from bed. T_{Vavg} drops to 27 °C, from peak value of 153 °C within 2778 s for RI_4in_40ECT while the value drops from 149.6 °C within 1497 s for RIII_6in_99ECT, which amounts to 46% reduction in time taken. Owing to their designs, both RII_5in_67ECT and RIV_8in_136ECT depict similar performance while requiring 20.1% more time than RIII_6in_99ECT for dropping to 27 °C.

Variation of hydrogen storage capacity (HSC):

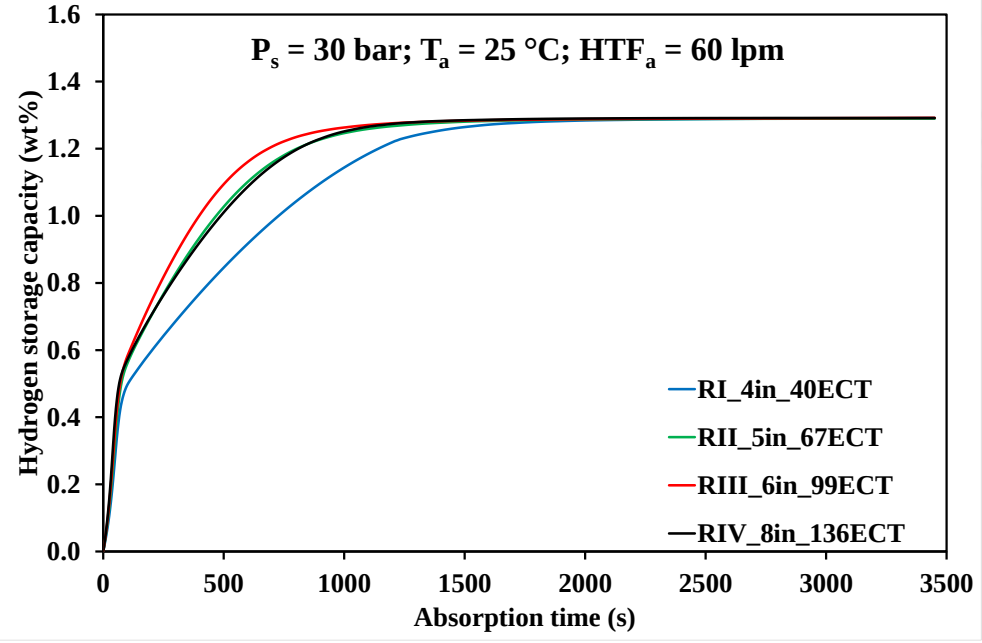

Fig.5.14. Effect of reactor geometry on variation of hydrogen storage capacity

The variation of HSC is similar to that of T_{Vavg} variation, as the rate of heat removal dictates the rate of hydrogen absorption. Reactor with higher heat transfer rate depicts better absorption kinetics, as can be observed from Fig.5.14. Total HSC of 1.29 wt% is achieved by all configurations, while 50% of total HSC is achieved within 140 s by RIII_6in_99ECT model.

For 80% of absorption amounting to HSC of 1.03 wt%, a duration of just 430 s is required by this model. Comparatively, RII_5in_67ECT and RIV_8in_136ECT model require 17.5% and 22.8% more time respectively to achieve HSC of 1.03 wt%. This is due to the fact that RII_5in_67ECT is longer than RIII_6in_99ECT which leads to higher increase in HTF temperature resulting in lesser temperature gradient and thereby leading to poor heat transfer. In case of RIV_8in_136ECT, it is broader than RIII_6in_99ECT and this causes a slight delay in complete absorption of bed near periphery region of model. Due to its sizable length, RI_4in_40ECT requires 82.5% more duration than RIII_6in_99ECT to achieve HSC of 1.03 wt%.

Variation of HTF outlet temperature:

As discussed, the HTF outlet temperature of RI_4in_40ECT is higher than the other models leading to slower heat removal rate. From Fig.5.15, it is observed that the HTF outlet temperature of this model attains a peak value of 55.6 °C and takes 1897 s for it to cool down to 27 °C, signifying slower heat transfer. Comparatively, HTF outlet temperature of RII_5in_67ECT requires 33.6% less duration to attain 27 °C.

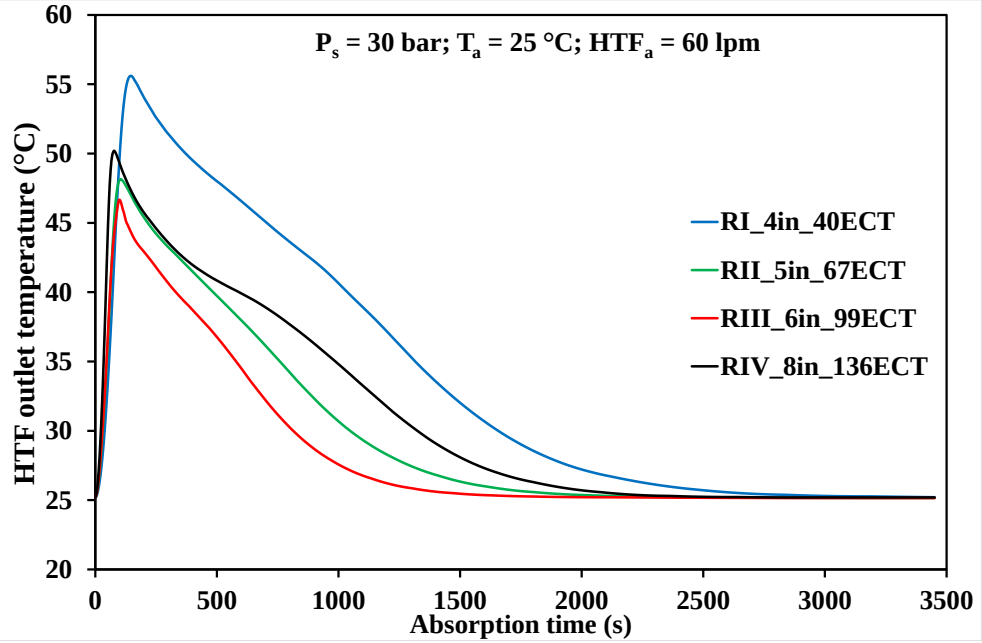

Fig.5.15. Effect of reactor geometry on variation of heat transfer fluid outlet temperature

Interestingly, the rate of decrease in HTF outlet temperature of RIV_8in_136ECT is similar to that of RII_5in_67ECT until about 440 s. Beyond this, the rate of decrease is slower due to larger radius of model causing delayed evolution of absorption heat in regions near periphery of model. HTF outlet temperature of this model attains a peak value of 50.2 °C and requires 1568 s for cooling down to 27 °C. Compared to all these models, HTF outlet temperature of RIII_6in_99ECT model attains a peak of 46.5 °C which reduces to 27 °C within 1001 s. This is a reduction of 47.3% in duration in comparison to RI_4in_40ECT. RIII_6in_99ECT shows better heat transfer and is able to liberate the generated heat of absorption faster than other models. This leads to robust hydriding kinetics which is the ultimate objective of the designed models. Additionally, it can be inferred that increasing the diameter or length of the model beyond the dimensions of these 4 reactor models would further reduce the hydriding performance. Based on the hydriding performance, RIII_6in_99ECT model is selected for further parametric investigations.

5.3.4 Parametric investigation on RIII_6in_99ECT model

Effect of hydrogen supply pressure (P_s):

In order to understand the effect of varying hydrogen supply pressure (P_s) on T_{Vavg} and HSC, P_s is varied from 5 bar to 35 bar in steps of 5 bar while absorption temperature and water flow rate is maintained at 25 °C and 30 lpm, respectively. As portrayed in Fig.5.16, varying P_s is having phenomenal effects on the rate of heat transfer and absorption kinetics of RIII_6in_99ECT that contains 50 kg of $LaNi_{4.7}Al_{0.3}$. From the absorption reaction rate equation, it is understood that the rate of absorption depends primarily on the pressure gradient (P_{grad}) between supply pressure (P_s) and equilibrium pressure (P_{eq}). At 5 bar supply pressure, P_{grad} is just 2.9 bar. However, increasing P_s to 10, 15, 20, 30 and 35 bar, respectively leads to P_{grad} of 7.3, 11.4, 15.1, 18.7, 22.4 and 26.1 bar, which in turn results in larger driving force for absorption reaction. At P_s of 5 bar, T_{Vavg} attains a peak value of 65.3 °C and requires 2720 s for

cooling down to 27 °C. Meanwhile, the reactor attains a HSC of just 0.72 wt% even after an absorption time of 3450 s, depicting slower reaction kinetics.

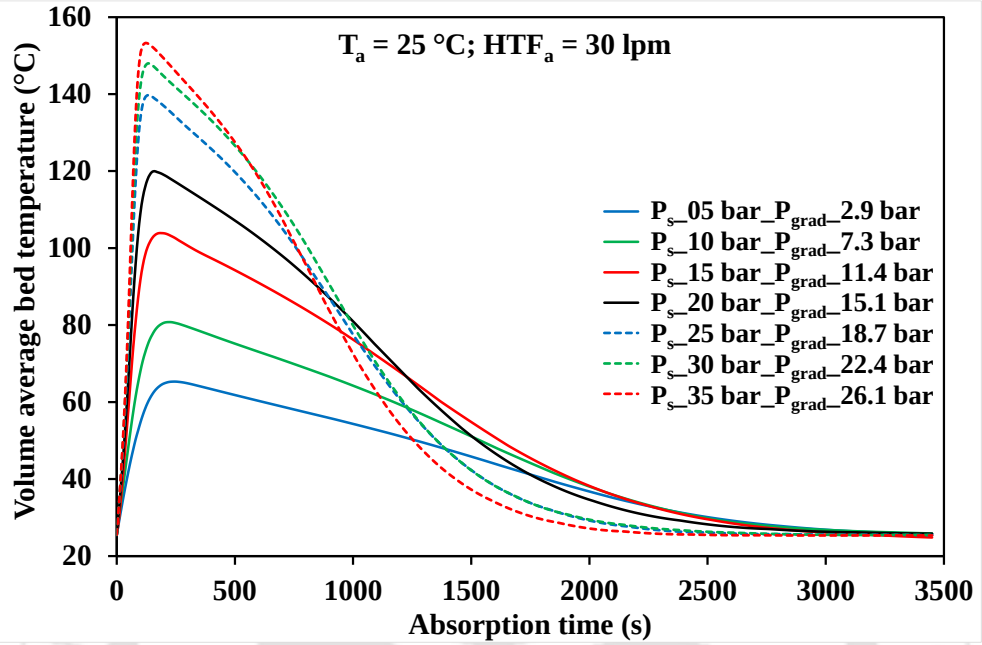

Fig.5.16. Effect of hydrogen supply pressure (P_s) on variation of volume average bed temperature

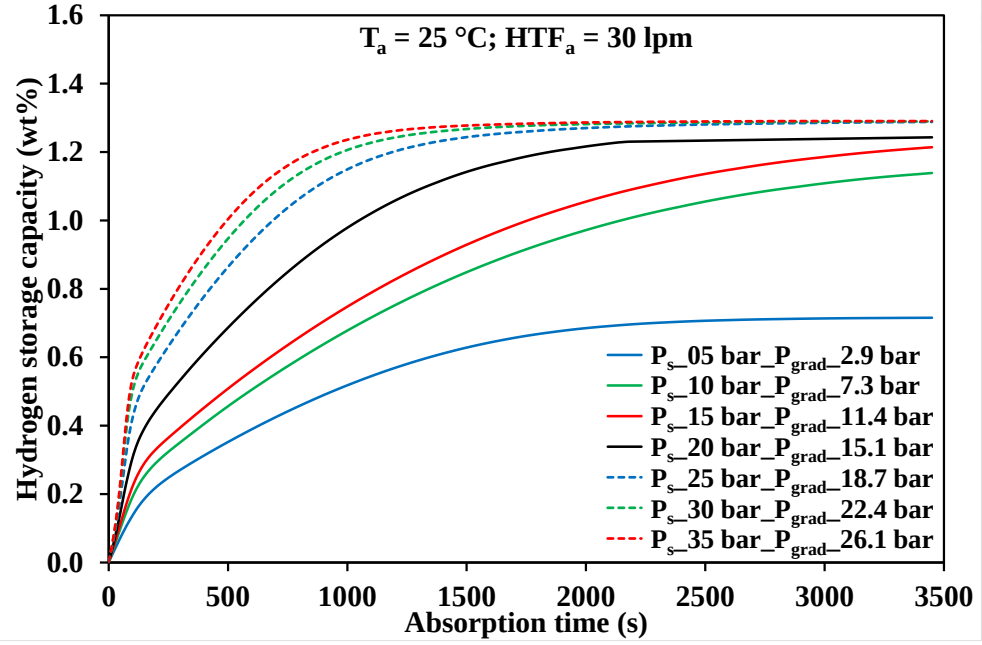

Fig.5.17. Effect of hydrogen supply pressure (P_s) on hydrogen storage capacity

Increasing the supply pressure to 10 bar and 15 bar, respectively yields a HSC of 1.14 wt% and 1.21 wt%. When P_s is further increased to 20 bar, HSC of 1.24 wt% is attained while T_{Vavg}

drops from 120 °C to 27 °C within 2600 s. It can be understood that increase in supply pressure up to 20 bar enhances HSC more than the rate of heat removal. Rapid reaction kinetics can be realized at supply pressure higher than 20 bar, wherein rapid reaction kinetics causes T_{Vavg} to attain higher peak value and in turn leads to faster heat transfer. For P_s of 25 bar, HSC is 1.28 wt% and peak value of T_{Vavg} is higher by 19.7 °C due to 23.8% increase in P_{grad} when P_s is increased from 20 bar to 25 bar. For this variation in P_s, time taken by T_{Vavg} for dropping down to 27 °C reduces by 22%. Further increase in P_s to 30 bar and 35 bar lead to HSC of 1.29 wt%, which demonstrates that P_s of 30 bar facilitates in achieving maximum absorption at the given supply condition. Though the peak T_{Vavg} is 153.2 °C at 35 bar which is 5.3 °C more than peak T_{Vavg} at 30 bar, MH bed in both cases cools down to 27 °C in about 2200 s depicting similar performance despite 17.9% increase in P_{grad}. This denotes saturation in absorption performance at P_s of 30 bar and hence, it is suitable for absorption of $LaNi_{4.7}Al_{0.3}$ in RIII_6in_99ECT.

Effect of absorption temperature (T_a):

To understand the effect of varying absorption temperature (T_a) on absorption kinetics, T_a is varied from 20 °C to 35 °C in steps of 5 °C while P_s is maintained at 20 bar and HTF flow rate is at 30 lpm. The absorption temperature is varied among this range considering various naturally available heat sinks and the wide range of driving potential offered by them. As it can be observed from Fig.5.18 and Fig.5.19 that the influence of absorption temperature (T_a) on T_{Vavg} and HSC, respectively is not as prominent as the effect of supply pressure. Within 160 s, T_a of 35 °C causes a peak T_{Vavg} of 121.4 °C while the same is just 2.6 °C less for T_a of 20 °C. Hence, hydriding rate is nearly same for different T_a during initial phase of reaction (Fig.5.19). However, lower T_a triggers slightly larger pressure gradient (P_{grad}) leading to better absorption kinetics. Owing to PCT characteristics of the alloy, average equilibrium pressure of the bed increases from 4.5 bar to 5.8 bar when T_a correspondingly increases from 20 °C to 35 °C. For T_a of 20 °C, T_{Vavg} of bed drops down to 37 °C within 1680 s while the P_{grad} was 15.5 bar. When

the T_a is increased to 25 °C, 30 °C and 35 °C, P_{grad} marginally reduces by 2.6%, 5.2% and 8.4%, respectively, which in turn causes 8.7%, 33.3% and 66.7% increase in the duration taken by T_{Vavg} of respective bed to attain 37 °C. This validates the fact that at lower T_a, P_{grad} is marginally higher leading to better heat transfer characteristics.

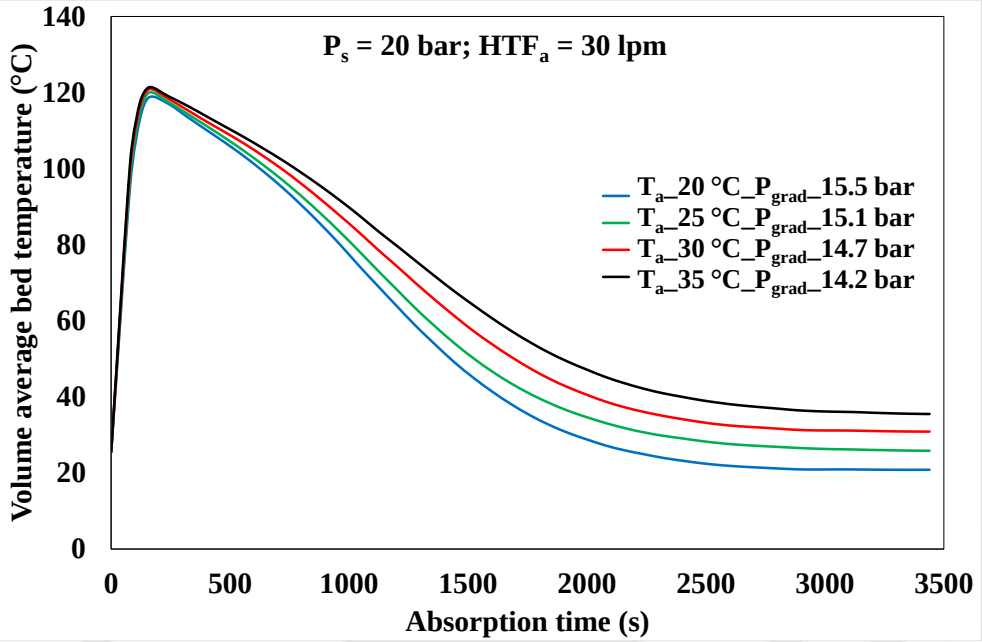

Fig.5.18. Effect of absorption temperature (T_a) on volume average bed temperature variation

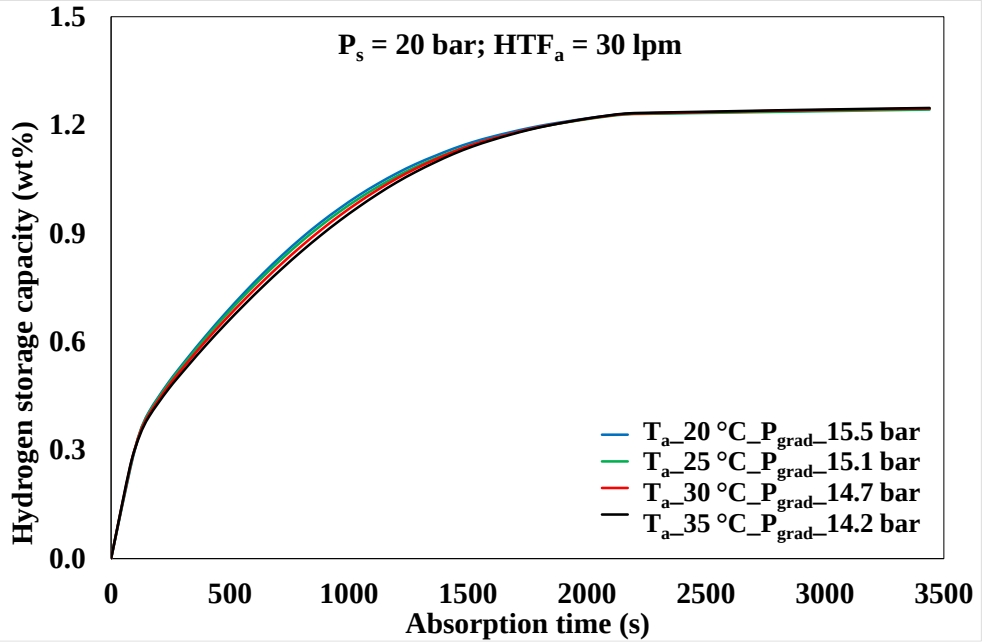

Fig.5.19. Effect of absorption temperature (T_a) on hydrogen storage capacity

Though total HSC of 1.24 wt% is achieved in all cases as P_s is 20 bar, hydriding rate is slightly better for T_a of 20 °C. Within 560 s, bed attains a HSC of 0.74 wt% for T_a of 20 °C. There was a comparative reduction of 1.1%, 2.6% and 4.5% in HSC attained within 560 s, when T_a is increased respectively to 25 °C, 30 °C and 35 °C. It is apparent that T_a has minimal influence on hydriding rate and HSC. Hence, the absorption of alloy can take place at ambient temperature, as it is less energy intensive to maintain.

Effect of HTF flow rate (HTF_a):

The flow rate of HTF (HTF_a) is also one of the parameters that significantly influences the absorption performance of the reactor. At a higher volumetric flow rate of water, the heat removal is faster which lead to larger pressure gradient and improved hydriding kinetics. The effect of HTF_a on the T_{Vavg} and HSC is presented in Fig.5.20 and Fig.5.21, respectively. At the absorption condition of 30 bar and 25 °C, HTF_a is varied from 10 lpm to 35 lpm in increments of 5 lpm. Within 140 s, a peak T_{Vavg} of 151 °C is attained for HTF_a of 10 lpm while for 35 lpm, it is 147.9 °C.

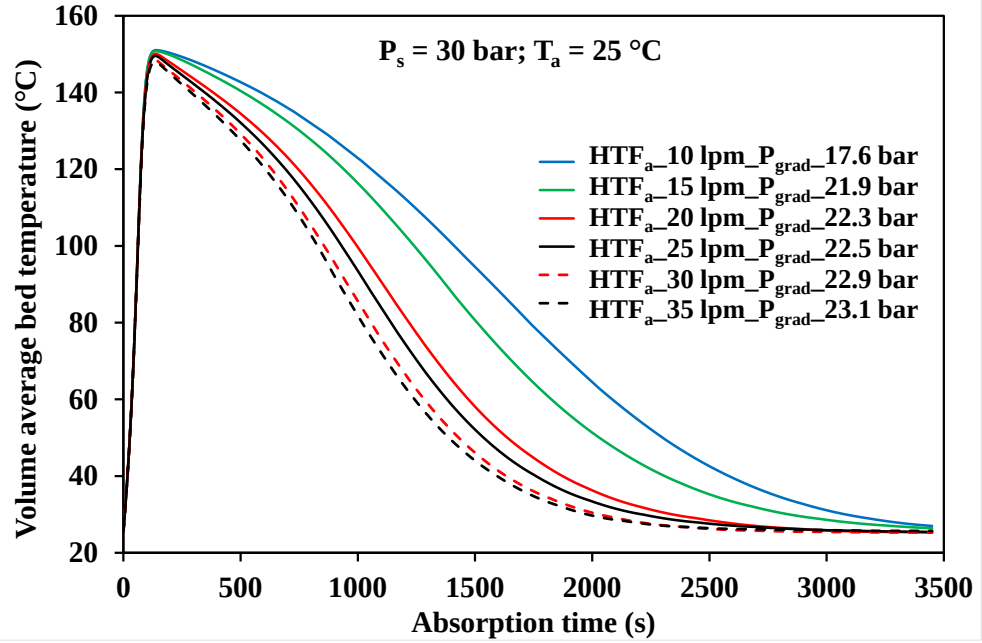

Fig.5.20. Effect of HTF flow rate (HTF_a) on variation of volume average bed temperature

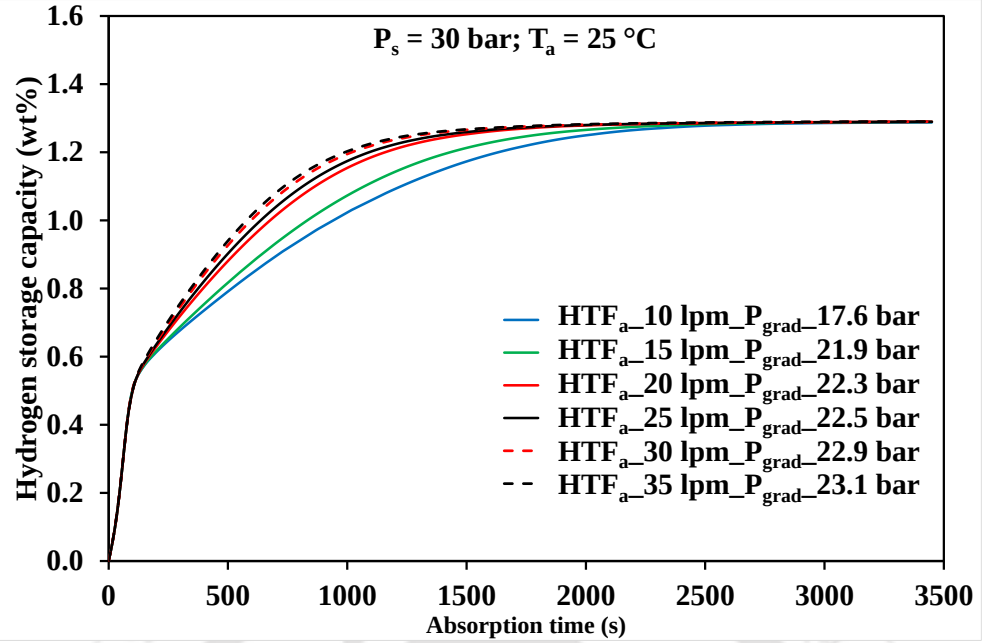

Fig.5.21. Effect of HTF flow rate (HTFa) on hydrogen storage capacity

HTF_a causes minuscule variation on peak T_{Vavg} attained as this temperature primarily depends on supply pressure. However, the rate of heat transfer from MH bed to HTF is highly influenced by HTF_a, which can be observed from the duration required by bed for dropping down to 27 °C. For HTF_a of 10 lpm, MH bed needs 3300 s while this duration reduces by 22.7%, 25%, 33.6% and 34.2% when HTF_a is increased to 15, 20, 25, 30 and 35 lpm, respectively. Although the maximum HSC of 1.29 wt% is achieved for different flow rate values, hydriding rate is rapid at higher HTF_a. HSC of 1.03 wt% is achieved within 1020 s, at HTF_a and P_{grad} of 10 lpm and 17.6 bar, respectively. Comparative reduction in absorption time of 11.7% and 28.4% is observed when HTF_a is correspondingly increased to 15 lpm and 20 lpm causing respective increase in P_{grad} to 21.9 bar and 22.3 bar. For HTF_a of 25 lpm, duration of 690 s is required by the MH bed to attain 1.03 wt%. Increasing HTF_a further to 30 lpm and 35 lpm results in achieving 1.03 wt% within 640 s and 620 s, respectively. It can be observed that HTF_a of 30 lpm and 35 lpm portrays similar hydriding kinetics as their driving potential is nearly equal. Hence, water flow rate of 30 lpm is suitable for better hydriding kinetics of RIII_6in_99ECT as it achieves 80% of HSC in 37.3% less duration than at HTF_a of 10 lpm. Having established

the improved performance characteristics of designed ECT reactors, the experimental investigation into MH based cooling systems implementing these reactors have been discussed further.

5.4 Experimental investigation on the performance of lab scale MHHSCS (Open cycle)

Operating conditions play an important role in controlling the performance of MH based thermal systems. In order to assess the effect of different operating parameters on the charging/discharging characteristics of the MH bed, parametric study has been conducted on 55 ECT reactor filled with 4 kg of $MmNi_{4.7}Fe_{0.3}$. For absorption study, the supply pressure was varied from 10 to 70 bar in steps of 10 bar, while the HTF temperature was maintained at 25 °C with a flow rate of 24 lpm. Further, to study the significance of absorption temperature, it was varied from 5 °C to 25 °C in steps of 5 °C with a constant HTF flow rate of 15 lpm while maintaining the hydrogen supply pressure constant at 40 bar. The amount of hydrogen absorbed and the bed temperature variation were analysed to compare the absorption performance. During the desorption study, at HTF flow rate of 15 lpm, the desorption temperature was varied from 5 °C to 30 °C while the reactor was desorbed to a constant pressure collection chamber maintained at 1 bar. In order to compare the effect of desorption temperature, the amount of hydrogen absorbed in the reactor before desorption study was fixed at 50 g. Along with the amount of hydrogen desorbed and the bed temperature variation, the cooling produced during the desorption cycle was also analysed.

Effect of varying hydrogen supply pressure on absorption performance:

As depicted in Fig.5.22 (a) and (b), the supply pressure (P_s) played a very prominent role in the amount of hydrogen absorbed and in the average bed temperature variation. For a supply pressure (P_s) of 10 bar, the amount of hydrogen absorbed was very less, i.e. 3.929 g in 32 s, which amounted to just 0.098 wt%. On increasing the supply pressure (P_s) further to 20 bar, 30 bar, 40 bar, 50 bar and 60 bar, the amount of hydrogen absorbed was reached to 5.1763 g

(0.13 wt%), 6.5771 g (0.16 wt%), 14.1548 g (0.36 wt%), 23.7296 g (0.59 wt%) and 28.0845 g (0.70 wt%), respectively in corresponding half cycle duration of 52 s, 84 s, 362 s, 586 s and 700 s. This signifies gradual improvement in the absorption capacity of the alloy with increasing supply pressure.

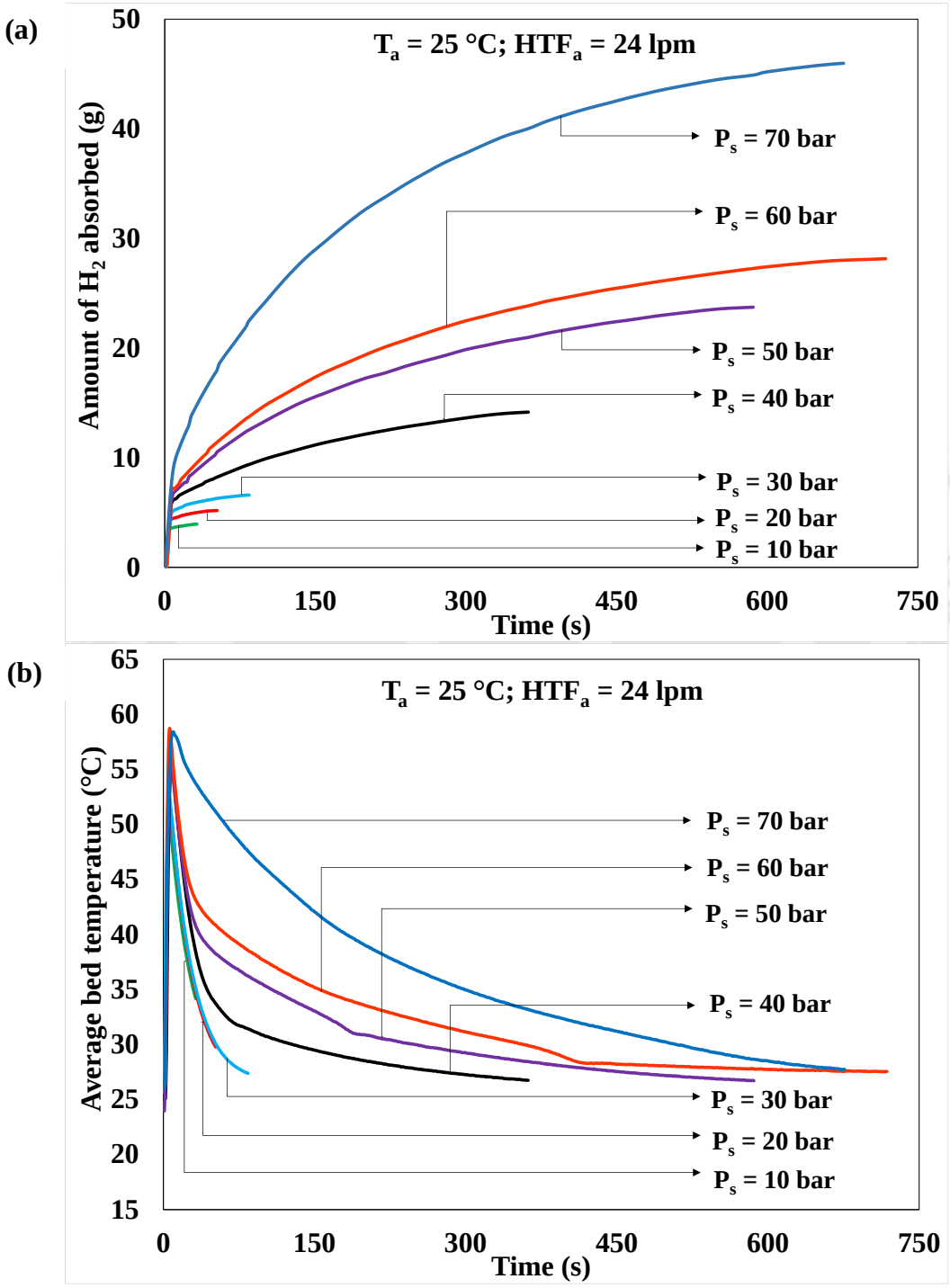

Fig.5.22. Variation in (a) amount of hydrogen absorbed and (b) average bed temperature by varying supply pressure during absorption

For P_s = 70 bar, a very significant lift in the hydrogen storage capacity was observed. Within 676 s, 45.984 g (1.15 wt%) of hydrogen was absorbed and the bed attained a peak temperature of 57.8 °C in just 7 s. The significant improvement in the absorption kinetics with increase in the H_2 supply pressure is due to the potential increase in the pressure gradient in between equilibrium bed pressure of MH alloy and the supply pressure, which indeed acts as the driving force for the boost up in the hydriding rate. Though the hydrogen absorption is significant at higher supply pressure, the parameter is not increased beyond 70 bar considering the operational feasibility and structural stability of the system.

Effect of varying temperature on absorption performance:

Similar to supply pressure, variation of absorption temperature (T_a) also plays a decisive role on the absorption kinetics of the chosen alloy, as observed from Fig.5.23 (a) and (b). The experiments were conducted at a fixed H_2 supply pressure (P_s) of 40 bar and varying absorption temperature (T_a) from 5 °C to 25 °C in a step of 5 °C. For higher absorption temperature, the amount of hydrogen absorbed and rate of absorption were very low. This is because of the lesser pressure gradient between the supply pressure (P_s) and equilibrium bed pressure at higher temperature for the present MH alloy. However, as the absorption temperature decreased, a substantial improvement in the absorption kinetics was observed. At 25 °C of absorption temperature (T_a), 10.979 g (0.27 wt%) of hydrogen was absorbed in 242 s, with the bed attaining a peak temperature of 56.3 °C in just 8 s. Further, when the absorption temperature (T_a) was decreased to 20 °C, 15 °C, 10 °C and 5 °C, the respective amount of hydrogen absorbed increased to 16.905 g (0.42 wt%), 28.342 g (0.71 wt%), 36.89 g (0.71 wt%) and 41.664 g (1.03 wt%) in corresponding durations of 442 s, 698 s, 792 s and 756 s. The improvement in the absorption performance at lower temperature is because of the lower equilibrium pressure of bed. Thus, lowering of equilibrium bed pressure at lower absorption temperature resulted in higher pressure gradient between the supply pressure and equilibrium

bed pressure, which finally led to rapid absorption kinetic of the MH bed. Though absorption is commendable at lower absorption temperature, maintaining it in the practical applications might prove to be energy intensive.

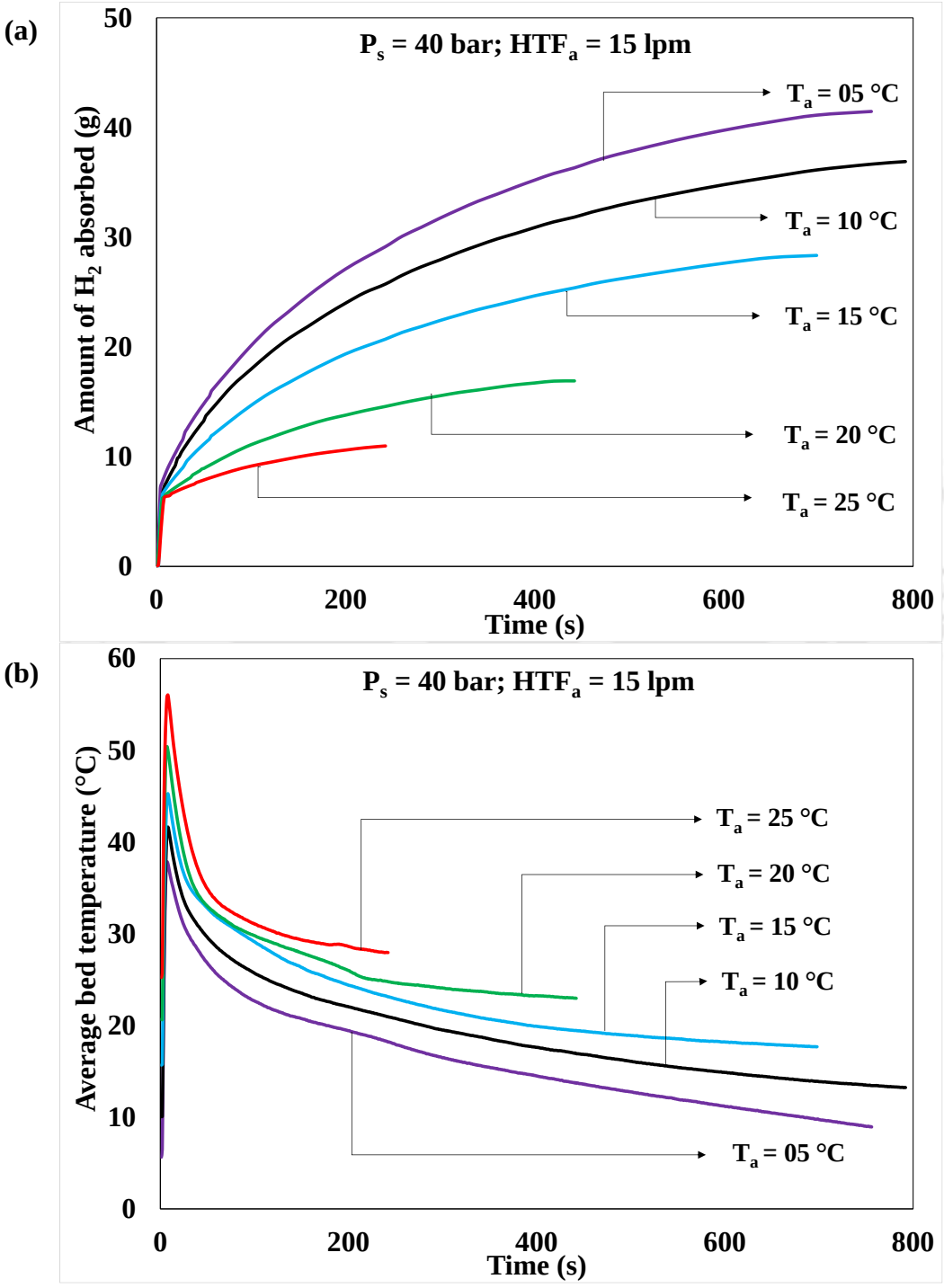

Fig.5.23. Variation in (a) amount of hydrogen absorbed and (b) average bed temperature by varying absorption temperature

Effect of varying temperature on desorption performance:

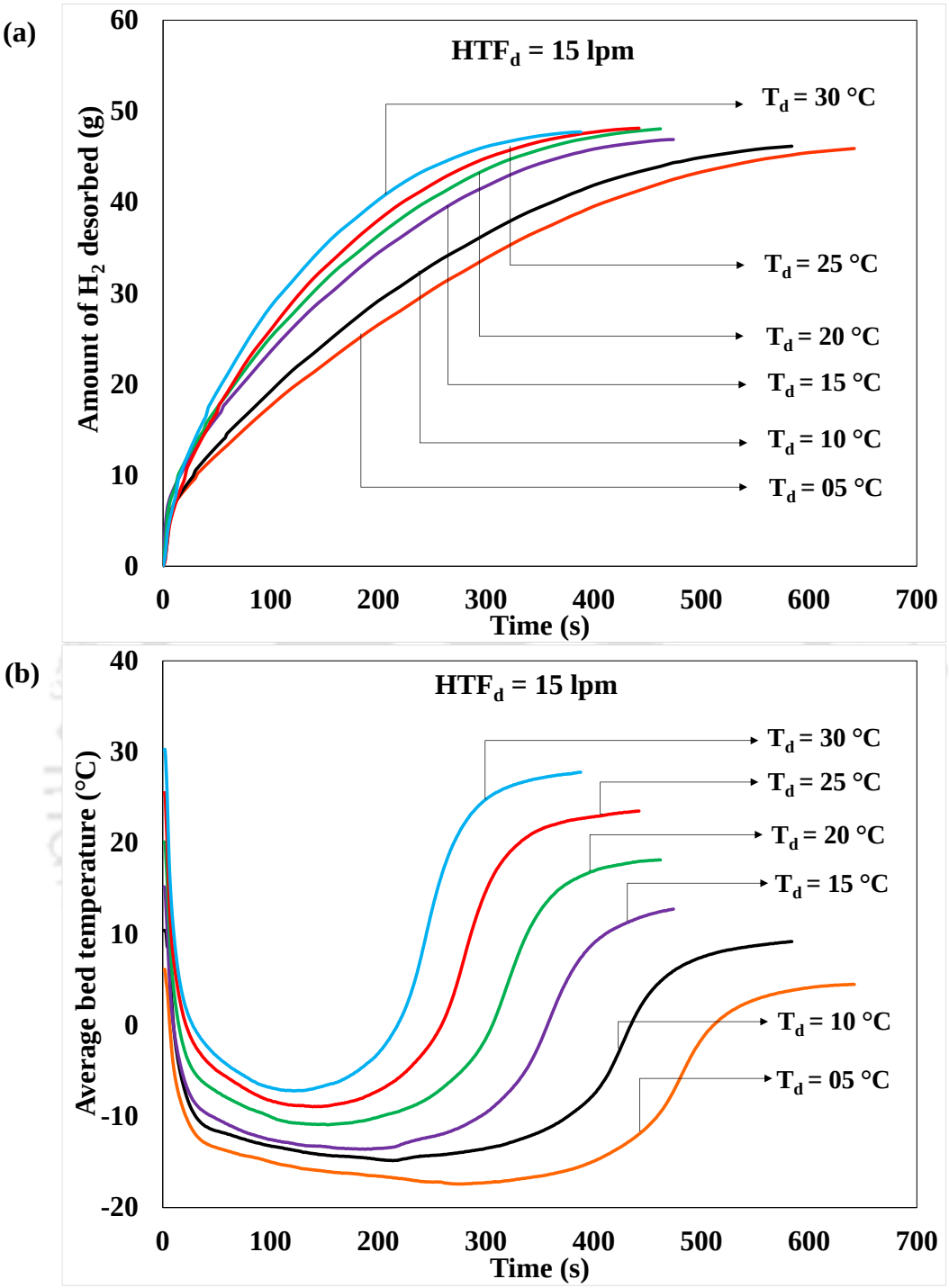

Fig.5.24. Variation in (a) amount of hydrogen desorbed and (b) average bed temperature by varying desorption temperature

The desorption half cycles were performed for fixed amount of hydrogen absorbed in the bed i.e. 50 g, and the desorbed hydrogen was released to collection chamber maintained at 1 bar. During desorption, supply of heat to the MH bed through the HTF, results in elevated

equilibrium pressure of the bed, and the pressure gradient between this equilibrium bed pressure and the outlet pressure leads to faster desorption rate of hydrogen, when the valve to the collection chamber is opened. The noteworthy desorption characteristics of this alloy in 55 ECT reactor is the highlight of this investigation. As depicted in Fig.5.24 (a) and (b), for fixed absorption of 50 g, the reversibility of the alloy was appreciably near 96% for desorption temperature (T_d) in the range of 20 °C to 30 °C. There was a slight decrease in the reversible desorption characteristics of the alloy at 5 °C, 10 °C and 15 °C, wherein the respective amount of desorbed hydrogen was 45.896 g, 46.162 g and 46.894 g.

The rate of desorption decreased at lower temperature due to the reduced pressure gradient between bed and collection chamber. The rapidity of the desorption reaction is evident from the half cycle time which was observed to be 642 s, 584 s, 474 s, 462 s, 442 s and 388 s respectively at the desorption temperature of 5 °C, 10 °C, 15 °C, 20 °C, 25 °C and 30 °C. The appreciable cooling effect that is produced during the desorption is due to the endothermic heat removed from the bed and HTF. The heat removal in MH bed can be observed from the prominent drop in average bed temperature depicted in Fig.5.24 (b). The bed temperature dropped to -17.4 °C in 274 s when HTF was supplied at 5 °C and the HTF flow rate was 15 lpm. However, when the HTF was supplied at 30 °C there was a temperature drop of 37.2 °C within 123 s. This significant temperature drop in the bed is because to the faster desorption kinetics caused due to the significant pressure gradient between the equilibrium bed pressure and the desorption environment of 1 bar.

Effect of desorption temperature on cooling effect produced:

The amount of cooling produced and rate of cooling at different desorption temperature have been represented in the Fig.5.25 (a) and (b). It can be observed that the cumulative cooling effect produced in the temperature range of 15 °C - 30 °C is admirable in the range of 450 kJ to 500 kJ. The details of the cooling produced is presented in Table 5.3. The net cooling

produced at desorption temperature of 15 °C, 20 °C, 25 °C and 30 °C were 453 kJ, 501 kJ, 493.1 kJ and 462.9 kJ respectively. Nearly 27.5% increase in cumulative cooling effect was observed when the desorption temperature was increased from 5 °C to 20 °C.

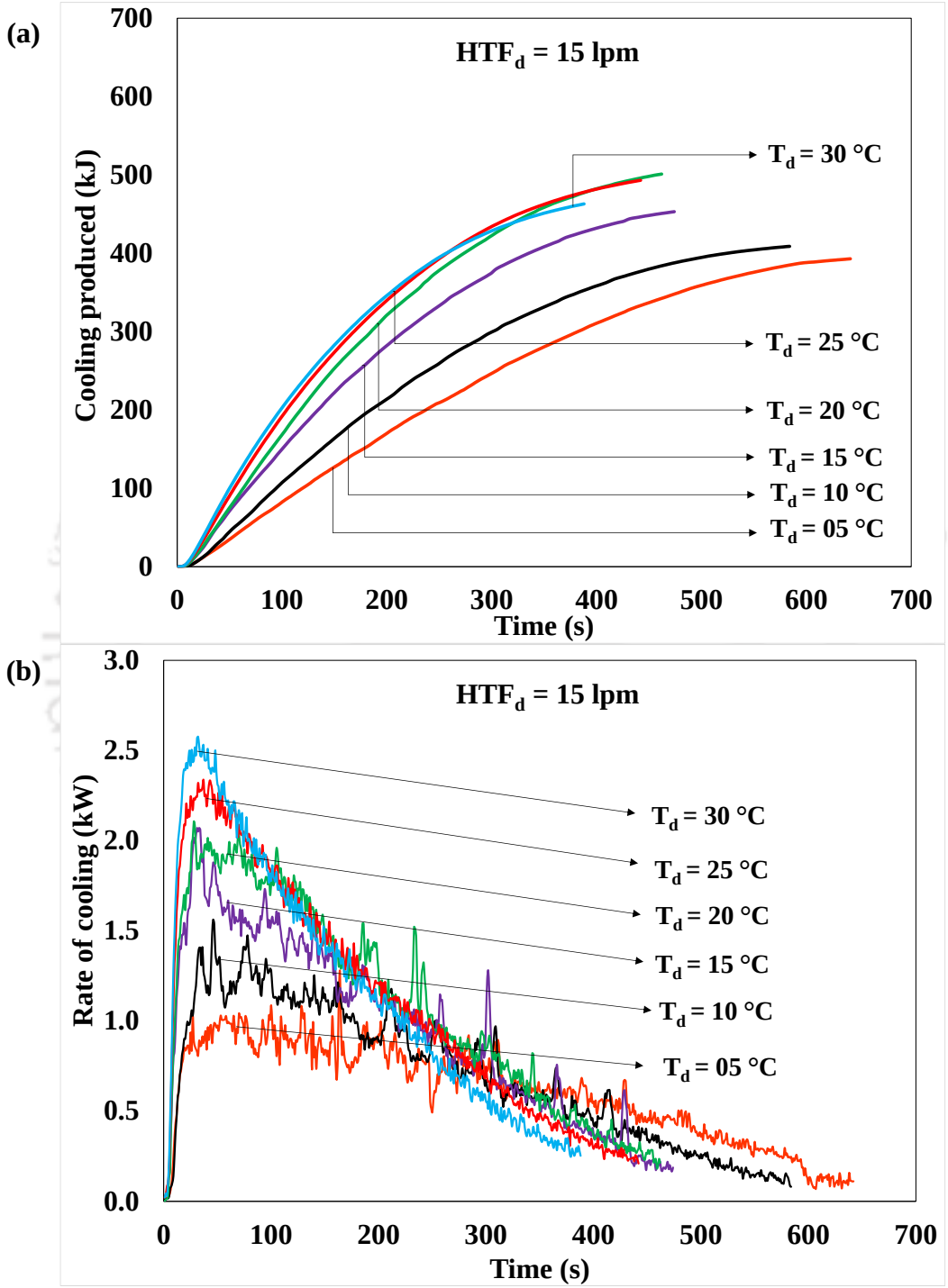

Fig.5.25. Variation in (a) cooling produced during desorption and (b) rate of cooling at different desorption temperature

At desorption temperature of 30 °C, the equilibrium bed pressure was comparatively higher, resulting in rapid desorption during initial 40 s. This rapid desorption further resulted in a higher peak cooling effect, as much as 2.6 kW. The average cooling rate was 1.2 kW while the desorption time was 388 s, which was 16% faster when compared to the duration at desorption temperature of 20 °C. Though the rate of desorption and cooling were higher, there was a slight decrease in the cumulative cooling obtained. With this, highly rapid desorption, the driving force had reduced towards the end of the reaction leading to 0.7% reduction in the amount of H_2 desorbed and 7.4% decrease in cumulative cooling effect.

It can be agreed that 462.9 kJ of cooling in 388 s is still an appreciable cooling performance at desorption temperature of 30 °C. Based on the cooling output and the alloy mass, specific cooling power (SCP) has been estimated. For 4 kg of $MmNi_{4.7}Fe_{0.3}$, the SCP varied from 153 W/kg of alloy to 298 W/kg of alloy, when desorption temperature was increased from 5 °C to 30 °C. Because of rapid cooling under these desorption conditions, dense ice formation on the reactor surface was observed during initial stabilisation of reactor system, before it was insulated. As depicted in Fig.5.26, this ice layer was observed after 180 s of the desorption half cycle, which had formed due to the condensation of atmospheric moisture coming in contact with outer surface of reactor during desorption.

Table 5.3. Cooling produced during desorption

Desorption Temperature (°C)	**Amount of hydrogen desorbed (g)**	**Time taken (s)**	**Cumulative cooling effect (kJ)**	**Peak rate of cooling (kW)**	**Specific cooling power (W/kg of alloy)**
5	45.896	642	393.0	1.3	153
10	46.162	584	408.9	1.6	175
15	46.894	474	453.0	2.1	239
20	48.063	462	501.0	2.1	271
25	48.139	442	493.1	2.3	279
30	47.729	388	462.9	2.6	298

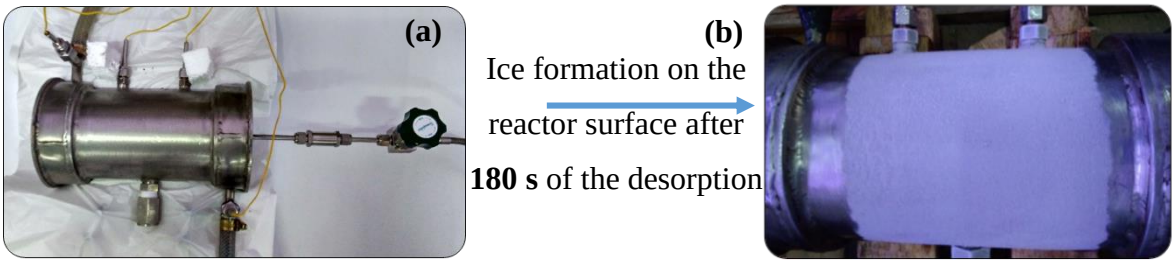

Fig.5.26. Pictorial view of reactor (a) before desorption and (b) after 180 s of desorption

Considering the excellent desorption characteristics of the $MmNi_{4.7}Fe_{0.3}$, this lab scale MHHSCS can be coupled with the fuel cell stack for delivering hydrogen at required rate with an added advantage of cooling the fuel cell stack. Similarly, it can be used for delivering hydrogen in a fuel cell powered automobile while simultaneously cooling the cabin space. The comparative performance of industrial scale MHHSCS has been discussed further.

5.5 Experimental investigation on the performance of industrial scale MHHSCS (Open cycle)

Based on the discussions drawn from the lab scale MHHSCS, it has been understood that the supply pressure plays a decisive role during absorption, while the desorption temperature influences the dehydriding performance. Hence, both these parameters have been varied during subsequent half cycle to study their effects on the performance.

Effect of varying hydrogen supply pressure on absorption performance:

The supply pressure was varied from 40 bar to 70 bar in steps of 10 bar while the bed was maintained at 5 °C through HTF flowing at 50 lpm. At supply pressure of 40 bar, 311.959 g of hydrogen was absorbed in 1763 s. With increase in supply pressure to 50, 60 and 70 bar, the corresponding improvement of 15.3 %, 23% and 30% were achieved in amount of hydrogen absorbed, as represented in Fig.5.27 (a). At 70 bar supply, 0.75 wt% was achieved within 364 s. However, for it to reach 1.02 wt%, duration of 1173 s was required. More than the limited absorption performance of the alloy, the cause for this reduction in rate is due to the supply cylinder. A commercial supply cylinder has about 420 g of hydrogen when fully filled, which

acted as an additional limiting factor. The enhanced rate of hydriding observed during initial 400 s has been reflected by the bed temperature variation as well, as represented in Fig.5.27 (b). The peak average bed temperature attained at supply pressure of 40 bar was 17.4 °C in 307 s. With increase in supply pressure, the peak increased while the time duration to attain the peak reduced considerably, depicting rapid absorption.

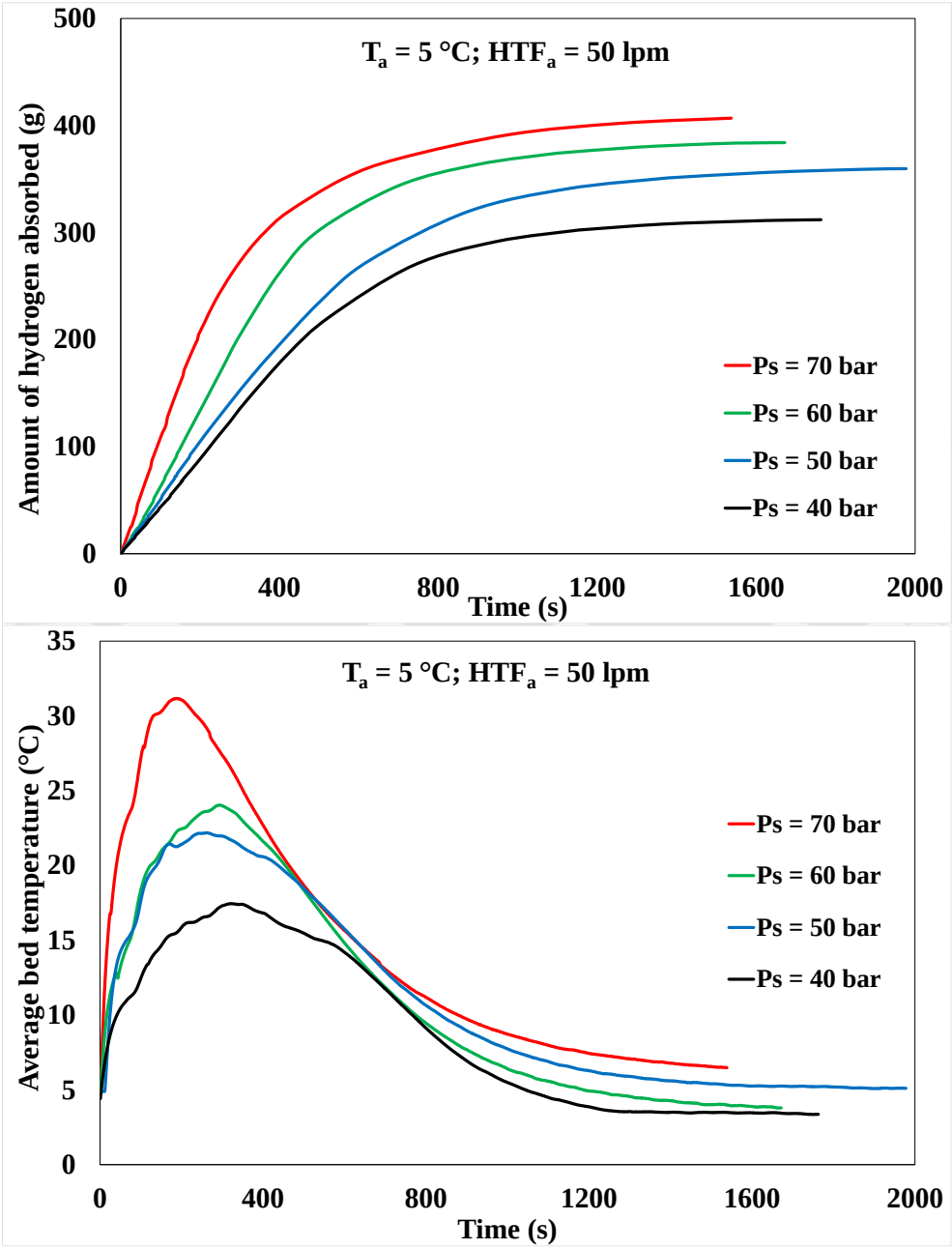

Fig.5.27. Variation in (a) amount of hydrogen absorbed and (b) average bed temperature by varying supply pressure during absorption of industrial scale model

The significant rate of temperature drop even in this industrial scale reactor reflects the enhanced heat transfer characteristics of the designed reactor. From peak temperature of 31.1 °C at 190 s, 20 °C drop in temperature was achieved within 800 s, which is considerably rapid for reactor of this scale. Even with absorption temperature as low as 5 °C, the absorption performance is curtailed by the alloy PCT characteristics.

Effect of varying temperature on desorption performance and cooling produced:

To understand the effect of desorption temperature on the dehydriding performance and the cooling obtained, the desorption pressure and HTF flow rate were fixed at 1 bar and 50 lpm, respectively while the desorption temperature was varied from 5 °C to 25 °C in steps of 10 °C. An absorbed hydrogen amount of 400 g (1 wt%) was ensured before each desorption cycle. At lower temperature of 5 °C and 15 °C, the dehydriding rate was comparatively lower than the lab scale model. At 5 °C, 336.045 g of hydrogen was desorbed in 4992 s, as represented in Fig.5.28 (a). The desorbed amount improved by 8.5 %, with 19% reduction in half cycle time at 15 °C. When the desorption was conducted at 25 °C, the desorption performance was comparatively remarkable. Within 2000 s, 0.75 wt% of hydrogen was desorbed and complete desorption was achieved in 3360 s.

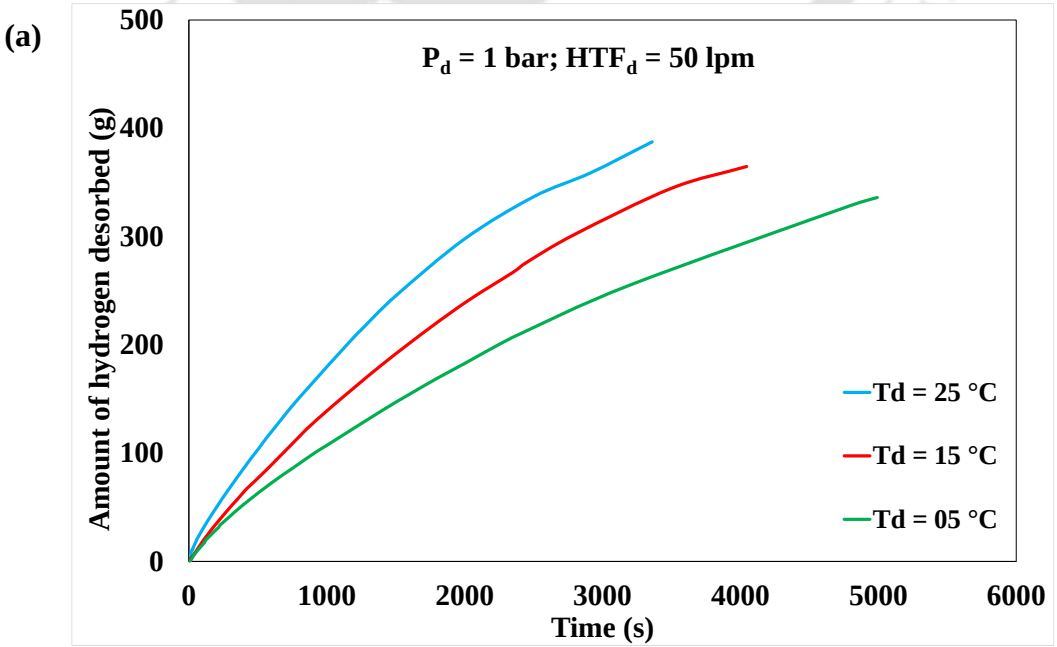

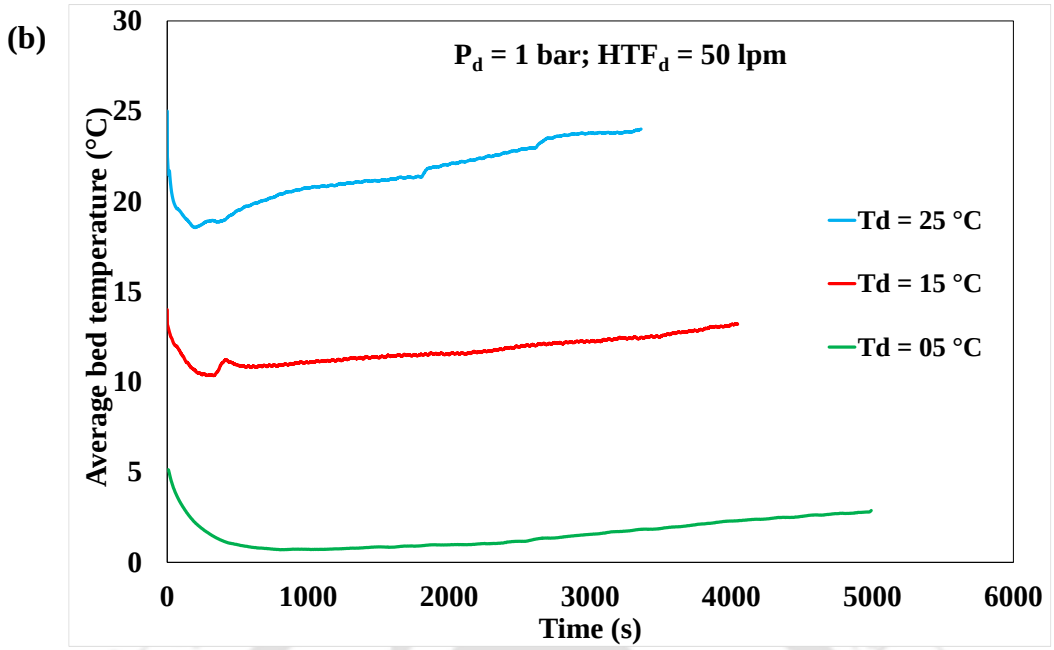

Fig.5.28. Variation in (a) amount of hydrogen desorbed and (b) average bed temperature by varying desorption temperature

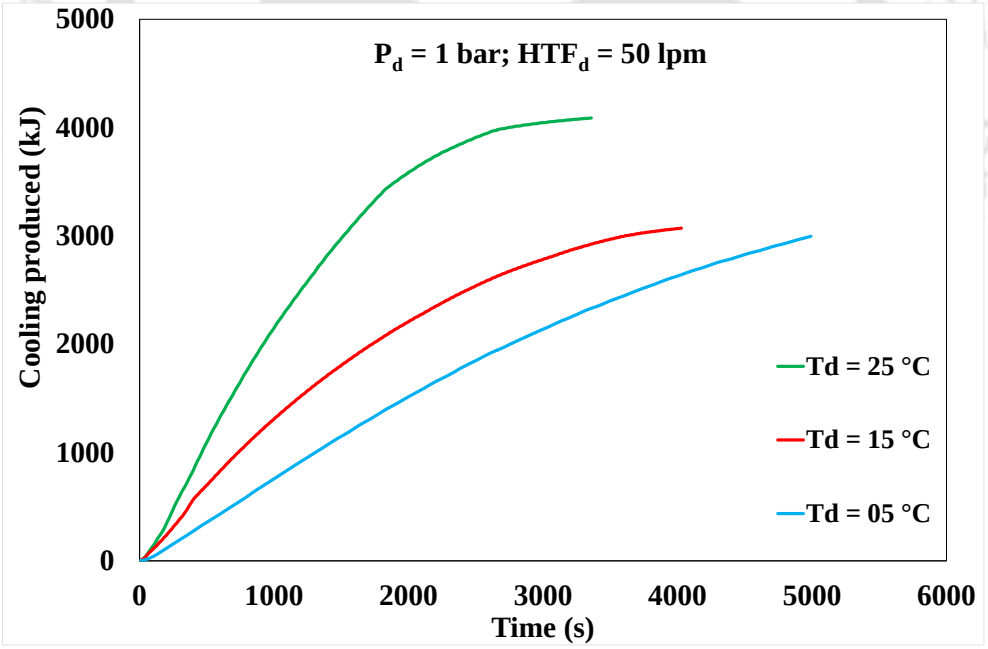

Fig.5.29. Variation in cooling produced during desorption at different desorption temperature

Overall the reversible storage capacity was 96% for 25 °C condition. As depicted in Fig.5.28 (b), the bed dropped 7.5 °C within 185 s, and the rate of average bed temperature increased towards desorption temperature was reasonably faster. The variation in the cooling effect at different desorption temperature has been represented in Fig.5.29. The system produced 2996.7

kJ and 3071.5 kJ of cumulative cooling at 5 °C and 15 °C, respectively. Due to the extended duration of half cycle time, the average peak cooling output was below 1 kW as well. However, 25 °C with flow rate of 50 lpm, the system achieved average cooling output of 1.2 kW with peak effect being as much as 3 kW attained at 413 s, as summarized in Table 5.4. Though the overall desorption and cooling performance of system of this large scale is appreciable at 25 °C, the scale or magnitude of the system results in an inherent limitation, despite the enhanced heat transfer characteristics of the designed system.

Table 5.4. Cooling produced by industrial scale metal hydride based hydrogen storage and cooling systems

Desorption Temperature (°C)	Amount of hydrogen desorbed (g)	Time taken (s)	Cumulative cooling effect (kJ)	Peak rate of cooling (kW)	Average rate of cooling (kW)
5	336.045	4992	2996.7	0.8	0.6
15	364.67	4045	3071.5	2.3	0.8
25	387.467	3360	4088.6	3.0	1.2

5.6 Experimental investigation on the performance of $LmNi_{4.91}Sn_{0.15}$ based CDMHCS (Closed cycle)

The performance of the formulated CDMHCS using two identical 60 ECT reactors, each filled with 2.75 kg of $LmNi_{4.91}Sn_{0.15}$ has been analysed to study the effects of various operating parameters that includes cycle time, cold fluid flow rate, and refrigeration and sink temperatures on the performance parameters in terms of coefficient of performance (COP), specific cooling power (SCP), total cooling load and amount of hydrogen transferred. The SCP value stated in CDMHCS is considering total mass of both alloys, unlike inn MHHSCS where only desorbing alloy has been considered.

Effect of cycle time:

The effect of cycle time variation on the COP, SCP and the amount of hydrogen transferred during one complete cycle has been represented in Fig.5.30 (a) and (b). At cold fluid flow rate

of 8 lpm, refrigeration temperature of 15 °C, sink temperature of 25 °C and cycle time of 4 min, the estimated values of COP and SCP values were 2.3 and 44 W/kg respectively.

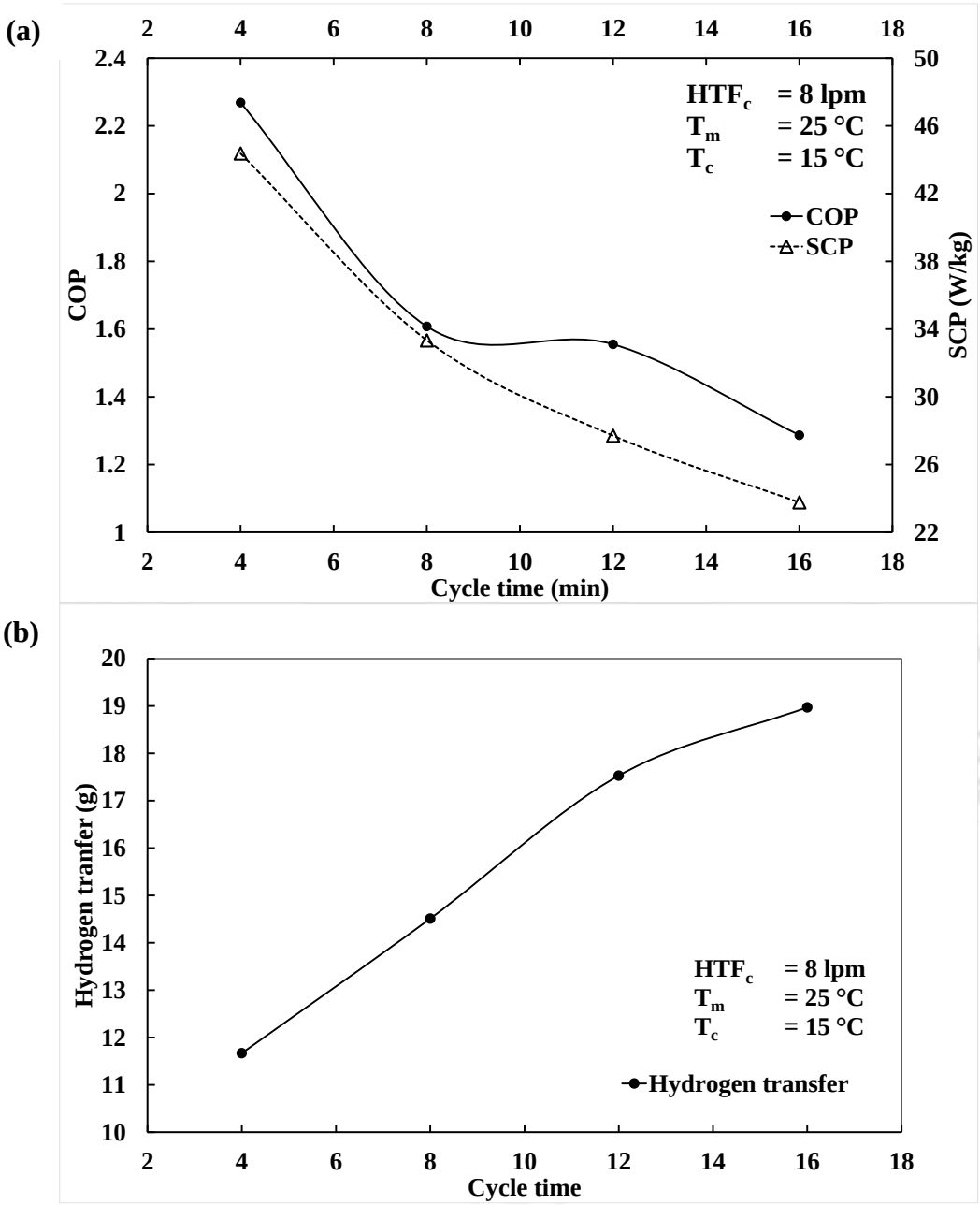

Fig.5.30. Effect of cycle time on (a) Coefficient of Performance and Specific Cooling Power, and (b) amount of hydrogen transferred

It was observed that the amount of H_2 transferred was found to increase by 63% with increase in cycle time from 4 min to 16 min. It is apparent that with increase in cycle time, the amount of hydrogen transfer would increase until complete desorption. However, the COP and SCP were found to reduce by 43% and 46%, respectively, for the same cycle time variation. With

increase in cycle time, the constant electrical power input being fed to the compressor reduces the COP and SCP values. Even though the hydrogen transfer was increasing with time, the rate of desorption reduced as is the nature of MH bed. It can be observed that cycle time above 8 min lead to significant reduction in COP and SCP, whereas, cycle time below 8 min resulted in ineffective hydrogen transfer. Hence, in the present investigations, 8 min (4 min half cycle time) was selected as reference cycle time for further investigations.

Effect of cold fluid flow rate:

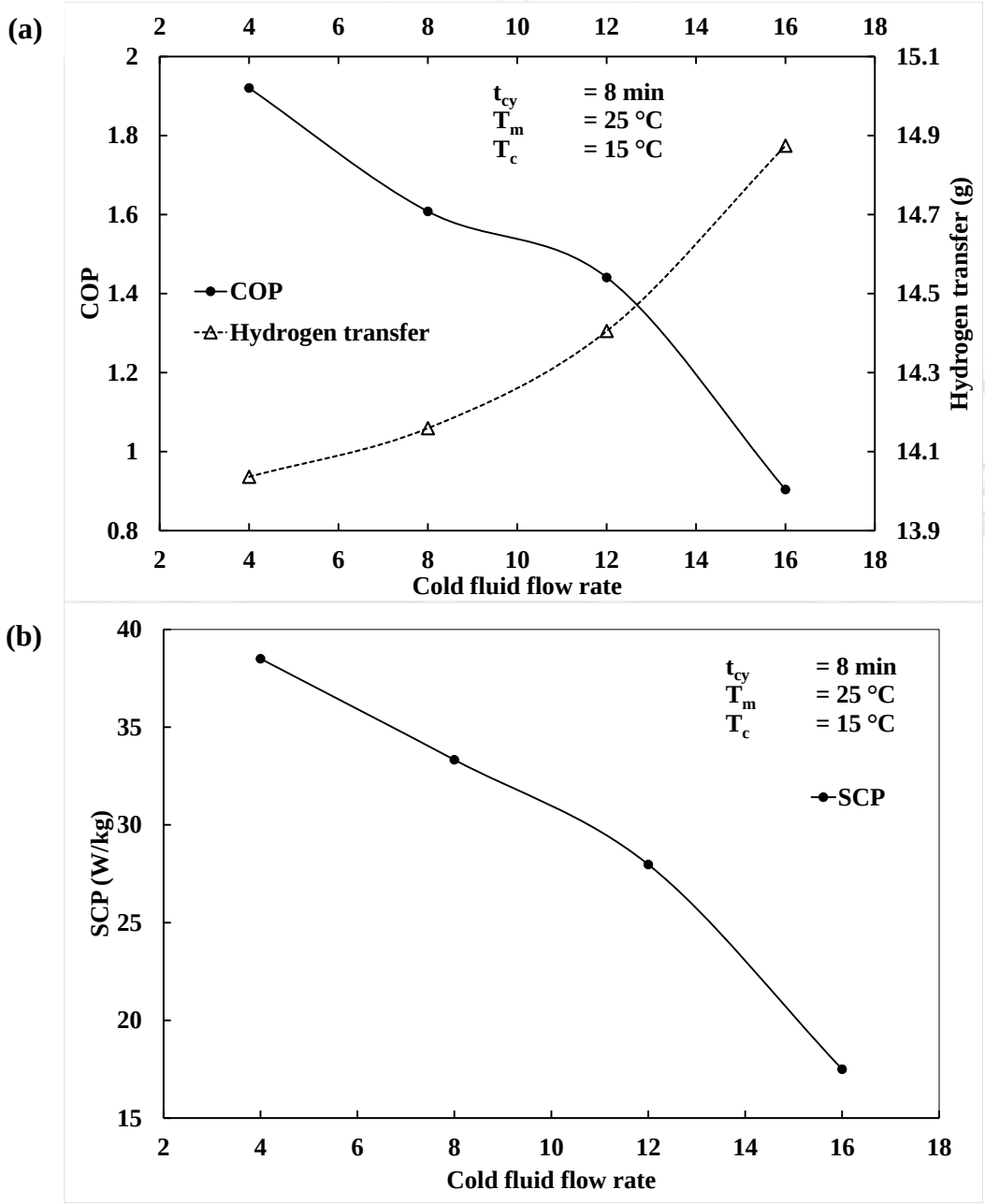

Fig.5.31. Effect of cold fluid flow rate on (a) Coefficient of Performance and amount of hydrogen transferred, and (b) Specific Cooling Power

With increase in cold fluid flow rate, both COP and SCP are reducing while the improvement in hydrogen transfer is marginal, as observed from Fig.5.31 (a) and (b). At the respective refrigeration and sink temperature of 15 °C and 25 °C, the maximum reported COP and SCP were 1.9 and 38.5 W/kg, at cold fluid flow rate of 4 lpm. With the increase in flow rate from 4 lpm to 16 lpm, the COP and SCP were found to decrease by 53% and 55%, respectively. The higher COP and SCP values at the lower fluid rate can be attributed to the larger temperature drop between the cold fluid inlet and outlet of the desorbing reactor. The amount of H_2 transferred increased by just 5% with increase in the cold fluid flow rate, indicating that cold fluid rate has lesser influence on the reaction kinetics. Ideally, the COP is expected to be high for higher fluid flow rates due to better heat transfer rate. However, due to the domination of internal MH bed heat transfer resistance, the rate of heat absorbed from the cooling fluid by the hydride was relatively less. For CDMHCS systems, it is advisable to operate the cold fluid at lower flow rate of 4 lpm to 8 lpm.

Effects of refrigeration and sink temperature:

(a)

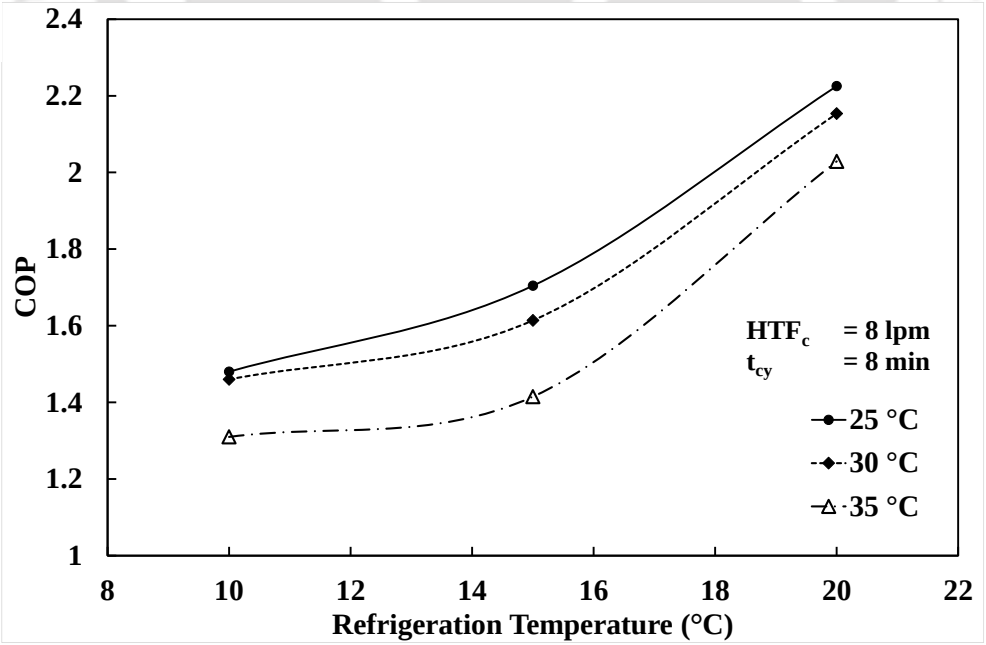

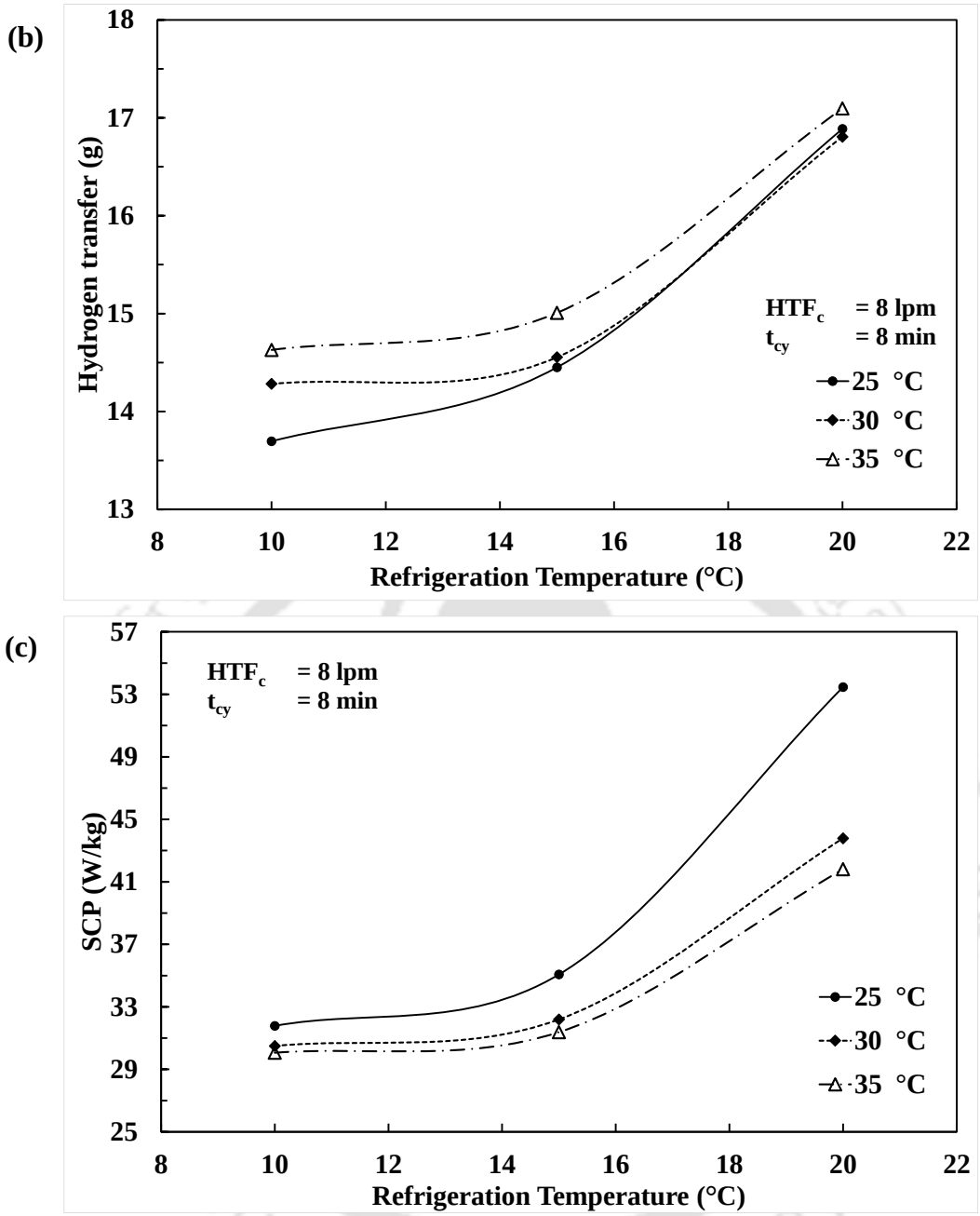

Fig.5.32. Effects of refrigeration and sink temperature on (a) Coefficient of Performance, (b) amount of hydrogen transferred and (c) Specific Cooling Power

To study the effects of refrigeration and sink temperature on the system performance, cold fluid flow rate and cycle time were fixed at 8 lpm and 8 min, respectively while the varying these temperatures. When refrigeration temperature was varied from 10 °C to 20 °C in steps of 5 °C with sink temperature fixed at 25 °C, the COP and SCP were found to increase from 1.4 to 2.3 and 32 W/kg to 54.5 W/kg, respectively, as represented in Fig.5.32 (a) – (c). The

ascending trend in COP and SCP were due to increase in the temperature gradient between the cold fluid and the reactor bed, which was the cause for better heat transfer. At sink temperature of 25 °C, 30 °C and 35 °C, the COP respectively increased by 50 %, 47.5% and 55% with increase in refrigeration temperature from 10 °C to 20 °C, indicating that better cooling effect and hydrogen transfer were obtained at higher refrigeration temperature. However, for a given refrigeration temperature, the COP was found to decrease to a maximum value of 18 %, when the sink temperature was varied from 25 °C to 35 °C. This is due to the fact that hydriding process in the absorbing reactor gets slower with increase in sink temperature, resulting in slower desorption kinetics.

At lower refrigeration temperature, owing to lower equilibrium bed pressure, the amount of hydrogen transferred between the coupled reactors was found to be low. With increase in refrigeration temperature, the increase in amount of H_2 transferred indicates better reaction kinetics, leading to favourable cooling effect. However, the variation in amount of H_2 transfer was between 1% and 7% with increase in sink temperature from 25 °C to 35 °C, indicating that the sink temperature variation has lesser influence on the amount of hydrogen desorbed.

(a)

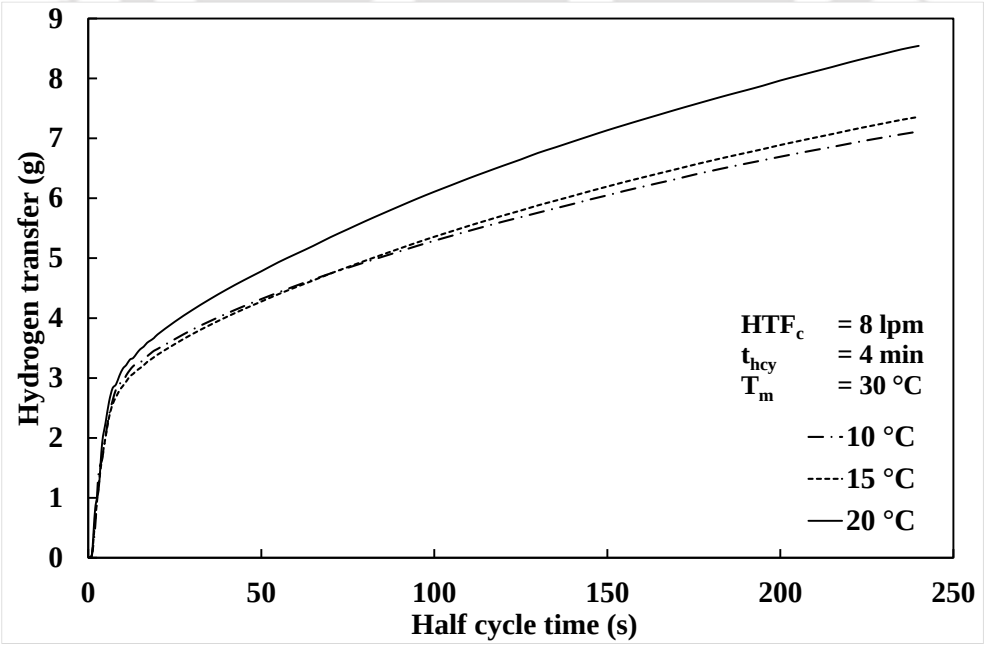

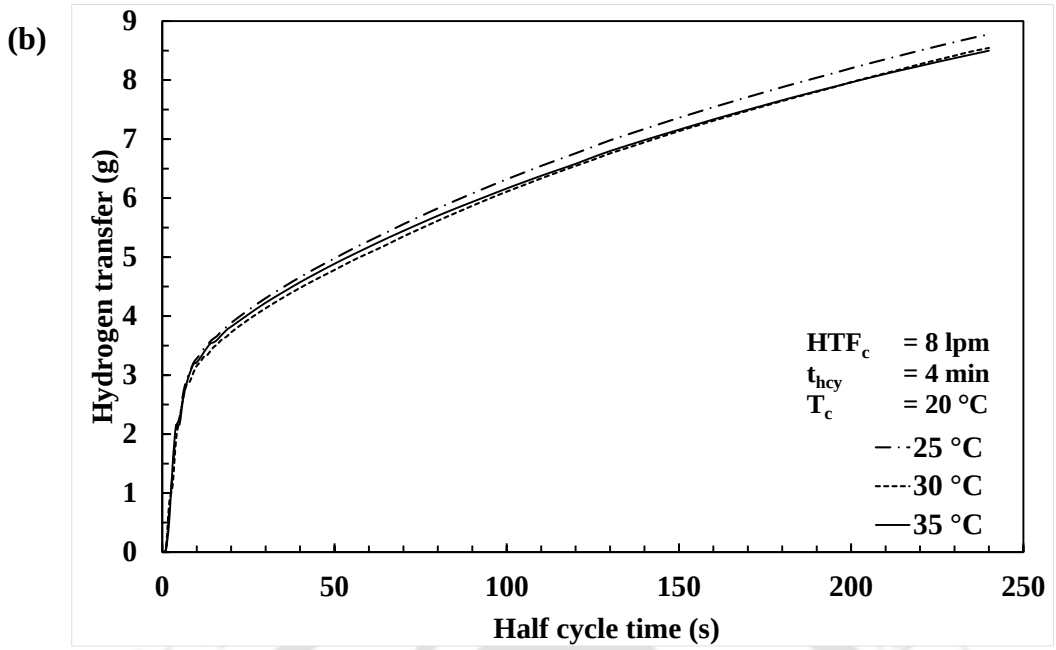

Fig.5.33. Cumulative hydrogen transfer in one half cycle time with different (a) refrigeration temperatures and (b) sink temperatures

The maximum COP and SCP were found to be 2.2 and 53.5 W/kg respectively at refrigeration and sink temperature of 20 °C and 25 °C. Reported value of COP is higher than those reported in literature (Park et al., 2002; Patel et al., 2013). The hydriding rate for one half cycle at different refrigeration and sink temperature have been represented in Fig.5.33. It was observed that the total amount of hydrogen transferred increased by about 20% with increase in refrigeration temperature from 10 °C to 20 °C. However, with increasing sink temperature from 25 °C to 35 °C, the reduction of 3% was observed in amount of hydrogen transfer, indicating that the effect of refrigeration temperature has greater influence than the sink temperature variation, on the system performance. Even though 32 g was initially absorbed by one reactor, the transfer during complete cycle was observed to be about 15 g only. This is due to the inherent thermal resistance in the bed and the PCT characteristics of the alloy which dictates the reversible storage capacity while being operated with the compressor.

Variation of hydride bed temperatures:

The variations of the average hydride bed temperatures of one reactor over three complete

cycles at different refrigeration and sink temperatures are respectively presented in Fig.5.34 (a) and (b).

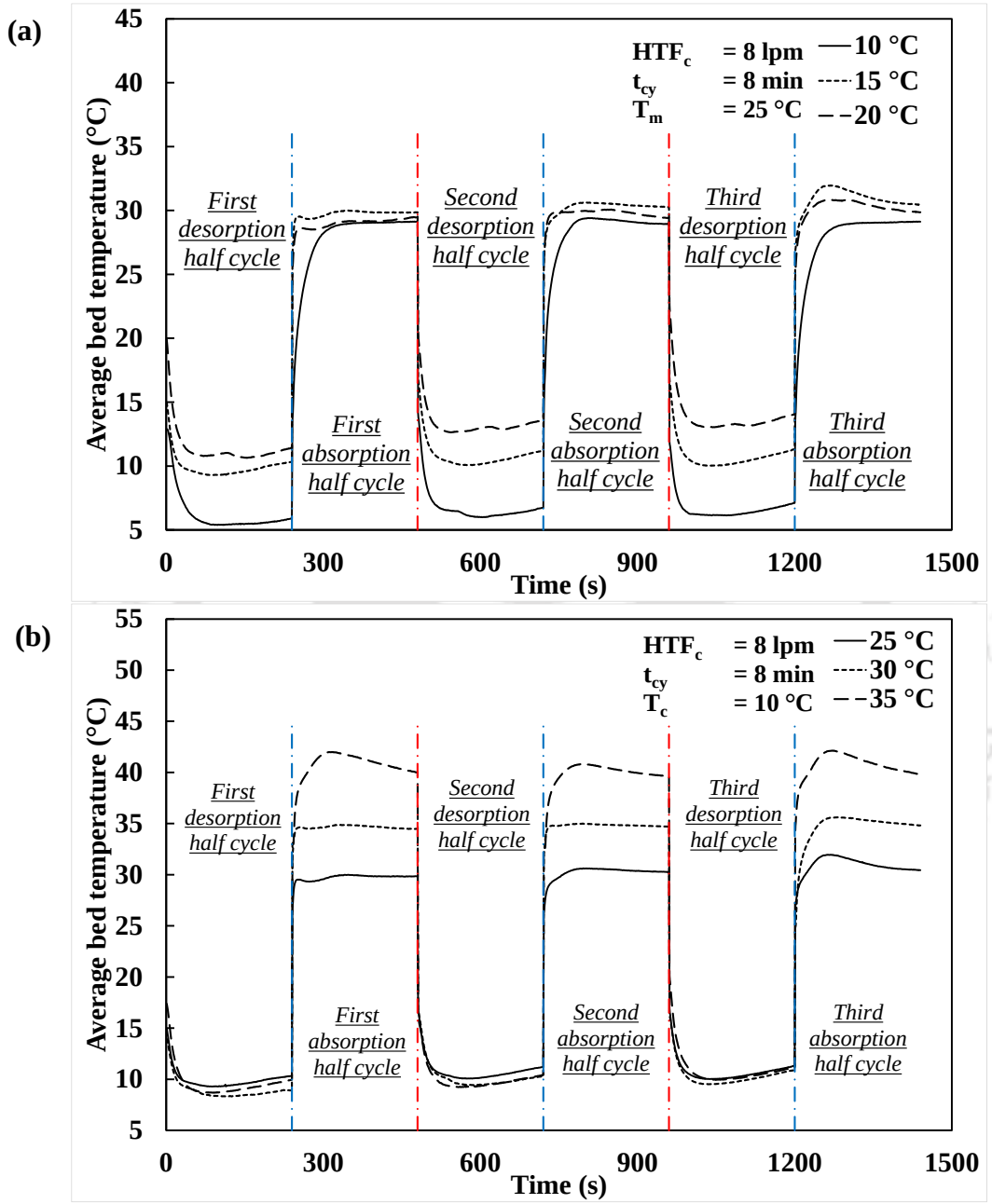

Fig.5.34. Variation of hydride bed temperature over three cycles with different (a) refrigeration temperature and (b) sink temperature

It can be observed that for any given refrigeration or sink temperature, the average bed temperature of the desorbing and absorbing reactor respectively dropped and increased rapidly during initial 20 s, indicating the existence of fast reaction kinetics during the

inception of the process. It was observed that the desorbing reactor bed temperature reduced to 6 °C for refrigeration temperature of 10 °C, whereas for 20 °C, the bed temperature dropped only to 13 °C. It is also evident that variation of sink temperature had minimum effect on the minimum hydride bed temperature achieved.

Reactor effectiveness:

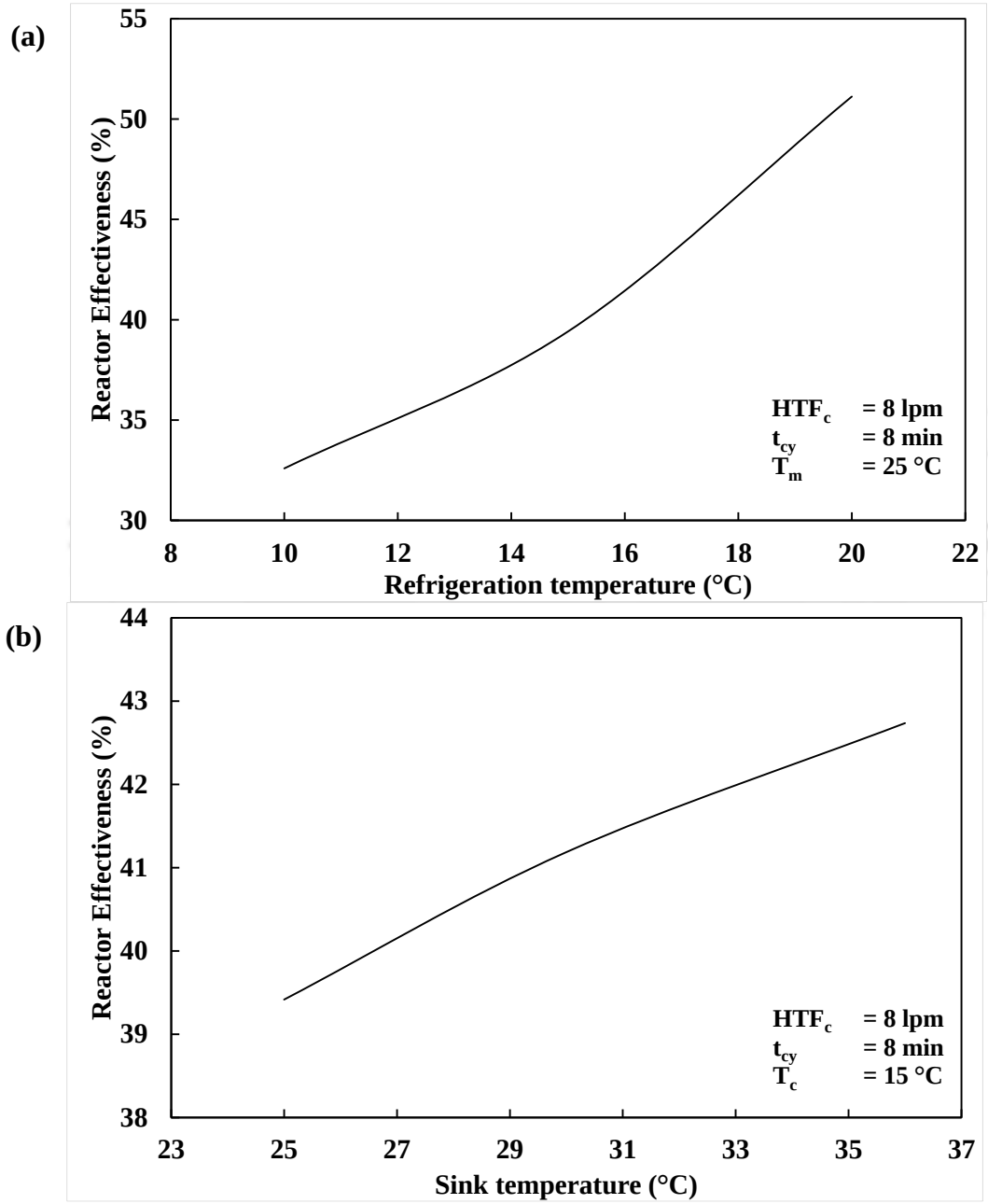

Fig.5.35. Reactor effectiveness for different (a) refrigeration temperature and (b) sink temperature

Effects of different refrigeration temperatures and sink temperatures on the reactor effectiveness for one complete cycle (8 min) are respectively presented in Fig.5.35. The reactor effectiveness depicted about 19% increase with increase in refrigeration temperature, while the increase was only about 3% with increasing sink temperature. Effect of refrigeration temperature on reactor effectiveness is comparatively significant due to increase in the temperature gradient between the cooling fluid and the reactor bed, which is the cause for greater amount of heat transfer.

Furthermore, the maximum value of reactor effectiveness was just above 50 %, which explains that only about 50 % of the cooling produced by the metal hydride bed is utilized by the HTF and the rest is utilized for cooling the reactor wall and metal hydride alloy. This indicates that there is a scope for COP and SCP improvement by enhancing the effective heat transfer between the hydride bed and the cooling fluid, and reducing the parasitic thermal mass of the reactor. The experimentally obtained high value of COP provides great promise for CDMHCS alternatives to conventional systems. The insights gathered from this investigation is advantageous in investigating the CDMHCS based on the newly synthesized alloy.

5.7 Experimental investigation on the performance of $La_{0.7}Ce_{0.1}Ca_{0.3}Ni_5$ based CDMHCS (Closed cycle)

With clearer understanding of CDMHCS from the previous investigation, $La_{0.7}Ce_{0.1}Ca_{0.3}Ni_5$ based CDMHCS was approached with a narrower focus towards performance investigation. The primary difference between both the alloys have been perceived to be their fundamental response towards absorption and desorption in CDMHCS. In case of $LmNi_{4.91}Sn_{0.15}$, the cooling performance was more prominent at lower cycle time as the initial pressure gradient between the bed and suction of compressor was more, which decreased with time leading to degradation in cooling performance. But in case of $La_{0.7}Ce_{0.1}Ca_{0.3}Ni_5$, a different behaviour has been observed. After implementing two identical 41 ECT reactors with OCJ in CDMHCS, half

cycles with complete transfer of hydrogen from one reactor to another was conducted. Upon stabilisation, it was observed that consistently around 45 g of hydrogen was exchanged between the reactors in each half cycle with a duration ranging between 35 to 40 min. This suggests a reversible transfer capacity of 1.2 wt% through the compressor. The HTF and bed temperature variation of MH bed during typical desorption has been depicted in Fig.5.36 (a).

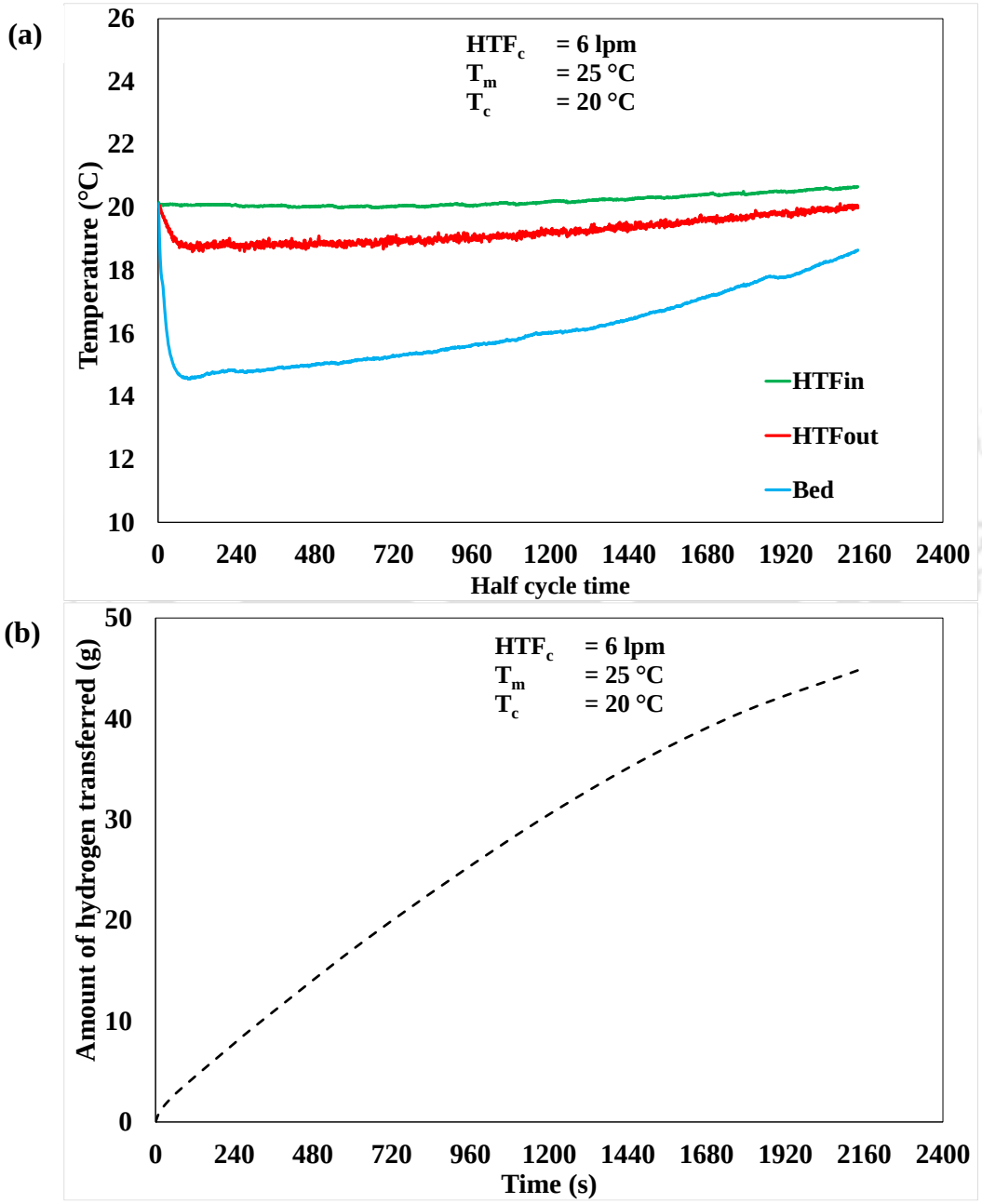

Fig.5.36. (a) Bed and heat transfer fluid temperature of desorbing bed, (b) and amount of hydrogen transferred during complete half cycle

The system was desorbed due to the driving force of compressor while cold fluid at 20 °C was flowing through the desorbing reactor at 6 lpm flow rate and the absorption temperature was 25 °C. As it can be observed, the bed temperature upon reducing to 14.5 °C, did not rapidly increase the HTF temperature of 20 °C. The rate of increase was observed to be steady, which was reflected in the dehydriding rate as well, as represented in Fig.5.36 (b). The rate of transfer was 0.046 g/s at 60 s which reduced subsequently 0.02 g/s by the end of 2140 s, wherein 44.801 g of hydrogen was transferred. This near steady rate of desorption is the primary reason behind the difference in cooling performance portrayed by $La_{0.7}Ce_{0.1}Ca_{0.3}Ni_5$ based CDMHCS.

Effect of cycle time:

To understand the effect of cycle time, the half cycle time was varied among 1 min, 2 min, 4 min, 5 min and subsequently incremented by 5 min till 35 min, while the refrigeration and sink temperature were respectively maintained at 20 °C and 25 °C, with fluid flowing at 6 lpm flow rate. The average COP and SCP obtained by varying the half cycle time has been represented in Fig.5.37 (a) and (b).

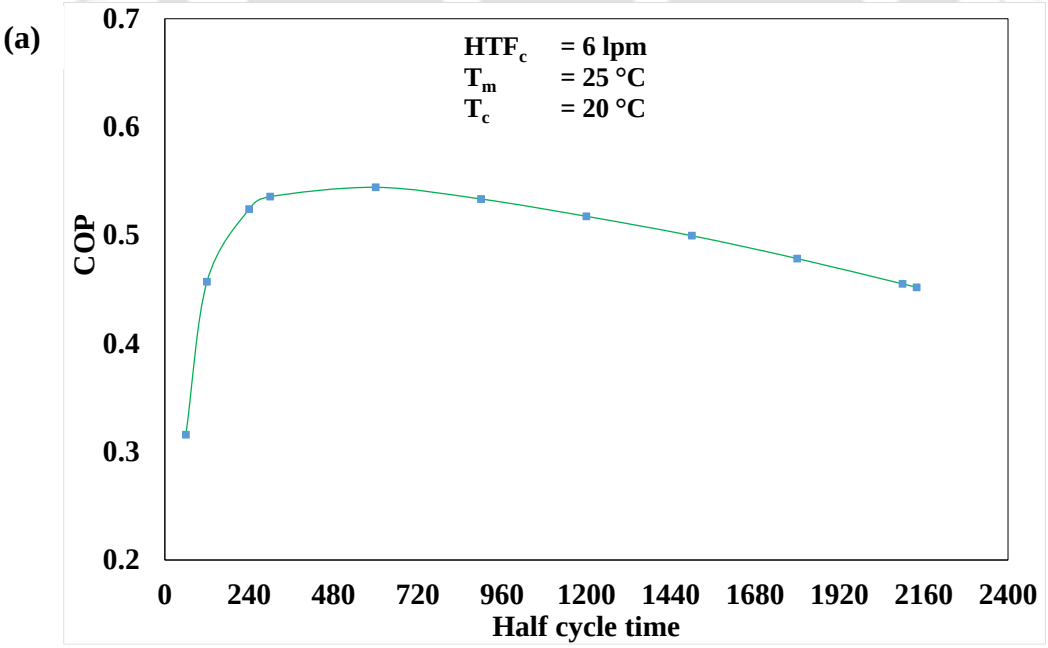

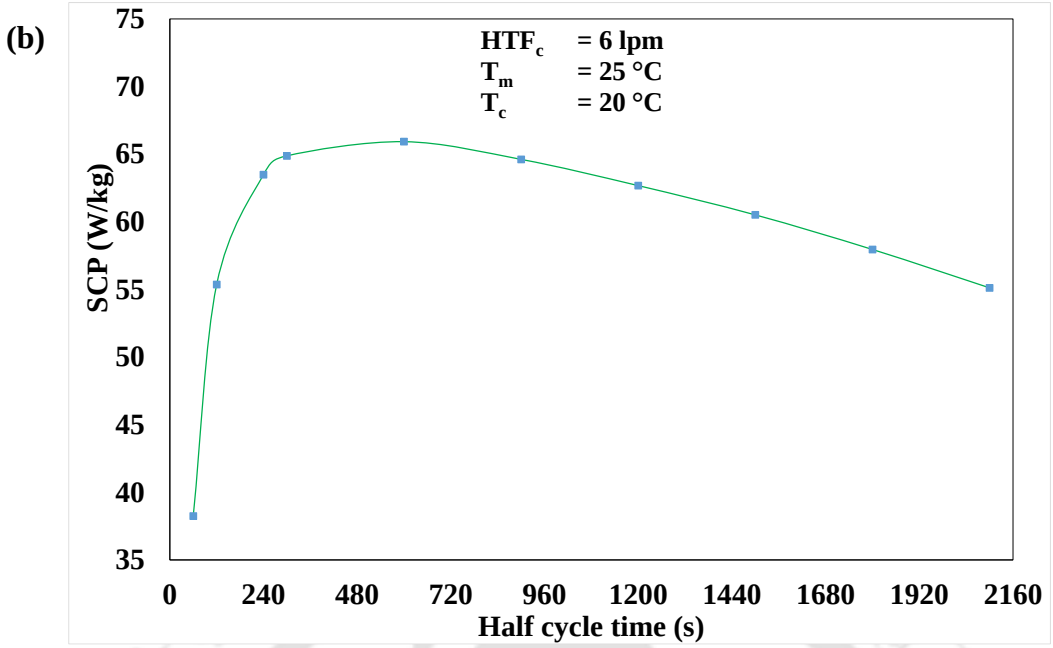

Fig.5.37. Variation of (a) Coefficient of Performance and (b) Specific Cooling Power due to variation of half cycle time

Initially, the desorption reaction is not rapid due to the lower equilibrium pressure of the alloy at refrigeration temperature. Hence, the power input by compressor is more than nominal resulting in lower COP of 0.3 to 0.4. As the cooling is not significant in the initial 1 min, the SCP was also low. With progress of time, the desorbing reactor produced steady cooling output as perceived by the uniform temperature difference between the inlet and outlet of desorbing bed. Simultaneously the electrical power input also went down as effort required for the hydrogen transfer reduced. The duration where this balance occurs was between half cycle time of 4 min and 14 min. Further increase in time led to reduction in performance as the rate of hydrogen transfer reduces slightly. Hence, further cycles were investigated by varying the half cycle time between 2 min and 14 min.

Effect of refrigeration temperature:

To observe the effects of the refrigeration temperature (T_c) on the system performance, T_c was varied from 10 °C to 25 °C in steps of 5 °C while the cold fluid flow rate and sink temperature were respectively maintained at 6 lpm and 25 °C. The resultant COP, SCP and amount of

hydrogen transferred at different half cycle time have been depicted in Fig.5.38 (a)-(c). For all the states, half cycle time of 2 min was detrimental as both COP and SCP were comparatively low. With increase in cycle time within operating range at fixed refrigeration temperature, COP and SCP of the system were observed to be stable without any discernible change. At T_c of 10 °C, the average COP and SCP were observed to be 0.34 and 36.7 W/kg. This performance respectively increases by 29% and 38% at T_c of 15 °C. At 20 °C, SCP was observed to be 63.9 W/kg and COP was 0.51.

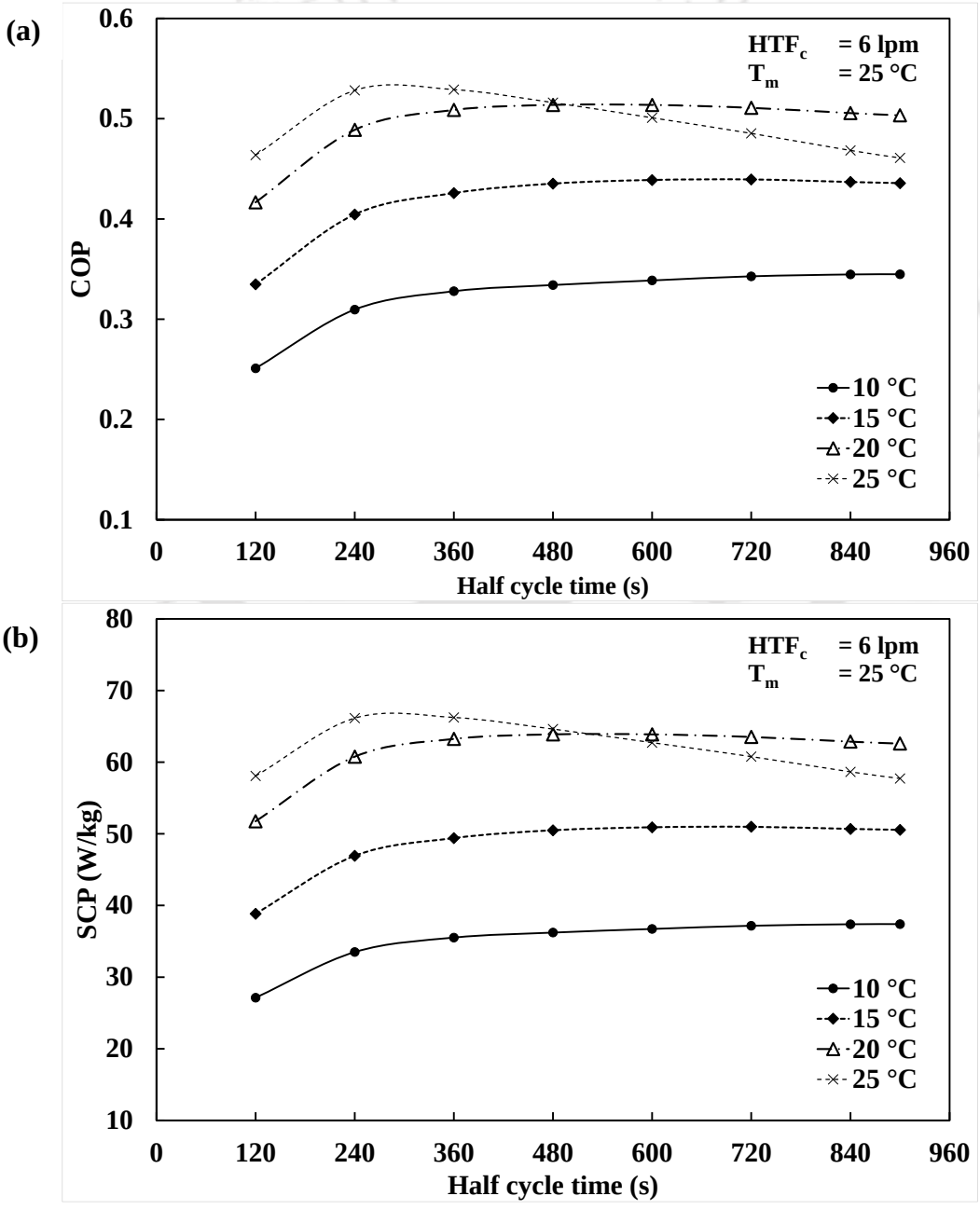

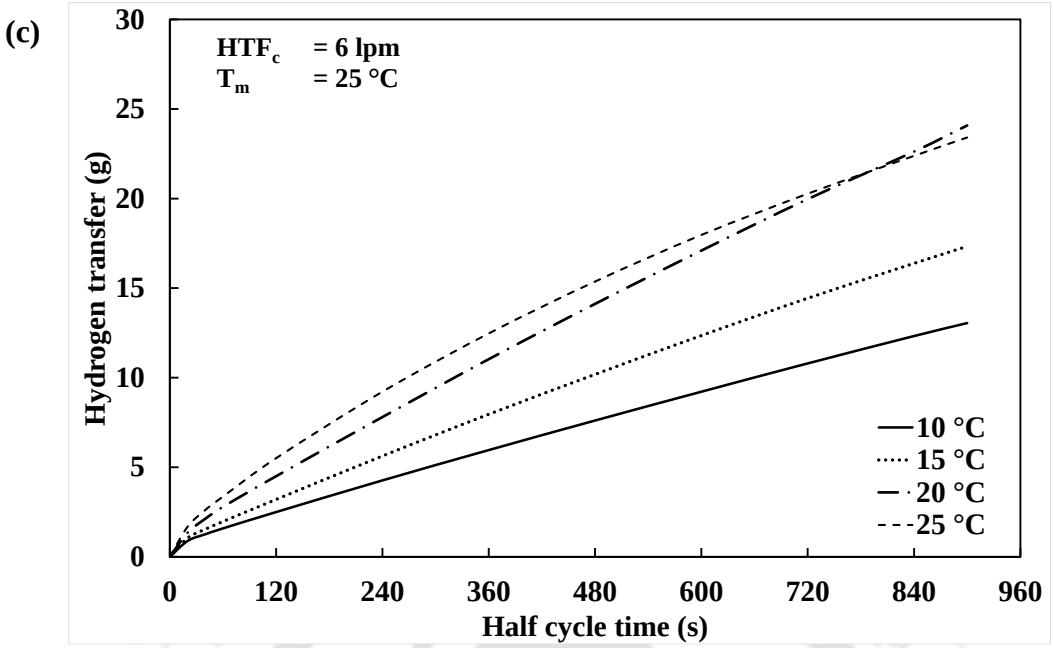

Fig.5.38. Variation of (a) Coefficient of Performance and (b) Specific Cooling Power and (c) amount of hydrogen transferred due to variation in refrigeration temperature

With increase in cycle time, amount of hydrogen transferred was increasing as expected. However, with increase in refrigeration temperature, steady increase in hydriding rate was observed as well. At 480 s, 7.609 g of hydrogen had been transferred at 10 °C, which doubled in value to 14.118 g of hydrogen being transferred at 20 °C. Though the increase in performance was steady till T_c of 20 °C, drastic variation was observed at T_c of 25 °C. At this refrigeration temperature, the system attained sharp peak performance at about half cycle time of 4 min, beyond which, its performance declined drastically.

Effect of sink temperature:

As observed in the previous investigation, the effect of sink temperature was not very drastic as that of refrigeration temperature. With increase of sink temperature from 25 °C to 35 °C while refrigeration temperature was maintained at 20 °C, the improvement in COP was very minuscule. However there was a reduction of about 6.6% when sink temperature was increased from 25 °C to 35 °C, as observed from Fig.5.39 (a)-(c). At T_m of 35 °C, the SCP reduced by 6.6% when T_m was increased from 25 °C. The hydriding rate was similar for both cases until

half cycle time of 480 s, beyond which the hydriding rate corresponding to T_m of 25 °C improved slightly. For given operating conditions, the peak COP and SCP of 0.53 and 66.2 W/kg of total alloy was observed at half cycle time of 4 min and cold fluid flow rate of 6 lpm. Though the selected alloy $La_{0.7}Ce_{0.1}Ca_{0.3}Ni_5$ has suitable PCT characteristics, due to the steady desorption rate portrayed by it has led to remarkably low COP of the resultant CDMHCS. However, the obtained SCP and cooling load are significant enough for this alloy to be considered for other modes of heat pump and cooling systems.

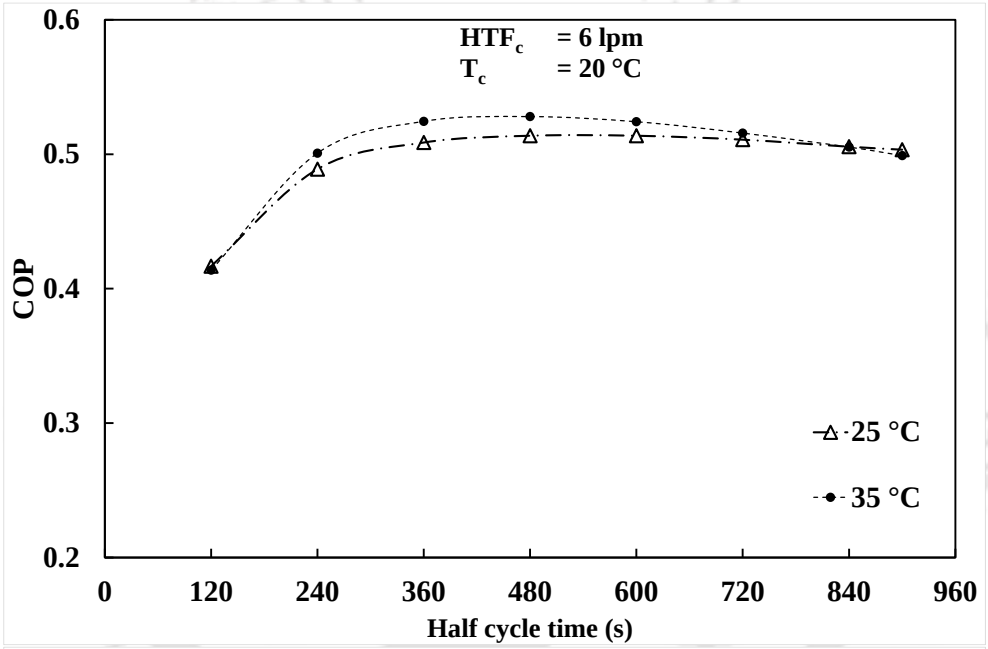

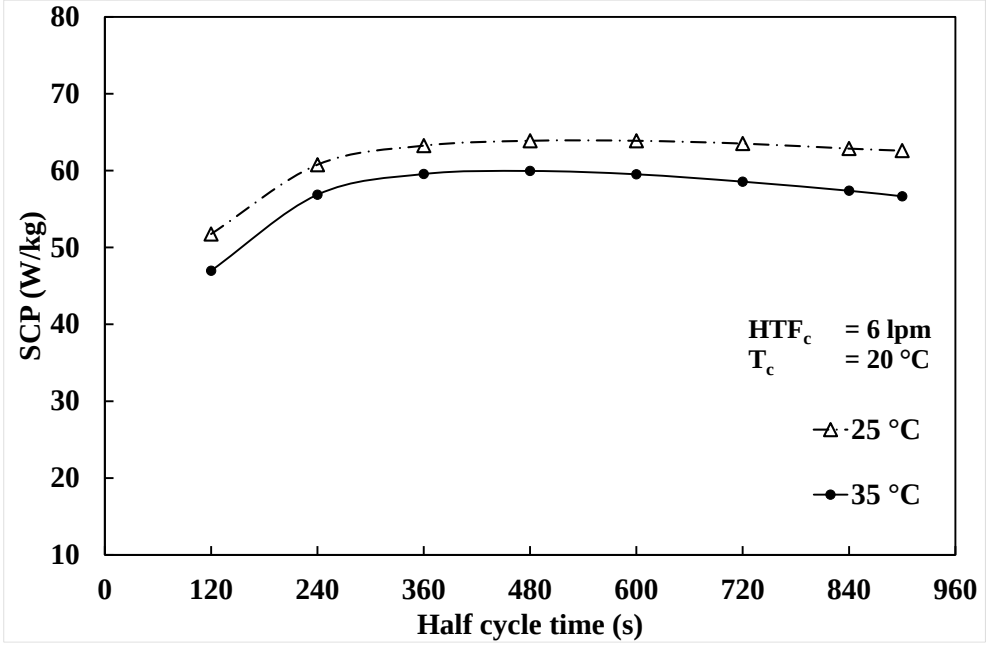

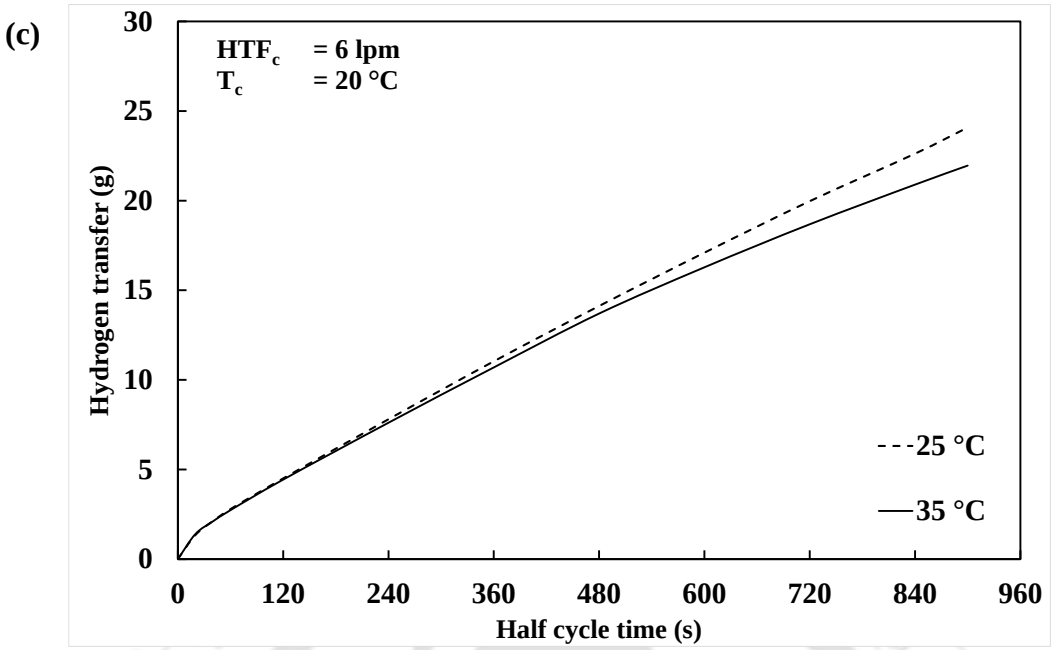

Fig.5.39. Variation of (a) Coefficient of Performance, (b) Specific Cooling Power and (c) amount of hydrogen transferred due to variation in sink temperature

5.8 Summary

The comparative performance of lab scale ECT reactors and absorption of industrial scale reactors are predicted through numerical modelling, based on which ECT reactors have been recommended for experimental investigations of open and closed cycle MH based cooling systems, due to their enhanced heat transfer characteristics. Experimentally, both open cycle MHHSCS and closed cycle CDMHCS have been investigated extensively through developed reactor and formulated experimental procedure. Remarkable cooling performance have been perceived in both modes of the system, making them promising candidates for alternative and eco-friendly cooling systems for both stationary and mobile applications.

CHAPTER 6

CONCLUSIONS AND FUTURE SCOPE

6.1 Preface

Towards the research works carried out on metal hydride based hydrogen storage and cooling systems for stationary and mobile applications, three stages of investigations have been conducted. The work initiated with developing a novel design methodology for the reactor design, and continued into formulation of thermal model and analysis which facilitated in development and performance investigation of experimental systems with practical applicability. The major conclusions obtained from these stages are summarised in this chapter.

6.2 Design methodology

A novel set of arithmetic correlations are developed as a base guiding principle for design of cylindrical reactors with embedded cooling tubes (ECT). The methodology is framed for selection of suitable reactor shell from the available nominal pipe sizes while considering the

operational constraint of end user applications. While developing this design methodology, following points of note are encountered:

- The underlying principle of this design methodology is to evenly distribute the ECT within the MH bed such that each cooling surface supported bed of uniform thickness.
- This is done while balancing the heat transfer enhancement through ECT against the resulting parasitic thermal mass of the empty reactor.
- Based on these correlations, reactors of 4 inch, 5 inch, 6 inch and 8 inch nominal pipe sizes named respectively as RI_4in_41ECT, RII_5in_67ECT, RIII_6in_99ECT and RIV_8in_136ECT are designed.
- It is interesting to note that the bed thickness of all these designs developed through this methodology is in the commendable range of 7.29 mm to 9 mm.

6.3 Thermal modelling

To analyse the performance of these designed ECT reactors as MH based hydrogen storage and cooling systems, three dimensional thermal model is developed and solved numerically. While modelling the MH reactor, gas transport phenomenon within MH bed, combined heat and mass transfer characteristics arising from absorption and desorption reaction, variable wall convective boundary at ECT interface and variation of hydrogen concentration within the bed are considered. There are two distinct analyses conducted and the major conclusions drawn from them are detailed below.

6.3.1 Performance comparison of lab scale ECT reactor designs through thermal modelling

Based on the proposed design methodology, 41 ECT reactor is designed with alloy capacity of 4 kg. To compare its performance, 60 ECT reactor design reported in literature of same length with similar alloy capacity is considered. As an intermediary design, 55 ECT reactor is

designed by modifying the design principle of 60 ECT, and this too is included in the comparative performance analysis. The developed thermal model of lab scale ECT reactor is validated against the experimental investigation of 55 ECT reactor filled with 4 kg of $MmNi_{4.7}Fe_{0.3}$ and good agreement is observed between predicted performance and experimental data. The absorption performance of these reactor designs are analysed using same alloy at supply condition of 50 bar, 25 °C and 24 lpm HTF flow rate, while the desorption performance is analysed at 25 °C and 15 lpm of HTF flow rate. The key findings of this analysis are as follows:

- Hydrogen storage capacity (HSC) of 0.64 wt% is achieved by 55 ECT and 60 ECT reactors in 450 s, while 41 ECT depicted slightly better HSC of 0.66 wt%.
- The influence of reactor design is more prominent in the temperature distribution than the hydriding rate. The bed temperature variation within bed of 41 ECT reactor is uniform throughout, due to which the average bed temperature achieved peak of 49.3 °C within 25 s and dropped to absorption condition of 25 °C within 300 s.
- On the other hand, 60 ECT reactor bed depicted three distinct temperature profiles due to which the heat transfer characteristic is not significant. Compared to 60 ECT reactor, absorption performance of 55 ECT reactor is marginally better. This variation bed temperature is reflected in HTF outlet temperature as well.
- Considering the PCT characteristics of $MmNi_{4.7}Fe_{0.3}$, the desorption performance is more distinct than the absorption performance of all three reactors. 60 ECT reactor desorbed 1 wt% within 150 s. However, this amount is 5.2% and 8.6% more in case of 55 ECT and 41 ECT reactor, respectively.
- The drop in average bed temperature of 41 ECT reactor is sharper which resulted in HTF outlet temperature of 23 °C. This is 2 °C drop in HTF temperature across 160 mm length within 8 s of desorption reaction.

- The desorption performance of 55 ECT reactor is commendable as well, resulting in 1.8 °C drop in HTF temperature within 25 s of desorption reaction.

Based on these findings, 41 ECT and 55 ECT reactors are chosen for experimental investigation of MH based cooling systems.

6.3.2 Performance prediction of industrial scale hydrogen storage system through thermal modelling

As the design methodology has facilitated the design of industrial scale reactors with 50 kg alloy capacity, the developed thermal model is utilized in analysing the storage performance of industrial scale reactor filled with 50 kg of $LaNi_{4.7}Al_{0.3}$ under various operating conditions. Prior to the analysis, the absorption performance of RIII_6in_99ECT reactor filled with 40 kg of $LaNi_{4.7}Al_{0.3}$ at supply condition 10 bar, 25 °C with 30 lpm HTF flow rate is utilized to positively validate the thermal model of industrial scale reactor. Having validated the model, the influence of RI_4in_41ECT, RII_5in_67ECT, RIII_6in_99ECT and RIV_8in_136ECT designs on absorption at 30 bar, 25 °C and 60 lpm HTF flow rate are analysed. By selecting the best design among them, the effect of varying supply pressure (5 to 35 bar), absorption temperature (20 °C to 35 °C) and HTF flow rate (10 lpm to 35 lpm) on the hydriding performance are analysed. The broad conclusions are as follows:

- Among the 4 designs, RIII_6in_99ECT reactor depicts best hydriding rate and heat transfer characteristics. It achieved total hydrogen storage capacity of 1.29 wt%, while 80% of total HSC is attained within 430 s.
- The effect of supply pressure is more prominent followed by the effect of varying HTF flow rate on the hydriding characteristics of $LaNi_{4.7}Al_{0.3}$ filled in RIII_6in_99ECT reactor. Comparatively, the influence of absorption temperature is negligible. This

variation is due to the influence of operating parameters on the resultant pressure gradient which is the driving potential for the absorption reaction.

- At supply condition of 30 bar, 25 °C and 30 lpm flow rate, total HSC of 1.29 wt% is predicted in 2060 s. The volume average bed temperature dropped from peak value of 153.2 °C to 27 °C in 2200 s. This is a 120.9 °C temperature drop in MH bed of 50 kg.
- It is observed that supply pressure of 30 bar at absorption temperature of 25 °C and 30 lpm HTF flow rate is more suitable for the operation of this MH based hydrogen storage system.

6.4 Experimental investigations

From the analysed reactor designs, lab scale and industrial scale open cycle metal hydride based hydrogen storage and cooling systems (MHHSCS) were fabricated and their performances were experimentally investigated under various operating conditions. Similarly, by employing two identical lab scale ECT reactors, compressor driven metal hydride based cooling systems (CDMHCS) were developed and their performance during quasi continuous cold generation was analysed.

6.4.1 Experimental investigation on the performance of MHHSCS (Open cycle)

The lab scale prototype of 55 ECT reactor was fabricated and filled with 4 kg of $MmNi_{4.7}Fe_{0.3}$. Upon activation, the hydriding performance of this lab scale prototype was analysed at different supply pressures (10 bar to 70 bar) and absorption temperatures (5 °C to 25 °C). The dehydriding rate and cooling performance of this lab scale reactor were investigated at different desorption temperatures of 5 °C to 30 °C with HTF flow rate of 15 lpm, while ensuring 50 g of hydrogen absorption in the previous half cycle. Based on the analysis, the study was extended to industrial reactor of 67 ECT which was filled with 40 kg of $MmNi_{4.7}Fe_{0.3}$. As the prominent influential parameters, the effect of varying supply pressure (40 bar to 70 bar) and

the effect of varying desorption temperature (5 °C to 25 °C) on the respective absorption and desorption performances of industrial scale model were tested. During this analysis, the absorption temperature and HTF flow rate were maintained constant at 5 °C and 50 lpm, respectively. Similar to lab scale model, 400 g of hydrogen was absorbed in previous half cycle before analysing the desorption performance. The significant outcomes of this analysis are briefed below:

- The lab scale prototype was activated in its 31st absorption cycle at the supply condition of 70 bar, 5 °C and 24 lpm HTF flow rate. The bed attained 1.2 wt% in 250 s and the maximum capacity of 1.36 wt% was achieved within 503 s.
- At 25 °C and 24 lpm flow rate, supply pressure below 40 bar resulted in poor hydriding rate. At 40 bar, 14.158 g of hydrogen was absorbed in 362 s. However, this capacity was increased by ~3.25 times when supply pressure was increased to 70 bar, and the absorption duration was just 676 s.
- Though prominent impact of varying supply pressure was expected as the driving force of absorption is pressure gradient, the varying absorption temperature also equally influenced the absorption performance owing to the PCT characteristics of the alloy. At supply of 40 bar and 15 lpm HTF flow rate, absorption capacity was increased by 3.8 times when absorption temperature was reduced from 25 °C to 5 °C.
- The desorption performance of $MmNi_{4.7}Fe_{0.3}$ was distinctly prominent compared to its absorption performance, wherein 96% of absorbed hydrogen was released in all cases. At 5 °C and 15 lpm flow rate, 45.896 g of hydrogen was desorbed in 642 s, thereby producing cooling output of 393 kJ. With increase in temperature to 25 °C, the desorbed amount increased to 48.139 g within 442 s of reactions, leading to 25.5% increase in cooling produced with peak output and SCP of 2.3 kW and 279 W/kg of cooling alloy.

- The desorption was so rapid that the average bed temperature was dropped by 37.2 °C in 123 s at desorption condition of 30 °C and 15 lpm. Before insulating the reactor, ice formation on the periphery of reactor surface was observed during desorption reaction due to condensation of atmospheric moisture coming in contact with the cooling surface.
- When the study was extended to industrial scale reactor, the performance was comparatively low. Upon activation, total absorption of 557.612 g (1.4 wt%) was achieved in 5915 s. At supply of 40 bar, 5 °C and 50 lpm flow rate, 311.959 g of hydrogen was absorbed in 1763 s. Increasing the supply pressure to 70 bar, 30% improvement in storage capacity was observed with 34% reduction in absorption time. However, the industrial scale system attained 0.75 wt% (~300 g) within 364 s, which was commendable for system of this scale.
- The desorption performance was comparatively slow in the case of industrial scale reactor. Though the heat transfer enhancement due to ECT was evident in industrial scale reactor, the bulk of the alloy caused an inherent limitation leading to slower desorption kinetics. At 25 °C and 50 lpm flow rate, 4088.6 kJ of cooling produced at an average rate of 1.2 kW in 3360 s, while the system exhibited a peak output of 3 kW at 413 s.

For $MmNi_{4.7}Fe_{0.3}$ based HSCS, absorption pressure of 50 bar at ambient temperature with HTF flow rate of 25 to 30 lpm would result in commendable storage performance. Desorption at same temperature and flow rate would lead to ample cooling output. This system is suitable for fuel cell based vehicles and stationary fuel stack structures, wherein hydrogen is supplied at pressure above 70 bar. These applications would benefit from the auxiliary cooling produced by the system.

6.4.2 Experimental investigation on the performance of CDMHCS (Closed cycle)

The experimental setup of CDMHCS was formulated with two identical 60 ECT reactors were filled with 2.75 kg of $LmNi_{4.91}Sn_{0.15}$ to analyse the quasi-continuous cold generation under various operating conditions. By modifying a hermetically sealed reciprocating compressor suitable for R-134a application, a dedicated driving force between the coupled reactors was achieved. The operating parameters including cycle time (4 min to 16 min), cold fluid flow rate (4 lpm to 16 lpm), refrigeration temperature (10 °C to 20 °C) and sink temperature (25 °C to 35 °C) were varied, and their impact on COP and SCP of the system were analysed along with amount of hydrogen transferred. The study was further extended to newly synthesized alloy with composition of $La_{0.7}Ce_{0.1}Ca_{0.3}Ni_5$. For this, two identical 41 ECT reactors with outer cooling jacket were fabricated and each was filled with 3.75 kg of alloy. The cycle time was varied between 4 min and 28 min in steps of 4 min. Concurrently, refrigeration temperature was varied 10 °C to 5 °C, while sink temperature from 25 °C to 35 °C. The cold fluid flow rate was fixed at 6 lpm. The difference in cooling performance and the underlying reason is explained in detail, as follows:

- For $LmNi_{4.91}Sn_{0.15}$ based CDMHCS, lower cycle time and cold fluid flow rate resulted in better COP and SCP values. Increase in cycle time from 4 min to 8 min resulted in corresponding reductions of 43% and 46% in COP and SCP. Similarly, increase in cold fluid flow rate from 4 lpm to 16 lpm resulted in COP and SCP reduction by 53% and 55%, respectively. However, the amount of hydrogen transferred was observed to increase with increase of both these parameters, as expected.
- With increase in cycle time, the energy input remained stable while the cooling output was reduced with reduction in rate of hydrogen transfer. Ideally, with increase in cold fluid flow rate, the heat transfer characteristics would improve leading to better cooling

effect. However, it was observed that the higher cold fluid flow rate enabled the bed to consume the requisite desorption heat from the bed itself instead of the HTF.

- Increase in refrigeration temperature from 10 °C to 20 °C at sink temperature of 25 °C, resulted in maximum increase in COP and SCP by 64.2% and 70.3%. Increase in sink temperature from 25 °C to 35 °C, resulted in 18% reduction in COP. Similarly, increase in refrigeration temperature had prominent positive effect in amount of hydrogen transfer compared to decrease in sink temperature.
- At supply condition of 20 °C refrigeration temperature and 25 °C sink temperature with cold fluid flow rate of 8 lpm in 8 min cycle resulted in maximum COP and SCP values of 2.2 and 53.5 W/kg of total alloy, respectively. The reactor effectiveness was estimated to be about 50% for this system.
- When the investigation was extended to $La_{0.7}Ce_{0.1}Ca_{0.3}Ni_5$ based CDMHCS, unique behaviour was observed. In case of $LmNi_{4.91}Sn_{0.15}$, only 50% of absorbed hydrogen was transferred in a complete half cycle. However, in $La_{0.7}Ce_{0.1}Ca_{0.3}Ni_5$ based CDMHCS, 75% of absorbed hydrogen was transferred in complete half cycle of about 36 min.
- It was observed that the cooling output rate was steady due to steady dehydriding rate of the alloy. Due to this steady rate of desorption, the cooling performance was not as robust as that of previous system, even though 41 ECT reactor depicted better cooling performance than 60 ECT, and was attached with an additional outer cooling jacket.
- The same trend as seen in in $LmNi_{4.91}Sn_{0.15}$ based CDMHCS with steady increase in COP and SCP was observed with increase in refrigeration temperature. However, the effect of sink temperature was comparatively marginal in this system.
- Maximum COP of 0.53 was achieved at cycle time of 8 min with cold fluid flow rate of 6 lpm, refrigeration temperature of 25 °C and sink temperature of 25 °C. Low COP value was an indication of lower rate of cooling output. However, SCP at same operating

condition was 66.2 W/kg of total alloy, which signifies the alloy has the requisite cooling ability.

By developing CDMHCS with ECT reactors, small scale air conditioners and on-board cooling systems are a definite possibility, which would be competitive with conventional VCRS system. With near ambient sink temperature and lower cold fluid flow rate and shorter cycle time, competitive COP and SCP can be achieved with minimum energy input.

6.5 Scope of future work

Based on the investigation and resultant conclusions, further research into metal hydride based cooling systems can be pursued in following avenues:

- Development of economically feasible MH based cooling system stemming from the research into synthesis and production of suitable alloys.
- Focused research into testing and adaptability of high capacity compressors for CDMHCS, thereby improving the performance of the system.
- Development of CDMHCS and MHHSCS with automated monitoring and control system, thereby improving efficiency.
- Development of streamlined implementation of MH based hydrogen storage and cooling systems in conjunction with electrolysers and fuel cells for end user applications.

REFERENCES

Afzal, M., Mane, R., Sharma, P., 2017. Heat transfer techniques in metal hydride hydrogen storage: A review. Int. J. Hydrogen Energy 42, 30661–30682. https://doi.org/10.1016/j.ijhydene.2017.10.166

Aldas, K., Mat, M.D., Kaplan, Y., 2002. A three-dimensional mathematical model for absorption in a metal hydride bed. Int. J. Hydrogen Energy 27, 1049–1056. https://doi.org/10.1016/S0360-3199(02)00010-1

Anbarasu, S., Muthukumar, P., Mishra, S.C., 2014a. Thermal modeling of $LmNi_{4.91}Sn_{0.15}$ based solid state hydrogen storage device with embedded cooling tubes. Int. J. Hydrogen Energy 39, 15549–15562. https://doi.org/10.1016/j.ijhydene.2014.07.088

Anbarasu, S., Muthukumar, P., Mishra, S.C., 2014b. Tests on $LmNi_{4.91}Sn_{0.15}$ based solid state hydrogen storage device with embedded cooling tubes - Part A: Absorption process. Int. J. Hydrogen Energy 39, 3342–3351. https://doi.org/10.1016/j.ijhydene.2013.12.090

Anbarasu, S., Muthukumar, P., Mishra, S.C., 2014c. Tests on $LmNi_{4.91}Sn_{0.15}$ based solid state hydrogen storage device with embedded cooling tubes - Part B: Desorption process. Int. J. Hydrogen Energy 39, 4966–4972. https://doi.org/10.1016/j.ijhydene.2014.01.039

Ariizumi, R., 2010. Renewable hydrogen: Key to a new civilization - Our world. United Nations Univ.

Askri, F., Ben Salah, M., Jemni, A., Ben Nasrallah, S., 2009a. Heat and mass transfer studies on metal-hydrogen reactor filled with $MmNi_{4.6}Fe_{0.4}$. Int. J. Hydrogen Energy 34, 6705–6711. https://doi.org/10.1016/j.ijhydene.2009.06.069

Askri, F., Ben Salah, M., Jemni, A., Ben Nasrallah, S., 2009b. Optimization of hydrogen storage in metal-hydride tanks. Int. J. Hydrogen Energy 34, 897–905. https://doi.org/10.1016/j.ijhydene.2008.11.021

Askri, F., Jemni, A., Nasrallah, S. Ben, 2003. Study of two-dimensional and dynamic heat and

mass transfer in a metal–hydrogen reactor. Int. J. Hydrogen Energy 28, 537–557. https://doi.org/10.1143/JPSJ.21.1880

Assfour, B., Leoni, S., Seifert, G., Baburin, I.A., 2011. Packings of carbon nanotubes - New materials for hydrogen storage. Adv. Mater. 23, 1237–1241. https://doi.org/10.1002/adma.201003669

Aydin, M.I., Karaca, A.E., Qureshy, A.M.M.I., Dincer, I., 2021. A comparative review on clean hydrogen production from wastewaters. J. Environ. Manage. 279, 111793. https://doi.org/10.1016/j.jenvman.2020.111793

Balachandar, G., Khanna, N., Das, D., 2013. Biohydrogen production from organic wastes by dark fermentation, in: Biohydrogen. Elsevier, pp. 103–144. https://doi.org/10.1016/B978-0-444-59555-3.00006-4

Bao, Z., Wu, Z., Nyamsi, S.N., Yang, F., Zhang, Z., 2013a. Three-dimensional modeling and sensitivity analysis of multi-tubular metal hydride reactors. Appl. Therm. Eng. 52, 97–108. https://doi.org/10.1016/j.applthermaleng.2012.11.023

Bao, Z., Yang, F., Wu, Z., Nyallang Nyamsi, S., Zhang, Z., 2013b. Optimal design of metal hydride reactors based on CFD-Taguchi combined method. Energy Convers. Manag. 65, 322–330. https://doi.org/10.1016/j.enconman.2012.07.027

Bedbak, S.S., Gopal, M.R., 2005. Performance analysis of a compressor driven metal hydride cooling system. Int. J. Hydrogen Energy 30, 1127–1137. https://doi.org/10.1016/j.ijhydene.2004.10.014

Bilgili, M., Ataer, Ö.E., 2005. Numerical analysis of hydrogen absorption in a P/M metal bed. Powder Technol. 160, 141–148. https://doi.org/10.1016/j.powtec.2005.08.018

Bououdina, M., Grant, D., Walker, G., 2006. Review on hydrogen absorbing materials - Structure, microstructure, and thermodynamic properties. Int. J. Hydrogen Energy 31, 177–182. https://doi.org/10.1016/j.ijhydene.2005.04.049

Bouzgarrou, F., Askri, F., Mellouli, S., Algarni, S., 2019. Numerical investigation of heat and mass transfer within different configurations of $LaNi_5$–H_2 reactor using the unstructured Lattice Boltzmann Method. Int. J. Hydrogen Energy 44, 31216–31229. https://doi.org/10.1016/j.ijhydene.2019.10.006

Cheng, H., Lu, C., Liu, J., Yan, Y., Han, X., Jin, H., Wang, Y., Liu, Y., Wu, C., 2017. Synchrotron radiation X-ray powder diffraction techniques applied in hydrogen storage materials - A review. Prog. Nat. Sci. Mater. Int. 27, 66–73. https://doi.org/10.1016/j.pnsc.2016.12.007

Chibani, A., Bougriou, C., Merouani, S., 2018. Simulation of hydrogen absorption/desorption on metal hydride $LaNi_5$–H_2: Mass and heat transfer. Appl. Therm. Eng. 142, 110–117. https://doi.org/10.1016/j.applthermaleng.2018.06.078

Choi, H., Mills, A.F., 1990. Heat and mass transfer in metal hydride beds for heat pump applications. Int. J. Heat Mass Transf. 33, 1281–1288. https://doi.org/10.1016/0017-9310(90)90257-U

Chung, C.A., Ho, C.J., 2009. Thermal-fluid behavior of the hydriding and dehydriding processes in a metal hydride hydrogen storage canister. Int. J. Hydrogen Energy 34, 4351–4364. https://doi.org/10.1016/j.ijhydene.2009.03.028

Diaz, H., Percheron-Guegan, A., Achard, J.C., Chatillon, C., Mathieu, J.C., 1979. Thermodynamic and structural properties of $LaNi_{5-y}Al_y$ compounds and their related hydrides. Int. J. Hydrogen Energy.

Ferekh, S., Gwak, G., Kyoung, S., Kang, H.G., Chang, M.H., Yun, S.H., Oh, Y.H., Kim, W., Kim, D., Hong, T., Ju, H., 2015. Numerical comparison of heat-fin-and metal-foam-based hydrogen storage beds during hydrogen charging process. Int. J. Hydrogen Energy 40, 14540–14550. https://doi.org/10.1016/j.ijhydene.2015.07.149

Gambini, M., Manno, M., Vellini, M., 2008. Numerical analysis and performance assessment of metal hydride-based hydrogen storage systems. Int. J. Hydrogen Energy 33, 6178–6187. https://doi.org/10.1016/j.ijhydene.2008.08.006

Gielen, D., Boshell, F., Saygin, D., Bazilian, M.D., Wagner, N., Gorini, R., 2019. The role of renewable energy in the global energy transformation. Energy Strateg. Rev. 24, 38–50. https://doi.org/10.1016/j.esr.2019.01.006

Gopal, M.R., Murthy, S.S., 1995a. Prediction of metal-hydride refrigerator performance based on reactor heat and mass transfer. Int. J. Hydrogen Energy 20, 607–614. https://doi.org/10.1016/0360-3199(94)00108-C

Gopal, M.R., Murthy, S.S., 1995b. Studies on heat and mass transfer in metal hydride beds. Int. J. Hydrogen Energy 20, 911–917. https://doi.org/10.1016/0360-3199(95)00026-A

Gopal, M.R., Murthy, S.S., 1992. Prediction of heat and mass transfer in annular cylindrical metal hydride beds. Int. J. Hydrogen Energy 17, 795–805. https://doi.org/10.1016/0360-3199(92)90024-Q

Goudy, A.J., Stokes, D.G., Gazzillo, J.A., 1983. The effect of heat transfer on the desorption kinetics of $LaNi_5H_6$. J. Less-Common Met. 91, 149–158.

Grashoff, G.J., Pilkington, C.E., Corti, C.W., 1983. Purification of Hydrogen. Platin. Met. Rev. 27, 157–169.

Groll, M., Supper, W., Mayer, U., Brost, O., 1987. Heat and mass transfer limitations in metal hydride reaction beds. Int. J. Hydrogen Energy 12, 89–97. https://doi.org/10.1016/0360-3199(87)90085-1

Guo, Z., Sung, H.J., 1998. Conjugate heat and mass transfer in metal hydride beds in the hydriding process. Int. J. Heat Mass Transf. 42, 379–382. https://doi.org/10.1016/S0017-9310(98)00145-8

Gupta, P., Tong, D., Wang, J., Zhuge, W., Yan, C., Wu, Y., Luo, S., He, X., Ma, F., 2020. Well-to-wheels total energy and GHG emissions of HCNG heavy-duty vehicles in China: Case of EEV qualified EURO 5 emissions scenario. Int. J. Hydrogen Energy 45, 8002–8014. https://doi.org/10.1016/j.ijhydene.2020.01.025

Hahne, E., Kallweit, J., 1998. Thermal conductivity of metal hydride materials for storage of hydrogen: Experimental investigation. Int. J. Hydrogen Energy 23, 107–114. https://doi.org/10.1016/s0360-3199(97)00020-7

Han, J.I., Lee, J.Y., 1989. Hydriding kinetics of $LaNi_5$ and $LaNi_{4.7}Al_{0.3}$. Int. J. Hydrogen Energy 14, 181–186. https://doi.org/10.1016/0360-3199(89)90052-9

Häussinger, P., Lohmüller, R., Watson, A.M., 2000. Hydrogen, in: Ullmann's Encyclopedia of Industrial Chemistry. Wiley-VCH Verlag GmbH & Co. KGaA, Weinheim, Germany. https://doi.org/10.1002/14356007.a13_297

Hua, T.Q., Ahluwalia, R.K., Peng, J.K., Kromer, M., Lasher, S., McKenney, K., Law, K., Sinha, J., 2011. Technical assessment of compressed hydrogen storage tank systems for

automotive applications. Int. J. Hydrogen Energy 36, 3037–3049. https://doi.org/10.1016/j.ijhydene.2010.11.090

IEA, 2020. Energy Policy Review: India 2020, International Energy Agency. Paris, France.

Jemni, A., Nasrallah, S. Ben, 1995a. Study of two-dimensional heat and mass transfer during absorption in a metal-hydrogen reactor. Int. J. Hydrogen Energy 20, 43–52. https://doi.org/10.1016/0360-3199(94)00115-G

Jemni, A., Nasrallah, S. Ben, 1995b. Study of two-dimensional heat and mass transfer during desorption in a metal-hydrogen reactor. Int. J. Hydrogen Energy 20, 881–891. https://doi.org/10.1016/0360-3199(94)00115-G

Jensen, J.O., Vestbø, A.P., Li, Q., Bjerrum, N.J., 2007. The energy efficiency of onboard hydrogen storage. J. Alloys Compd. 446–447, 723–728. https://doi.org/10.1016/j.jallcom.2007.04.051

Kaplan, Y., 2009. Effect of design parameters on enhancement of hydrogen charging in metal hydride reactors. Int. J. Hydrogen Energy 34, 2288–2294. https://doi.org/10.1016/j.ijhydene.2008.12.096

Kim, G.-H., Lee, J.-Y., 1987. Changes of hydrogenation properties induced by thermal cyclings in $MmNi_{4.5}Al_{0.5}$ and $MmNi_{4.15}Fe_{0.85}$. J. Less-Common Met. 132, 123–132. https://doi.org/10.1002/chin.198728027

Kim, K.J., Feldman, K.T., Lloyd, G., Razani, A., 1997a. Compressor-driven metal-hydride heat pumps. Appl. Therm. Eng. 17, 551–560. https://doi.org/10.1016/S1359-4311(96)00067-1

Kim, K.J., Feldman, K.T., Lloyd, G., Razani, A., Shanahan, K.L., 1998. Performance of high power metal hydride reactors. Int. J. Hydrogen Energy 23, 355–362. https://doi.org/10.1016/s0360-3199(97)00058-x

Kim, K.J., Feldman, K.T., Razani, A., 1997b. Cooling and power efficiency diagrams for compressor-driven, metal-hydride slurry air conditioners. Energy 22, 787–796.

Kline, S.J., McClintock, F.A., 1953. Describing Uncertainties in Single-Sample Experiments. Mech. Eng. 75, 3–8.

Kumar, E.A., Maiya, M.P., Murthy, S.S., Viswanathan, B., 2009. Structural, hydrogen storage and thermodynamic properties of some mischmetal-nickel alloys with partial substitutions for nickel. J. Alloys Compd. 476, 92–97. https://doi.org/10.1016/j.jallcom.2008.08.083

Li, S.L., Wang, P., Chen, W., Luo, G., Chen, D.M., Yang, K., 2009. Hydrogen storage properties of $LaNi_{3.8}Al_{1.0}M_{0.2}$ (M = Ni, Cu, Fe, Al, Cr, Mn) alloys. J. Alloys Compd. 485, 867–871. https://doi.org/10.1016/j.jallcom.2009.06.111

Li, S.L., Wang, P., Chen, W., Luo, G., Han, X.B., Chen, D.M., Yang, K., 2010. Study on hydrogen storage properties of $LaNi_{3.8}Al_{1.2-x}Mn_x$ alloys. Int. J. Hydrogen Energy 35, 12391–12397. https://doi.org/10.1016/j.ijhydene.2010.08.049

Libowitz, G.G., 1962. Nonstoichiometry and lattice defects in transition metal hydrides. J. Appl. Phys. 33, 399–405. https://doi.org/10.1063/1.1777131

Linder, M., Kulenovic, R., 2011. An energy-efficient air-conditioning system for hydrogen driven cars. Int. J. Hydrogen Energy 36, 3215–3221. https://doi.org/10.1016/j.ijhydene.2010.11.101

Linder, M., Mertz, R., Laurien, E., 2010. Experimental results of a compact thermally driven cooling system based on metal hydrides. Int. J. Hydrogen Energy 35, 7623–7632. https://doi.org/10.1016/j.ijhydene.2010.04.184

Liu, Y.L., Zhao, Y.Z., Zhao, L., Li, X., Chen, H. gang, Zhang, L.F., Zhao, H., Sheng, R.H., Xie, T., Hu, D.H., Zheng, J.Y., 2010. Experimental studies on temperature rise within a hydrogen cylinder during refueling. Int. J. Hydrogen Energy 35, 2627–2632. https://doi.org/10.1016/j.ijhydene.2009.04.042

Lototskyy, M., Sekhar, B.S., Muthukumar, P., Linkov, V., Pollet, B.G., Satya Sekhar, B., Muthukumar, P., Linkov, V., Pollet, B.G., 2015. Niche applications of metal hydrides and related thermal management issues. J. Alloys Compd. 645, S117–S122. https://doi.org/10.1016/j.jallcom.2014.12.271

Lototskyy, M. V., Tolj, I., Pickering, L., Sita, C., Barbir, F., Yartys, V., 2017. The use of metal hydrides in fuel cell applications. Prog. Nat. Sci. Mater. Int. 27, 3–20. https://doi.org/10.1016/j.pnsc.2017.01.008

Lototskyy, M. V., Yartys, V.A., Pollet, B.G., Bowman, R.C., 2014. Metal hydride hydrogen

compressors: A review. Int. J. Hydrogen Energy 39, 5818–5851. https://doi.org/10.1016/j.ijhydene.2014.01.158

Ma, J., Wang, Y., Shi, S., Yang, F., Bao, Z., Zhang, Z., 2014. Optimization of heat transfer device and analysis of heat & mass transfer on the finned multi-tubular metal hydride tank. Int. J. Hydrogen Energy 39, 13583–13595. https://doi.org/10.1016/j.ijhydene.2014.03.016

Magnetto, D., Mola, S., Dacosta, D.H., Golben, M., Rosso, M., 2006. A metal hydride mobile air conditioning system. SAE Tech. Pap. 115, 1150–1159. https://doi.org/10.4271/2006-01-1235

Martin, M., Gommel, C., Borkhart, C., Fromm, E., 1996. Absorption and desorption kinetics of hydrogen storage alloys. J. Alloys Compd. 238, 193–201. https://doi.org/10.1016/0925-8388(96)02217-7

Mat, M.D., Kaplan, Y., 2001. Numerical study of hydrogen absorption in an Lm - Ni_5 hydride reactor, International Journal of Hydrogen Energy. Pergamon. https://doi.org/10.1016/S0360-3199(01)00030-1

Mazumdar, S., Bhattacharyya, S., Ramgopal, M., 2005a. Compressor driven metal hydride cooling systems - Mathematical model and operating characteristics. Int. J. Refrig. 28, 798–809. https://doi.org/10.1016/j.ijrefrig.2005.02.002

Mazumdar, S., Ramgopal, M., Bhattacharyya, S., 2005b. Thermodynamic analysis and optimization of compressor-driven metal hydride cooling systems. Int. J. Hydrogen Energy 30, 631–641. https://doi.org/10.1016/j.ijhydene.2004.10.003

Mellouli, S., Askri, F., Dhaou, H., Jemni, A., Ben Nasrallah, S., 2010. Numerical simulation of heat and mass transfer in metal hydride hydrogen storage tanks for fuel cell vehicles. Int. J. Hydrogen Energy 35, 1693–1705. https://doi.org/10.1016/j.ijhydene.2009.12.052

Mellouli, S., Dhaou, H., Askri, F., Jemni, A., Ben Nasrallah, S., 2009. Hydrogen storage in metal hydride tanks equipped with metal foam heat exchanger. Int. J. Hydrogen Energy 34, 9393–9401. https://doi.org/10.1016/j.ijhydene.2009.09.043

Melnichuk, M., Silin, N., 2012. Guidelines for thermal management design of hydride containers. Int. J. Hydrogen Energy 37, 18080–18094.

https://doi.org/10.1016/j.ijhydene.2012.09.046

Melnichuk, M., Silin, N., Andreasen, G., Corso, H.L., Visintin, A., Peretti, H.A., 2010. Hydrogen discharge simulation and testing of a metal-hydride container. Int. J. Hydrogen Energy 35, 5855–5859. https://doi.org/10.1016/j.ijhydene.2009.12.127

Miyamoto, M., Yamaji, K., Nakata, Y., 1983. Reaction kinetics of $LaNi_5$. J. Less-Common Met. 89, 111–116. https://doi.org/10.1016/0022-5088(83)90254-0

Mohammadshahi, S.S., Gray, E.M.A., Webb, C.J., 2016. A review of mathematical modelling of metal-hydride systems for hydrogen storage applications. Int. J. Hydrogen Energy 41, 3470–3484. https://doi.org/10.1016/j.ijhydene.2015.12.079

Mohan, G., Prakash Maiya, M., Srinivasa Murthy, S., 2007. Performance simulation of metal hydride hydrogen storage device with embedded filters and heat exchanger tubes. Int. J. Hydrogen Energy 32, 4978–4987. https://doi.org/10.1016/j.ijhydene.2007.08.007

Moradi, R., Groth, K.M., 2019. Hydrogen storage and delivery: Review of the state of the art technologies and risk and reliability analysis. Int. J. Hydrogen Energy 44, 12254–12269. https://doi.org/10.1016/j.ijhydene.2019.03.041

Muthukumar, P., Abraham, K., Prasad, U.A.R., Maiya, M.P., Murthy, S.S., 2003. Screening of metal hydrides for engineering applications, in: Proceeding of ECOS 2003. Copenhagen, Denmark, pp. 93–100.

Muthukumar, P., Groll, M., 2010. Metal hydride based heating and cooling systems: A review. Int. J. Hydrogen Energy 35, 3817–3831. https://doi.org/10.1016/j.ijhydene.2010.01.115

Muthukumar, P., Linder, M., Mertz, R., Laurien, E., 2009a. Measurement of thermodynamic properties of some hydrogen absorbing alloys. Int. J. Hydrogen Energy 34, 1873–1879. https://doi.org/10.1016/j.ijhydene.2008.12.052

Muthukumar, P., Madhavakrishna, U., Dewan, A., 2007. Parametric studies on a metal hydride based hydrogen storage device. Int. J. Hydrogen Energy 32, 4988–4997. https://doi.org/10.1016/j.ijhydene.2007.08.010

Muthukumar, P., Maiya, M.P., Murthy, S.S., 2005. Experiments on a metal hydride-based hydrogen storage device. Int. J. Hydrogen Energy 30, 1569–1581. https://doi.org/10.1016/j.ijhydene.2004.12.007

Muthukumar, P., Ramana, S.V., 2009. Numerical simulation of coupled heat and mass transfer in metal hydride-based hydrogen storage reactor. J. Alloys Compd. 472, 466–472. https://doi.org/10.1016/j.jallcom.2008.04.088

Muthukumar, P., Ramana, S. V., 2010. Study of heat and mass transfer in $MmNi_{4.6}Al_{0.4}$ during desorption of hydrogen. Int. J. Hydrogen Energy 35, 10811–10818. https://doi.org/10.1016/j.ijhydene.2010.02.069

Muthukumar, P., Satheesh, A., 2013. Analysis of crossed van't Hoff metal hydride based heat pump. Int. J. Hydrogen Energy 38, 11415–11420. https://doi.org/http://dx.doi.org/10.1016/j.ijhydene.2013.06.070

Muthukumar, P., Satheesh, A., Linder, M., Mertz, R., Groll, M., 2009b. Studies on hydriding kinetics of some La-based metal hydride alloys. Int. J. Hydrogen Energy 34, 7253–7262. https://doi.org/10.1016/j.ijhydene.2009.06.075

Muthukumar, P., Satheesh, A., Madhavakrishna, U., Dewan, A., 2009c. Numerical investigation of coupled heat and mass transfer during desorption of hydrogen in metal hydride beds. Energy Convers. Manag. 50, 69–75. https://doi.org/10.1016/j.enconman.2008.08.028

Muthukumar, P., Singh Patel, K., Sachan, P., Singhal, N., 2012a. Computational study on metal hydride based three-stage hydrogen compressor. Int. J. Hydrogen Energy 37, 3797–3806. https://doi.org/10.1016/j.ijhydene.2011.05.104

Muthukumar, P., Singhal, A., Bansal, G.K., 2012b. Thermal modeling and performance analysis of industrial-scale metal hydride based hydrogen storage container. Int. J. Hydrogen Energy 37, 14351–14364. https://doi.org/10.1016/j.ijhydene.2012.07.010

Nazir, H., Muthuswamy, N., Louis, C., Jose, S., Prakash, J., Buan, M.E., Flox, C., Chavan, S., Shi, X., Kauranen, P., Kallio, T., Maia, G., Tammeveski, K., Lymperopoulos, N., Carcadea, E., Veziroglu, E., Iranzo, A., Kannan, A.M., 2020. Is the H_2 economy realizable in the foreseeable future? Part II: H_2 storage, transportation, and distribution. Int. J. Hydrogen Energy. https://doi.org/10.1016/j.ijhydene.2020.05.241

Nishizaki, T., Miyamoto, K., Yoshida, K., 1983. Coefficients of performance of hydride heat pumps. J. Less-Common Met. 89, 559–566. https://doi.org/10.1016/0022-5088(83)90372-7

Nonobe, Y., 2017. Development of the fuel cell vehicle mirai. IEEJ Trans. Electr. Electron. Eng. 12, 5–9. https://doi.org/10.1002/tee.22328

Oliver, F.W., Morgan, W., Hammond, E.C., Wood, S., May, L., 1985. Mössbauer studies on $LaNi_{4.7}Sn_{0.3}$ and its hydride. J. Appl. Phys. 57, 3250–3251. https://doi.org/10.1063/1.335114

Park, J.G., Han, S.C., Jang, H.Y., Lee, S.M., Lee, P.S., Lee, J.Y., 2002. The development of compressor-driven metal hydride heat pump (CDMHHP) system as an air conditioner. Int. J. Hydrogen Energy 27, 941–944. https://doi.org/10.1016/S0360-3199(01)00187-2

Park, J.G., Jang, K.J., Lee, P.S., Lee, J.Y., 2001. The operating characteristics of the compressor-driven metal hydride heat pump system. Int. J. Hydrogen Energy 26, 701–706. https://doi.org/10.1016/S0360-3199(01)00006-4

Patel, P.K., Sekhar, B.S., Muthukumar, P., 2013. Feasibility study on compressor-driven metal hydride based cooling system, in: 3rd National Conference on Refrigeration and Air Conditioning (NCRAC-2013). Chennai, pp. 12–14.

Patil, S.D., Gopal, M.R., 2013a. Analysis of a metal hydride reactor for hydrogen storage. Int. J. Hydrogen Energy 38, 942–951. https://doi.org/10.1016/j.ijhydene.2012.10.031

Patil, S.D., Gopal, M.R., 2013b. Entropy generation and its relation to heating and cooling requirements of a metal hydride hydrogen storage reactor. Int. J. Hydrogen Energy 38, 13687–13693. https://doi.org/10.1016/j.ijhydene.2013.08.018

Phate, A.K., Maiya, M.P., Murthy, S.S., 2007. Simulation of transient heat and mass transfer during hydrogen sorption in cylindrical metal hydride beds. Int. J. Hydrogen Energy 32, 1969–1981. https://doi.org/10.1016/j.ijhydene.2006.09.020

Rather, S. ullah, 2020. Preparation, characterization and hydrogen storage studies of carbon nanotubes and their composites: A review. Int. J. Hydrogen Energy 45, 4653–4672. https://doi.org/10.1016/j.ijhydene.2019.12.055

Ren, J., Musyoka, N.M., Langmi, H.W., Mathe, M., Liao, S., 2017. Current research trends and perspectives on materials-based hydrogen storage solutions: A critical review. Int. J. Hydrogen Energy 42, 289–311. https://doi.org/10.1016/j.ijhydene.2016.11.195

Richmond, S., Bridgewater, J.S., Ward, J.W., Allen, T.H., 2010. The solubility of hydrogen

and deuterium in alloyed, unalloyed and impure plutonium metal. IOP Conf. Ser. Mater. Sci. Eng. 9, 012036. https://doi.org/10.1088/1757-899x/9/1/012036

Ron, M., 1984. A hydrogen heat pump as a bus air conditioner. J. Less-Common Met. 104, 259–278. https://doi.org/10.1016/0022-5088(84)90411-9

Sakintuna, B., Lamari-Darkrim, F., Hirscher, M., 2007. Metal hydride materials for solid hydrogen storage: A review. Int. J. Hydrogen Energy 32, 1121–1140. https://doi.org/10.1016/j.ijhydene.2006.11.022

Sandrock, G., 1997. State-of-the-art review of hydrogen storage in reversible metal hydrides for military fuel cell applications. New Jersey, USA.

Sastri, M.V.C., Viswanathan, B., Murthy, S.S., 1998. Metal Hydrides: Fundamentals and Applications. Narosa Publishing House.

Satheesh, A., Muthukumar, P., 2010a. Performance investigations of a single-stage metal hydride heat pump. Int. J. Hydrogen Energy 35, 6950–6958. https://doi.org/10.1016/j.ijhydene.2010.04.043

Satheesh, A., Muthukumar, P., 2010b. Performance investigation of double-stage metal hydride based heat pump. Appl. Therm. Eng. 30, 2698–2707. https://doi.org/10.1016/j.applthermaleng.2010.07.021

Satheesh, A., Muthukumar, P., Dewan, A., 2009. Computational study of metal hydride cooling system. Int. J. Hydrogen Energy 34, 3164–3172. https://doi.org/10.1016/j.ijhydene.2009.01.083

Sekhar, B.S., Ito, H., Kato, A., Nakano, A., 2016. Research and development of a laboratory scale Totalized Hydrogen Energy Utilization System. Int. J. Hydrogen Energy 41, 1224–1236. https://doi.org/10.1016/j.ijhydene.2015.10.105

Sekhar, B.S., Lototskyy, M., Kolesnikov, A., Moropeng, M.L., Tarasov, B.P., Pollet, B.G., 2015. Performance analysis of cylindrical metal hydride beds with various heat exchange options. J. Alloys Compd. 645, S89–S95. https://doi.org/10.1016/j.jallcom.2014.12.272

Selvam, P.K., Muthukumar, P., Linder, M., Mertz, R., Kulenovic, R., 2013. Measurement of thermochemical properties of some metal hydrides-Titanium (Ti), Misch metal (Mm) and Lanthanum (La) based alloys. Int. J. Hydrogen Energy 38, 5288–5301.

https://doi.org/10.1016/j.ijhydene.2013.02.009

Sharma, V.K., Anil Kumar, E., Srinivasa Murthy, S., 2015. Influence of dynamic operating conditions on the performance of metal hydride based solid sorption cooling systems. Int. J. Hydrogen Energy 40, 1108–1115. https://doi.org/10.1016/j.ijhydene.2014.11.084

Sharma, V.K., Kumar, E.A., 2017. Thermodynamic analysis of novel multi stage multi effect metal hydride based thermodynamic system for simultaneous cooling, heat pumping and heat transformation. Int. J. Hydrogen Energy 42, 437–447. https://doi.org/10.1016/j.ijhydene.2016.09.154

Singh, A., Maiya, M.P., Murthy, S.S., 2015. Effects of heat exchanger design on the performance of a solid state hydrogen storage device. Int. J. Hydrogen Energy 40, 9733–9746. https://doi.org/10.1016/j.ijhydene.2015.06.015

Singh, R.K., Gupta, B.K., Lototsky, M. V., Srivastava, O.N., 2004. On the synthesis and hydrogenation behaviour of $MmNi_{5-x}Fe_x$ alloys and computer simulation of their P-C-T curves. J. Alloys Compd. https://doi.org/10.1016/j.jallcom.2003.11.005

Sinigaglia, T., Lewiski, F., Santos Martins, M.E., Mairesse Siluk, J.C., 2017. Production, storage, fuel stations of hydrogen and its utilization in automotive applications-a review. Int. J. Hydrogen Energy 42, 24597–24611. https://doi.org/10.1016/j.ijhydene.2017.08.063

Souahlia, A., Dhaou, H., Askri, F., Mellouli, S., Jemni, A., Ben Nasrallah, S., 2011a. Experimental study and characterization of metal hydride containers. Int. J. Hydrogen Energy 36, 4952–4957. https://doi.org/10.1016/j.ijhydene.2011.01.074

Souahlia, A., Dhaou, H., Askri, F., Sofiene, M., Jemni, A., Ben Nasrallah, S., 2011b. Experimental and comparative study of metal hydride hydrogen tanks. Int. J. Hydrogen Energy 36, 12918–12922. https://doi.org/10.1016/j.ijhydene.2011.07.022

Suda, S., Komazaki, Y., Narasaki, H., Uchida, M., 1991. Development of a double-stage heat pump: experimental and analytical surveys. J. Less-Common Met. 172–174, 1092–1110. https://doi.org/10.1016/S0022-5088(06)80017-2

Sun, D., Deng, S., 1989. Study of the heat and mass transfer characteristics of metal hydride beds: a two-dimensional model. J. Less-Common Met. 155, 271–279.

U.S. Department of Energy, 2015a. Comparative properties of hydrogen and other fuels. URL: https://h2tools.org/hyarc/hydrogen-data/comparative-properties-hydrogen-and-other-fuels (accessed 10.1.2021).

U.S. Department of Energy, 2015b. Fuel cell technologies office multi-year research, development, and demonstration plan - 3.3 Hydrogen storage. URL: https://www.energy.gov/eere/fuelcells/downloads/fuel-cell-technologies-office-multi-year-research-development-and-22 (accessed 10.1.2021).

U.S. Department of Energy, 2015c. Properties of hydrogen at normal boiling point. URL: https://h2tools.org/hyarc/hydrogen-data/properties-hydrogen-normal-boiling-point (accessed 10.1.2021).

U.S. Department of Energy, 2009. Workshop notes from "Compressed natural gas and hydrogen fuels: Lessons learned for the safe deployment of vehicles." URL: https://www.energy.gov/eere/fuelcells/downloads/workshop-notes-compressed-natural-gas-and-hydrogen-fuels-lessons-learned (accessed 15.1.2021).

UNFCCC, 2016. The Paris Agreement. United Nations Framew. Conv. Clim. Chang. URL: https://unfccc.int/process-and-meetings/the-paris-agreement/the-paris-agreement/ (accessed 10.1.2021).

Visaria, M., Mudawar, I., 2012. Coiled-tube heat exchanger for High-Pressure Metal Hydride hydrogen storage systems - Part 1. Experimental study. Int. J. Heat Mass Transf. 55, 1782–1795. https://doi.org/10.1016/j.ijheatmasstransfer.2011.11.035

Weckerle, C., Bürger, I., Linder, M., 2017. Novel reactor design for metal hydride cooling systems. Int. J. Hydrogen Energy 42, 8063–8074. https://doi.org/10.1016/j.ijhydene.2017.01.066

Wei, T.Y., Lim, K.L., Tseng, Y.S., Chan, S.L.I., 2017. A review on the characterization of hydrogen in hydrogen storage materials. Renew. Sustain. Energy Rev. 79, 1122–1133. https://doi.org/10.1016/j.rser.2017.05.132

Yang, F., Meng, X., Zhang, Z., Yu, Y., 2008. Selection of alloys in a metal hydride heat pump-A new procedure. Int. Refrig. Air Cond. Conf. 2, 1–8.

Yang, M., Cheng, G., Xie, D., Zhu, T., Dong, Y., Ke, H., Cheng, H., 2018. Study of

hydrogenation and dehydrogenation of 1-methylindole for reversible onboard hydrogen storage application. Int. J. Hydrogen Energy 43, 8868–8876. https://doi.org/10.1016/j.ijhydene.2018.03.134

Yasuda, N., Tsuchiya, T., Okinaka, N., Akiyama, T., 2013. Application of metal hydride sheet to thermally driven cooling system. Int. J. Hydrogen Energy 38, 7469–7476. https://doi.org/10.1016/j.ijhydene.2013.04.011

Yip, H.L., Srna, A., Yuen, A.C.Y., Kook, S., Taylor, R.A., Yeoh, G.H., Medwell, P.R., Chan, Q.N., 2019. A review of hydrogen direct injection for internal combustion engines: Towards carbon-free combustion. Appl. Sci. 9, 1–30. https://doi.org/10.3390/app9224842

Yukesh Kannah, R., Kavitha, S., Preethi, Parthiba Karthikeyan, O., Kumar, G., Dai-Viet, N.V., Rajesh Banu, J., 2021. Techno-economic assessment of various hydrogen production methods – A review. Bioresour. Technol. 319, 124175. https://doi.org/10.1016/j.biortech.2020.124175

Zacharia, R., Rather, S.U., 2015. Review of solid state hydrogen storage methods adopting different kinds of novel materials. J. Nanomater. 2015. https://doi.org/10.1155/2015/914845

Zhang, F., Zhao, P., Niu, M., Maddy, J., 2016. The survey of key technologies in hydrogen energy storage. Int. J. Hydrogen Energy 41, 14535–14552. https://doi.org/10.1016/j.ijhydene.2016.05.293

Zhou, L., Zhou, Y., Sun, Y., 2004. Enhanced storage of hydrogen at the temperature of liquid nitrogen. Int. J. Hydrogen Energy 29, 319–322. https://doi.org/10.1016/S0360-3199(03)00155-1

Züttel, A., 2003. Materials for hydrogen storage. Mater. Today 6, 24–33. https://doi.org/10.1016/S1369-7021(03)00922-2

APPENDIX A

REACTOR SHELL SELECTION

Cylindrical reactor shell size for each design is chosen from nominal pipe size that are listed in ASME B36.19M. It is observed from Table A.1 that for same nominal pipe size of 6 inch, different schedule numbers are available with increasing tube wall thickness. From the concept of thin cylinders, allowable stress (σ_h) is given by,

$$\sigma_h = \frac{P_{\max} * D_i}{2 * t_{wall}} \qquad \text{(Eqn.A.1)}$$

where D_i is inner diameter and t_{wall} is wall thickness, while P_{max} is maximum operating pressure which is fixed at 8 MPa (80 bar) considering high pressure testing conditions. From ASTM A240 standard that specifies the mechanical properties of stainless steel, the yield strength of SS316 is taken as 205 MPa. Based on this, factor of safety is estimated as the ratio of yield strength over allowable stress.

Table A.1. Dimensions of SS316 pipes for nominal pipe size of 6 inch

Nominal pipe size (inch)	**Outer diameter (mm)**	**Schedule no.**	**Thickness (mm)**	**Allowable stress (MPa)**	**Resulting factor of safety**
6	168.28	5S	2.77	235.00	0.87
6	168.28	10S	3.40	189.98	1.08
6	168.28	40S	7.12	86.54	2.37
6	168.28	80S	10.97	53.36	3.84

Though resulting factor of safety for schedule number 80S pipe is high at 3.84, using it will be a case of over-specification as the parasitic thermal mass will be high due to increased weight of pipe. Hence, schedule number 40S pipe which has a factor of safety more than 2 is chosen for the size selection of 6 inch reactor shell. Following this protocol, 40S schedule pipes of nominal sizes 4 inch, 5 inch and 8 inch are chosen for comparative reactor design analysis.

APPENDIX B

ERROR ANALYSIS

The uncertainty in measurement of parameters have been estimated using the method proposed by Kline and McClintock (1953). The principle of estimation of uncertainty is as follows:

Consider a variable N dependent on various indepedndent measeured variables such as u_1, u_2, … u_n, then,

$$N = f(u_1, u_2, ..., u_n) \qquad \text{(Eqn.B.1)}$$

If the uncertainty in measured quantity N be ΔN and that for independent variables be Δu_1, Δu_2,… Δu_n, then the uncertainty ΔN is given by,

$$\Delta N = \frac{\partial N}{N} = \sqrt{\left[\left(\frac{\partial f}{\partial u_1}\right)\Delta u_1\right]^2 + \left[\left(\frac{\partial f}{\partial u_2}\right)\Delta u_2\right]^2 + ... + \left[\left(\frac{\partial f}{\partial u_n}\right)\Delta u_n\right]^2} \qquad \text{(Eqn.B.2)}$$

where, $\pm\partial N$ is the error in N. The primary measured parameters in the experimental investigations are temperature, amount of hydrogen transferred and the flow rate of HTF during the reactions. Hence, the error in their individual measurements are estimated.

1. Temperature measurement

The temperature at different locations is measured using calibrated metal-sheathed K-type thermocouples. The maximum possible uncertainty in the case of temperature measurement is estimated from the minimum value of the measured quantity and its accuracy. The minimum bed temperature measured is -17.4 °C and the accuracy is ± 0.5 °C for K-type thermocouple. Hence, the maximum uncertainty in temperature measurement is:

$$\frac{\partial T}{T} = \pm\frac{0.5}{17.4} = \pm 0.029 = \pm 2.9\% \qquad \text{(Eqn.B.3)}$$

2. Supply pressure measurement

The supply pressure is set through pressure regulator by monitoring pressure transmitter. The minimum set pressure was 10 bar and the accuracy of pressure transmitter is ± 0.5 bar. Hence, the maximum uncertainty in supply pressure measurement is:

$$\frac{\partial P}{P} = \pm\frac{0.5}{10} = \pm 0.05 = \pm 5\% \qquad \text{(Eqn.B.4)}$$

3. Measurement of hydrogen transferred

The amount of hydrogen transferred is obtained from Coriolis mass flow meter. The minimum value of hydrogen transferred was 2.57 g in 60 s. Hence, the maximum uncertainty in measurement of hydrogen transfer is:

$$\frac{\partial m_{H_2}}{m_{H_2}} = \pm\sqrt{\left(\frac{0.001}{2.57}\right)^2 + \left(\frac{0.1}{60}\right)^2} = \pm 0.0017 = \pm\ 0.17\% \qquad \text{(Eqn.B.5)}$$

4. Measurement of hydrogen transferred

Similarly, the flow rate of HTF is measured from flow meter for duration of 60 s. Hence, the maximum uncertainty in measurement of HTF flow rate calculated from volume and time

is:

$$\frac{\partial m_{HTF}}{m_{HTF}} = \pm\sqrt{\left(\frac{10}{1000}\right)^2 + \left(\frac{0.1}{60}\right)^2} = \pm 0.0101 = \pm\ 1.01\% \quad \text{(Eqn.B.6)}$$

5. Estimation of hydrogen storage capacity

The hydrogen storage capacity of MH is estimated as the amount of hydrogen absorbed/desorbed per kg of MH alloy (wt%). Minimum alloy considered in the system is of 2.75 kg which was filled using weighing balance with accuracy of ± 0.5 g. Hence, the maximum uncertainty in estimation of hydrogen storage capacity is:

$$\frac{\partial HSC}{HSC} = \pm\sqrt{\left(\frac{0.001}{2.57}\right)^2 + \left(\frac{0.0005}{2.75}\right)^2 + \left(\frac{0.1}{60}\right)^2} = \pm 0.0017 = \pm\ 0.17\% \quad \text{(Eqn.B.7)}$$

6. Estimation of heat transfer rate

The heat transfer rate is estimated from measured values of HTF flow rate and temperature as stated in Section 4.2.2. The maximum uncertainty in estimation of heat transfer rate is:

$$\frac{\partial \dot{Q}_t}{\dot{Q}_t} = \pm\sqrt{\left(\frac{0.5}{17.4}\right)^2 + \left(\frac{10}{1000}\right)^2 + \left(\frac{0.1}{60}\right)^2} = \pm 0.0305 = \pm\ 3.05\% \quad \text{(Eqn.B.8)}$$

7. Estimation of SCP

The SCP is estimated from heat transfer rate and mass of alloy as stated in Section 4.3.3. The maximum uncertainty in estimation of SCP is:

$$\frac{\partial SCP}{SCP} = \pm\sqrt{\left(\frac{0.5}{17.4}\right)^2 + \left(\frac{10}{1000}\right)^2 + \left(\frac{0.1}{60}\right)^2 + \left(\frac{0.0005}{2.75}\right)^2} = \pm 0.0305 \quad \text{(Eqn.B.9)}$$

$$\frac{\partial SCP}{SCP} = \pm\ 3.05\%$$

8. Estimation of COP

The COP is estimated from heat transfer rate and mass of alloy as stated in Section 4.3.3.

The maximum uncertainty in estimation of SCP is:

$$\frac{\partial COP}{COP} = \pm\sqrt{\left(\frac{0.5}{17.4}\right)^2 + \left(\frac{10}{1000}\right)^2 + \left(\frac{0.1}{60}\right)^2 + \left(\frac{0.0005}{2.75}\right)^2 + \left(\frac{0.0002}{0.01}\right)^2} \quad \text{(Eqn.B.10)}$$

$$\frac{\partial COP}{COP} = \pm 0.0365 = \pm\ 3.65\%$$

APPENDIX C

SPECIFICATIONS OF INSTRUMENTS

The specifications of instruments used for the experimental investigations are listed below:

1. Thermocouple

Type	:	K-type (metal-sheathed)
Make	:	Industrial Heators
Range	:	0 to 1400 °C
Accuracy	:	± 0.5 °C

2. Pressure transmitter

Make	:	Equinox
Model	:	EQ-PT-1000
Range	:	0 to 100 bar
Accuracy	:	± 0.5% of full scale
Output signal	:	4 to 20 mA

3. Data Acquisition System

Make	:	Keysight
Model	:	Agilent 34972A
Scan rate	:	22 to 66 channels/second
Scan intervals	:	0 to 99 hours; 1 ms time step
Accuracy	:	6 digits of resolution with 0.004%

4. Mass flow meter

Type	:	Coriolis mass flow meter
Make	:	Emerson Process Management Pvt. Ltd.
Model	:	CMFS007M323N2BMECZZ
Fluid	:	Hydrogen
Flow range	:	0 to 50 g/min
Flow accuracy	:	± 0.35% of full scale
Sensitivity	:	0.001g
Temperature range	:	-10 to 100 °C
Operating pressure	:	0 to 150 bar
Output type	:	4 to 20 mA signal

5. Hydrogen flow control valves

Make	:	Swagelok, USA
Type	:	Pack less metallic bellow type needle
Model	:	SS-4BG
Pressure range	:	0 to 120 bar
Temperature range	:	0 to 450 °C
End fittings	:	1/4 inch NPT

6. Recirculating Constant Temperature Bath

Make	:	Siskin Instruments
Model	:	Siskin Profchill RCC 7000 ST 40 Recirculating Chiller
Temperature range	:	-30 °C to 50 °C
Pumping speed	:	50 l/min
Cooling capacity	:	7 kW at 0 °C
Heating capacity	:	3.5 kW

7. Recirculating Constant Temperature Bath

Make	:	Siskin Instruments
Model	:	Siskin ProfclassHCB 200s heating circulating bath
Temperature range	:	40 °C to 110 °C
Pumping speed	:	50 l/min
Heating capacity	:	9 kW

8. Vacuum pump

Make	:	RAN VAC Technologies
Model	:	RV 2035
Pump-1	:	Rotary vacuum pump
Pumping speed	:	585 l/min
Vacuum pressure range	:	999 to 10^{-3} mbar

LIST OF PUBLICATIONS

In Peer-reviewed Journals

1. Nithin N. Raju, P. Muthukumar, P. Vivek Selvan, K. Malleswararao, Design methodology and thermal modelling of industrial scale reactor for solid state hydrogen storage, International Journal of Hydrogen Energy 44 (2019) 20278-20292.
2. Nithin N. Raju, Alok Kumar, K. Malleswararao, P. Muthukumar, Parametric Studies on $LaNi_{4.7}Al_{0.3}$ based Hydrogen Storage Reactor with Embedded Cooling Tubes, Energy Procedia 158 (2019) 2384-2390.
3. Alok Kumar, Nithin N. Raju, P. Muthukumar, Parametric Studies on $MmNi_{4.7}Fe_{0.3}$ based Reactor with Embedded Cooling Tubes for Hydrogen Storage and Cooling Applications, Journal of Energy Storage, 35 (2021) 102317.
4. Alok Kumar, Nithin N. Raju, P. Muthukumar, P. Vivek Selvan, Experimental studies on industrial scale metal hydride based hydrogen storage system with embedded cooling tubes, International Journal of Hydrogen Energy 44 (2019) 13549-13560.
5. P. Muthukumar, Alok Kumar, Nithin N. Raju, K Malleswararao, Muhammad M. Rahman, A Critical Review on Design Aspects and Developmental Status of Metal Hydride Based Thermal Machines, International Journal of Hydrogen Energy 43 (2018) 17753-17779.
6. P. Muthukumar, Manojkumar S. Patil, Nithin N. Raju, Mohd. Imran, Parametric investigations on compressor driven metal hydride based cooling system, Applied Thermal Engineering, 97 (2016) 87-99.

Book Chapters

1. Nithin N. Raju, S. Jana, P. Muthukumar, Influence of Geometric Configuration on Charging Characteristics of $MmNi_{4.6}Fe_{0.4}$ based Hydrogen Storage Device. In: Singh S., Ramadesigan V. (Eds.) Advances in Energy Research, Vol. 1 (2020). Springer Proceedings in Energy. Springer, Singapore, pp. 397-410.

Conferences

1. Nithin N. Raju, Sayantan Jana, P. Muthukumar, Influence of Geometric Configuration

on Charging Characteristics of $MmNi_{4.6}Fe_{0.4}$ Based Hydrogen Storage Device, 6th International Conference on Advances in Energy Research (ICAER 2017), 10th – 15th December 2017, IIT Bombay, Mumbai, India.

2. Nithin N. Raju, P. Muthukumar, K. Malleswararao, Determination of Absorption Conditions for $LaNi_{4.7}Al_{0.3}$ Based Hydrogen Storage Device: A Numerical Investigation, 5th International Conference on Computation Methods for Thermal Problems (Thermacomp 2018), 9th – 11th July 2018, IISc Bangalore, India.
3. Nithin N. Raju, Alok Kumar, K. Malleswararao, P. Muthukumar, Parametric Studies on $LaNi_{4.7}Al_{0.3}$ based Hydrogen Storage Reactor with Embedded Cooling Tubes, 10th International Conference on Applied Energy (ICAE 2018), 22nd – 25th August 2018, Hong Kong Polytecnic University, Hong Kong, China.
4. Nithin N Raju, Alok Kumar, P. Muthukumar, Experimental Studies on Metal Hydride based Hydrogen Storage and Cooling Applications, 21st – 23rd November 2019, Refcold 2019, Hyderabad, India.
5. Alok Kumar, Nithin N Raju, P. Muthukumar, Parametric Studies on $MmNi_{4.7}Fe_{0.3}$ based Reactor with Embedded Cooling Tubes for Hydrogen Storage and Cooling Applications, International Conference on Innovations in Thermo-Fluid Engineering and Sciences (ICITFES-2020), 10th – 12th February 2020, NIT Rourkela, India.
6. Alok Kumar, Nithin N Raju, P. Muthukumar, Experimental Studies on $MmNi_{4.7}Fe_{0.3}$ based Hydrogen Storage Device for Cooling Application, 6th National Conference on Refrigeration and Air Conditioning, 20th – 22nd February 2020, IIT Madras & KLN College of Engineering, India.